Universidade de Aveiro Departamento de Engenharia Mecânica
2012

Joana de Sousa Martins

Capacidade de proteção contra ondas de choque de sistemas multi-camada incorporando materiais celulares

Blast-wave absorption capacity of sandwich structures incorporating cellular materials

Universidade de Aveiro Departamento de Engenharia Mecânica
2012

Joana de Sousa Martins

Capacidade de proteção contra ondas de choque de sistemas multi-camada incorporando materiais celulares

Blast-wave absorption capacity of sandwich structures incorporating cellular materials

Tese apresentada à Universidade de Aveiro para cumprimento dos requisitos necessários à obtenção do grau de Doutor em Engenharia Mecânica, realizada sob a orientação científica do Doutor Filipe Miguel Horta e Vale Teixeira-Dias, Professor Auxiliar com Agregação do Departamento de Engenharia Mecânica da Universidade de Aveiro.

o júri / the jury

presidente / president

Prof. Doutor Armando da Costa Duarte
professor catedrático da Universidade de Aveiro

Prof. Doutora Helena Margarida Nunes Pereira
professora catedrática do Instituto Superior de Agronomia da Universidade Técnica de Lisboa

Prof. Doutor António Joaquim Mendes Ferreira
professor catedrático da Faculdade de Engenharia da Universidade do Porto

Prof. Doutor José Joaquim de Almeida Grácio
professor catedrático da Universidade de Aveiro

Prof. Doutor Filipe Miguel Horta e Vale Teixeira-Dias
professor auxiliar com agregação da Universidade de Aveiro

Prof. Doutor José Miguel Almeida da Silva
professor auxiliar da Universidade da Beira Interior

Prof. Doutor Rui António da Silva Moreira
professor auxiliar da Universidade de Aveiro

To my mother. Without your constant presence throughout my life everything would be worth nothing.

To Nelson, whose friendship and dedication are a mainstay in my life.

Finally to João for the help, patience, kindness and love.

"My definition of an expert in any field is a person who knows enough about what's really going on to be scared."
(Phillip James Plauger)

acknowledgements

There are several people I would like to thank, for different reasons. First of all, I have no words to express how grateful I am to my supervisor Professor Filipe Teixeira-Dias, for proposing this work to me and for the support, patience, guidance and above all for his friendship.

I am also very thankful to Capt. IMM Frederik Coghe, Dr. Dimitrios Kakogiannis and Eng. Bruno Reymen for their supervision during my stay in the Royal Military Academy in Brussels. Their help was also fundamental throughout my work.

My acknowledgements go also to Eng. António Coelho and Eng. Rui Palavra from Amorim Cork Composites for their help in manufacturing the specimens tested in this work.

I also thank Eng. António Festas for his availability.

I would also like to acknowledge the financial support given by the Portuguese Science and Technology Foundation (FCT — Fundação Portuguesa para a Ciência e a Tecnologia) through grant SFRH/BD/43380/2008 and project PTDC/EME-PME/73503/2006.

To all my colleagues and professors in the GRIDS research group in the University of Aveiro I would like to express my gratitude. Their presence and support was fundamental.

I would also like to thank all of my professors at the University of Aveiro, who significantly contributed for my personal and academic education, namely Professor Nikolai A. Sobolev, who was always available.

Last, but not least, I thank my friends and family, particularly my mother Maria and my forever friend Nelson Serra, my boyfriend João and my friends Bernardete, Dulce, Guilhermina, Margarida, Marisa, Raquel and Teresa for their love and care, and for being there all the time.

palavras-chave

Estrutura sanduíche, onda de choque, absorção de energia, material celular, aglomerado de cortiça.

resumo

A incorporação de materiais absorsores de energia (AE) em sistemas de proteção é uma clara possibilidade de melhoraria do seu desempenho, devido à elevada relação entre a sua resistência e o seu peso, e a excelente capacidade para absorverem energia quando solicitados dinamicamente. As propriedades mecânicas da cortiça (*e.g.* a baixa densidade e a elevada rigidez e resistência específicas) sugerem que este material — assim como os seus derivados — podem apresentar propriedades excelentes quando aplicados como núcleos em sistemas AE do tipo estrutura sanduíche. Esta dissertação engloba trabalho experimental e numérico. O primeiro conjunto de testes experimentais consistiu na caracterização experimental dinâmica (ondas de choque de explosivos) do comportamento de dois micro-aglomerados de cortiça (MAC), NL20 e TB40. Um pêndulo balístico de 4 cabos foi usado para a medição do impulso transmitido a uma amostra de MAC impactada por uma onda de choque com origem na detonação de um explosivo energético. Foi registado o movimento do pêndulo e os valores de força resultantes. Um modelo numérico do problema recorrendo ao método dos elementos finitos (MEF) foi também desenvolvido, apresentando uma elevada correlação com a análise experimental, permitindo assim o desenvolvimento de um modelo constitutivo adequado à modelação do comportamento dinâmico dos MAC neste tipo de solicitações. Na segunda fase de testes experimentais, os MAC testados anteriormente são incorporados como núcleos em estruturas sanduíche com faces de alumínio (liga 5754-H22). Foram medidos os valores de defleção e o impulso transmitido ao pêndulo através do movimento oscilatório. São determinados os efeitos da densidade e da espessura dos núcleos na resposta estrutural do sistema. Também neste caso foi desenvolvido um modelo recorrendo ao MEF e posteriormente validado com resultados experimentais.

keywords Sandwich structure, blast-wave, energy absorption, cellular material, cork compound.

abstract Structures incorporating energy absorbing materials (EA) are highly relevant in the design of blast protection systems due o their high strength-to-weight ratio and excellent energy absorption capacity under dynamic loading. The mechanical properties of cork (*e.g.* low density and high specific stiffness and strength) suggest that this material — and its compounds — may have excellent properties when acting as core in energy absorbing sandwich structures. This thesis focuses on experimental and numerical work. The first experimental set of tests presented consisted in the experimental characterisation of the dynamic (blast) behaviour of two micro-agglomerated cork compounds (MAC), NL20 and TB40. A 4-cable ballistic pendulum was used to measure the impulse transmitted to the specimen subjected to a shock-wave originated from the detonation of a high explosive. The displacement/movement of the pendulum and load values were measured. A numerical study of the problem using the finite element method (FEM) led to a good correlation with the experimental analysis leading to the development of a material constitutive model that suited the dynamic behaviour of the studied MAC compounds along the analysed loading regimes. On the second stage of the experimental work the two micro-agglomerated cork compounds tested previously were incorporated as cores in sandwich structures with 5754-H22 aluminium alloy face sheets. The deflection of the front and back face sheets was measured as well as the transmitted impulse from the oscillatory movement of the pendulum. The effects of the core thickness and density on the structural response were determined. A numerical model of the problem, again using the FEM, was developed which was then validated with the experimental results.

Table of Contents

List of Figures

List of Tables

List of Acronyms

ALE	Arbitrary Lagrangian Eulerian
ANFO	Ammonium Nitrate and Fuel Oil
CONWEP	Conventional Weapons
EA	Energy Absorber
EOS	Equation of State
EVE	E-Glass Vinyl Ester composites
FE	Finite Element
FEA	Finite Element Analysis
FEM	Finite Element Method
FML	Fibre-Metal Laminates
fps	frames per second
FRP	Fibre Reinforced Plastic
HE	High Explosive
JWL	Jones-Wilkins-Lee
MAC	Micro-Agglomerated Cork
PE	Plastic Explosives
PFV	Photron FASTCAM Viewer
PS	Protection System
PVDF	Polyvinylidene Fluoride
RDX	Research Department Explosive
RMA	Royal Military Academy
SDOF	Single-Degree-of-Freedom
SEM	Scanning Electron Microscopy
SHPB	Split Hopkinson Pressure Bar
TNT	Trinitrotoluene
VARTM	Vacuum Assisted Resin Transfer Moulding

Part I

Introduction and state-of-the-art

Chapter 1

Motivation, objectives and reading guide

A brief description of the subject being investigated is made in this chapter along with the motivation. The main objectives defined for this research work are presented. A reading guide to this thesis is also proposed with information on the subjects that can be found in each part chapter of the thesis.

1.1 Motivation

Today, with the current events concerning terrorist attacks, it is imperative to perform research and development in issues related to the impact resistance of engineering structures subjected to blast-waves. The need to protect structures from high intensity dynamic loading such as, for example, explosive reactions, has been stimulating and renewing the interest on new materials and structures [Xue and Hutchinson 2003, Xue and Hutchinson 2004]. The development of protection systems against shock-waves originated by either terrorist attacks (using explosive devices) or other situations originating blast-waves (*e.g.* accidental explosions), plays an important role in the development defence armour applications.

Explosions are phenomena that cause an extremely fast increase of heat and pressure in the environment. This resultant overpressure propagates as a pressure wave and can travel at supersonic velocities [Krehl 2009]. In such phenomena, the pressure decays exponentially as the stand-off distance (distance between the centre of the detonation and the target in consideration) increases. Generally, the magnitude of peak pressure of an explosion is often much higher than the static collapse pressure of the structures that may be subjected to these blast-waves. Due to this high pressure — and consequent high loading rates in the materials — some materials usually undergo large plastic deformations. Nonetheless, before they reach collapse some of these materials — which

can experience large plastic strains — have the advantage of absorbing/dissipating high levels of energy. These kind of materials are often known as energy absorbers (EA) [Zhu *et al.* 2008a]. The amount of energy that a material (or structure) can absorb is the characteristic that ultimately defines its reliability and liability in military and defence armour applications. Cellular materials, honeycomb materials and structures, foams, composite materials, *etc.* are considered to be potential candidates as energy absorbers [Xue and Hutchinson 2003, Xue and Hutchinson 2004, Zhu *et al.* 2008a, Zhu *et al.* 2008b, Sousa-Martins *et al.* 2012, Sousa-Martins *et al.* 2013].

Comparing energy absorbers with other structures, that can only absorb small amounts of energy and undergo only small elastic deformations, EA have the ability to sustain intense impact loads by, for example, drastically changing their geometry, by strain-hardening and strain rate effects. In addition, fracture is also considered as an energy absorption mechanism on some materials, as for example, ceramics. Nonetheless, unlike the description made above for EA (*i.e.* high levels of energy are absorbed before collapse), ceramics are materials which do not experience elastic deformation and almost instantly after impact fail. Thus, fracture is the most common mechanism of deformation in most ceramic materials due to their low ductility (*e.g.* the impact from a pressure wave).

The need to protect certain structures from high intensity dynamic loading (such as those originated from explosive reactions) has stimulated and renewed the interest on the study of the dynamic behaviour of metallic structures (among others) subjected to high strain rate loading. As it is known, a possible approach is to use layered systems such as sandwich structures to disperse the mechanical impulse transmitted to the structure and protecting structures, people, vehicles, *etc.* [Xue and Hutchinson 2003, Xue and Hutchinson 2004]. If sandwich structures are being used as EA, energy can be absorbed by the face sheets if significant bending or stretching is allowed to occur. Sandwich structures, namely their cores, can sustain large deformations under almost constant load, enabling them to absorb large amounts of energy. Presently, the most frequent core materials used for sandwich structures are metallic [Qiu *et al.* 2005, Nemat-Nasser *et al.* 2007]. Some work has been done, for example, in protection and defence systems incorporating cellular and porous materials [Rathbun *et al.* 2006, Zhu *et al.* 2008b, Dharmasena *et al.* 2008, Karagiozova *et al.* 2009, Nurick *et al.* 2009]. However, the work done so far is almost all limited to the use of materials with a regular structure (*e.g.* honeycomb structures) and/or metallic (*e.g.* metal foams). However, when the weight of the sandwich structure plays an important role, non-metallic cellular materials must also be considered and investigated [Wang *et al.* 2009, Langdon *et al.* 2012, Hassan *et al.* 2012, Sousa-Martins *et al.* 2013].

Cellular materials are good candidates in the fields of energy absorption. The designation "cellular" is due to the geometry of these materials which are made by empty cell elements (either open or closed) [Pereira 2007]. Most cellular materials are characterised by exhibiting linear elastic behaviour until the yield stress followed by a region of constant stress for increasing strain. Thus, this capacity of sustaining very

large strains at low stress values, perfectly fits the requirements of an EA. Cork is a natural cellular material. Some studies report the application of cork as a possible innovative solution for an EA [Nóvoa *et al.* 2004, Gameiro *et al.* 2007b, Gameiro and Cirne 2007, Castro *et al.* 2010, Silva *et al.* 2011, Sousa-Martins *et al.* 2012, Sousa-Martins *et al.* 2013, Alcântara *et al.* 2013, de Carvalho *et al.* 2013].

The research presented in this thesis intends to incorporate new innovative non-metallic and light-weight core solutions as a core in a sandwich structure prototype. Cork derivatives were used as candidate EA for the sandwich structure core. The materials used, also known as micro-agglomerated cork (MAC) compounds, are made of cork granules and specific binders. The final aim consists on the characterisation of the behaviour of sandwich structure prototypes in the dynamic loading regime. The dynamic solicitation of the sandwich structures was achieved using explosives. Before the prototype of a sandwich structure could be developed and manufactured, several steps had to be considered and analysed. These steps and other objectives of this investigation will be presented in the following section.

1.2 Objectives

The main objective of the investigation reported in this thesis was to cooperate in an active way for the development of a protection system (PS) against blast-waves, originated both by terrorist attacks or accidents. In the scope of this investigation, several stages had to be covered, such as: review of the current state-of-the-art on protection systems and shock dissipation, followed by the development, design and modelling of a prototype sandwich structure that incorporates cellular materials. Potential applications for this prototype can be civil and military vehicles, infrastructures, luggage containers, armoured doors, *etc.* Summarising, the main objectives of this work are the following:

- Perform a detailed bibliographic review of the current state-of-the-art;
- Characterisation of the mechanical behaviour of layered protection systems (sandwich structures) in blast scenarios;
- Development/implementation of the corresponding experimental procedures;
- Study of the effects of physical parameters on the performance of the PS, such as geometry, materials, mass of the explosive charge and corresponding stand-off distance;
- Development of constitutive models and numerical procedures to model the shock and blast energy absorption by cellular materials, namely MAC compounds;
- Implementation and validation of the constitutive models with the experimental data and results; and

- Numerical analysis and validation of the behaviour of the PS prototype using finite element method techniques.

1.3 Reading guide

This thesis is divided in four parts. Each of these parts is subdivided in chapters, making a total of eleven chapters.

The first part of this thesis includes chapters 1 to 4. A brief presentation of the subject of investigation is made, in chapter 1, along with the general motivation. The main objectives of this research work are primarily presented. In addition, a reading guide is presented, where a glimpse of the contents of each chapter is given to the reader.

An overview on explosives and their properties is the scope of chapter 2. Low and high explosives are referenced and a special focus is given to the subgroups that include the high explosives category. A dimensional analysis of the explosive will also be taken into consideration. In order to evaluate the effect of explosive charges and the interaction of blast-waves with structures, some background knowledge is needed. In this chapter a review on the types of explosive loading is also presented. The main focus is given to the air blast loading, in which the explosive charge is detonated in air. The phenomena that derive from such types of loading are referred and categorised in phases. Concepts such as the blast-wave pressure decay and pressure profile are explained and a reference to the blast loading response of structures is made.

Several topics will be covered in chapter 3, such as a review on the most relevant literature available about the response of sandwich structures to blast loading, failure modes in these structures and energy absorption in cellular materials. A state-of-the-art review on cork is also presented. Production, types of cork compounds, microscopic structure, mechanical behaviour, mechanical properties and applications of cork are described here.

Chapter 4 is entirely dedicated to the constitutive modelling of the materials used. As is well known, constitutive modelling leads to the definition of the material behaviour. In the first part of this chapter, an introduction with background knowledge on constitutive modelling concepts is given, in order to better understand the second part of the chapter, which is related to the numerical material models used in the scope of this work. A detailed description of the constitutive behaviour of the materials is presented.

Part II of this document (that includes chapters 5 to 7) deals with the experimental analyses performed within the scope of this work. As the main objective of this investigation is the study and analysis of the capacity of MAC compounds to absorb energy when loaded by blast-waves, a setup where the sandwich structures can be tested, had to be developed. A 4-cable ballistic pendulum was the setup chosen for this purpose.

After a brief review on the application of ballistic pendulums to blast-wave absorption, a presentation of the experimental facilities used as well as the equipment inherent to the ballistic pendulum is described in chapter 5. The experimental characterisation of the dynamic behaviour of micro-agglomerated cork (MAC) is presented in chapter 6. A 4-cable ballistic pendulum system was used to measure the transmitted impulse to cylindrical specimens subjected to blast-waves originated from the detonation of a high explosive. The displacement and the transmitted impulse of the pendulum were measured and the coefficient of restitution of the whole system was determined.

The second component of the investigation here presented covers the experimental characterisation of two MAC compounds incorporated as cores in sandwich structures with aluminium alloy (5754-H22) face sheets. The results from these analyses are presented in chapter 7. Several sandwich structures were tested with constant thickness of the face sheets and different core thicknesses. These structures were fixed to the 4-cable ballistic pendulum and subjected to blast-waves originated by the detonation of 30 g of C4 high explosive at a stand-off distance of 300 mm. The deflection of the front and back face sheets was measured as well as the overall movement of the pendulum. The influence of the thickness and core density on the structural response of the sandwich structure was analysed.

Part III, which includes chapters 8 to 10, is dedicated to the numerical modelling of the experimental tests using the finite element method (FEM). The first chapter in this part is an overview on finite element analysis and available commercial software to blast-wave absorption fields of investigation. A brief approach to the principles of FEM analysis is presented.

The blast-wave absorption numerical modelling of the cylindrical specimens tests is covered in chapter 9. Two different approaches were used to model these phenomena. The first one considers the effects of the explosive, that is, only a blast pressure wave is created (the explosive is not modelled) that impacts the structure. The second approach deals with the lagrangian and eulerian formulation of the involved materials, where the both explosive and the air are modelled/and discretised, and their interaction with the structures is analysed.

The third chapter regarding numerical modelling is chapter 10 where the numerical model developed and implemented to test the efficiency of the MAC compound cores in the sandwich structure protection system is described. The geometrical model of the target is presented and constitutive models are detailed for all involved materials: MAC compound cores and aluminium alloy face sheets. Boundary conditions and contact definitions are also described in this chapter.

Part IV (including chapter 11) ends this thesis. In this chapter the main conclusions are pointed out and possible future lines of research and work are suggested.

Chapter 2

Explosions, blast-waves and their interaction with structures

With this chapter it is intended to give the reader an overview on explosives and their properties. Low and high explosives will be referenced and a special focus will be given to the subgroups that complete the high explosives category. A review on the types of explosive loading is presented. The main focus is on air blast loading. Concepts such as pressure decay and pressure profile in a blast-wave are explained and a reference to the blast loading response of structures is made.

Explosion phenomena can be characterised by an extremely fast increase of heat and pressure. This resultant overpressure propagates as a wave (*i.e.* travels at supersonic velocity) [Krehl 2009]. In explosive phenomena the pressure decays exponentially as the stand-off distance increases. The stand-off distance is the distance between the source (centre) of the explosion and the impacted structure. An overview of the main concepts behind explosion phenomena and explosives is given in the following sections.

2.1 Types of explosive loading

There are several different types of loading within blast: (i) air blast loading, in which the explosive is detonated in air; (ii) underwater blast loading, in which the explosive is detonated in a fluid (often water) and (iii) simulated blast loading where no explosives are used, since the loading is achieved in equivalent forms, such as for example a gas gun (mainly for research purposes) [Shukla *et al.* 2010]. The work here presented focuses on the first type of blast loading, that is, air blast loading. The image in figure 2.1 shows a 500 ton high explosive charge being detonated in air. This particular photograph was taken in April 1965 on Kahoolawe Island, Hawaii. The hemispherical front wave from the blast event is perceptible in this image (see arrows in figure).

Figure 2.1: Detonation of 500 ton of high explosive charge in air (adapted from [SH 2012]).

2.1.1 Air blast loading

Air blast loading phenomena can be divided into significantly distinct phases, namely [Smith and Hetherington 1994]:

- *Phase 1*: A condensed high explosive is initiated/detonated and the explosion reaction generates hot gases which achieve very high pressures and temperatures. Resulting maximum pressure is often in the range of 100 to 300 kbar and temperatures in the range of 3000 to 4000°C.

- *Phase 2*: Conditions from *Phase 1* lead to a violent expansion of the gases from the explosive and the surrounding air is forced out of the space it occupies. These explosion gases compress the air located along its front, consecutively forming the so called blast-wave.

- *Phase 3*: The pressure associated to the explosion gases decreases to atmospheric pressure as the blast-wave moves away from the source of the explosion, with the pressure in the front wave also decreasing with increasing distance from the source. Thus, the pressure of the explosion gases decreases as the gases expand. However, the final pressure does not equal ambient pressure. Explosion gases tend to cool down which make their pressure lower than ambient pressure. This "negative" pressure happens due to the inertia of the flow of the burnt gas that will drop below ambient pressure. During this phase, often called negative pressure phase, even though the static pressure of explosion gases is the atmospheric pressure, since gas molecules have kinetic energy associated with it, more time and distance will be required to equal their momentum to zero then lowering the pressure to under atmospheric pressure values.

2.1.2 Pressure decay and blast-wave profile

The shape of the pressure-time profile for, for example, a high explosive in air, is shown in figure 2.2, where P_b is overpressure (or air blast pressure), t_a is the time of arrival of the blast-wave and P_atm is the atmospheric pressure. The term overpressure refers to the pressure above ambient atmospheric pressure. The peak pressure occurs immediately after detonation. The pressure's exponential decay to the pre-shock level occurs at time $t_\mathrm{a} + t_\mathrm{d}$ [Zhu and Lu 2007]. The value of the peak instantaneous overpressure P_b will depend on the distance of the point of measurement from the centre of the explosion [Bulson 1997]. The impulse of the load, I, is defined as the area enclosed by the load-time curve (defined generically by $F(t)$) and the time axis (time integral) and its magnitude is given by the following expression:

$$I = \int_{t_\mathrm{a}}^{t_\mathrm{a}+t_\mathrm{d}} F(t)\mathrm{d}t. \tag{2.1}$$

An equivalent expression, expressed in terms of pressure, as in the following equation,

$$I_\mathrm{s}^* = \int_{t_\mathrm{a}}^{t_\mathrm{a}+t_\mathrm{d}} P(t)\mathrm{d}t, \tag{2.2}$$

gives the specific impulse (I_s^*) (impulse divided by the area). In equation 2.2 $P(t)$ is the overpressure as a function of time. When the incident pressure wave encounters a structure while travelling, it produces a reflected pressure wave. Consequently, pressure intensity near a hard surface is enhanced because the reflected wave adds to the incident wave, leading to pressure amplitude that is higher (for example, if an undeformable rigid structure is assumed) than the incident pressure wave [Bulson 1997].

2.2 Response of structures

The structural response and damage level of structures depend not only on the applied load (*e.g.* pressure load) but also on the structure's own characteristics, such as its geometry, materials, *etc.* A large number of aspects contribute to increase the complexity of the analysis of the dynamic response of blast loaded structures. Variables such as the non-linearity of the material's behaviour and the high strain rates involved in such phenomena are just two of the many complexities present in such field of investigation. Blast load events are characterised by high associated strain rates, typically in the range of 10^2 to 10^4 s^{-1} [Ngo *et al.* 2007]. Typical strain rates from several types of loadings are shown in figure 2.3.

2.2.1 Static and dynamic loading

The main differences between static and dynamic loading will be presented in the following paragraphs. As an example, a house subjected to a blast-wave can be reduced

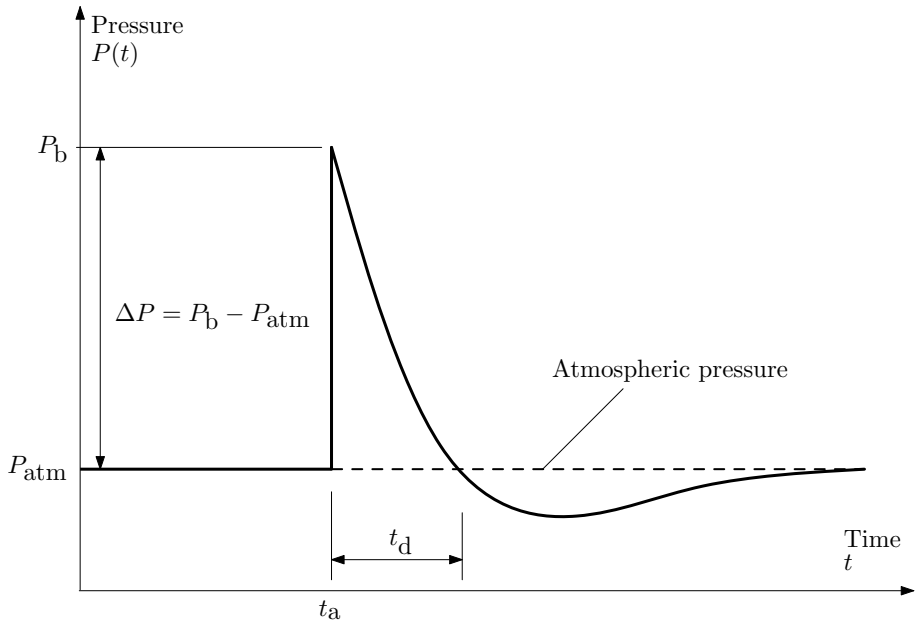

Figure 2.2: Schematic representation of the pressure profile of a blast-wave as a function of time.

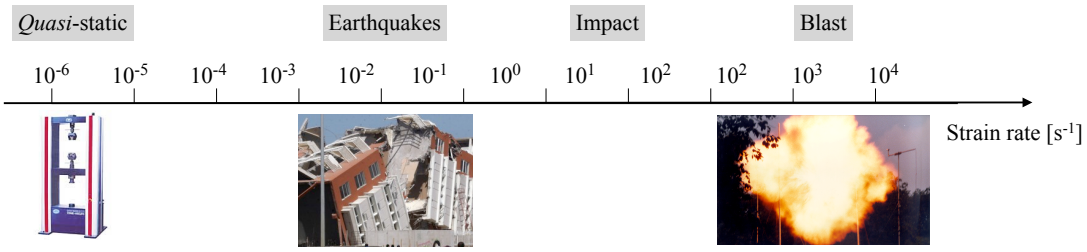

Figure 2.3: Typical values for strain rates in different loading scenarios (adapted from [Ngo *et al.* 2007]).

to a single-degree-of-freedom (SDOF) system, as can be seen in figure 2.4. In the first simplification the roof is represented by a rigid beam, while the walls are represented by vertical cantilevers. However, this approximation can be simplified to a single spring-mass system. The load-time profile area is triangular. The response of the system is represented by the displacement of the mass m and is not only dependent on the mass itself and load applied but also on the natural frequency of the system, given by,

$$T = 2\pi\sqrt{\frac{m}{k}}, \tag{2.3}$$

where k is the stiffness of the system.

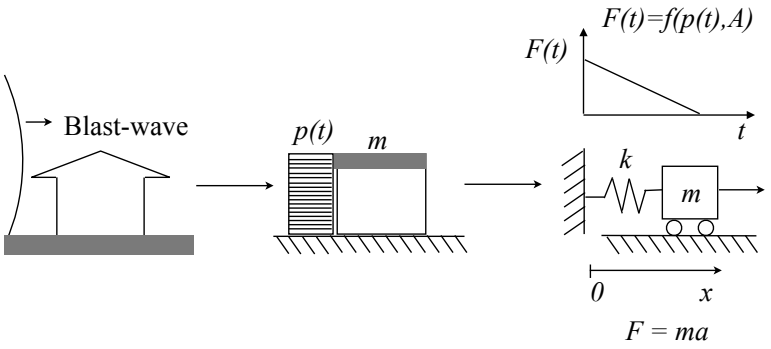

Figure 2.4: A house subjected to a blast-wave, reduced to a single-degree-of-freedom system (adapted from [Bjerketvedt *et al.* 1992]).

In figure 2.5, the ratio between the displacements in dynamic and the static regime of the SDOF system is plotted against t/t_{load} in the case of the triangular load. The duration of the applied load is represented by t_{load}. It should be noticed that in this example no damping was considered. If damping was present in this system, mass m will eventually come to rest after some time.

The structural response to blast loading is significantly influenced by the ratio between the duration of the applied load and the natural frequency of the system (t_{load}/T) [Ngo *et al.* 2007]. For low (t_{load}/T) the maximum displacement is lower than the maximum displacement for the static load ($x_{\max}$ [static]$= F/k$), while for high (t_{load}/T) values, the maximum displacement can be higher than the static load maximum displacement. Although the simplicity in this SDOF analysis is evident, real structures have many degrees of freedom, making the analysis much more complex. However, this simplified analysis can help illustrate the generic behaviour of structures subjected to dynamic loading.

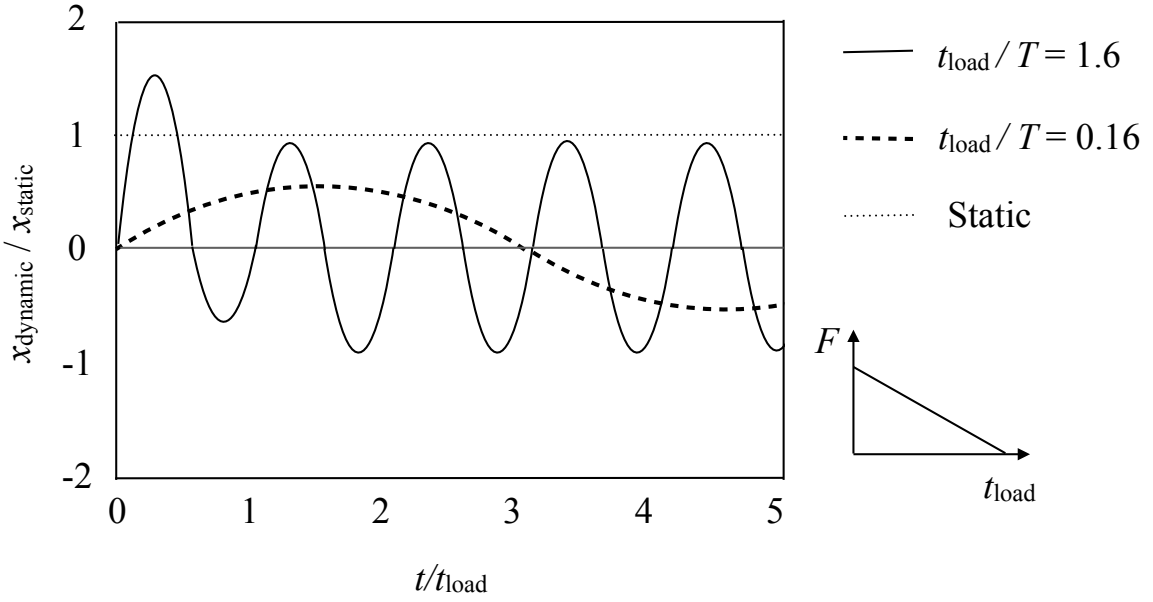

Figure 2.5: Ratio between the displacements in dynamic and the static regime of the SDOF system plotted against the adimensional time t/t_{load} for the case of a triangular load (adapted from [Bjerketvedt *et al.* 1992]).

2.2.2 Impulsive loading

The response of a structure in a blast scenario is related both to its natural period and to the duration of the event. The work here presented is related to the impulsive loading of structures, that is, to situations where a structure is subjected to a single impulsive load characterised by a short live period (that is, the load duration is short relative to the response time of the system). One example is when an explosive charge is detonated and the resultant pressure wave impacts a solid body. The load on a structure is often expressed as a combination of the peak overpressure and the impulse delivered to the exposed area of the structure [Needham 2010]. As the load on the surface of a specific structure may dramatically change depending on the position of the measurement, one way to overcome this is to divide the projected area of the structure in a finite number of parts which, if small enough, can be considered to be uniformly loaded. In the impulsive loading regime, the duration of the load is short relative to the response time of the system (which is influenced by the natural frequency of the system) [Krauthammer 2008]. Figure 2.6 (a) is a schematic representation of this situation, where the load applied to a structure is removed before it can undergo significant deformation. In the *quasi*-static loading regime (see figure 2.6 (b)), the load-time profile is larger than the maximum load response time, meaning that the applied load dissipates very little before maximum deformation or resistance is achieved by the system at time $t = t_{\text{max}}$. In this case, the response (resistance history) depends only the load peak and the structural stiffness of the system (k). Additionally, and similarly

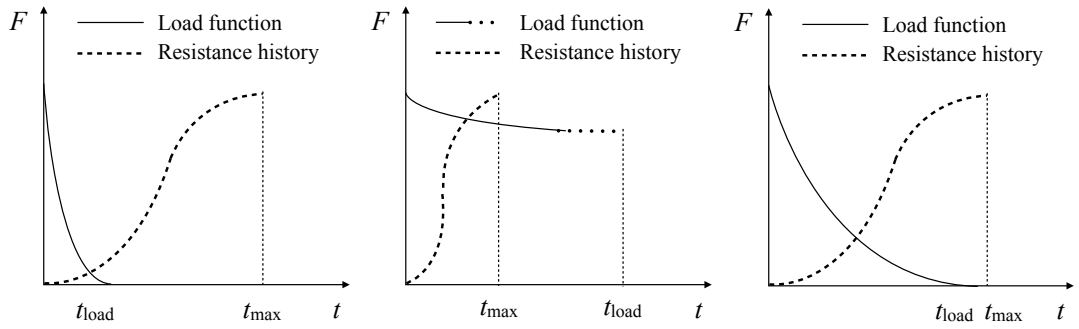

Figure 2.6: Schematic representation of time responses for different types of loading: (a) impulsive, (b) *quasi*-static and (c) dynamic loading (adapted from [Krauthammer 2008]).

to the impulsive loading regime, the maximum response of the *quasi*-static regime is independent of the loading-time profile. In the dynamic regime the duration of the load and system response time are approximately the same or of the same magnitude as can be seen in figure 2.6 (c) and the response of the system is more complex. In this specific case the load-time profile has a significant influence on the response of the system.

2.3 Dimensional analysis of the explosive

The geometry of the explosion source strongly determines how fast the blast pressure decreases from the centre of the explosion [Krehl 2009]. The following three basic cases can be distinguished in terms of the influence of the geometry of the explosion source:

- One-dimensional (1D) explosion models are commonly used in shock-wave research due to their simplicity, which allows scientists to quickly test theories. A classical example of a one-dimensional approach is a bursting membrane in a shock tube.

- Ideal cylindrical explosions can be modelled by sufficient long wires and correspond to the two-dimensional (2D) explosion case.

- All man-made explosions are, however, three-dimensional (3D). If a sufficiently large distance is observed between the detonation point and the load imparted part or structures, the shape of the explosive product propagation roughly approaches the ideal case of a true spherical shock-wave. This type of explosion wave is associated to the most difficult analytical treatment and distinguishes from the first two approaches because the pressure decay with distance is much faster.

2.4 Types of explosions

There are three different main types of explosions: mechanical, nuclear and chemical.

Mechanical explosion can be identified, for example, in the bursting of a sealed or partially sealed container under internal pressure.

Nuclear explosions result from an instantaneous fusion or fission process. These terms refer to physical phenomena where, for example, in the fission process, a nucleus from an atom is split apart and large amounts of energy are released. Fusion processes occur when small nuclei are combined with a consequent release of energy. Nuclear explosions are intrinsically related to high-temperature and high-pressure physics. Such events are accompanied by the emission of electromagnetic radiation over a wide spectral range, such as light, heat, radio-waves and gamma rays, generally referred to as "thermal radiation".

Chemical explosions may be defined as extremely rapid conversion of the solid or liquid bulk of an explosive into gas or vapour which is highly expanded by the heat generated during the transformation and, consequently, occupies many times the volume of the original substance [Krehl 2009]. This work focuses on chemical explosions. This type of explosion is necessarily connected to an exothermic reaction of a chemical explosive. Explosions in air are related to a fast release of energy from a specific point in space. The signature "blast" is associated to these types of explosions. When a condensed high explosive material detonates, almost 100% of the released energy is converted into blast energy [Smith and Hetherington 1994]. It is worth noting that the concept of blast energy is associated to both thermal and kinetic energy, since explosions release energy in these two main forms. Chemical explosions release thermal energy in the form of heat. Gases from the explosive are formed in a explosion phenomena, which rapidly expand producing the shock-wave. Thus, explosives release energy into the surrounding environment both as heat and as work.

2.5 Classification of explosives

Explosives are solid or liquid[1] substances in a metastable[2] state. This condition allows explosives to experience rapid chemical reactions without the participation of external reactants such as atmospheric oxygen [Meyer *et al.* 2007]. Several different criteria can be used when classifying explosives. A brief description to some of these criteria is presented in the following paragraphs.

[1] Gases and gaseous mixtures can also be explosive. Explosive mixtures are often generated spontaneously (*e.g.* leaks in gas pipes).

[2] Metastability of a body or system: refers to a state of apparent equilibrium, although capable of changing to a more stable state.

2.5.1 Chemical decomposition reaction and sensitivity

Explosives can be classified according to their chemical decomposition reaction. The two types of decomposition here presented refer to deflagration and detonation. In deflagration the decomposition of the material is propagated by a flame front which moves relatively slowly through the explosive material. Deflagration is characteristic of low explosives. There are two different types of low explosives: propellant and pyrotechnic. Propellants burn to propel projectiles such as artillery shells, small-arms rounds and rockets [Smith and Hetherington 1994]. The propellants can also be guns or rocket propellants. Black powder is an example of a gun propellant and liquid fuels are rocket propellants. Pyrotechnic explosives are materials such as flashes, flares or fireworks. These are capable of undergoing self-contained and self-sustained exothermic chemical reactions for the production of gases, light, heat, smoke and/or sound.

Detonation refers to the process where the decomposition is propagated by an explosive shock-wave that travels through the explosive material. Detonation is associated to high explosives. These materials detonate to create shock-waves, to burst or to shatter materials. High explosives can also be classified in terms of their chemical sensitivity, which is the ease with which the chemical reaction can be initiated. A primary explosive is one that can be easily detonated by simple ignition from a spark, flame or impact. Examples of these types of explosives are mercury fulminate, lead and silver azide, *etc.* Secondary explosives are not as easy to detonate as primary explosives and the detonation is initiated by the detonation impact of an initial (primary) explosive. These can be classified as military or industrial explosives. Trinitrotoluene (TNT) and Research Department Explosive (RDX) are examples of military explosives. ANFO (also known as AN/FO) is a widely used bulk industrial explosive mixture of ammonium nitrate (AN) and fuel oil (FO). The main use of ANFO is in dry blast-holes. ANFO is suitable for most dry blasting applications. A schematics on the classification of explosives is presented in figure 2.7.

The images in figure 2.8 are two examples of primary and secondary explosives. A blasting cap for primary explosives is shown in figure 2.8 (a) and two blocks of TNT, in which it is possible to see that the primary explosive has already been attached, are shown in figure 2.8 (b).

2.5.2 Explosive power

Another classification criteria used to classify explosives is related to their explosive power or, in other words, their ability to do work. The explosive power is intrinsically related to the energy delivered by the explosive (*i.e.* fragment projection, air-blast, high-velocity jet and underwater shock, *etc.*). The explosive power of an explosive is determined by its power index, P_{index}, which corresponds to the product of the heat of the explosion, Q, to the gas volume per unit mass of explosive, V, relative to the

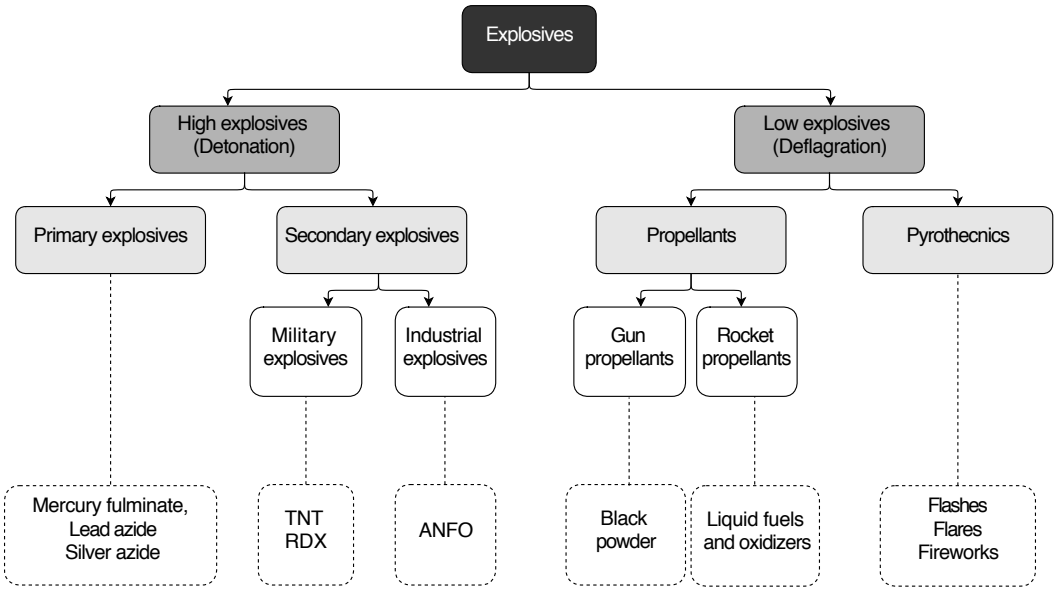

Figure 2.7: Classification of explosives and examples (adapted from [Meyer *et al.* 2007]).

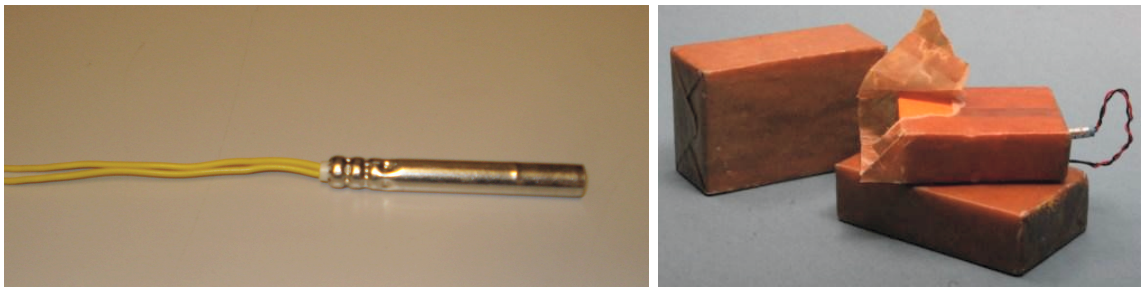

(a) (b)

Figure 2.8: (a) Blasting cap and detonator for primary explosives and (b) TNT explosive.

power index of picric acid, as in the following equation:

$$P_{\text{index}} = \frac{(QV)_{\text{explosive}}}{(QV)_{\text{picric}}}, \tag{2.4}$$

where, $Q_{\text{picric}} = 3745$ J/g and $V_{\text{picric}} = 790$ cm^3/g [Smith and Hetherington 1994]. The power indexes of some primary and secondary explosives are listed in table 2.1.

Table 2.1: Power indexes of primary and secondary explosives (adapted from [Smith and Hetherington 1994]).

Sensitivity	**Explosive**	P_{index}
Primary	Lead styphnate	21
	Lead azide	13
	Mercury Fulminate	14 [GS 2012]
Secondary	Nitro-glycerine	159
	RDX	159
	TNT	117
	RDX/TNT (60/40)	138

2.5.3 Detonation capacity

Explosives can also be distinguished based on their brisance which is the destructive fragmentation effect of a charge on its neighbourhood or, in other words, a measure of the shattering capability of an explosive [Meyer *et al.* 2007]. Effectively, explosive brisance can be seen as a measure of the speed with which the maximum pressure is achieved after the explosive detonation. This property can also be seen as the detonation capacity of the explosive. Among others, parameters that influence the brisance of an explosive are, for example, its detonation rate (that is, the speed at which the chemical reaction occurs or the rate of the reaction), loading density (or compactness of the explosive) and heat of explosion[3]. In brisant explosives, shock-waves are formed due to the extremely high detonation rate. Plastic explosives (PE) are high detonation capacity brisance explosives. As an example, RDX is plasticised with vaseline or other plasticisers.

The designation "composition" when associated to an explosive means that the explosive material is made from several components. As an example, composition C4 is a military grade plastic explosive, consisting of a hexogen and a plasticiser, which may or may not be an explosive itself. Explosives such as composition C4 can be easily moulded into specific geometries. The percentages of RDX and plasticisers for composition explosives are listed in table 2.2.

[3] "The heat of explosion of an explosive material, an explosive mixture, gunpowder or propellant is the heat liberated during its explosive decomposition." [Meyer *et al.* 2007]

Table 2.2: Formulations for composition C explosives (adapted from [Meyer *et al.* 2007]).

Composition	**RDX** [%]	**Plasticiser** [%]	**Type of plasticiser**
C	88.3	11.7	Non explosive
C2	80.0	20.0	Explosive
C3	78.0	22.0	Explosive
C4	90.0	10.0	Polyisobutylene[†]

[†] Polyisobutylene is a binding agent in plastic explosives such as C4, used to make the explosive less sensitive to premature detonation as well as to make it easier to handle and shape.

2.6 TNT equivalent

TNT equivalent is the designation of a specific normalisation technique where the mass of an explosive charge is converted to an equivalent mass of TNT. There are several methods to estimate the equivalent mass of TNT. A widely used method to determine the TNT equivalent is related to the Chapman-Jouguet theory [Krehl 2009]. Such theory described the supersonic combustion wave. For simplification purposes, a few assumptions are made according to the Chapman-Jouguet theory [Cooper 1996], such as:

- The flow is one-dimensional;
- The front of the detonation is a place of discontinuity;
- When the gases from the product of the reaction leave the detonation front, they are assumed to be in a state of equilibrium, meaning that the chemical reaction is already completed;
- After leaving the detonation front the gases from the product of the reaction can be affected by the surrounding and boundary conditions;
- A steady state process is assumed, that is, the detonation velocity is constant.

According to this theory the detonation wave is treated as a discontinuity with infinite reaction rate. This discontinuity is between two different states (unreacted explosive and detonation products) [Cooper 1996], where the reaction takes place and the unburnt gas will almost instantaneously be changed to burnt gas. Thus, if a comparison is made with a shock-wave, a transition exists at the shock front, between the compressed and unpressed gas, whereas in an explosive wave, the detonation front separates two chemically different states of unburnt and burnt gases [Krehl 2009]. The Chapman-Jouguet detonation velocity refers to the velocity of the supersonic combustion wave. Based on the Chapman-Jouguet theory it is possible to calculate the detonation velocity (D), the detonation pressure (P_{CJ}), *etc.* if the gas mixture is known. The

Chapman-Jouguet theory does not require any information about the chemical reaction rate (*i.e.* chemical kinetics). The equivalent TNT mass of an explosive can be estimated from the Chapman-Jouguet detonation velocities [DK 2012] according to the following equation:

$$M_{\mathrm{TNT}} = M \frac{D^2}{D_{\mathrm{TNT}}^2}, \tag{2.5}$$

where M_{TNT} and M are the equivalent mass for TNT and the explosive charge, respectively. D and $D_{\mathrm{TNT}} = 0.693$ cm/μs are the Chapman-Jouguet velocity for TNT and for the explosive charge, respectively. Another way to compare the explosive power of a certain explosive charge with the explosive power of TNT is by using the relation

$$M_{\mathrm{TNT}} = \frac{QV}{(QV)_{\mathrm{TNT}}}, \tag{2.6}$$

where Q and V were previously defined as the heat of the explosion and the gas volume per unit mass of explosive, respectively [Akhavan 2004]. As an example, C4 has a TNT equivalent factor of 1.2 [Yandzio and Gough 1999,RE 2012]. In general terms, it can be stated that the power index and the TNT equivalent are higher for secondary explosives than for primary explosives.

Chapter 3

Energy absorbers, cork and its compounds

Several topics will be mentioned in this chapter, namely a reference to the available literature on the response of sandwich structures to blast loading, failure modes in these structures and energy absorption with cellular materials. Subjects such as production, types of cork compounds, microscopic structure, mechanical behaviour, mechanical properties and applications are mentioned.

3.1 Protection systems and energy absorbers

The development of new systems that can protect against shock-waves originated by terrorist (or others) attacks, plays an important role in defence armour applications. The fast increase of heat and pressure in the environment and the consequent loading rate on structures, produced by the explosion, can induce large plastic deformations. Nonetheless, structures which can experience large plastic strains before reaching collapse have the advantage of absorbing high levels of energy and are known as energy absorbers (EA) [Zhu *et al.* 2008a]. As previously stated, cellular materials, honeycomb structures, foams, composite materials, *etc.* are potential candidates as energy absorbers [Xue and Hutchinson 2003, Xue and Hutchinson 2004, Zhu *et al.* 2008a, Zhu *et al.* 2008b, Sousa-Martins *et al.* 2012, Sousa-Martins *et al.* 2013]. A description on some of the main characteristics of one of the above listed EA (cellular materials) is made in the following paragraphs.

3.1.1 Cellular materials

Relevant work on the research and development of protection and defence systems has been carried out in the last few decades considering the incorporation of cellular materials. However, most of the work and research done so far is limited to the use of cellular

materials with regular structure (*e.g.* honeycomb structures) and metal foams, with significant associated costs. A material is designated cellular if it is made by empty cell elements with a total volume fraction lower than 30% [Pereira 2007]. The word cell has its origin in the latin word *cella* which means "small compartment", "pore" or "enclosed space". The cell's faces can either be open or covered by membranes, giving origin to open or closed cellular materials, respectively [Gameiro 2007]. In addition, cellular materials can either be natural or synthetic. Natural cellular materials are available in nature in many different ways: bone structure, coral, wood, cork, *etc.* Ashby [Ashby 1983] made the following observation regarding natural cellular materials: "When modern man builds large load-bearing structures, he uses dense solids: steel, concrete, glass. When nature does the same, she uses cellular materials: wood, bone, coral. There must be good reasons for it.". Synthetic cellular materials (*e.g.* synthetic foams) can be produced from very different base materials, including metals, polymers, ceramics, composites, paper, glass, *etc.* Examples of different types of cellular solids are shown in figure 3.1. In terms of failure and damage, cellular materials can absorb energy through plastic bending, buckling or even fracture of the cells walls.

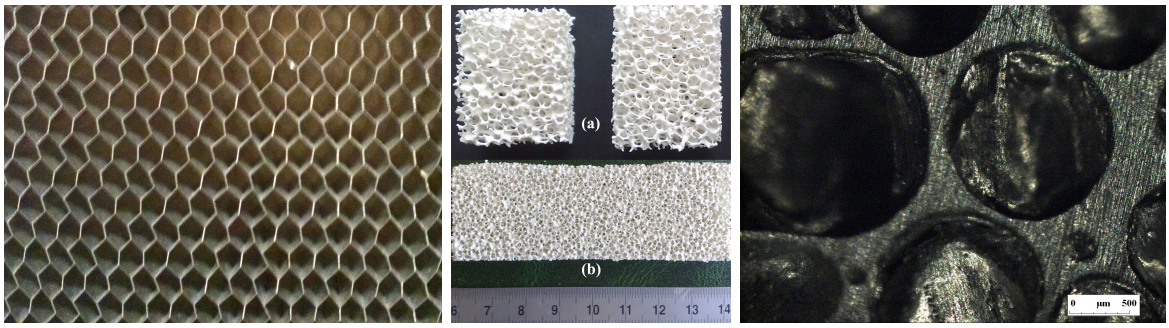

(a) (b) (c)

Figure 3.1: Examples of different types of cellular solids: (a) Honeycomb cellular solid; (b) Three-dimensional open cell cellular solid [Zhang *et al.* 2012] and, (c) Three-dimensional closed cell cellular solid (image courtesy of Isabel Duarte).

In terms of the stress-strain (σ–ε) curve of cellular materials, some main characteristics can also be mentioned. A typical stress-strain curve for a cellular material is shown in figure 3.2. As previously stated, cellular materials have approximately linear elastic behaviour up until the yield stress (σ_e). After this point, cellular materials begin to present a plateau (constant stress for increasing strains). After this plateau cell walls start to collapse, which can be evidenced in the curve in figure 3.2 as a sudden increase in stress (starting at strain ε_d). This last region is usually known as the densification regime. One of the main conclusions that can be derived from the behaviour of a cellular material is that these materials can sustain very large strains for very low stress values.

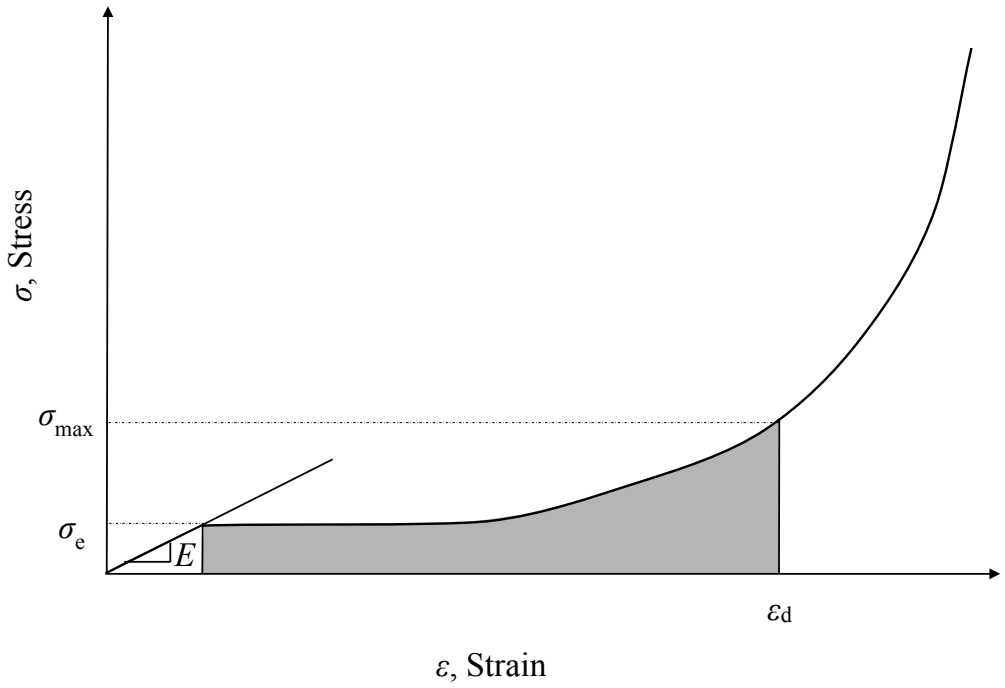

Figure 3.2: Typical stress-strain curve of a cellular material.

3.1.2 Energy absorbers cores in sandwich structures

Cellular materials are very good candidates as cores in sandwich structures solutions due to (among other characteristics) their very low density. Some energy absorbers currently used in sandwich structures solutions are presented in this section.

The structural response of sandwich structures for applications in protection systems against blast-waves is a well documented issue [Gibson and Ashby 1997, Mines *et al.* 1998, Roach *et al.* 1998, Lu and Yu 2003, Rizov *et al.* 2005, Meo *et al.* 2005, Hutchinson and Xue 2005, Rathbun *et al.* 2006, Radford *et al.* 2006, Langdon *et al.* 2007, Vaziri and Hutchinson 2007, Theobald and Nurick 2007, Tagarielli *et al.* 2007, Nemat-Nasser *et al.* 2007, Zhu and Lu 2007, Zhu *et al.* 2008b, Dharmasena *et al.* 2008, Zhu *et al.* 2009a, Zhu *et al.* 2009b, Nurick *et al.* 2009, Tagarielli *et al.* 2010].

Analytical models for the prediction of the dynamic behaviour of sandwich beams and panels when subjected to uniform shock-waves are reported in the literature [Radford *et al.* 2006]. These models were validated, for example, by Qiu *et al.* [Qiu *et al.* 2004, Qiu *et al.* 2005] using numerical studies. The results obtained proved that it is possible to derive reasonable correlations between the numerical results and the analytical model predictions. Consequently, and given the actual world reality, it is fully justified that investments are made in research (both experimental and numerical) and development of new materials, structures, and protection systems capable of absorbing and dissipating energy from explosive reactions.

The use of composite materials with application on protective structures is also

well documented in the literature [Sierakowski and Hughes 2006, Buchan and Chen 2007, Langdon *et al.* 2009]. An example of an application of a composite material in a sandwich structure for blast-wave absorption applications is the use of fibre-metal laminates (FML). FML are structural hybrid materials composed of layered metallic and fibber reinforced polymer panels. These materials were developed as a light-weight alternative to the structural metals traditionally used, particularly for fatigue resistance. One commercial type of FML is GLARE®. GLARE® panels are composed by thin aluminium foils and epoxy resin laminates reinforced with glass fibbers. There are several types of GLARE® depending on the configuration of the composite layers. This orientation plays an important role in terms of the final application. As an example, GLARE® 3 and GLARE® 5 are selected for impact applications [Vlot 2001]. Regarding the final interest and main topic in investigation in this work, GLARE® panels have been studied under the influence of shock-waves and their shock-wave absorption capacity was analysed [Langdon *et al.* 2009]. Through these preliminary experimental tests the authors observed that GLARE® panels presented a similar behaviour to the one observed for monolithic metal plates and, in addition, that GLARE® panels appeared to offer potential for blast resistance.

Another candidate EA core for sandwich structures subjected to blast-waves was presented by Nurick *et al.* [Nurick *et al.* 2009]. These authors analysed the inelastic response of sandwich structures with thin aluminium skins adhesively bonded to a honeycomb metallic core. These panels were subjected to an oriented/localised shock-wave impact, generated from the close-distance detonation of a disc shaped explosive. The orientation of the shock-wave was achieved through a tube operating as a wave guide. These authors demonstrated that the response of the panels is much more efficient in the uniform blast situation than when the panels are subjected to a localised distribution, achieved through the tube. This experimental study was later compared and validated by numerical simulation results by Karagiozova *et al.* [Karagiozova *et al.* 2009]. From the presented results it was concluded that the load transferred to the sandwich back panel depends on the intensity of the blast, the thickness of the core and the overall flexibility of the sandwich panel.

3.2 Deformation and failure modes in sandwich structures

Sandwich structures can experience different deformation and failure modes when loaded by a blast-wave. In order to understand how a sandwich will deform, fail and eventually collapse under such circumstances, an important aspect to take into account is to know how the core alone will behave on such adverse conditions. A description of the stages that a sandwich structure experiences in blast scenarios is made in this section. In addition, the effects of parametric changes in the structures are also referenced (*e.g.* core thickness, geometry and mass of the explosive). With this

description, a perspective on the EA behaviour in such conditions is intended to be given in order to compare the obtained performance with the energy absorber used in this investigation (MAC compounds).

Dharmasena *et al.* [Dharmasena *et al.* 2008] described each of the stages involved in the response of sandwich structures subjected to blast loads. The three stages a sandwich structure goes through when subjected to a blast load are represented in figure 3.3. An impulsive load (pressure pulse) is transmitted to the front face of the structure (figure 3.3 (a)) which will cause the movement of the front face sheet (figure 3.3 (b)). Thus, the front face sheet will move with velocity v_{front} towards the back face sheet. Stage I ends when the front face sheet has acquired its full momentum ($m_{\text{front}} v_{\text{front}}$). The front face sheet movement is resisted by core compression (for example, a cellular core). In the core a densification zone is created near the front face sheet that propagates towards the back face sheet. This velocity of the plastic wave traveling through the (compressed) core is

$$v_{\text{plastic}} = \sqrt{\frac{E_{\text{t}}}{\bar{\rho}}}, \tag{3.1}$$

where E_{t} is the tangent modulus of the core structure material and $\bar{\rho}$ is its relative density [Wadley *et al.* 2007]. Core crushing takes place during stage II. This stage is intrinsically related to several properties of the core material, such as the density, geometry of the core cells, mechanical properties of the material, *etc.* Stage III starts when the back face sheet of the sandwich acquires a velocity v_{back} and overall bending of the panel occurs. Although the main part of the core densification happened in stage II, in stage III core compression can still happen because, if highly crush-resistant cores are used a larger distance between face sheets exists, hence a higher panel bending resistance [Dharmasena *et al.* 2008]. In this stage, not only the front and back plates are allowed to stretch, but also the core. The core collapse and bending/stretching of the face sheets and core are the main mechanisms for energy dissipation/absorption. Metallic honeycombs are one of the most used materials in sandwich structure cores for blast loading absorption applications. These are three-dimensional regular cellular materials, in which the shape of the cell may vary (*e.g.* square or hexagonal).

3.2.1 Influence of the mass of the explosive

Blast tests in air were reported by Dharmasena *et al.* [Dharmasena *et al.* 2008] to study the dynamic mechanical response of honeycomb core sandwich structures made from a super-austenitic stainless steel alloy. The stand-off distance was kept constant while the impulse was varied by varying the mass of the charge. Lower impulse values led to bending of the faces and progressive buckling of the cell walls close to the center of the structure. Cell wall buckling and core densification increased as the impulse increased. A cross section of a honeycomb core showing core crushing, cell wall folding and debonding is shown in figure 3.4.

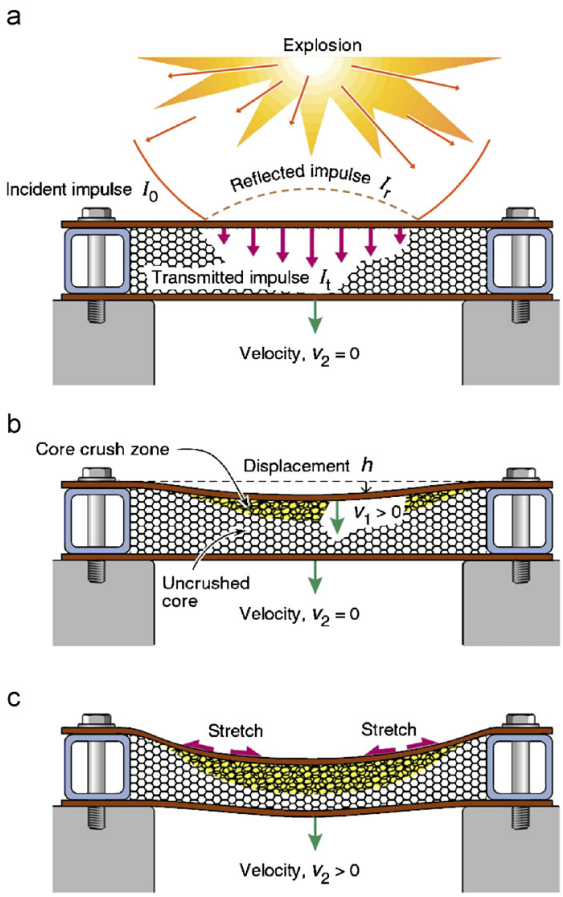

Figure 3.3: Generic response of sandwich structures to blast loading [Dharmasena *et al.* 2008]: (a) impulse loading (Stage I), (b) core crushing (Stage II) and (c) panel bending (Stage III).

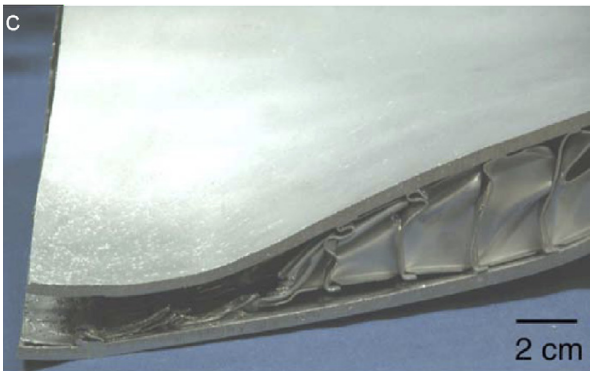

Figure 3.4: Cross section of a honeycomb sandwich structure showing core crushing, cell wall folding and core debonding [Dharmasena *et al.* 2008].

3.2.2 Influence of the core thickness

In terms of the influence of the core thickness, Langdon and Nurick [Langdon and Nurick 2010] studied the response of honeycomb core sandwich panels to blast loading, with aluminium and composite face sheets. Different thicknesses for the core were used, namely 13 and 25 mm. Aluminium alloy and Fibre Reinforced Plastic (FRP) composites were tested as face sheets. Langdon and Nurick [Langdon and Nurick 2010] concluded that thicker honeycomb cores lead to lower final deflections on the sandwich. In terms of failure and damage, core crushing, core shearing, debonding of the face sheets, permanent deformation, cracking of the composite face sheets and tearing was observed. As an example, debonding of the core from the face sheets observed in the experiments by these authors is shown in figure 3.5.

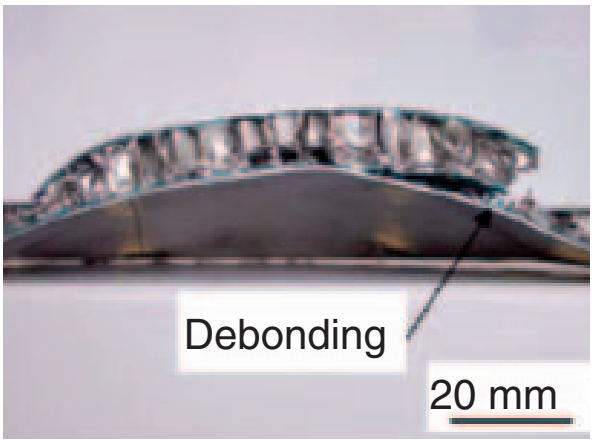

Figure 3.5: Debonding of the core from the face sheets [Langdon and Nurick 2010].

3.2.3 Influence of the core cell geometry

Cells in cellular materials can assume several geometries. The influence of the geometry of the cells as well as the thickness of the cells walls on the performance of sandwich structures with cellular cores will be considered in this section. Zhu *et al.* [Zhu *et al.* 2008b] made an extensive study and experimental characterisation of sandwich structures with metallic cellular cores on blast scenarios. Parameters such the face sheet thickness, cell size, foil thickness of the honeycomb and mass of the charge were analysed in order to derive conclusions of their influence on the structural response of the system. The geometries and dimensions of the specimens are presented in figure 3.6. Two different parameters characterise the geometry of a single cell. These are the thickness of the cell wall, t, and the cell width, l.

In terms of the effect of the core cell geometry, the main conclusions that these authors derived were [Zhu *et al.* 2008b]:

- For the case where the cell sizes are kept constant while the cell wall thicknesses

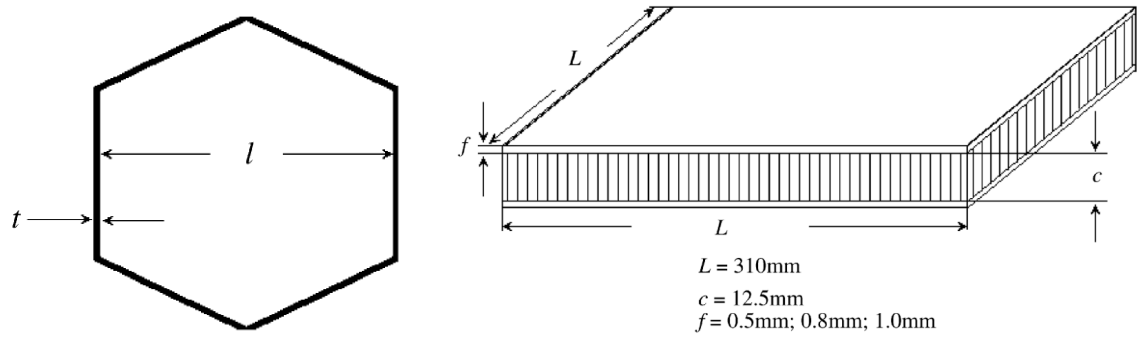

(a) (b)

Figure 3.6: (a) Single cell and (b) geometry and dimension of the specimens used by Zhu *et al.* [Zhu *et al.* 2008b].

are variable, an increase on cell wall thickness will result in smaller back face deflection;

- If the cell wall thickness is kept constant while the cell sizes are increased, Zhu *et al.* [Zhu *et al.* 2008b] observed an increase on the back face deflection; and

- If two different types of core with variable cell size and cell wall thickness, but with similar values of mass are tested (the average mass of core actually reflects its relative density [Zhu *et al.* 2008b]) an increase in values of relative density of honeycomb[1] cores induces a decrease in the face deflection values.

3.3 The origin of cork

From the description on the previous sections it is clear that cellular materials are being widely introduced and used in new technological and industrial applications. As previously mentioned, cork is a natural cellular material and is the main focus of this research work. A review of the state-of-the-art on cork, its nature, behaviour, and applications is presented. Subjects such as production, types of cork compounds, microscopic structure, mechanical behaviour, mechanical properties and applications are mentioned.

Cork is the outer bark of the cork oak three (*Quercus suber* L.) that grows in countries such as, for example, Portugal, Spain, Algeria and California [Gibson and Ashby 1997].

In botanic anatomy, cork is a protective tissue that separates the living cells of the plant from the outside environment. Cork cells, named phellem, are grown from the cortex cells via an intermediate structure known as cork cambium (phellogen) [Pereira

[1]Core relative density can be defined by the density of the honeycomb core structure, divided by the density of the solid (density of the metal) [Zhu *et al.* 2008b].

2007]. The cellular division of the phellogen is linked to the physiological cycle of the tree and to the factors that influence it, namely the environmental conditions. Cork has excellent insulation properties (to air and water, for example) since the walls of its cels are covered with a thin layer of an unsaturated fat acid, named suberin, hence the species designation *Quercus suber*.

The extraction of cork from the cork oak tree is achieved by cyclic cuts and striping of cork from the tree. This process normally takes place between late Spring and Summer. The striping process of cork is shown in figure 3.7. The longevity of the cork oak tree is frequently between 250 and 300 years. However, the effective production of cork can only last until 150 to 200 years. The first extraction should generally happen between the 20^{th} and the 30^{th} year, when the diameter of the tree is approximately 20 to 25 cm [Fortes *et al.* 2005]. The radial growth (thickening) of the stem happens mostly between May and October.

It is well known that the major application of cork is related to the wine industry. Cork has to be extracted at least three times before it can be used in the production of cork tops, since in the first two extractions the material presents a significant number of cracks and grooves due to the intense stresses present in the growth of the stem (thickening).

Figure 3.7: Stripping cork (outer bark) from the cork oak tree (picture courtesy of Paulo Serafim).

Cork is not characteristic of the *Quercus suber* tree. In fact, all trees have a thin layer of cork in their bark. What makes the *Quercus suber* different from the other trees is that, at maturity, cork forms a layer with several centimetres of thickness around

the stem of the tree. The purpose of this thick layer is to insulate the tree from the heat and loss of moisture, and perhaps to protect it from animals, since the last layer of suberin has an unpleasant taste [Gibson and Ashby 1997].

3.3.1 Microscopic structure

Cork is a natural cellular material composed of closed cells. In the specific case of cork, the solid volume fraction is approximately 15%. The volume occupied by the cells has a polyhedral shape, with the solid cell walls all connected to adjacent cells.

Cork was one of the first materials to be observed on the microscope. In the 17^{th} century Robert Hooke (1635-1703) documented in detailed hand drawings his microscopic observations of extremely thin membranes of cork. These drawings (see figure 3.8) were published in his book Micrographia in 1665 [Hooke 1665]. For the first time it was observed that cork was made by small structures that were named "cells".

To accurately describe the micro-structure of cork a reference must be made to the cell global orientation in space and to its original position in the tree [Pereira 2007]. A diagram of a cork tree section showing the coordinate system is shown in figure 3.9 (a). As can be seen from the schematic representation of a cork cell in figure 3.9 (b), the microstructure of cork is intrinsically related to the growth of the tree. The axial direction (direction 2), in most straight standing stem trees, corresponds to the vertical upward direction of growth. Directions 1 and 3 are the tangential and radial directions, respectively. The average dimensions of a cork cell wall are approximately 45, 20 and 1 μm, for its height, hexagonal base side and cell wall thickness, respectively [Fortes *et al.* 2005]. Therefore, two sections can be distinguished in figure 3.9 (b). On the first section (plane β) the cells have an approximately hexagonal shape. On the second section (see α) cells are characterised by having an approximately rectangular shape. From these observations it is possible to conclude that cork is a material that presents structural anisotropy and is often referred to have three principal directions to define its orientation in the cork oak tree: (i) the tangential direction (tangential to the stem circumference), (ii) the axial direction (along the axis of the stem) and (iii) the radial direction (along the radius of the stem).

Scanning electron microscopy (SEM) can be used to observe the microstructure of cork. This technique is often used to observe samples with a conductive surface. The materials to be tested are normally coated with an ultra thin coating of electrically conducting material, applied either by low-vacuum sputter coating or by high-vacuum evaporation. Special attention must be taken on coating since it can be difficult to reverse and may hide the smaller features on the specimen. The surface of the object is scanned point by point with a focused electron beam. The interactions of the electron beam with atoms at (or near) the surface of the sample generate signals that give information about the sample's topography, chemical composition, crystalline structure and orientation. A two-dimensional image is then generated over a selected area of the surface of the sample [Ankiewicz 2010].

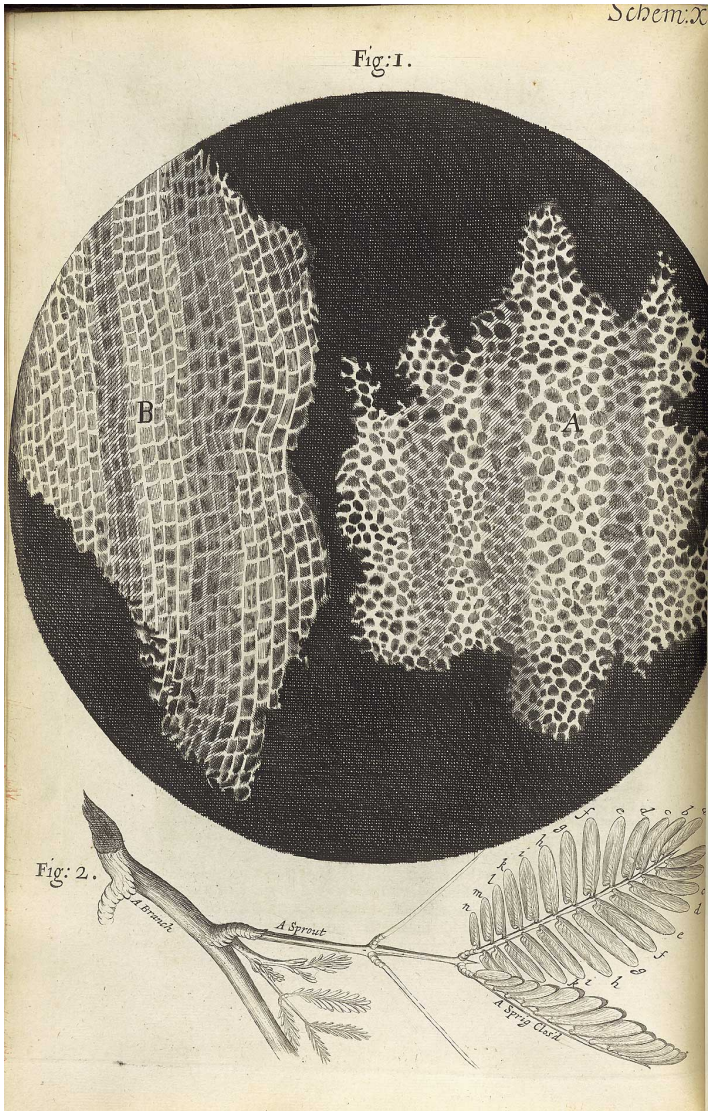

Figure 3.8: Cellular structure of cork as drawn by Robert Hooke. This image first appeared in his book "Micrographia: or Some physiological descriptions of minute bodies made by magnifying glasses. With observations and inquiries thereupon" [Hooke 1665, Pereira 2007].

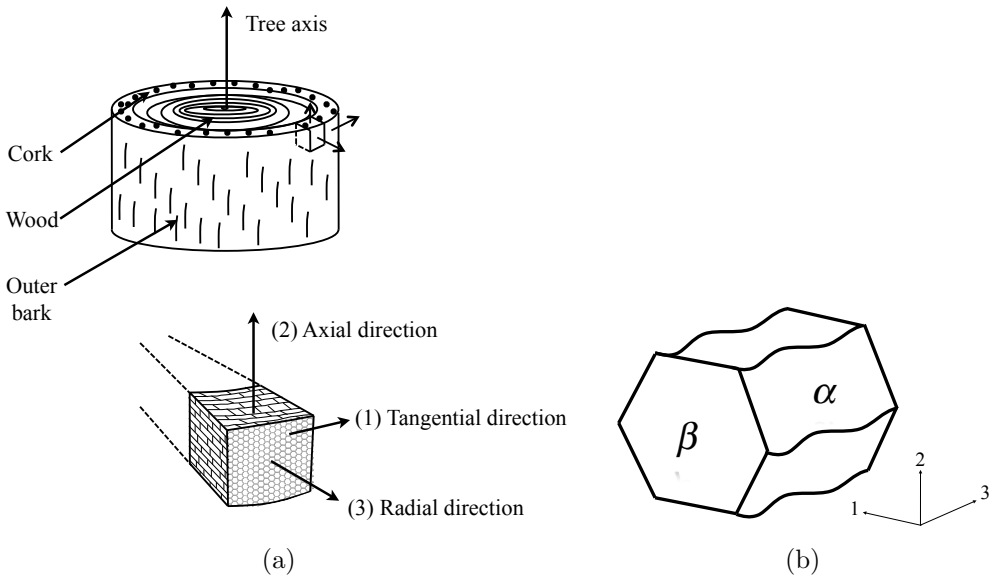

Figure 3.9: (a) Diagram of a cork tree section showing the coordinate system (adapted from [Gibson and Ashby 1997]). (b) Schematic representation of a cork cell. Directions 1, 2 and 3 correspond to tangential, axial and radial direction, respectively.

In the work here presented SEM measurements were performed using a Hitachi SU-70 scanning electron microscope at 15 keV from the Department of Materials Science and Ceramics Engineering in the University of Aveiro. Selected images of SEM on cork are shown in figure 3.10. Figure 3.10 (a) clearly shows a view perpendicular to the α section (see figure 3.9 (b)), correspondent to the rectangular shaped orientation in a cell of cork. In figure 3.10 (b), another relative dimension from a cork cell is shown: the hexagonally shaped orientation, which can be seen perpendicular to plane β. The hexagonal base side length was calculated and found to be ≈ 22 μm.

In figure 3.10 (c) is a view into different orientation planes and figure 3.10 (d) shows the average height for the cork cells and thickness of the cell walls, which were calculated and found to be approximately of 48 μm and 1.7 μm, respectively. These values are in accordance to the values given in the literature [Fortes *et al.* 2005].

3.3.2 Mechanical properties

The cellular structure of cork is responsible for its low density value. As was stated before, cork is made of closed cells. However, the cells in its surface are open, which contributes to its high friction coefficient. Suberin (that is the main structural component of the walls of the cells of cork [Pereira 2007]) is thus responsible for some mechanical properties of cork and, in addition, the impermeability of cork. The majority of cork's mechanical properties can be explained due to its cellular structure. These remarkable properties explain the wide range of applications for cork. Summarising, the cellular structure of cork explains its low density, and the fact that cork is formed by closed cells rich in suberin allows the material to present, for example, low thermal

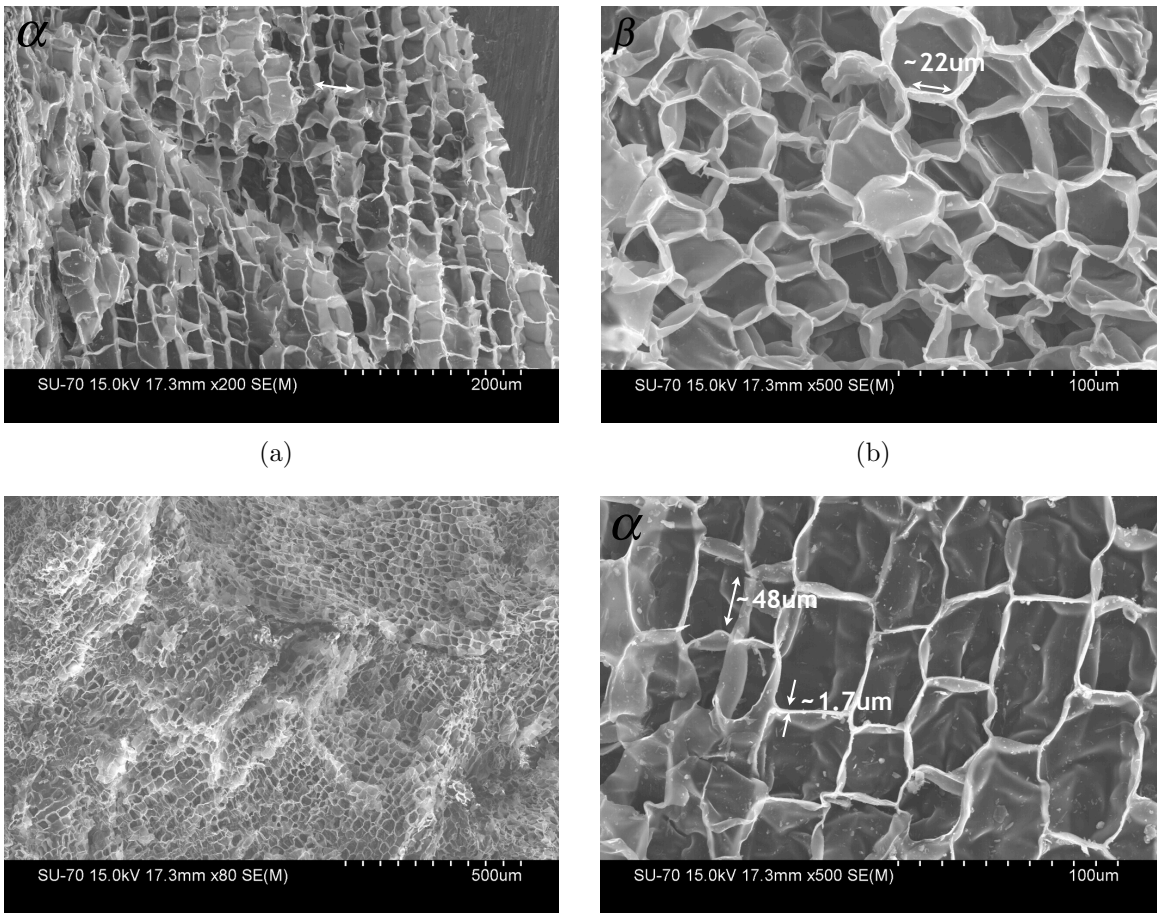

(a) (b)

(c) (d)

Figure 3.10: Scanning Electron Microscope images of the cellular structure of cork with different magnification. Magnification of (a) 200, (b) 500, (c) 80 and (d) 500 times.

and acoustical conductivity, impermeability and high resilience and ability to absorb vibrations [Gameiro 2007].

Several studies have been published along the years on the mechanical characterisation of cork. The Young modulus of cork has been proved to be one and a half times higher along the prism axis than it is in the other two directions [Fortes and Nogueira 1989, Rosa and Fortes 1991]. Some of the most relevant mechanical properties of cork are compiled in table 3.1 [Gibson and Ashby 1997].

Table 3.1: Mechanical properties of cork [Gibson and Ashby 1997].

Young Modulus		
Tangential direction Axial direction	E_1 E_2	13±5 MPa
Radial direction	E_3	20 ± 7 MPa
Shear Modulus		
in 1-2 plane	G_{12}	4.3 ± 1.5 MPa
in 1-3 plane in 2-3 plane	G_{13} G_{23}	2.5 ± 1.0 MPa
Collapse stress		
Tangential direction Axial direction	$(\sigma_e)_1$ $(\sigma_e)_2$	0.7 ± 0.20 MPa @ 6% strain
Radial direction	$(\sigma_e)_3$	0.8 ± 0.29 MPa @ 4% strain
Fracture stress		
Tangential direction Axial direction	$(\sigma_f)_1$ $(\sigma_f)_2$	1.1 ± 0.2 MPa @ 9% strain
Radial direction	$(\sigma_f)_3$	1.0 ± 0.2 MPa @ 5% strain
Poisson ratio		
in 1-2 and 2-1 planes	$\nu_{12} = \nu_{21}$	$0.25 - 0.50$
in 1-3 and 3-1 planes in 2-3 and 3-2 planes	$\nu_{13} = \nu_{31}$ $\nu_{23} = \nu_{32}$	$0 - 0.10$

3.4 Types of cork compounds

One of the major problems associated to the microstructure of cork is related to the dispersion in cell sizes in either different samples of cork or even within the same sample. The shape of these cells is related to the period of growth of the cells. Earlycork cells are larger and have thinner cell walls while latecork cells have thicker walls and a much smaller prism height [Pereira 2007]. Another problem related to natural structure of cork is the presence of defects and variability of its porosity. These characteristics affect the incorporation of this material in new applications and technologies. In order to reduce the influence of these issues, the investigation here considered is restricted to the use of micro-agglomerated cork compounds (MAC compounds). MAC compounds

are man-made materials which consist of a single body of moulded natural cork granules, joined using different types of binders/adhesives (*e.g.* polyurethane, melanine or rubber) [Gil 2009]. The strength and, therefore, the applicability of a specific MAC compound is strictly related to the physical and chemical properties of the adhesive used. Bonded cork granules are separated and classified according to their density and grain dimensions.

Studies reveal that cork agglomerates are an ideal core material for lightweight sandwich structures (*e.g.* aerospace applications) [Gil 2009, Silva *et al.* 2011]. Cork (and its compounds) characteristics that evidence the remarkable properties that might be advantages when acting as a core on sandwich structures are, for example, its low density.

If the previously referred defects present in natural cork are surpassed new ideas for applications of sandwich structures with cork compounds appear. Thus, the idea behind this work was the incorporation of cork compounds in the core of sandwich structures for blast-wave absorption applications. In this work two different types of MAC compounds were investigated: NL20 and TB40, both part of the CORECORK® product range, produced by Amorim Cork Composites. CORECORK® offers excellent fire, smoke and toxicity protection properties, as well as good mechanical behaviour, processing characteristics, low water absorption and high damping behaviour with reduction of structural vibration and noise generation. These materials are made of cork granules and specific binders and are available in blocks, sheets, rolls and strips. Some mechanical properties of the two MAC compounds studied in this work are listed in table 3.2.

Table 3.2: Mechanical properties of NL20 and TB40 cork compounds [TR 2011].

Property	**NL20**	**TB40**	**Units**
Density	200	440	kg/m^3
Compressive strength	0.5	0.7	MPa
Compressive modulus	6.0	8.5	MPa
Tensile strength	0.7	–	MPa
Shear strength	0.9	–	MPa
Shear modulus	5.9	–	MPa
Hardness	–	80	Shore A

The *quasi*-static stress-strain ($\sigma - \varepsilon$) compression curves for NL20 and TB40 MAC compounds are shown in figure 3.11. These were acquired in a Shimadzu™ AG-50 kN G universal testing machine at a cross beam velocity of 4 mm/min.

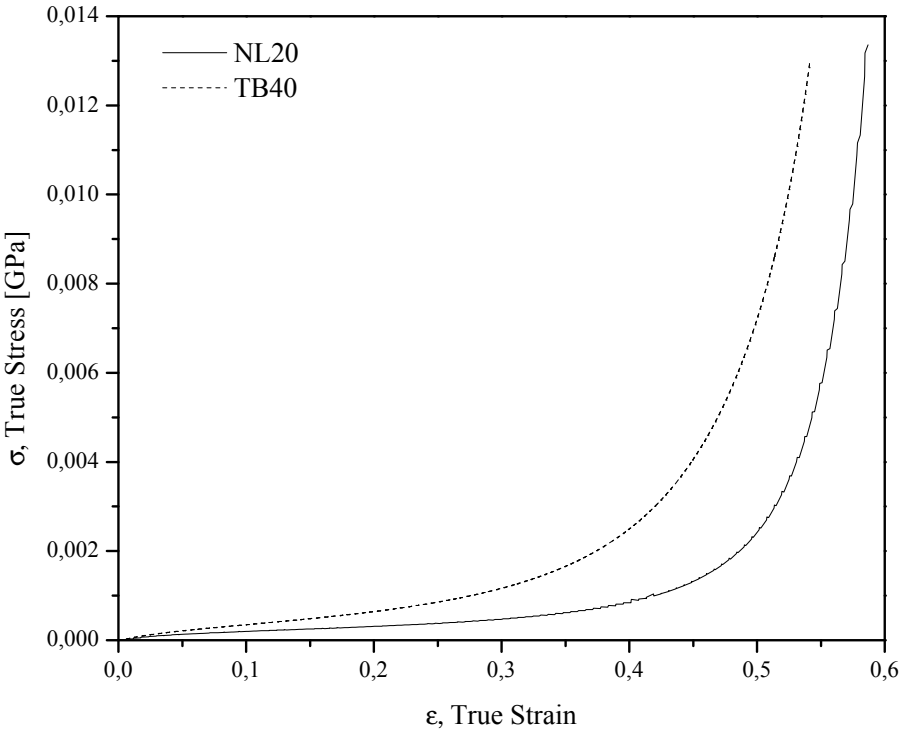

Figure 3.11: *Quasi*-static stress-strain ($\sigma - \varepsilon$) curves for NL20 and TB40 MAC compounds.

3.5 Applications of cork

Cork has always been associated to its use as cork tops. However, its modern commercial applications focus not only on its use as cork tops but also as innovative applications designed based on its remarkable characteristics (*e.g.* light-weight, acoustic and thermal insulation properties, *etc.*). In the following section a limited selection of applications for cork is presented.

Bottle insulation

Bottle insulation (cork tops) is the most used application for cork. Some wine specialists admit that cork tops are perfect since, for example, to seal wines which require storage and maturation for many years, with this material small amounts of oxygen are allowed to enter in the bottle which help in the chemical reactions that take place during the maturation of the wine [CP 2012].

The elastic properties of cork, namely the low value of the Young modulus (see table 3.1) and the low bulk modulus (assuming a null Poisson ratio for cork $K = E/3$ [Gibson and Ashby 1997]) improve its sealing capacity (the latter characterises the resistance of a material to hydrostatic compression). As cork has a low bulk modulus there is no need to increase the pressure to induce a relatively high decrease in volume. Tops made from solid polymers have, (above their glass transition temperature) like cork,

low values of E but higher values for the bulk modulus, making the process of inserting the top in a bottle harder, thus giving poor seal when they are inserted [Gibson and Ashby 1997].

Three types of cork tops are shown in figure 3.12. The one on the left (figure 3.12 (a)) is made from agglomerated cork. A top made of natural cork can be seen in figure 3.12 (b). The image on the right (figure 3.12 (c)) is a cork top made from a combination of natural cork disks and agglomerated cork.

It would be expected that cork tops obtained by cutting the axis of the cork parallel to the prism axis of the cells of cork would produce the best seal due to the geometry of the cell of cork and its properties which would be used to best advantage. However, this is not the best seal achieved with cork, since natural cork contains lenticels which are tubular channels that connect the outer surface of the bark with the inner surface. Lenticels are tunnels from which the oxygen is allowed into the three and carbon dioxide is expelled. Thus, cork tops cut in this way will leak [Gibson and Ashby 1997]. Hence, this problem is surpassed with the combination of two natural discs where leakage is avoided by laminating the two discs together so that lenticels do not connect [Gibson and Ashby 1997]. The cork top, when forced into the bottle, is compressed in the plane where it is isotropic (radial direction) and, therefore, exerts a uniform pressure on the inside of the neck; and the axial load needed to push the cork into the bottle produces no radial expansion (that if happened, would block the insertion of the cork top) because of the null (in theory) Poisson ratio (see table 3.1, ν_{31}) [Gibson and Ashby 1997]. Additionally cork agglomerates are adhesively joined to the upper part of the cork tops, since insertion is no longer a problem in this part of the cork, but still the porosity of the agglomerate will allow oxygen to enter (see figure figure 3.12 (c)).

(a) (b) (c)

Figure 3.12: Cork tops (bottle seals) made from: (a) agglomerated cork; (b) natural cork and (c) natural and agglomerated cork.

Acoustical insulation

The cellular microstructure of cork (with a number of cells per cubic centimetre in the order of 4 to 7×10^7 for earlycork and 10 to 20×10^7 for latecork [Pereira 2007]) leads to excellent insulation properties which allow this material to be applied in various fields of sound insulation [Fortes *et al.* 2005, Pereira 2007]. Earlycork cells are formed in the first period of growth of the tree whereas latecork cells are formed in the end of the growing season. Cork has been used for several centuries in churches, libraries, universities and homes due to its ability to reduce echo and sound transmission. In addition, the acoustical insulation capacity of cork is enhanced by the structure of the cells, since there are no gaps between them and the cells are closed.

Friction

Friction properties of cork also make the application of this material in floors very interesting. Friction between a shoe and cork can come from two different types of sources: adhesion and anelastic loss [Gibson and Ashby 1997]. On the one hand, adhesion happens when the two interacting surfaces come in contact, atomic bonds form and for them to break up, work must be done. On the other hand, anelastic loss happens since cork is not perfectly elastic. Hence, when walking on a cork floor, the bumps from the shoes will deform cork, and due to the inexistent total elastic recovery of cork, the bumps formed in the deformed floor (permanent rugosity) will lead to a large friction coefficient.

Design and architecture

As stated before, cork has been used in churches, libraries, universities and homes throughout the years due to its acoustical insulation properties. However, when the use of this material in construction is considered not only the insulation properties of cork play an important role. The aesthetic characteristics of cork and its overall texture are widely considered for industrial design and architecture purposes. The two following examples were selected in order to exemplify this type of application of cork:

- Corticeira Amorim, the world leader in the production of cork and cork compounds, that produces materials made from (or that incorporate) cork or cork compounds, supplied this material for the Shanghai World Expo 2010. The theme was "Better City, Better Life", therefore cork was selected to be applied both on the inside and on the outside of the Pavilion of Portugal since this material fits the image of a green ecological material. The building has a facade area of 3640 m^2 and the project was designed by the portuguese architect Carlos Couto, settled in Macao. An outside image of the building can be seen in figure 3.13.

- Another example is related to the incorporation of cork in automotive applications for industrial design purposes. As an example, PLASCORK® — Automotive (Amorim Cork Composites — Corticeira Amorim group) is a development

project to pursue sustainable as well as aesthetical solutions for vehicle interiors [PC 2012]. The aim of this project is to make improvements in various fields, such as the security (*e.g.* shock absorption); comfort (*e.g.* thermal and acoustic isolation); and decorative/design.

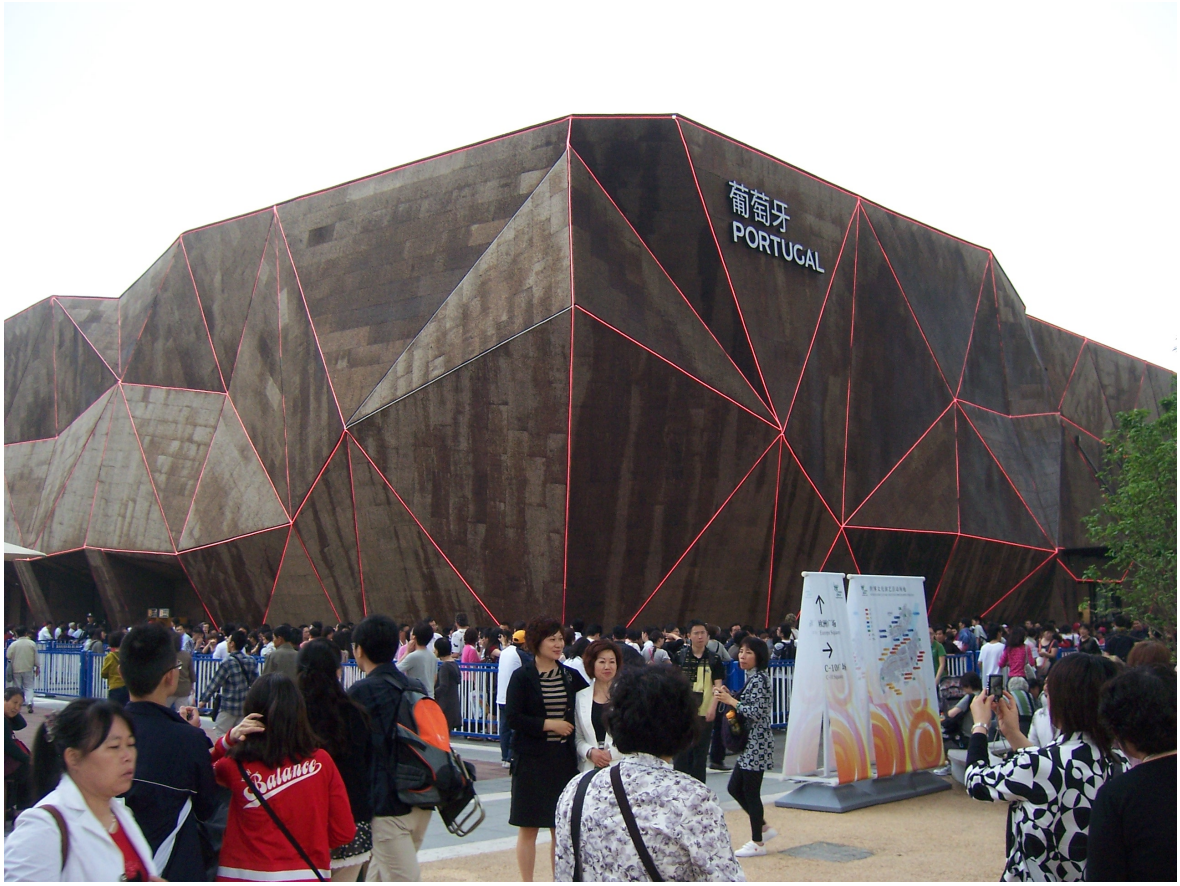

Figure 3.13: The 3640 m^2 facade of the Portugal Pavilion in the Shanghai World Expo 2010. The building is covered with 28 tons of insulation cork board — considered to be the most environmentally friendly insulation solution (picture courtesy of Hugo Mesquita).

Energy absorption

Finally, the energy absorption capacity of the material is the most important of the selected applications of cork in the scope of this work. As a natural cellular material, cork presents a stress-strain ($\sigma - \varepsilon$) behaviour similar to the schematic representation of a cellular material stress-strain curve in figure 3.2. Cork cells have low collapse stress and the peak stress on impact is also low [Gibson and Ashby 1997]. However, this is surpassed because large compressive strains can occur as the cells walls of cork progressively collapse, thus a great amount of energy may be absorbed [Gibson and Ashby 1997].

Examples were considered in order to exemplify the application of cork in impact energy absorption, namely the application of cork in sports. Nelo® kayaks is a Portuguese company which produces competition and leisure kayaks incorporating CORECORK®. CORECORK® is a registered mark for specific cork compounds, with specific mechanical and physical properties. NL10, NL20 and NL30 are examples of some CORECORK® compounds. The density is the main characteristic difference between these materials (*e.g.* NL20 has a density of 200 kg/m^3). CORECORK® compounds are being used in the sandwich construction of innovative lightweight racing kayaks, providing lightness and stiffness. In addition, this is also a material that is very easy to cut and assembly.

3.6 Brief literature review on cork

Many studies have been made on the characterisation of cork and its compounds [Rosa and Fortes 1988a, Rosa and Fortes 1988b, Fortes and Nogueira 1989, Rosa and Fortes 1991, Vaz and Fortes 1998, Gameiro and Cirne 2007, Gameiro *et al.* 2007a, Gameiro *et al.* 2007b, Paulino *et al.* 2009, Castro *et al.* 2010, Moreira *et al.* 2010, Sousa-Martins *et al.* 2012]. Not only the characterisation of cork was the goal of these studies but also the discovery of new applications and improvement of the most existing ones for this natural and green material. Relevant work in terms of the field of investigation considered in this thesis on the characterisation of cork and its applications will be presented in this section.

3.6.1 Books and reviews

M.A. Fortes (1938–2007) was one of the first persons to publish studies on the mechanical characterisation of cork in Portugal. M.A. Fortes was involved with publications with various results in fields of cork investigation and characterisation such as the stress relaxation and creep of cork [Rosa and Fortes 1988b], deformation and fracture of cork in tension [Rosa and Fortes 1991] and the friction properties of cork [Vaz and Fortes 1998]. One of the first investigations where M.A. Fortes was involved was related to the study of the influence of strain rate on the compression behaviour of cork [Rosa and Fortes 1988a] considering the anisotropy of the material. An analysis on the elastic recovery of cork specimens was also reported.

The book "A Cortiça", by Fortes *et al.* [Fortes *et al.* 2005] is a reference as the portuguese written book on cork. The subjects covered in this book are wide, such as the cork oak tree and the production of cork, the cellular microstructure of the material, mechanical, physical and chemical properties of cork, applications, behaviour of cork in traction, compression and fracture, among others.

Another book was published by Pereira [Pereira 2007] "Cork: Biology, Production and Uses". In addition to its great scientific value, this publication opened doors in the scientific community as a reference scientific book on cork in english language.

A review on cork and cork composites was recently published by Gil [Gil 2009]. This review presents a report on cork composites available in the market and their applications. A distinction is made between two different types of cork agglomerates. The first type of cork agglomerate is composition cork, which is a compound achieved by the combination of cork granules and an external binder, similar to the CORECORK® product range. The second type is made only of cork granules without any external binding component. Since it is made of only one substance it cannot be considered as a composite material. The author also refers some applications for these agglomerates.

Cork compounds have been used for a long time as fillers and expansion joints. Filler and expansion joints are used to neutralise the expansion and contraction phenomena in concrete constructions or mechanical parts. Cork can play a remarkable role in such applications due to its elastic recovery. Cork gaskets are also being produced since this material can accommodate large elastic distortion and volume change due to its cellular structure [Gil 2009]. In addition, its closed cell walls are impermeable to water and oils, which makes cork a strong competitor when compared to plastic gaskets. Gil [Gil 2009] also reported experimental results on sandwich cork composites with a core of conventional cork granulates using epoxy resin as the adhesion element. This author affirms that "cork agglomerates developed with epoxy resin present significantly better core shear stress limits, even when compared with Rohacell® [Gil 2009]", which is a rigid foam also very common in sandwich applications. It is also mentioned that sandwich structures which incorporate cork compounds in their cores "presented considerably higher load values than those obtained for other type of high performance core materials (such as Rohacell®) and the extraordinary recovery capacity verified in the cork agglomerates sandwiches displacement curves is an exclusive and intrinsic characteristic of cork".

3.6.2 Dynamic and material characterisation studies

Gameiro *et al.* [Gameiro *et al.* 2007a] performed an experimental study of the *quasi*-static and dynamic behaviour of cork under compressive loading, in order to characterise different types of cork (in terms of direction of the cellular structure — radial and non-radial) and compare them to industrially produced compounds (agglomerates and micro-agglomerates). Split Hopkinson Pressure Bar (SHPB) measurements were performed on four types of cork (disks) with average strain rates ranging from 200 to 600 s^{-1}. In terms of comparison between compounds, dynamic stress-strain curves for both agglomerated and micro-agglomerated[2] compounds were very similar, independently of the sample test and strain rate. These results allowed those authors to determine that "in the dynamic range considered (200 and 600 s^{-1}), the variation of strain rate, does not have an influence on the mechanical behaviour of the agglomer-

[2]Agglomerated cork compounds are distinct from micro-agglomerated cork compounds cork in terms of the cork granules size. Agglomerated cork compounds are made from cork granules with sizes ranging from 3 to 6 mm, whereas for micro-agglomerated cork compounds the range is from 0.5 to 2 mm [Gameiro 2007].

ates". Nonetheless, comparing the dynamic plateau of the stress-strain curves to the static curves, it was found that the dynamic one is larger. Agglomerates are, therefore, materials whose behaviour is dependent on the strain rate, when comparing *quasi*-static with dynamic regimes. As expected, when it comes to non-radial and radial cork disks the differences between dynamic and static regimes were found to be much more significant.

Paulino *et al.* [Paulino *et al.* 2009, Paulino and Teixeira-Dias 2011] presented a numerical study where several materials were tested to infer on the best performance for vehicle safety materials. Materials such as metal foams and polymer foams were tested and compared with MAC compounds. The authors proposed an expression for an energy absorption index that is a quantitative distinction between materials in impact and crashworthiness applications. MAC compounds got the best performance, when compared to the other materials, since these compounds not only absorbed the higher amount of energy but also exhibit "a tendency to maintain an ideal behaviour in terms of energy absorption, while aluminium foam reduces its efficiency for higher initial kinetic energy values" [Paulino *et al.* 2009]. Regardless of what was expected, due to its wide application in safety vehicle systems, polyurethane foams gave the worst results in terms of energy absorption.

One relevant work by Castro *et al.* [Castro *et al.* 2010] was published in 2010, entitled "Cork agglomerates as an ideal core material in lightweight structures". The authors performed static bending tests on simply supported sandwich panels, with carbon/epoxy for the face sheets and three different types of core materials: Nomex®, Rohacell® and cork agglomerates. In addition, different types of cork agglomerates were fabricated with conventional cork granulates but using epoxy resin as adhesive element. The intention of these authors was to characterise the mechanical strength inherent to those materials when subjected to different production variables. Dynamic tests, using a drop tower were also performed by subjecting sandwich panels to impact tests. The relevant conclusions, in the scope of this thesis, are from the dynamic tests, were it was observed that:

- Sandwich structures with cork based compound cores presented higher load values than sandwich structures with other cores (Nomex® and Rohacell®); and

- Sandwich structures with optimised cork agglomerates presented higher energy absorption capacity than other foam cores tested and very little damage was registered.

Alcântara *et al.* [Alcântara *et al.* 2013] made a characterisation study (*i.e.* the mechanical properties and mechanical behaviour) of a new cork based composite material (Core-Y). This material was produced by combining cork granules with an epoxy resin. An experimental and numerical study was performed by those authors. From the conclusions obtained with this study the ability of Core-Y to support compression loads (static or dynamic) stands out. The authors refer that Core-Y can be a good candidate

to different applications when used as inserts inside structural elements subjected to impact, such as in the automobile industry.

Another study was also developed in fields of minimisation of the vulnerability of building structures (that had cork or a cork compound in its constitution) subjected to seismic activity. De-Carvalho *et al.* [de Carvalho *et al.* 2013] developed a composite material that can contribute to the dissipation of energy and reduction of the vulnerability of constructions. The new composite material (CorBe) was obtained by combining the properties of cork with common construction mortars, with the incorporation in building's walls as its final application. Several tests were made, namely, resistance to compression, determination of rupture deformation and initial elastic modulus determination. In order to get an estimation of the energy dissipated by this material, cyclic tests were also made and the equivalent damping was determined and analysed. Comparing CorBE specimens with others without cork in its constitution, CorBe specimens exhibited a clear improvement in uniaxial and diagonal compression tests, for the strains levels imposed.

Chapter 4

Constitutive modelling

The basic concepts and theory needed to better understand the material models used in the finite element (FE) analysis performed in the scope of this investigation are mentioned. In the final part of the chapter, all the material models used in the FE analysis are presented.

Constitutive modelling is the accurate definition of the behaviour of materials. An introduction with background is given in the first part of this chapter in order to better understand the numerical material models that are needed for the finite element (FE) analysis in the scope of this investigation. These numerical approaches will be the scope of the the second part of this chapter.

4.1 Kinematics

Whittaker, in his book "A treatise on the analytical dynamics of particles and rigid bodies" [Whittaker 1988] describes kinematics stating that "It is natural to begin this discussion by considering the various possible types of motion in themselves, leaving out of account for a time the causes to which the initiation of motion may be ascribed; this preliminary enquiry constitutes the science of kinematics." In other words, kinematics is the field of knowledge that studies motion and deformation without reference to the cause.

4.1.1 Motion

Consider the deformable body represented in figure. The body is an assembly of material particles labeled by the coordinates $\mathbf{X}$, with respect to cartesian basis E_i, at their initial positions at time $t_0 = 0$ (reference configuration). The current positions of these particles are located, at time t, by the coordinates $\mathbf{x}$, with respect to an alternative cartesian basis e_i. In the explanation that follows the bases E_i and e_i are

considered to be coincident. Nonetheless, the notational distinction between the two bases is maintained to allow the association of quantities with initial (or reference) configuration to current configuration. The current coordinates of a defined particle can then be given as a function of the initial position and time, as in the following equation [Fung and Tong 2001, Bonet and Wood 2008, de Souza Neto *et al.* 2008]:

$$\mathbf{x} = \phi(\mathbf{X}, t). \tag{4.1}$$

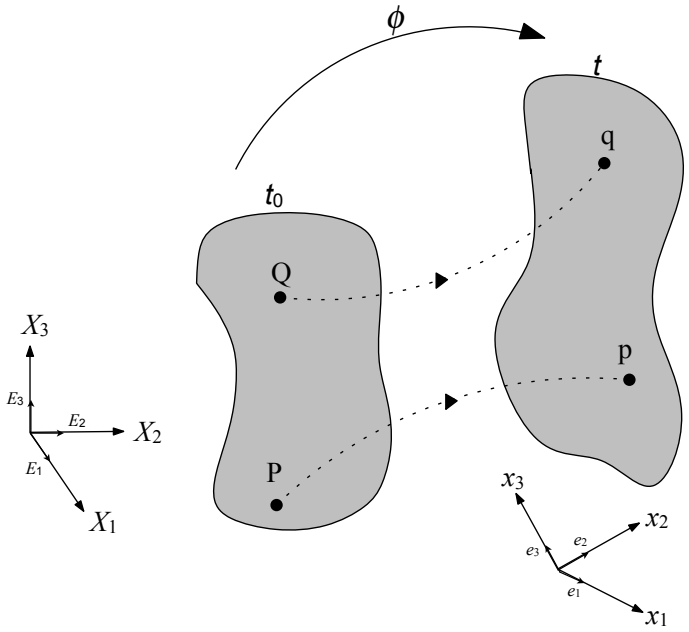

Figure 4.1: Motion of a deformable body from initial (or reference) configuration ($t_0 = 0$) to the current configuration ($t > 0$) (adapted from [Bonet and Wood 2008]).

4.1.2 Deformation gradient

The material deformation gradient tensor is present in all equations which relate quantities before, during and after the deformation. It is a tensor that allows to write the spatial position of two neighbouring particles after deformation, in terms of their relative material positions before deformation. The deformation gradient can be referred to as a two-point tensor since if transforms vectors in the initial configuration to the current configuration [Bonet and Wood 2008, Fung and Tong 2001]. This tensor can be expressed as

$$\mathbf{F} = \frac{\partial \phi}{\partial \mathbf{X}} = \nabla_0 \phi, \tag{4.2}$$

where ∇_0 is the gradient operator with respect to the material configuration. The elemental vectors $\mathrm{d}x_\mathrm{q}$ and $\mathrm{d}x_\mathrm{p}$ can be obtained in terms of $\mathrm{d}X_\mathrm{Q}$ and $\mathrm{d}X_\mathrm{P}$ according to

$$\mathrm{d}\mathbf{x} = \mathbf{F}\mathrm{d}\mathbf{X}. \tag{4.3}$$

4.2 Material behaviour laws

When, for example, a material is subjected to an external mechanical solicitation it must have a proper mechanical model that mathematically describes the behaviour of the continuum medium. A set of equations, in which it is ensured that the medium remains continuum and that relates different representative variables (namely between stress and strain) must then be defined. These equations are the material behaviour laws, that is, the constitutive model.

4.2.1 Elastic constitutive equations

In an elastic medium, the three-dimensional case corresponding to the determination of the linear stress field can be written by Hooke's law, that is,

$$\boldsymbol{\sigma} = \mathbf{D} : \boldsymbol{\varepsilon}, \tag{4.4}$$

where $\boldsymbol{\sigma}$ and $\boldsymbol{\varepsilon}$ are Cauchy's stress and strain tensors, respectively, and $\mathbf{D}$ is the elasticity tensor. Rewriting this equation using Voigt notation leads to [Lemaitre 2001, Teixeira-Dias *et al.* 2010]

$$\begin{Bmatrix} \sigma_{xx} \\ \sigma_{yy} \\ \sigma_{zz} \\ \tau_{xy} \\ \tau_{yz} \\ \tau_{zx} \end{Bmatrix} = \mathbf{D} \begin{Bmatrix} \varepsilon_{xx} \\ \varepsilon_{yy} \\ \varepsilon_{zz} \\ \gamma_{xy} \\ \gamma_{yz} \\ \gamma_{zx} \end{Bmatrix}, \tag{4.5}$$

with

$$\mathbf{D} = \frac{E}{(1+\nu)(1-2\nu)} \begin{bmatrix} (1-\nu) & \nu & \nu & 0 & 0 & 0 \\ \nu & (1-\nu) & \nu & 0 & 0 & 0 \\ \nu & \nu & (1-\nu) & 0 & 0 & 0 \\ 0 & 0 & 0 & \frac{(1-2\nu)}{2} & 0 & 0 \\ 0 & 0 & 0 & 0 & \frac{(1-2\nu)}{2} & 0 \\ 0 & 0 & 0 & 0 & 0 & \frac{(1-2\nu)}{2} \end{bmatrix} \tag{4.6}$$

where E and ν are the Young modulus and Poisson ratio.

4.2.2 Plasticity criteria

Most of the existing engineering materials cannot be considered to behave as purely elastic or hyperelastic materials for all levels of stress [Bodner and Symonds 1979,Fung and Tong 2001,Lemaitre 2001,Yu *et al.* 2006,de Souza Neto *et al.* 2008]. The difference between elastic/hyperelastic materials and those that do not behave elastically is related to the fact that for the latter, when applied loads are removed they fail to return to the initial undeformed configuration, leading to permanent deformation. Hence, to better understand inelastic constitutive models, a brief background on plasticity will be provided in the following sections.

Plasticity criteria define the stress state, that can be elastic or plastic, of a certain material point, as well as the transition between these two states (elastic and plastic). Mathematically, a plasticity criterion F defines a surface in the stress field where $F(\sigma) = 0$, thus defining a yield surface. This surface corresponds to all the stress states for which plastic strain starts to occur. Experimental tests and theoretical studies [Bridgman 1952] have shown that, for metals, a certain set of restrictions must be made for the mathematical representation of such yield surfaces. These hypotheses are often considered in the formulation of plasticity criteria [Rodrigues and Martins 2005] and are the following:

1. Hydrostatic stress states do not contribute to plastic deformation or, in other words, the criteria should be independent of hydrostatic pressure;

2. The yield surface must be convex, due to the fact that convexity and the non-existence of singularities on the surface ensure an univocal relation between the plastic deformation velocity tensor and a given stress state; and

3. The plasticity criteria must be associated with a plasticity law, that is, a set of equations that describes the relations between representative variables in a plastic deformation case.

4.2.3 Evolution laws

Once the concept of yield surface has been introduced, it is now necessary to describe how this surface may evolve with time and, particularly, with deformation. The process that is described by the evolution of the yield surface is designated by hardening. There are two major laws for the evolution of yield surfaces: isotropic hardening and kinematic hardening. Isotropic hardening assumes that the current yield surface is obtained from a uniform expansion of the initial surface. In other words, this means that when the yield surface is being updated for a new stress state, the centre remains coincident with the initial position (pure expansion). Kinematic hardening assumes that when plastic deformation processes occur the yield surface is being constantly updated and its centre moves in the stress field. However, the shape and size of the surface are kept constant (pure translation) [Dunne and Petrinic 2005]. A model accounting for both

expansion and translation of the yield surface is called "mixed hardening". These two hardening laws will be further explored in the following sections.

4.2.4 Elastic-plastic constitutive equations

A non-linear approach to the analysis of a problem is needed when the relation between the applied loads and the resulting displacements is not linear ($F \neq ku$). There are three different types of non-linearity:

1. Material non-linearity: non-linear elasticity, plasticity, fluency, damage, *etc.*;

2. Geometric non-linearity: large displacements, large rotations, large deformations, *etc.*; and

3. Non-linearity in the boundary conditions: contact conditions, friction, *etc.*

Only one of the previous conditions needs to be true to assume non-linear model behaviour and consequent non-linear analysis of the problem. Incremental and iterative procedures are required for this type of problems in order to obtain a correct approach to the solution.

Elastoplasticity occurs for stress values that lead to irreversible deformation. The material will behave elastically until a certain stress value: the yield stress. For stresses beyond this yield stress value the material is said to behave plastically. Supposing that loading continues and assuming (as an approximation) that the yield stress remains constant, the material is said to have a perfectly plastic behaviour. However, if loading continues and plastic stress (after yield) evolves with strain then, the material experiences hardening phenomena [Bodner and Symonds 1979].

4.2.5 Yield criterion

In the following elastic-plastic formulation the von Mises yield criterion is used and will be explained. Additionally, isotropic and kinematic hardening are explained in detail. A linear plastic flow rule (that is, a mathematical description of the increment of plastic strain when yielding occurs) is assumed. The von Mises criterion is frequently used to describe plastic yielding in metals. According to this criterion plastic yielding begins when the J_2 stress deviator invariant reaches a critical value [de Souza Neto *et al.* 2008], that is,

$$W_{\mathrm{d}}^{e} = \frac{J_2}{2G}, \tag{4.7}$$

where W_{d}^{e} is the elastic distortional energy per unit volume and G is the elastic shear modulus. The stress invariant J_2 can be expressed in terms of the deviatoric stresses

s, principal stresses or generic Cauchy stress components as

$$\begin{aligned} J_2 &= \frac{1}{2} s_{ij} s_{ij} = \frac{1}{6}\left[(\sigma_1-\sigma_2)^2 + (\sigma_2-\sigma_3)^2 + (\sigma_1-\sigma_3)^2\right] \\ &= \frac{1}{2}(\sigma_x^2+\sigma_y^2+\sigma_z^2) + \tau_{xy}^2 + \tau_{yz}^2 + \tau_{xz}^2. \end{aligned} \tag{4.8}$$

If equations 4.7 and 4.8 are combined, the elastic distortion energy per unit volume becomes

$$W_{\mathrm{d}}^{\mathrm{e}} = \frac{J_2}{2G} = \frac{1}{2G}\left\{\frac{1}{6}\left[(\sigma_1-\sigma_2)^2 + (\sigma_2-\sigma_3)^2 + (\sigma_1-\sigma_3)^2\right]\right\} = \frac{3}{4G}\tau_{\mathrm{oct}}^2, \tag{4.9}$$

where τ_{oct} is the octahedral shear stress. As stated before, the yield criterion must be independent from the hydrostatic pressure, meaning that this volumetric pressure does not lead to plastic deformation. Therefore, the von Mises criterion is equivalent to stating that "plastic yielding begins when the distortional elastic strain-energy reaches a critical value" [de Souza Neto *et al.* 2008]. Consequently, this criterion is said to be pressure-insensitive. This independence between hydrostatic stress and yielding lead us to find a material plane called the octahedral plane, where the stress state can be decoupled into dilational strain energy and distortional strain energy. In dilation, stresses are the same in all directions and there is no shear. The contribution of the elastic distortion energy can be obtained considering a given material under an axial load (where $\sigma_1 = \sigma_0$ and $\sigma_2 = \sigma_3 = 0$). The critical elastic energy by unit volume will thus be given by

$$W_{\mathrm{d}}^{e} = \frac{3}{4G}\tau_{\mathrm{oct}}^2 = \frac{3}{4G}\left(\frac{1}{3}\sqrt{2\sigma_0^2}\right)^2. \tag{4.10}$$

If equations 4.7 to 4.10 are combined, the following expression is obtained for the von Mises yield criterion:

$$(\sigma_1-\sigma_2)^2 + (\sigma_2-\sigma_3)^2 + (\sigma_1-\sigma_3)^2 = 2\sigma_0^2. \tag{4.11}$$

The von Mises yield criterion can also be established related to a cartesian axis system in the following way [Rodrigues and Martins 2005]:

$$F(\sigma) = (\sigma_x-\sigma_y)^2 + (\sigma_y-\sigma_z)^2 + (\sigma_z-\sigma_x)^2 + 6(\tau_{xy}^2+\tau_{yz}^2+\tau_{xz}^2) - 2\sigma_0^2 = 0. \tag{4.12}$$

Isotropic hardening

As said before, in isotropic hardening it is assumed that the evolution of the yield surface is, at any state of hardening, a uniform (isotropic) expansion of the initial yield surface without translation, that is, the centre of the new updated surface remains invariant in the (σ_1, σ_2, σ_3) space.

A proper relation between stress and plastic strain must be defined. To obtain a suitable scalar measure of the effective plastic strain, the magnitude of the accumulated

plastic strain can be defined as [de Souza Neto *et al.* 2008]

$$\varepsilon^{\mathrm{p}}_{\mathrm{eff}} = \int_0^t \sqrt{\left(\frac{2}{3}\dot{\varepsilon}^{\mathrm{p}}_{ij}\dot{\varepsilon}^{\mathrm{p}}_{ij}\right)}\mathrm{d}t. \tag{4.13}$$

The next step is to define the yield stress, σ_{y}, as a function of the effective plastic strain, $\varepsilon^{\mathrm{p}}_{\mathrm{eff}}$. There are several hardening functions that obey an elastic-plastic behaviour. The most common forms are the linear strain-hardening relations, for the one dimensional case, generically defined as

$$\sigma_{\mathrm{y}}(\varepsilon^{\mathrm{p}}_{\mathrm{eff}}) = \sigma_0 + h\varepsilon^{\mathrm{p}}_{\mathrm{eff}}, \tag{4.14}$$

or the power-law hardening relations, generically defined as

$$\sigma_{\mathrm{y}}(\varepsilon^{\mathrm{p}}_{\mathrm{eff}}) = \sigma_0 + h(\varepsilon^{\mathrm{p}}_{\mathrm{eff}})^{1/m}. \tag{4.15}$$

σ_0 is the initial yield stress and h and m are material parameters that can be obtained experimentally. These two approaches to isotropic hardening, are schematically represented in figures 4.2 (a) and (b) [Dunne and Petrinic 2005].

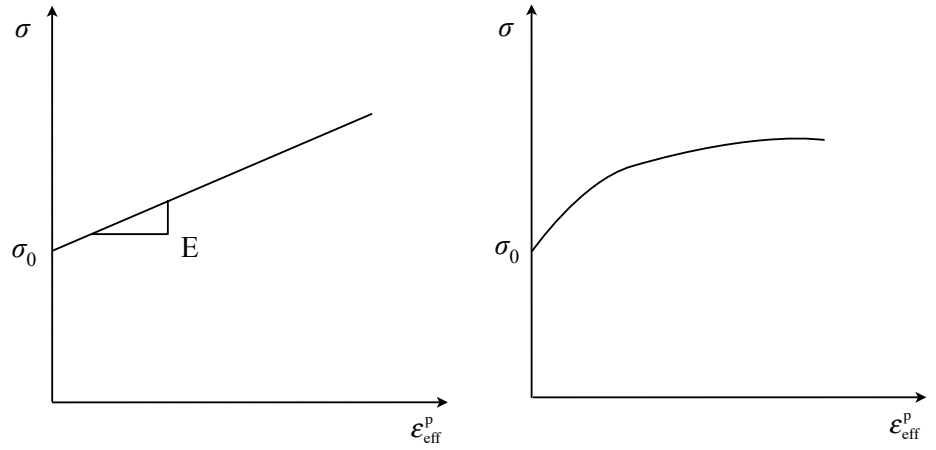

Figure 4.2: (a) Linear strain-hardening and (b) power-law strain-hardening.

Kinematic hardening

An isotropic hardening law may not be very helpful in situations where components are subjected to cyclic loading. This happens because the Bauschinger effect is not taken into account. It is frequently observed in experiments that, after being loaded (and hardened) in one direction, some materials exhibit lower resistance to plastic yielding in the opposite direction (softening) [de Souza Neto *et al.* 2008, Bower 2010]. This phenomenon is commonly known as the Bauschinger effect and can be described with the introduction of kinematic hardening.

In kinematic hardening, the center of the yield surface translates in the direction of the plastic strain but its shape and dimension remains the same. As the material is being deformed, for example, in tension (stretched), the yield surface translates along with the increasing stress, thus modelling strain hardening.

The evolution of kinematically hardening von Mises yield surface (in the deviatoric plane) used to model the phenomenon associated with the translation of the yield surface is given by [Dunne and Petrinic 2005],

$$F(\sigma) = 0 = \sqrt{\frac{3}{2}(\xi_{ij}\xi_{ij})} - \sigma_y, \tag{4.16}$$

where ξ is,

$$\xi_{ij} = (s_{ij} - \alpha_{ij}). \tag{4.17}$$

The relative stress tensor, defined as ξ in equation 4.17, corresponds to the difference between the deviatoric stress tensor, s, and the symmetric deviatoric tensor, α, which is also known as the back-stress tensor. The back-stress tensor represents the translation of the yield surface in the space of stresses, that is, the updated position of the centre of the yield surface [de Souza Neto *et al.* 2008], while σ_{y} is the yield stress, given by the sum of the initial yield stress σ_0 to the stress increment $\beta E_{\mathrm{p}}\varepsilon^{\mathrm{p}}_{\mathrm{eff}}$, as in

$$\sigma_{\mathrm{y}}(\varepsilon^{\mathrm{p}}_{\mathrm{eff}}) = \sigma_0 + \beta E_{\mathrm{p}}\varepsilon^{\mathrm{p}}_{\mathrm{eff}}. \tag{4.18}$$

The parameter $\beta \in [0, 1]$ was introduced to enhance the difference in the equation from fully isotropic ($\beta = 0$) to fully kinematic hardening ($\beta = 1$). E_{p} is the plastic hardening modulus. This hardening law predicts that the stress-plastic strain curve is a straight line with slope E_{p} given by [Hallquist 2006],

$$E_{\mathrm{p}} = \frac{E_{\mathrm{t}}E}{E - E_{\mathrm{t}}}, \tag{4.19}$$

where E_{t} is the tangent hardening modulus.

Hardening is modelled by the motion of the yield surface. Therefore, it is necessary to relate the back-stress tensor α to the plastic strain history. One simple approach to model features of the plastic response of solids under cyclic loading is given by [Dunne and Petrinic 2005]

$$\mathrm{d}\alpha_{ij} = \frac{2}{3}E_{\mathrm{p}}\mathrm{d}\varepsilon^{\mathrm{p}}_{ij}. \tag{4.20}$$

4.3 Material models

The constitutive laws used to model the behaviour of the materials investigated within the frame of this work will now be reviewed in detail. As stated in previous chapters, sandwich structures with micro-agglomerated cork (MAC) compound cores and aluminium face sheets were experimentally and numerically tested. Plasticity models were

chosen to model the behaviour of the face sheets of the sandwich structures subjected to blast-waves. An explanation on the implementation of the plasticity model for both isotropic and kinematic hardening is provided in the following sections. This implementation is applicable for the aluminium material model. For the specific case of the MAC compounds, a different approach has to be used since this is a cellular material. Special attention is also given to the numerical modelling of both the explosive and the air.

4.3.1 Plastic kinematic constitutive model

Material type `*Mat_Plastic_Kinematic` from the LS-Dyna^{TM} material database was used for the aluminium plates. This material model is adequate to model either plasticity for both isotropic and kinematic hardening or a combination of both. The input parameters for this material type are its density ρ^{Al}, Young modulus E^{Al}, Poisson ratio ν^{Al}, initial yield stress σ_0^{Al} and tangent modulus $E_{\mathrm{t}}^{\mathrm{Al}}$.

The implementation of this material model starts with the elastic update of the deviatoric stresses. In the next paragraphs, the generic steps needed to implement the model are explained, where the following parameters are introduced [Hallquist 2006]:

- The trial stress tensor components: $\sigma_{ij}^{\mathrm{tr}}$;
- The stress tensor components in step n (current step): σ_{ij}^{n};
- The stress tensor components in step $(n+1)$ (updated step): σ_{ij}^{n+1};
- The elastic tangent modulus matrix components: C_{ijkl};
- The incremental strain tensor components: $\Delta\varepsilon_{\mathrm{kl}}$.

For the sake of clarity some relations referred in previous sections will be repeated in the following paragraphs. The components of the trial elastic stress tensor and deviatoric stress tensor at state $n+1$ are determined with

$$\sigma_{ij}^{\mathrm{tr}} = \sigma_{ij}^{n} + C_{ijkl}\Delta\varepsilon_{kl}, \tag{4.21}$$

$$s_{ij}^{\mathrm{tr}} = \sigma_{ij}^{\mathrm{tr}} - \frac{1}{3}\sigma_{kk}^{\mathrm{tr}}, \tag{4.22}$$

respectively, where the superscript tr designates trial variables. After this, the yield function is calculated and, according to the equation 4.16, the yield surface becomes,

$$F(\sigma) = \frac{3}{2}\xi_{ij}^{\mathrm{tr}}\xi_{ij}^{\mathrm{tr}} - \sigma_y^2 = 0, \tag{4.23}$$

where $\xi_{ij}^{\mathrm{tr}} = (s_{ij}^{\mathrm{tr}} - \alpha_{ij})$. If yielding is not yet present, that is, no plastic strain is registered, the elastic regime prevails and the trial guess corresponds to the correct one. However, if yielding occurs a plastic strain update is needed, the stresses are

scaled back to the yield surface and the position of its centre is updated (if kinematic hardening is assumed), that is:

- If $F \leq 0$ there is no yielding and, therefore an elastic regime is still present;
- If $F > 0$ then yielding occurred and the effective plastic strain increment is determined using

$$\varepsilon_{\text{eff}}^{\text{p}^{n+1}} = \varepsilon_{\text{eff}}^{\text{p}^{n}} + \Delta\varepsilon_{\text{eff}}^{\text{p}} = \varepsilon_{\text{eff}}^{\text{p}^{n}} + \frac{\Lambda - \sigma_{\text{y}}}{3G - E_{\text{p}}}. \tag{4.24}$$

where $\Lambda = \sqrt{\frac{3}{2}\xi_{ij}^{\text{tr}}\xi_{ij}^{\text{tr}}}$. The stresses have to be scaled back using,

$$\sigma_{ij}^{n+1} = \sigma_{ij}^{\text{tr}} - \frac{3G\Delta\varepsilon_{\text{eff}}^{\text{p}}}{\Lambda}\xi_{ij}^{\text{tr}}. \tag{4.25}$$

Finally, the position of the centre of the yield surface has to be updated by evaluating the back stresses as

$$\alpha_{ij}^{n+1} = \alpha_{ij}^{n} + \frac{\beta E_{\text{p}}\Delta\varepsilon_{\text{eff}}^{\text{p}}}{\Lambda}\xi_{ij}^{\text{tr}}. \tag{4.26}$$

4.3.2 Honeycomb material constitutive model

The constitutive equations of a material model are an essential part in order to assess the good or bad agreement between experimental and numerical results.

Several material models are implemented in LS-Dyna™ to describe the behaviour of cellular materials [DK 2012]. However, many of these are not suitable to model cork in the way that this work needs, simply because they are material models for specific applications. However, the `*Mat_Honeycomb` [DK 2012, Hallquist 2006] material model can be adapted for cork. It is an orthotropic material model before densification because the components of the orthotropic stress tensor are uncoupled. This is in accordance to the fact that the Poisson ratio of these materials in the uncompacted configuration (*i.e.* before densification) is very low and can be considered to be approximately zero [Hallquist 2006]. In the plateau region, values of the Young modulus vary from its initial value to the value when the material is completely compacted. This variation is linear and is a function of the relative volume[1]. What distinguishes this material model from others for the numerical modelling of crushable and cellular materials is the possibility to introduce a stress-strain curve (σ–ε) that describes the behaviour of the material. This material model needs several material parameters as input, such as:

- The Young modulus in densification: E_{d};
- The Poisson ratio in densification: ν_{d};
- The material density: ρ;

[1]Relative volume is the ratio between the current volume and initial volume of the material [DK 2012, Hallquist 2006].

- The initial yield stress in densification: σ_0^{d};
- The relative volume in densification: V_{f};
- The experimental stress-strain curve (a set of (σ, ε) points): LC.

The trial stress tensor increments are determined in the honeycomb material model using equation 4.21. At this stage the material is still uncompacted. The superscript tr is used to refer that the stresses are still being determined in the elements with Hooke's law. Afterwards, the stresses are compared with the value of stress given by an experimental curve (LC) and in case of this value is higher than the experimental the calculation proceeds correcting the stresses. Mathematically, if one component of the elemental stresses verifies the condition

$$|\sigma_{ij}^{n+1,\mathrm{tr}}| > \sigma_{ij}^{LC}, \tag{4.27}$$

that is, higher than the experimental stress values given by the load curve, then the stress tensor components are updated according to

$$\sigma_{ij}^{n+1} = \sigma_{ij}^{LC} \frac{\sigma_{ij}^{n+1,\mathrm{tr}}}{|\sigma_{ij}^{n+1,\mathrm{tr}}|}. \tag{4.28}$$

When the material is in the densification regime, the material model describes an elastic-perfectly plastic material and the stress updates are carried out according to

$$s_{ij}^{\mathrm{tr}} = s_{ij}^{n} + 2G(\Delta\varepsilon_{ij}^{'})^{n+1}, \tag{4.29}$$

where the deviatoric strain increment is given by

$$\Delta\varepsilon_{ij}^{'} = \Delta\varepsilon_{ij} - \frac{1}{3}\Delta\varepsilon_{kk}\delta_{ij}, \tag{4.30}$$

where δ_{ij} is the Kronecker-delta, given by

$$\delta_{ij} = \begin{cases} 1 & \text{if } i = j \\ \\ 0 & \text{if } i \neq j \end{cases}. \tag{4.31}$$

The stresses are then checked to verify if the effective trial stresses exceed the yield stress of the densified material, according to

$$s_{\mathrm{eff}}^{\mathrm{tr}} > \sigma_{\mathrm{y}}^{\mathrm{d}}, \tag{4.32}$$

where

$$s_{\mathrm{eff}}^{\mathrm{tr}} = \sqrt{\left(\frac{3}{2} s_{ij}^{\mathrm{tr}} s_{ij}^{\mathrm{tr}}\right)}. \tag{4.33}$$

If condition 4.32 is met the stresses are scaled back the to the yield surface, according to

$$s_{ij}^{n+1} = \frac{\sigma_{\mathrm{y}}}{s_{\mathrm{eff}}^{\mathrm{tr}}} s_{ij}^{\mathrm{tr}}. \tag{4.34}$$

The pressure can now be updated using the elastic bulk modulus, K, in the form

$$p^{n+1} = p^n - K\Delta\varepsilon_{kk}^{n+1}. \tag{4.35}$$

These pressure values are then used to obtain the final value for the Cauchy stress components, that is,

$$\sigma_{ij}^{n+1} = s_{ij}^{n+1} - p^{n+1}\delta_{ij}. \tag{4.36}$$

4.3.3 Explosive material constitutive model

The most suitable material model for the explosive is `*Mat_High_Explosive_Burn` from the LS-Dyna$^{\mathrm{TM}}$ material database. It is possible to model the detonation of high explosives with this material model knowing: the density of the material, ρ, the detonation velocity of the high explosive, D, and the Chapman-Jouguet pressure, P_{CJ} [Wilkins 1964, Giroux 1973]. An equation of state (EOS) also needs to be defined. This will be further described in section 4.3.5.

On a first approach the material model calculates the lighting time t_1 for each finite element of the explosive, that is,

$$t_1 = \frac{d_{\mathrm{det}}}{D}, \tag{4.37}$$

where d_{det} is the distance between the detonation point and the centre of the element. If multiple detonation points are present within the simulation model, the closest detonation point to the element is used to determine the correspondent lighting time [DK 2012].

The explosive burn fractions are determined in a second stage. The model allows three types of calculation methodologies for the burn fractions. In the first calculation methodology the explosive is modelled as an ideal elastic-plastic material, allowing the material to be compressed without detonation. For example, in LS-Dyna$^{\mathrm{TM}}$ the detonation is triggered manually using the implemented `*Initial_Detonation` function. Mathematically, the burn fraction F_1 is determined by,

$$F_1 = \begin{cases} \frac{2(t-t_1)DA_{\mathrm{max}}^{\mathrm{e}}}{3V^{\mathrm{e}}} & \text{if } t > t_1 \\ \\ 0 & \text{if } t \leq t_1 \end{cases} \tag{4.38}$$

where $A_{\mathrm{max}}^{\mathrm{e}}$ is the cross section area of the finite element, V^{e} is the finite element's volume and t the current time. This first methodology was used within the scope of this research.

In the second calculation methodology, any volumetric compression will lead to the

detonation of the explosive, and the burn fraction is determined according to:

$$F_2 = \frac{1 - V}{1 - V_{\mathrm{CJ}}}, \tag{4.39}$$

where V is the relative volume and V_{CJ} is the Chapman-Jouguet relative volume, given by [AM 2005, DK 2012]

$$V_{\mathrm{CJ}} = \frac{\rho_0 D^2 - P_{\mathrm{CJ}}}{\rho_0 D^2}, \tag{4.40}$$

where ρ_0 is the surrounding environment density. Another calculation methodology is possible by combining the two previously mentioned methodologies. The detonation can be therefore triggered, for example, with an artificial/computational detonator (`*Initial_Detonation`) or by volumetric compression, and the burn fraction is determined according to

$$F = \max\{F_1, F_2\}. \tag{4.41}$$

The burn fraction, F, is then multiplied by the equation of state of the high explosive (HE), in accordance to:

$$p = F p_{\mathrm{EOS}}(V, U^*), \tag{4.42}$$

where p_{EOS} is the pressure from the equation of state that governs the material and U^* is the internal energy density per unit of initial volume [DK 2012].

4.3.4 Air constitutive model

Material model `*Mat_Null` was used to model the air in the FEM analysis. For solid elements, equations of state can be called through this material model to avoid deviatoric stress calculations. This happens because air is assumed to have a hydrodynamic material behaviour[2] [Du Bois and Schwer 2007], that is,

$$\text{if} \quad s' << |p| \quad \text{then} \quad s' \approx 0 \quad \text{and} \quad \sigma_{xx} \approx \sigma_{yy} \approx \sigma_{zz} \approx -p. \tag{4.43}$$

The density of this fluid is an input for the material model. As stated, in this specific case the material law is defined by the equation of state that defines the pressure values as a function of both the density and the internal energy [DK 2012].

4.3.5 Equation of state

An equation of state is a relation between state variables [Winterbone 1996]. More specifically, an equation of state is a thermodynamic equation describing the state

[2]Hydrodynamic material: A material is called hydrodynamic if the deviatoric stresses are much smaller then the pressure and can be neglected. Examples of hydrodynamic material response are: (i) materials with very low shear stiffness (fluids) and (ii) very high compressive loading of metals, where the yield stress limits the deviatoric response because pressure exceeds yield stress by two orders of magnitude or more [Du Bois and Schwer 2007].

of matter under a given set of physical conditions. The thermodynamic state of a homogeneous material that does not suffer any chemical reaction or phase changes can be defined by two variables of state [Serway and Jewett 2003]. Mathematically, an EOS defines the relation between different state variables (*e.g.* the internal energy, pressure, temperature and volume). Some numerical modelling problems need the definition of an EOS in addition to the constitutive model. Materials subjected to high strain rates or even the propagation of shock-waves, are often modelled by additionally using an EOS in the definition of the material's behaviour. Within this investigation, two EOS were used for the description of the air and the high explosive. The particularities of these two EOS are described in the following paragraphs.

Jones-Wilkins-Lee EOS

There are several types of EOS. Their differences are mostly related to the types of materials they can describe and how their volumetric compression (or expansion) evolves. For the explosive burn material model Jones-Wilkins-Lee (JWL) EOS is the most effective. The most general form of the JWL equation of state defines the blast pressure as [DK 2012, Urtiew and Hayes 1991]

$$P_{\mathrm{b}} = A\left(1-\frac{\omega}{R_1}\right)e^{-R_1 V} + B\left(1-\frac{\omega}{R_2 V}\right)e^{-R_{12} V} + \frac{\omega U^*}{V}. \tag{4.44}$$

This EOS is used whenever high explosive detonations are present. This EOS is used in LS-Dyna$^{\mathrm{TM}}$ with `*Mat_High_Explosive_Burn` material model, which determines the lighting time for the explosive finite elements. In the previous relation (equation 4.44) the pressure is defined as a function of the relative specific volume, V, and the internal energy per unit of initial volume of the explosive charge, U^* [Urtiew and Hayes 1991]. Parameters A, B, R_1, R_2 and ω are material constants related to the type of explosive. A and B are pressure coefficients, R_1 and R_2 principal and secondary eigenvalues, respectively, and ω is the fractional part of the normal Tait equation adiabatic exponent [Urtiew and Hayes 1991]. These constants can be easily found in reference books or publications for various explosives [Dobratz and Crawford 1985]. Those used in the FE analysis of this work correspond to TNT (trinitrotoluene), since TNT equivalent was used. The values used are listed in table 4.1.

Linear Polynomial EOS

The `*EOS_Linear_Polynomial` EOS is the one that best suits the behaviour of air. This polynomial EOS, linear in the specific (volumetric) internal energy, U^*, defines the initial thermodynamic state of the material and the pressure, according to [DK 2012]

$$p = C_0 + C_1\mu + C_2\mu^2 + C_3\mu^3 + \left(C_4 + C_5\mu + C_6\mu^2\right)U^*. \tag{4.45}$$

Table 4.1: Input parameters for the equation of state of TNT.

Parameter	**Value**
A	609.77 GPa
B	12.95 GPa
R_1	4.50
R_2	1.40
ω	0.25
E	9.00 GPa
v_0	1.00

Parameters C_0 to C_6 in this equation are material constants determined experimentally and μ is given by,

$$\mu = \frac{\rho}{\rho_0} - 1, \tag{4.46}$$

where $\frac{\rho}{\rho_0}$ is the ratio of the current density to the initial density. Gases that follow a classical gamma (γ) law can also be modelled with the linear polynomial EOS, by setting $C_0 = C_1 = C_2 = C_3 = C_6 = 0$ and $C_4 = C_5 = \gamma - 1$, where γ is the ratio of specific heats [Hallquist 2006]. The pressure can then be determined according to,

$$p = (\gamma - 1)\frac{\rho}{\rho_0}U^*. \tag{4.47}$$

The parameters used in the FE analysis for the linear polynomial EOS to model air are listed in table 4.2 [Otsuka *et al.* 2004, Kakogiannis *et al.* 2010].

Table 4.2: Input parameters for the equation of state of air.

Parameter	**Value**
γ	1.4
U^*	253×10^{-6} GPa
ρ_0	1.225×10^{-3} g/cm^3

Part II

Experimental tests

Chapter 5

Experimental setup and background

After a brief review on the application of ballistic pendulums, a description of the experimental facilities used throughout this work, as well as the equipment inherent to the ballistic pendulum is presented in this chapter.

The experimental setup developed and used is described in detail in this chapter. A brief description on the background on experimental work with explosions and their effects on structures (*e.g.* the use of ballistic pendulums) are mentioned. The most relevant advantages and disadvantages associated with the use of the ballistic pendulum are pointed out. Some of the relevant work regarding the applications of ballistic pendulums in blast research is presented. The specific pendulum used within the scope of this work is described. All the equipment, as well as the theory inherent to the experimental data analysis, is also described in detail in this chapter.

5.1 Background

Ballistic pendulums have been widely used to measure the total impulse transmitted to structures from blast-waves. This kind of setup has been used for several decades [Nurick and Shave 1996, Hanssen *et al.* 2002, Karagiozova *et al.* 2005, Jacob *et al.* 2007, Zhu *et al.* 2008b, Langdon and Nurick 2010, Sousa-Martins *et al.* 2012] and is a reliable and reasonably simple to build setup.

The advantages of this setup, as opposed to other solutions, are that the system responds to the total momentum imparted to the impacted area. Effects of the air blast are included in the imparted momentum. Despite the advantages of such systems, care must be taken into account when designing them. High values of the pendulum's mass will lead to very small responses in terms of displacements while too low masses lead to very high translation movements, which jeopardise the accuracy of the system. Another

important aspect to consider is that the blast must not surround the pendulum before the loading on the front face of the structure is completed. This can be avoided if the pendulum is attached in place that assures that the time that takes for the blast-wave to travel from its source to the back of the pendulum is higher that the positive phase duration of the blast-wave [Needham 2010].

In 1984 Nurick and Martin [Nurick and Martin 1984] used an experimental apparatus and procedure that followed the one presented from Bodner and Symonds in 1979 [Bodner and Symonds 1979]. This was one of the first published reports on the use of a ballistic pendulum to evaluate the effects of blast loads in specimens and structures.

A plate edge is fully clamped and mounted on a specimen holder placed in front of the ballistic pendulum in order to measure the impulse directly. To measure the deflection experienced by the plate, a condenser microphone[1] was used by these authors. The complete setup can be seen in figure 5.1.

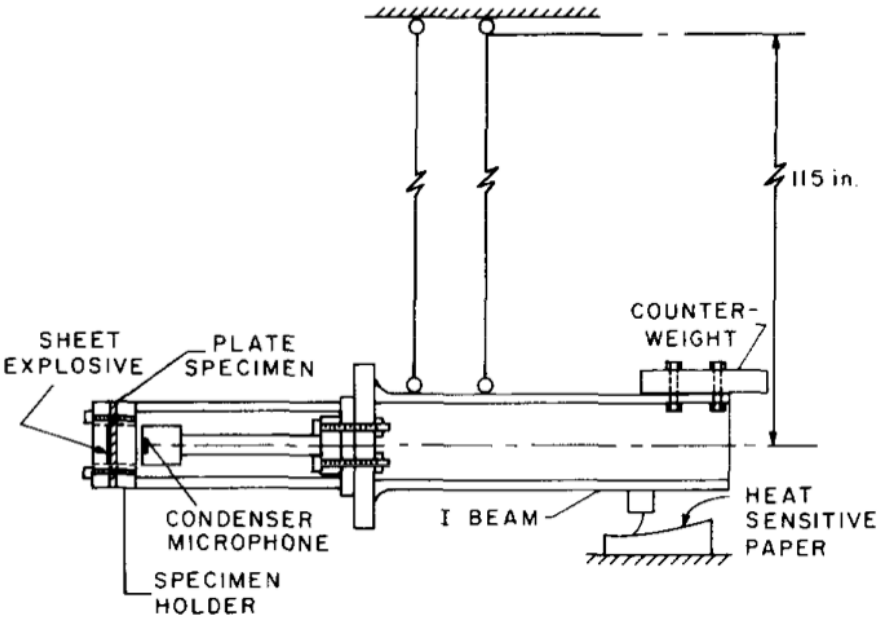

Figure 5.1: The setup of Bodner and Symonds [Bodner and Symonds 1979].

In 2008 Zhu *et al.* [Zhu *et al.* 2008b] used a 4-cable ballistic pendulum system to measure the impulse imparted on blast loaded specimens which consisted of two aluminium alloy face sheets and a honeycomb core. The setup is similar to the one used by Nurick *et al.* and other authors [Bodner and Symonds 1979, Nurick and Martin 1984, Nurick and Martin 1989, Nurick *et al.* 1996, Franz *et al.* 2002, Cloete *et al.* 2003, Karagiozova *et al.* 2005] when studying small explosive loading. Zhu *et al.* [Zhu *et al.* 2008b] used a PVDF (polyvinylidene fluoride) pressure gauge to record

[1] A condenser microphone is capacitor used to record displacement as function of time since the deflection of the plate changes the effective capacitance which produces a change in signal on the oscilloscope.

the explosion pressure-time history based on the piezoelectric effect[2]. An insight of the PVDF pressure gauge used is shown in figure 5.2. This sensor is fixed on the centre of the plate to record the explosion pressure-time history. In addition, Zhu *et al.* [Zhu *et al.* 2008b] used a laser displacement transducer to measure the translation movement of the pendulum. As an alternative, other authors use a recording pen for the same measurement [Jacob *et al.* 2004, Bambach 2008, Bambach *et al.* 2010].

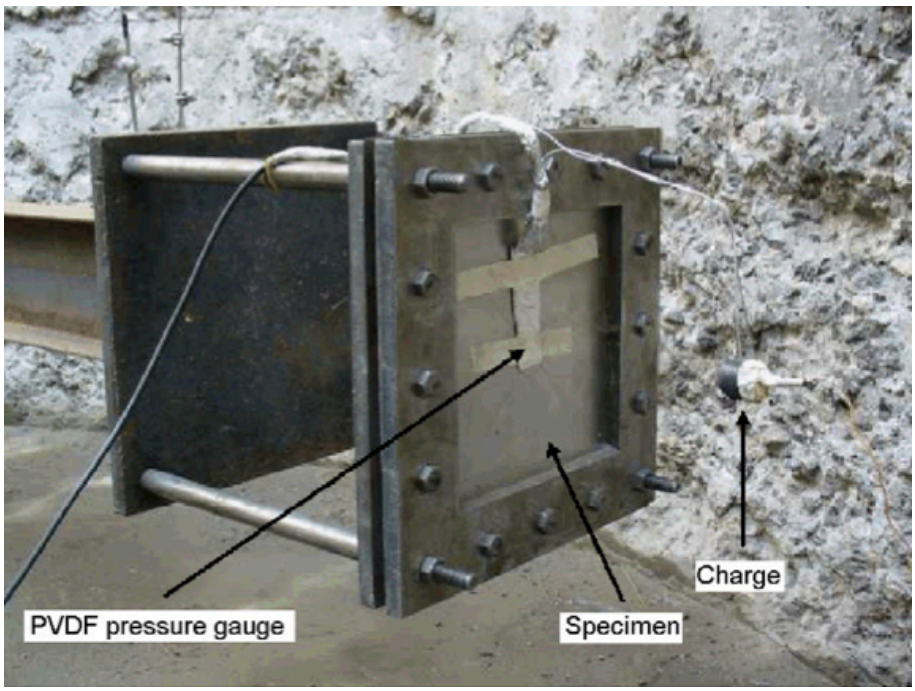

Figure 5.2: Ballistic pendulum and PVDF pressure gauge used by Zhu *et al.* [Zhu *et al.* 2008b].

5.2 Linear oscillator

Before the experimental setup used is described and explained, a full explanation on the equations that describe the motion of the ballistic pendulum is needed. The equations that describe the pendulum's movement derive from the analysis of the simple pendulum which is an idealisation of a real pendulum and a model for the linear oscillator. Some assumptions are made in this analysis, such as, for example, that during oscillation there is no air resistance. The following paragraphs refer to linear oscillator theory.

As an example, consider a projectile that is fired on a large mass structure suspended with wires [Serway and Jewett 2003]. The amplitude of the resulting oscillation and the impulse transmitted to the front face of the pendulum can be determined. The

[2]Piezoelectric effect: When pressure is applied normal to the gauge, a state of stress is created around its sensing element, causing an electrical field to be produced across its element.

natural period T can also be determined by averaging a number of measured pendulum oscillations.

The generic linearised equation of motion for a ballistic pendulum is [Rodrigues 2003]

$$\ddot{x} + 2\beta\dot{x} + \omega_{\mathrm{n}}^2 x = 0, \tag{5.1}$$

where $\beta = C/2M$ is the damping constant and $\omega_{\mathrm{n}} = 2\pi/T$ is the natural frequency of the system. C is the system damping and M the total mass of the ballistic pendulum. One possible solution for equation 5.1 is

$$x = \frac{e^{\beta t}\dot{x}_0}{\omega_{\mathrm{d}}} \sin(\omega_{\mathrm{d}} t), \tag{5.2}$$

where $\omega_{\mathrm{d}} = (\omega_{\mathrm{n}}^2 - \beta^2)^{1/2}$ is the damped frequency and $\dot{x}_0$ is the initial velocity of the pendulum after impact. This velocity can be obtained from the following relation

$$\dot{x}_0 = \frac{2\pi}{T} x_1 e^{-0.25\beta T}. \tag{5.3}$$

If, for example, the horizontal displacements of the pendulum are know for 1/4 and 3/4 of the period, the damping constant β can be determined as

$$\beta = \frac{2}{T} \ln\left(\frac{x_1}{x_2}\right), \tag{5.4}$$

where

$$x_1 = \frac{\dot{x}_0 T}{2\pi} e^{-0.25\beta T} \qquad \text{and} \qquad x_2 = \frac{\dot{x}_0 T}{2\pi} e^{-0.75\beta T}. \tag{5.5}$$

The impulse can then be given by the following equation:

$$I_p = M\dot{x}_0. \tag{5.6}$$

Substituting equation 5.3 in equation 5.6 the impulse is then given by,

$$I_p = M\frac{2\pi}{T} x_1 e^{-0.25\beta T}. \tag{5.7}$$

5.3 The ballistic pendulum

The experimental tests on micro-agglomerated cork (MAC) compound specimens were made in the laboratory for Analysis of Explosion Effects in the Civil and Material Engineering Department of the Royal Military Academy (RMA) in Brussels. This department does research on the interaction of blast-waves with structures, with particular emphasis on progressive collapse phenomenon. The tests were performed in a pyrotechnic laboratory, specifically prepared to analyse pyrotechnical shock load effects on critical mechanical components.

The ballistic pendulum used in the experimental tests performed on MAC compounds is described in the following paragraphs. A description of all the experimental procedures, as well as some theory needed to better understand the experimental data analysis is mentioned within the following sections. Two different types of specimens were tested in the scope of this research: (i) cylindrical MAC specimens and (ii) sandwich structures with MAC compound cores. The following sections focuses on the setup and equipment used to test each of these specimens.

5.3.1 Setup for cylindrical MAC compound specimens

A 4-cable ballistic pendulum setup system was used to characterise cylindrical MAC compound specimens when subjected to blast-waves. This setup allowed to measure the transmitted impulse from the blast to a specimen. Some of the specimens that were used to make these measurements are shown in figure 5.3. Three specimens with 50, 75 and 100 mm of height, and a constant diameter of 45 mm, for each cork compound, were tested. Each set of results was then averaged. Their name was given in terms of type of MAC compound, height and mass of explosive (that is was tested with). As an example, specimen NL20-50-7 corresponds to a specimen made with the MAC compound NL20, that has a height of 50 mm and that was tested (blast loaded) with 7 g of explosive. Some of the physical properties of NL20 and TB40 MAC compounds were already referred in chapter 3 (see table 3.2). An image of the complete pendulum setup used for the cylindrical specimens is presented in figure 5.4. The setup used is presented in the schematic representation in figure 5.5. The cylindrical specimen (number 7 in figure 5.5) is placed on one end of the pendulum and the base (number 6 in figure 5.5) on which it is placed is adapted for this kind of structures. C4 cylindrical charges in contact with a striking mass (striker) were used to create the blast load. A detonator (number 11 in figure 5.5) taped to 1 g of primary HE is attached to the centre of the main explosive. 7 and 8 g of C4 (number 10 in figure 5.5) were used at a stand-off distance of 13 mm. This stand-off distance was achieved by placing a polystyrene pad (number 9 in figure 5.5) between the striker and the explosive. An image of the explosive molded cylindrically is shown in figure 5.6 (a) and the polystyrene pad used to make the 13 mm stand-off distance is shown in figure 5.6 (b). This component completely burns in the detonation phase. After detonation of the explosive, the polystyrene pad disintegrates and consequently has no apparent effect on the loading of the panel [Theobald and Nurick 2010]. The striker (number 8 in figure 5.5) is accelerated due to the blast and crushes the specimen. The striker dimensions are 50 mm of diameter and 7 mm of height. The resulting impulsive load induces a translation in the pendulum which is then recorded by the laser (number 1 in figure 5.5) placed at one end of the pendulum. The laser is a Mel Mikroelektronik GmbH — series M7 laser displacement sensor. These sensors (series M7) are analog laser distance measuring systems, for contact-free detection of distances and distance derived variables (*e.g.* position and thickness of targets) [ML 2007]. Among its principal characteristics are the adjustable measuring

(a) Height = 50 mm

(b) Height = 75 mm

(c) Height = 100 mm

(d) Height = 50 mm

(e) Height = 75 mm

(f) Height = 100 mm

Figure 5.3: Specific energy measurements specimens made from: (a) to (c) NL20 MAC compound and (d) to (f) TB40 MAC compound.

Figure 5.4: 4-cable ballistic pendulum setup used to test cylindrical MAC specimens.

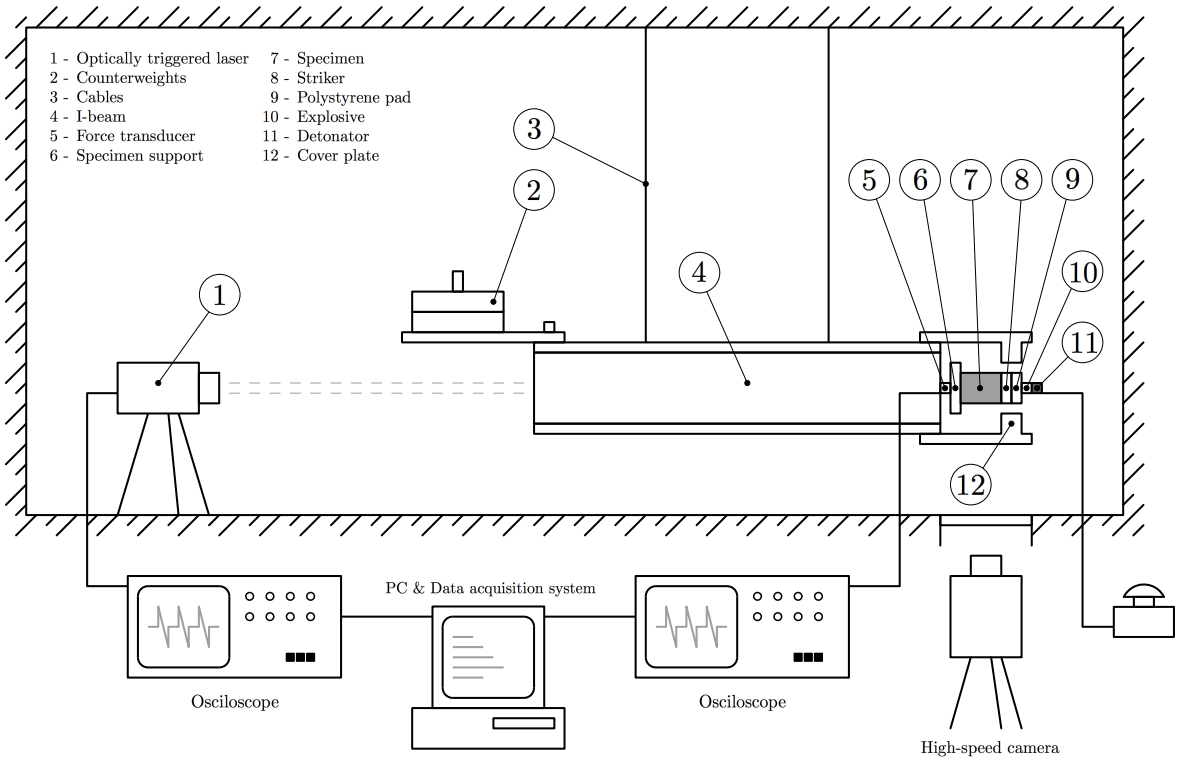

Figure 5.5: Schematic representation of the experimental setup of the ballistic pendulum adapted for cylindrical MAC compound specimens.

(a) (b)

Figure 5.6: (a) Plastic explosive C4 molded cylindrically.(b) Polystyrene pad placed between the explosive and the striker.

frequency, the resolution of 0.1 μm, the insensitiveness to texture and colour and the adjustable threshold value for distance limits.

Once the oscillation amplitude is recorded by the laser, the impulse on the pendulum's front face can be determined. The specimen's base has a force transducer (number 5 in figure 5.5) attached to it which was used to record all the load profiles from all the measurements with the cylindrical MAC compound specimens. An ICP® dynamic load sensor (model 203B) was used. This series of impact sensors operates in a range of loads from 0.04 to 222.4 kN. The measuring surface is located on the top of the sensor and measures the normal component of loads applied, as can be seen in figure 5.7. As the compression loads are applied directly on the sensor surface a positive output is recorded.

A cover plate (number 12 in figure 5.5) is used to block the pressure wave that travels around the whole setup after the detonation and the high speed camera that records the experiments is protected by a plexiglass screen, as can be seen in figure 5.8. The high speed camera is a FASTCAM-Ultima APX 120K by Photron. The two main components of this equipment are the camera head (figure 5.9 (a)) and the processor (figure 5.9 (b)). The processor has a memory extensible up to 8 Gb to store the recorded images. The camera also has a video output connector to display the recorded images on a video monitor, an IEEE1394 digital interface to control the camera from a PC and download the recorded image data, as well as input and output connectors for external synchronisation and trigger signals [MC 2004].

Photron FASTCAM Viewer (PFV) software for high speed camera imaging was used to analyse the experimental data from the high speed camera. With this software it is possible to study the linear dependence of the displacement of an object in pixels in time (*i.e.* a picture element or a single dot and smallest element in a visual display) and the actual displacement. A reference for the system was defined and this was achieved by determining a specific distance in the setup (also captured by the camera). The relation between pixels and distance is kept constant throughout the experiments

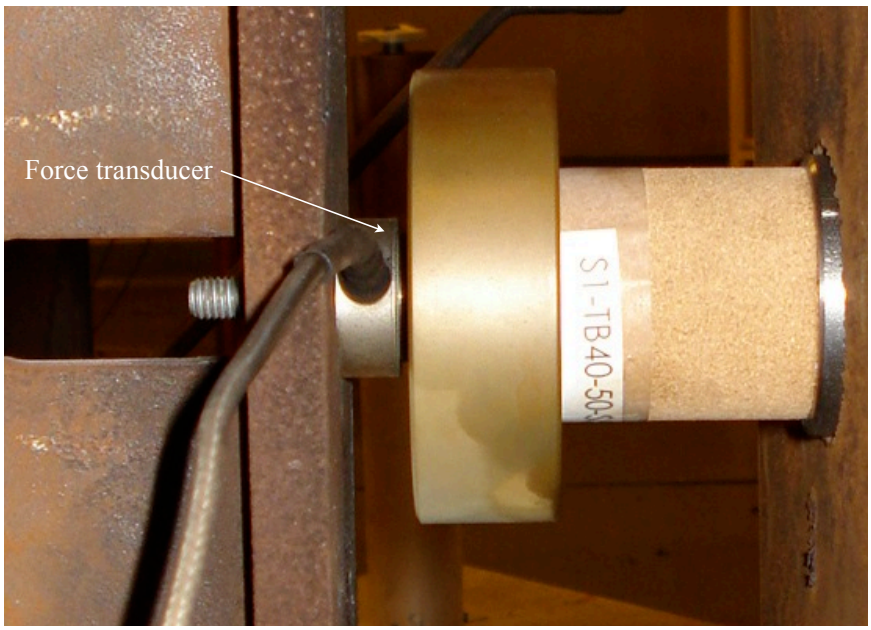

Figure 5.7: Force transducer placed on the axis of the MAC compound specimen and base.

Figure 5.8: High speed camera and protection plexiglass screen used to record all blast experiments.

Figure 5.9: (a) Head of the high speed camera used in the first set of experiments and (b) high speed image processor.

(the position of the camera is kept constant at all times). The software interface used is shown in figure 5.10. It was assumed in the experiments that this reference distance, d_{ref}, corresponds to the distance between the cover plate and the I-beam (see figure 5.5). In terms of pixels this reference distance is designated by $d_{\text{ref}}^{\text{pixels}}$. The recording rate is also known and corresponds to the measured frames per second (fps) frequency. Finally, it was considered that the object, the striker in this case, travels from P_{i} to P_{f} (initial and final pixel position of one specific and fixed point on the striker), where $P_{\text{f}} - P_{\text{i}} = \Delta P$. Therefore, the relation

$$\Delta x = \frac{\Delta P d_{\text{ref}}}{d_{\text{ref}}^{\text{pixels}}} \tag{5.8}$$

can be applied to determine the displacement (and consequent velocity) of the striker when it travels $\Delta F = F_{\text{f}} - F_{\text{i}}$ frames.

5.3.2 Setup for sandwich structures with MAC compound cores

Within the framework of the present work, in addition to the two types of MAC compound cylindrical specimens tested, tests were also performed using the same MAC compounds incorporated as cores in sandwich structures with 5754-H22 aluminium alloy face sheets. These sandwich structures have constant thickness of the face sheets, different core thicknesses and were fixed on the 4-cable ballistic pendulum and subjected to blast-waves originated from the detonation of a high explosive (C4).

The sandwich structures were manufactured using NL20 and TB40 MAC compound cores with five distinct core thicknesses: 10, 15, 20, 25 and 30 mm. Sets of three iden-

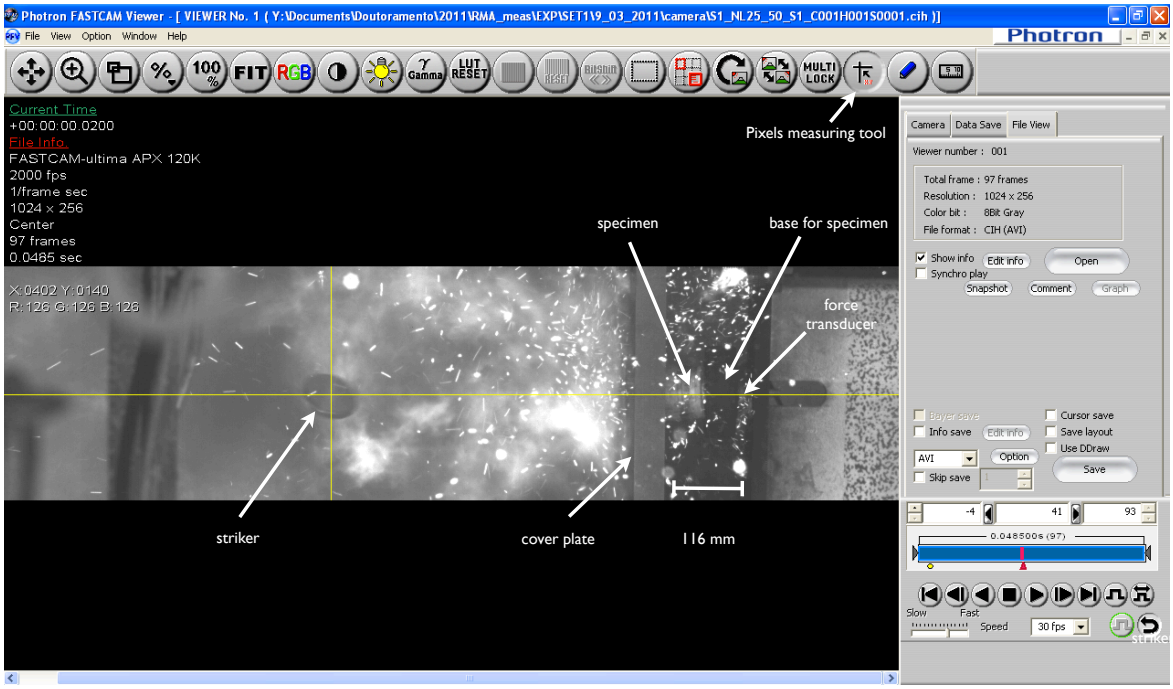

Figure 5.10: Screenshot of the user interface of the Photron FASTCAM Viewer (PFV) software.

tical sandwich structures were made, leading to a total of 15 specimens for each MAC compound core. Therefore, all the results presented here are obtained by averaging results. 1 mm thickness 5754-H22 aluminium alloy face sheets were used on the sandwich structures. The properties of the aluminium alloy used are listed in table 5.1.

Table 5.1: Mechanical properties of aluminium 5754-H22 [Sousa-Martins *et al.* 2013].

Property	**Al 5754-H22**
Density	2.670 g/cm^3
Young modulus	70.3 GPa
Yield stress	185 MPa
Poisson ratio	0.33

The face sheets were adhesively joined to the MAC cores and water jet cut. All the sandwich structures were manufactured by ACC — Amorim Cork Composites and its name was given according to the MAC compound used and thickness of the core. As an example, the designation NL20-15 corresponds to the sandwich structure NL20 core with 15 mm of thickness. Overall and thickness views of a NL20 MAC compound core sandwich panel are shown in figures 5.11 (a) and (b), respectively. The areal densities of the sandwich structures used within the scope of this work were measured and found

to be in the range of 7.4 to 11.4 kg/m^2. For comparison purposes, a study on the blast resistance of sandwich composites made with face sheets of E-Glass Vinyl Ester composites (EVE) and Corecell^{TM} (*i.e.* styrene foams) cores made by vacuum assisted resin transfer moulding (VARTM)[3] was presented by Wang *et al.* [Wang *et al.* 2009], where the average value of areal density of the samples is 19.02 kg/m^2.

(a) (b)

Figure 5.11: (a) Overall and (b) thickness (cross section) views of a NL20 MAC compound core sandwich structure.

As previously referred earlier in this section, an adaptation to the previous system used for cylindrical specimens was made to the 4-cable ballistic pendulum in order to test sandwich structures.

The dimensions of the clamping frames and support structure which was adapted to the pendulum are shown in figures 5.12 (a) and (b), respectively. The sandwich structures have in-plane dimensions of 320 × 320 [mm^2] and the effective impact area (the exposed area) of 200 × 200 [mm^2]. From figure 5.12 (b) the imposed stand-off distance of 300 mm is evidenced.

A schematic representation of the whole experimental apparatus and an image of the pendulum setup are shown in figures 5.13 and figure 5.14, respectively.

The clamping system (number 6 in figure 5.13) is fixed to the front of the pendulum with four threaded spacers (number 5 in figure 5.13). A spherical 30 g (number 8 in figure 5.13) charge of C4 was fixed and aligned with the centre of the sandwich structures at a fixed stand-off distance of 300 mm. The impulsive load from the detonation induces a translation movement to the pendulum. The laser displacement sensor (number 1 in figure 5.13) was again used to register the translation movement of the pendulum, which was then recorded by an oscilloscope. The counterweights (number 2

[3]VARTM: the process of vacuum infusion where the composite is molded using a rigid mould to provide part geometry and a thin flexible membrane over the fibber, with outer atmospheric pressure compressing the fibber tight against the rigid mould surface [RC 2012].

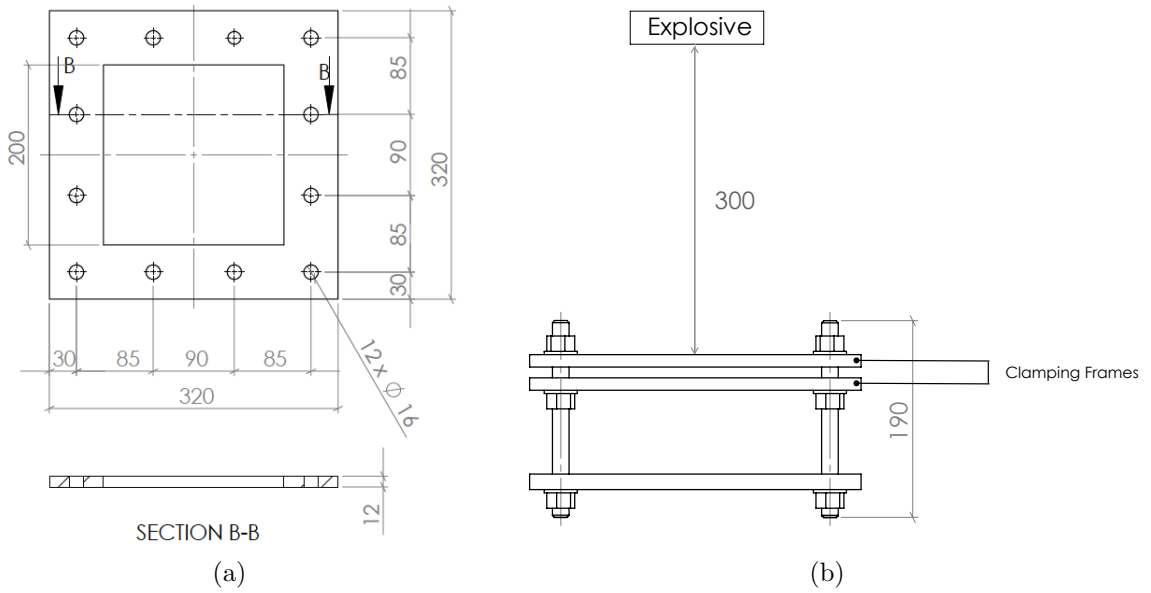

Figure 5.12: (a) Dimensions of the clamping frames and (b) schematics of the support structure which was adapted to the 4-cable ballistic pendulum.

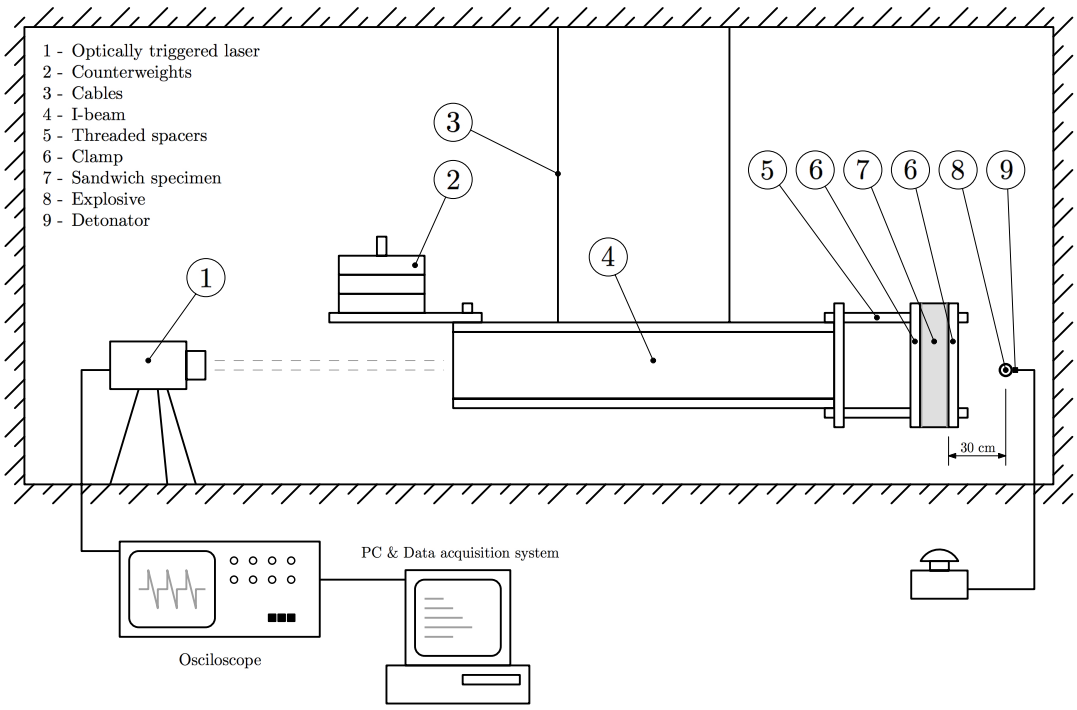

Figure 5.13: Schematic representation of the experimental setup of the ballistic pendulum adapted for sandwich structures with MAC compound cores.

Figure 5.14: (a) 4-cable ballistic pendulum setup used to test sandwich structures with a MAC compound core.

in figure 5.13) are also visible in the opposite end of the pendulum. These are used to keep the perfect alignment of the system, due to the additional mass that was added to the pendulum from the addition of the support component for sandwich structures.

Chapter 6

Experimental analysis for MAC characterisation

The experimental characterisation of the dynamic (blast) behaviour of micro-agglomerated cork is discussed. The experimental results are analysed and discussed thoroughly in this chapter. The displacement of the pendulum and the transmitted impulse were measured and the coefficient of restitution of the whole system was determined.

6.1 Introduction

The experimental setup and equipment used for the characterisation of the micro-agglomerated cork (MAC) compound was described in detail in the previous chapter. Cylindrical MAC compound specimens with two different densities NL20 (ρ = 200 kg/m^3) and TB40 (ρ = 440 kg/m^3) fixed on a 4-cable ballistic pendulum were subjected to a blast-wave originated from the detonation of 7 and 8 g of C4. Three different heights of these specimens were considered (50, 75 and 100 mm), while the radius of the specimens was kept constant throughout the experiments. In terms of data acquired during the experiments the following was obtained: (i) the displacement of the pendulum, (ii) the resulting loads, measured by a force transducer placed on the back of the specimen and (iii) high speed camera videos of the entire process. In the current chapter these results are presented, discussed and analysed.

6.2 Load-time profile analysis

As previously stated, values of load were measured using with a dynamic load sensor (*i.e.* force transducer). The impulse transmitted to the pendulum can be determined from these load values following the procedure explained in the following paragraphs.

A possible way to measure the impulse directly from the blast is by using rigid specimens (*e.g.* a steel cylinder) and attaching the HE charge directly to it. If the impulse transmitted to the rigid specimen is known, it can then be compared with other specimens subjected to the same conditions. This comparison will serve as a basis for the the energy dissipation analysis. In the specific case of the investigation here presented, the impulse values obtained in rigid and MAC compounds specimens can be compared and the efficiency of the energy absorber (EA) can be analysed, since the lower values of impulse transmitted to the pendulum the more efficient the EA. Hence, two different experiments were made with a rigid specimen. 7 and 8 g of C4 were used in these experiments. The force transducer measurements from the rigid specimen are shown in figure 6.1. From the analysis of the results obtained with this specimen it can be seen that the maximum load peak registered is between 150 and 175 kN for 7 and 8 g of C4, respectively. The shape of the curve has an initial (approximately) triangular impulse followed by several lower intensity peaks, most certainly due to stress wave reflections or vibrations of the specimen support. It is also noticeable that the maximum load peak achieved for 8 g is lower than for 7 g. Although this is not an expectable result it can be seen that the secondary load peaks registered are higher for 8 g of C4. In addition, the width of the first peak is higher for 8 g of C4.

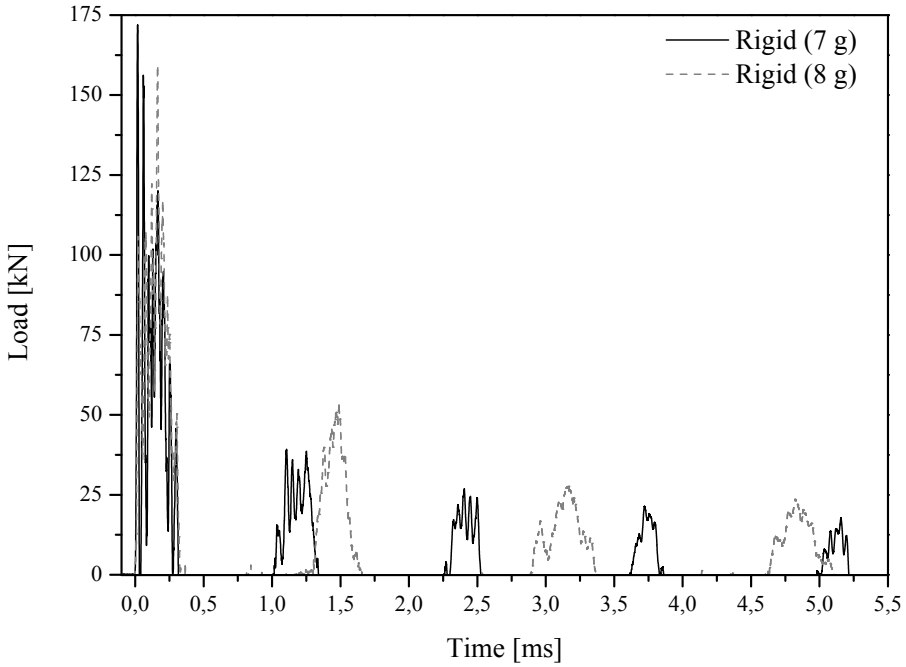

Figure 6.1: Load-time profile for the rigid specimen for 7 and 8 g of C4.

In order to evaluate the impulse transmitted to the pendulum, a mathematical integration of the first peak of the load was performed. Only the first peak is chosen for the integration due to the previously referred possible origins of the secondary lower intensity peaks. The transmitted impulse values determined from the integration of the first peak of the load are shown in figure 6.2. The maximum value of transmitted

impulse obtained was approximately 16 and 23 Ns for 7 and 8 g of C4, respectively. Higher values for 8 g of C4 are registered in the rigid specimen, due to the higher width of the first peak of the load in this case (larger area above the first load peak).

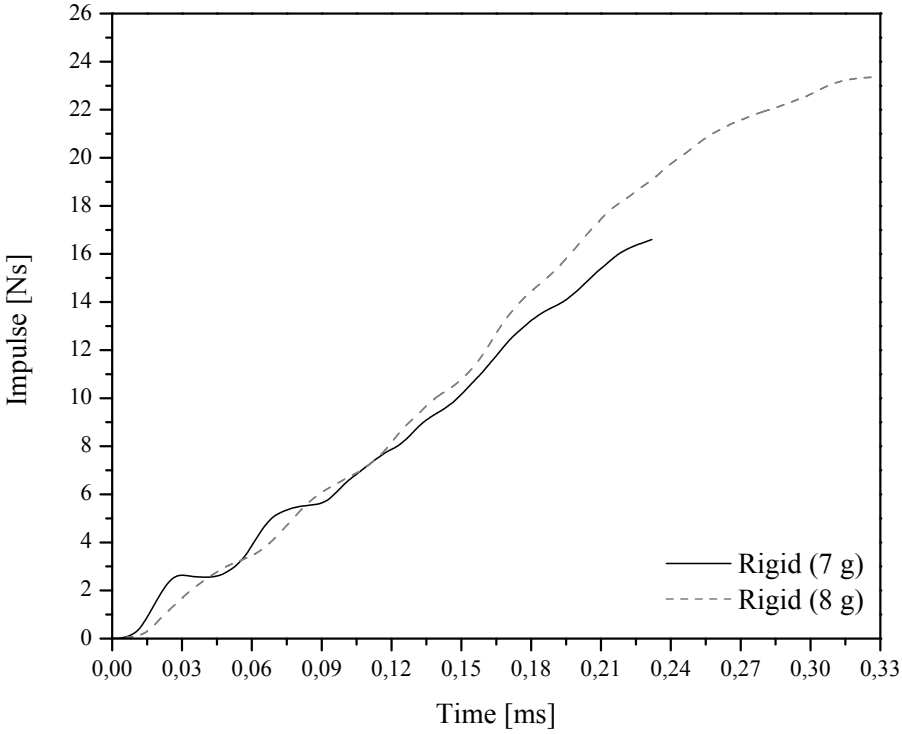

Figure 6.2: Transmitted impulse registered with the rigid specimen for 7 and 8 g of C4.

Concerning now the MAC compound specimens the load profiles are shown in figures 6.3 to 6.6. As with the rigid specimen, both MAC compounds load-time profiles present an initial triangular impulse which is then followed by several lower intensity peaks. The explanation for these secondary peaks presented in the rigid specimen analysis remains possibly valid in this case (vibration of the base of the specimens or/and stress wave reflections).

Comparing with the rigid specimen, the preliminary conclusions that can be taken in terms of energy dissipation analysis is that MAC compounds are indeed performing dissipation of energy, since the load values that they present are significantly lower than the ones of the rigid specimen.

The impulse values, determined by direct integration of the first load peak for all specimens (7 and 8 g of C4) are shown on figures 6.7 and 6.8. These results were compared with results obtained for a rigid specimen and a considerable decrease from rigid specimen analysis to MAC specimen analysis was found, which again is a possible indicator of its efficiency as an EA. The slope change evident in some of impulse-time profiles are most probably due to slight bending (leading to buckling) that occurred in some specimens. More evidences that support this affirmation are presented in the following paragraphs.

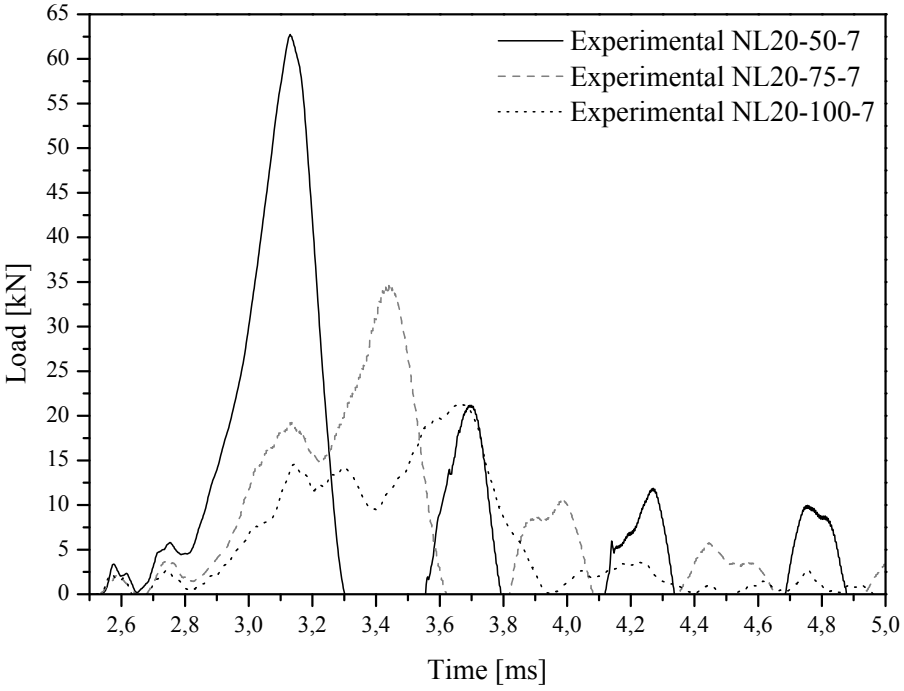

Figure 6.3: Load-time profiles for NL20 specimens (7 g of C4).

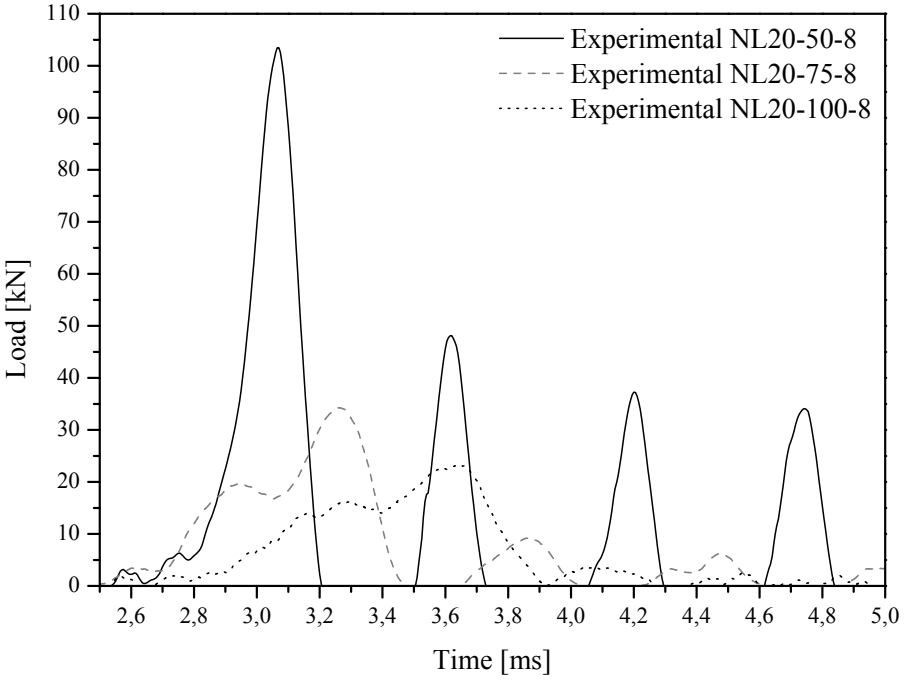

Figure 6.4: Load-time profiles for NL20 specimens (8 g of C4).

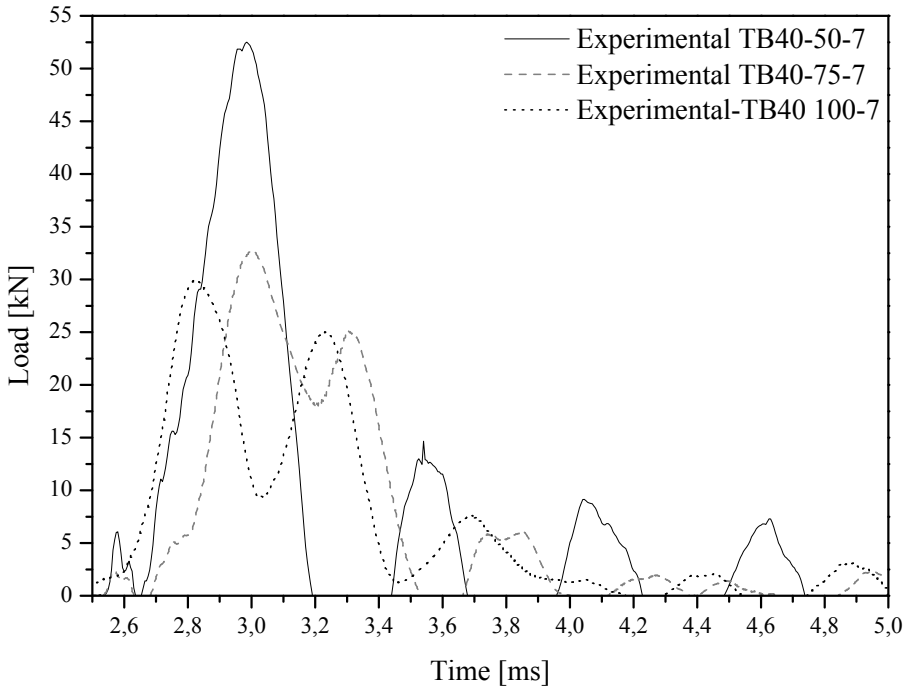

Figure 6.5: Load-time profiles for TB40 specimens (7 g of C4).

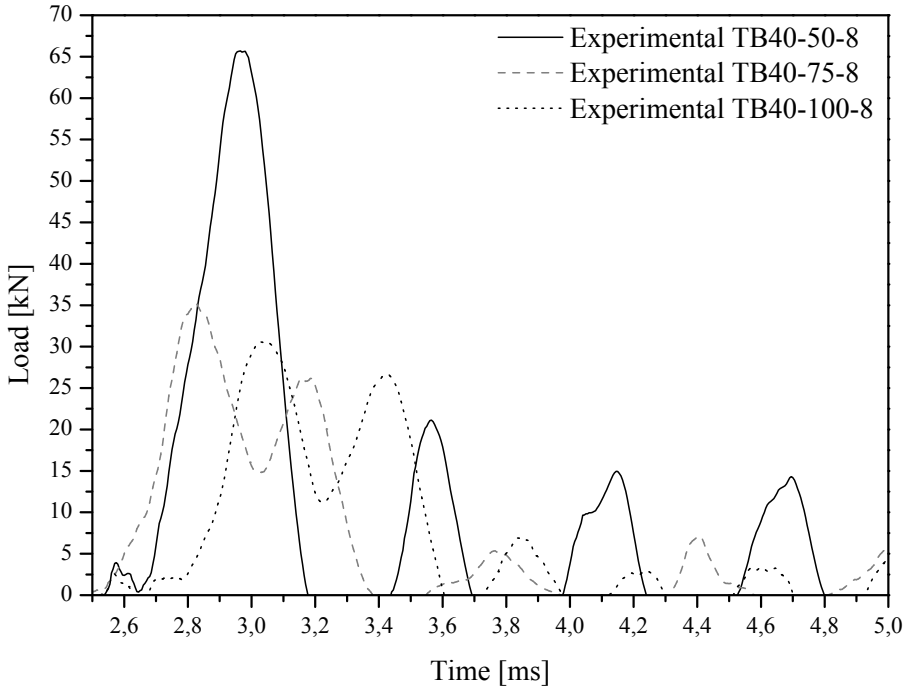

Figure 6.6: Load-time profiles for TB40 specimens (8 g of C4).

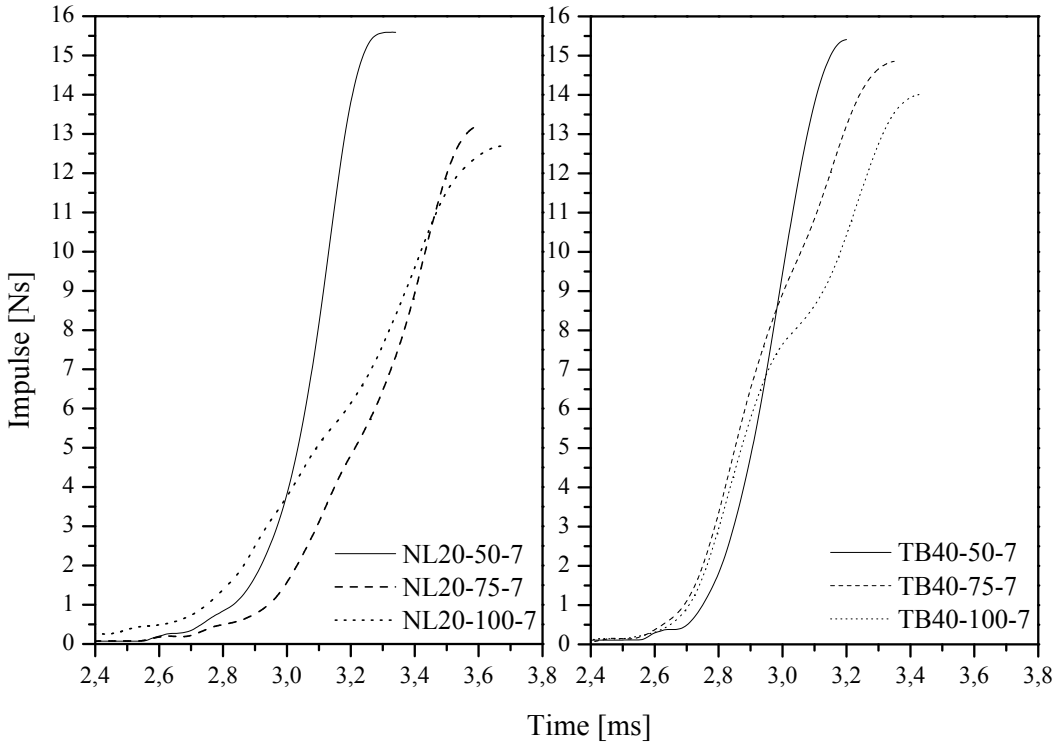

Figure 6.7: Experimental impulse-time profiles for 7 g of C4.

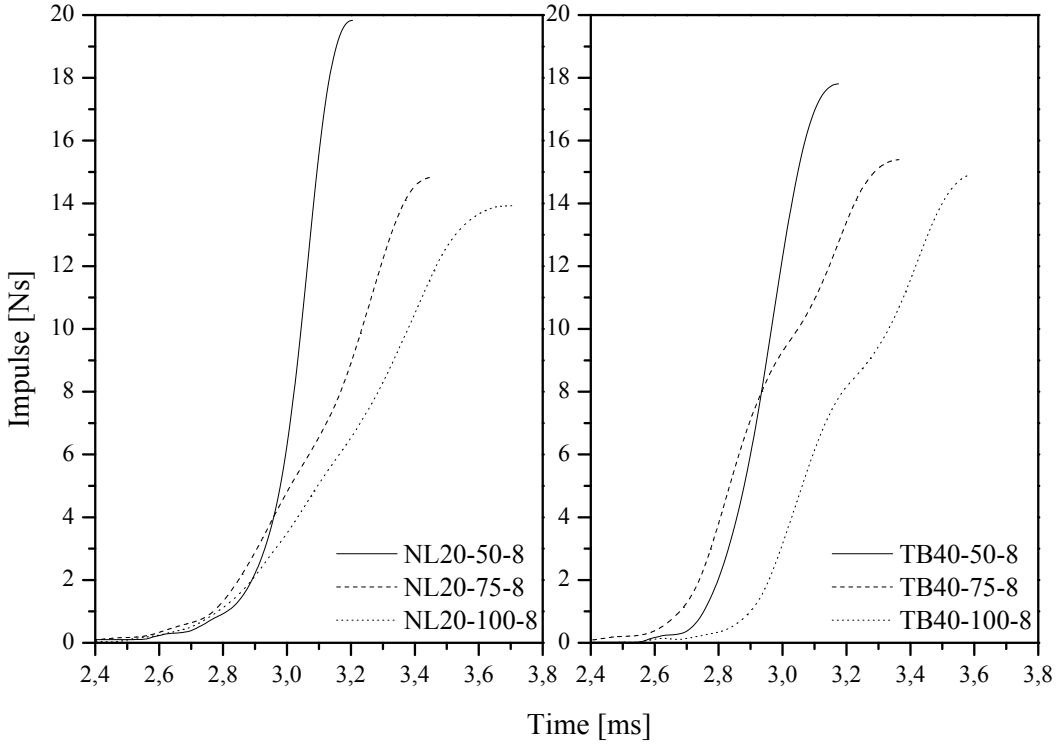

Figure 6.8: Experimental impulse-time profiles for 8 g of C4.

6.2.1 Influence of the density

In terms of the density of the MAC compound, and as an example, the 50 mm height NL20 specimen (NL20-50-7) has a maximum load peak of approximately 65 kN (see figure 6.3) while for the denser specimen TB40-50-7 a maximum load of approximately 53 kN was obtained (see figure 6.5) with 7 g of C4. The same happens with 8 g of C4, where NL20-50-8 specimen has a maximum load peak of approximately 105 kN (see figure 6.4) while the TB40-50-8 specimen exhibits a maximum load of approximately 58 kN (see figure 6.6). Hence, the higher the density of the MAC compound, the lower the maximum load peak is observed.

6.2.2 Influence of the mass of explosive

In terms of the influence of C4 mass (figures 6.3 and 6.4) a significant increase on the load occurs when the mass of C4 increases 1 g, as would be expected. Both MAC compounds reveal this behaviour. Nonetheless, the higher the density of the MAC compound the lower the values of the maximum load. When the C4 mass is increased in 1 g, the effect on the load is only evident for the 50 mm specimens.

After being blast loaded during the experiments, some of the specimens were trapped in the pendulum between the base of the specimen and the cover plate, as can be seen in figure 6.9. This happened because the striker was trapped after impacting the specimen (possibly due to some misalignment that happened during the blast). In addition to this, it was noticed that these specimens experienced slight bending, and consequently buckling, as can be seen in the final aspect of the longer specimens (figure 6.10 for the NL20 and TB40 MAC compounds). Hence, the lower values of the maximum load peak obtained for longer specimens (for both NL20 and TB40 MAC compounds) can most probably be attributed to slight bending.

6.2.3 Influence of the specimen's height

An increase in the height of the specimen leads to a decrease in the magnitude of the load peak as can be seen, for example, from the results obtained for the specimen NL20-100-7, shown in figure 6.3 where a load peak of approximately 20 kN was registered. For the NL20-50-7 specimen, the maximum load peak is approximately 65 kN. The same happens for TB40 specimens where, for example, in the TB40-100-7 specimen (see figure 6.5) the maximum load peak is approximately 30 kN (for TB40-50 the maximum load peak is approximately 53 kN). This decrease is not expectable and its origin is attributed to the previously mentioned slight bending phenomena that occurred in longer specimens.

Figure 6.9: NL20-100-7 specimen trapped in the pendulum between the base of the specimen and the cover plate.

(a) (b)

Figure 6.10: (a) NL20-100 and (b) TB40-100 specimens after being tested.

6.3 Restitution coefficient analysis

The values of the impulse determined using the linear oscillator theory for 7 and 8 g of C4 are shown in table 6.1. I_{p} and I_{b} correspond to the impulse from the pendulum (after collision) and the impulse from the blast, respectively. m_{s} and v_s are the mass of the striker and its initial velocity, respectively. $v_{\mathrm{s}}^{\mathrm{f}}$ and v_p^{f} are the final velocities of the striker and pendulum, respectively. $v_{\mathrm{s}}^{\mathrm{f}}$ was determined from the high speed camera recordings, according to the explanation presented in chapter 5. This velocity was determined knowing the linear function of displacement of an object in pixels (*i.e.* a picture element or a single dot and smallest element in a visual display) and real displacement. In the following paragraphs an analysis of the restitution coefficient of the striker-pendulum collision is presented.

Table 6.1: Parameters from the restitution coefficient analysis: mass of the striker, m_{s}; initial and final velocity of the striker v_{s} and v_{s}^f, respectively; final velocity of the pendulum, v_{p}^f; impulse from the pendulum and from the blast I_{p} and I_{b}, respectively; restitution coefficient, c, and percentage of energy dissipation, E_{dis}.

Sample	m_{s} [kg]	v_{p}^f [m/s]	v_{s}^f [m/s]	I_{p} [Ns]	I_{b} [Ns]	v_{s} [m/s]	c [–]	E_{dis} [%]
NL20-50-7	0.10596	0.087	16.21	11.5542	9.8363	92.817	0.174	82.6
NL20-75-7	0.10600	0.082	10.62	10.8615	10.486	98.928	0.104	89.6
NL20-100-7	0.10600	0.106	0	15.3953	14.072	132.75	0	—
NL20-50-8	0.10637	0.099	13.35	13.0982	11.678	109.79	0.121	87.9
NL20-75-8	0.10605	0.084	5.746	11.1136	10.910	102.89	0.065	93.5
NL20-100-8	0.10632	0.081	0	10.6879	10.688	100.52	0	—
TB40-50-7	0.10700	0.0932	18.8	12.3	10.3	96.960	0.192	80.8
TB40-75-7	0.10600	0.0788	0	10.4	10.7	100.67	—	—
TB40-100-7	0.10600	0.0790	11.1	10.5	10.2	95.892	0.112	88.8
TB40-50-8	0.10600	0.0977	11.1	12.9	12.5	118.18	0.105	89.5
TB40-75-8	0.10600	0.0998	16.5	13.2	8.4	79.187	0.310	69.0
TB40-100-8	0.10600	0.0853	0	11.3	11.3	106.69	—	—

The presence of a crushable material, such as the MAC compound, between the striking mass and the ballistic pendulum changes the restitution coefficient of the collision, c. This coefficient plays an important role in the relation between the initial impulse that was applied on the striking mass and the impulse that will change the momentum of the ballistic pendulum.

It is known that, in a collision, as a result of the compression phase, part of the kinetic energy of the system can be lost/dissipated due to several different ways, such as plastic deformation of contact surfaces and generation of heat and sound. Consequently, the impulse that the parts involved in the collision impart on each other during the restitution phase, I_{r}, would, in general, be smaller than the impulse they impart to

each other in the compression phase, I_c, that is [Lu and Yu 2003],

$$c = \frac{I_r}{I_c} = \frac{\int_{t_c}^{t_f} F(t)\mathrm{d}t}{\int_{t_0}^{t_c} F(t)\mathrm{d}t}. \tag{6.1}$$

The ratio of impulses in the previous equation is the kinetic coefficient of restitution ($c \in [0;1]$). This restitution coefficient is dependent on several properties of the bodies which are involved in the collision (*e.g.* velocities and orientations when they collide). Hence, this coefficient can only be determined by experiments or by a detailed analysis of the deformation of the two bodies during the collision [Lu and Yu 2003]. If the contact force between the two bodies is represented as a function of time, the profile presented in figure 6.11 can be obtained.

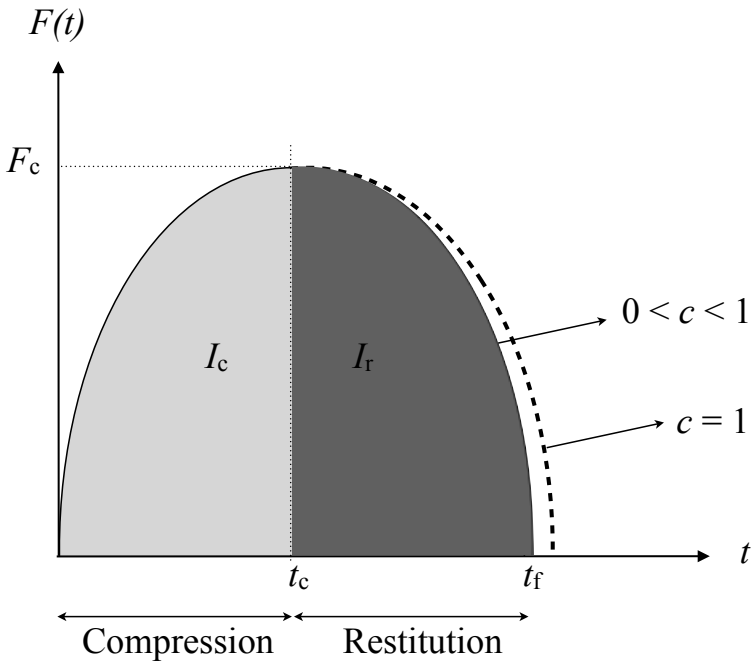

Figure 6.11: Contact force between the bodies as a function of time (adapted from [Lu and Yu 2003]).

If this curve is known the total impulse can be determined from the definition of impulse, according to the sum of the two shaded areas in figure 6.11, that is,

$$I_f = I_c + I_f. \tag{6.2}$$

The kinetic restitution coefficient is the ratio between the two shaded areas. Using the notation in table 6.1 for the restitution it is possible to obtain

$$\begin{aligned} -I_r &= m_s(v_s^f - v_c) \text{ (striker)} \\ I_r &= m_p(v_p^f - v_c) \text{ (pendulum)} , \end{aligned} \tag{6.3}$$

where v_c is the compression velocity, given by

$$v_c = m_s - \frac{m^* v^{*0}}{m_s} = m_s + \frac{m^* v^{*0}}{m_p}, \tag{6.4}$$

where $m^* = m_s m_p/(m_s + m_p)$ is the equivalent mass of the system. The final relative velocity between striker and pendulum is then given by

$$v^{*f}(t) = v_s^f(t) - v_p^f(t), \tag{6.5}$$

while the initial relative velocity is

$$v^{*0}(t) = v_s^0(t) - v_p^0(t). \tag{6.6}$$

If these two relative velocities are compared, the following is obtained,

$$\frac{v^{*f}}{v^{*0}} = \frac{v_s^f - v_p^f}{v_s^0 - v_p^0}. \tag{6.7}$$

Equation 6.7 can be further simplified to yield

$$\frac{v^{*f}}{v^{*0}} = \frac{v_s^f - v_p^f}{v_s^0}, \tag{6.8}$$

since $v_p^0 = 0$ in the experiments (the pendulum starts from rest). Thus, the kinematic coefficient of restitution is related to the relative velocities of the two bodies before and after the collision [Lu and Yu 2003].

The restitution coefficient was determined for each experiment. If the collision between striker and pendulum is completely elastic, a restitution coefficient $c = 1$ is found, meaning that the impulse from the restitution phase is equal to the impulse from the compression phase ($I_r = I_c$) or, in terms of relative velocity, $v^{*f} = v^{*0}$. In this case the kinetic energy remains the same before and after the collision between the bodies. However, if the collision between striker and pendulum is fully inelastic, a restitution coefficient of $c = 0$ is obtained, meaning that the striker and pendulum remain together after impact, that is, $v_s^f = v_p^f$, meaning that all energy is being dissipated. It should be noticed that in the experiments, as was previously mentioned, some of the specimens were trapped in the pendulum. This cannot be compared to the completely inelastic collision case, where the striker and pendulum only move together after collision. This situation only happened due to the striker being trapped.

Following this analysis, it can be stated that the closer c is to 1 the less energy is being dissipated on the collision. Restitution coefficients are determined for every experiment where the striker was not trapped. The final velocity of the pendulum was determined using the conservation of momentum, according to

$$p_i = p_f, \tag{6.9}$$

which is the same as

$$m_{\mathrm{s}} v_{\mathrm{s}} = m_{\mathrm{s}} v_{\mathrm{s}}^{f} + m_{\mathrm{p}} v_{\mathrm{p}}^{f} + I_{\mathrm{s}} \omega_{\mathrm{s}}, \tag{6.10}$$

where p_{i} and p_{f} are the initial and final momentum and $I_{\mathrm{s}}\omega_{\mathrm{s}}$ is the rotational component of movement of the striker. This component was determined for the experiments using the high speed camera recordings. However, the rotational component of the movement of the striker is very small, which allowed to neglect its contribution in equation 6.10, yielding

$$m_{\mathrm{s}} v_{\mathrm{s}} \cong m_{\mathrm{s}} v_{\mathrm{s}}^{f} + m_{\mathrm{p}} v_{\mathrm{p}}^{f}. \tag{6.11}$$

The restitution coefficient values are listed in table 6.1 along with the corresponding energy dissipation estimates (see parameter E_{dis} in table 6.1). From these results it can be concluded that the MAC specimens NL20-50 and NL20-75 contribute to approximately 82.6% and 89.6% of the energy dissipation (7 g of C4), respectively. When using 8 g of C4 the energy dissipation increases to 87.9% (NL20-50) and 93.5% (NL20-75). TB40 higher density MAC compound specimens present lower values of energy absorption: 80.8% (TB40-50) and 88.8% (TB40-100) for 7 g of explosive, and 89.5% (TB40-50) and 69% (TB40-75) for 8 g of C4. Summarising, in terms of energy dissipation, NL20 MAC compound is preferable since its restitution coefficient is closer to zero.

However, it must be stated that this approach using rigid body analysis has evident limitations, such as the capability of describing transient stresses, loads or strains. When the interaction between two bodies occurs in short periods of time and local deformation is significant, the effect of stress waves propagating inside the body must be considered in order to obtain a good agreement with reality. However, this analysis is considered to be acceptable as a possible preliminary analysis of the applicability of MAC compounds as energy absorbers in blast wave situations.

Chapter 7

Sandwich structures with MAC cores

In this chapter the experimental results analysis are presented concerning the behaviour of sandwich structures. The deflection of the front and back face sheets was measured as well as the movement of the pendulum to investigate the effects of the core thickness and core density on the structural response.

7.1 Introduction

As mentioned in chapter 5 the ballistic pendulum used to test cylindrical micro-agglomerated cork (MAC) compound specimens was adapted to allow for the measurements in the sandwich structures. The sandwich structures were tested with constant thickness of the face sheets and different MAC compound core thicknesses. These structures were fixed on the 4-cable ballistic pendulum and subjected to blast-waves originated from the detonation of 30 g of C4 at a fixed stand-off distance of 300 mm. In terms of data acquired during these experiments the following parameters were measured: translational movement (displacement) of the ballistic pendulum, using a laser displacement sensor, and deflection values of the front and back face sheets of the sandwich structures. In the current chapter these results are presented, discussed and analysed.

7.2 Impulse

The impulse transmitted to the front of the pendulum was determined from the amplitude of the oscillation obtained from the laser sensor.

The natural period $T = 3.34$ s of the pendulum was determined by averaging a number of oscillations. The pendulum adapted for the sandwich structures weighted

more than the setup prepared for the cylindrical structures, with a total mass $M = 158.88$ kg. Impulse values determined from the relations described in section 5.2 (see equations 5.3 to 5.7) and the laser sensor measurements for all the experiments are listed in table 7.1.

Table 7.1: Impulse transmitted to the pendulum, I_p, initial velocity of the pendulum, $\dot{x}_0$, and damping constant, β.

Sample	I_p [Ns]	$\dot{x}_0$ [mm/s]	β [s^{-1}]
NL20-10	15.869	99.880	0.023
NL20-15	15.849	99.759	0.017
NL20-20	13.939	87.735	0.002
NL20-25	14.737	92.760	0.019
NL20-30	16.369	110.669	0.070
TB40-10	15.522	104.624	0.040
TB40-15	14.098	92.758	0.033
TB40-20	15.873	99.908	0.045
TB40-25	15.503	97.580	0.033
TB40-30	15.190	95.607	0.027

A tendency for a decrease of the impulse transmitted to the pendulum with the increase of the thickness of the core was observed for the structures with lower core thicknesses (up to 20 mm), for the NL20 MAC compound core, as can be seen from the first set of results in table 7.1 (results above the dashed line). However, thickness of the core values higher than 20 mm led to increasing transmitted impulses and, consequently, increasing initial velocities of the pendulum.

Although it is not as noticeable, the behaviour found in NL20 sandwich structures can also be observed for the TB40 (denser) core sandwich structures. However, for the TB40 specimens, this effect is evident starting at a lower core thickness of 15 mm. In others words, TB40 MAC core sandwiches have decreasing values of impulse transmitted to the pendulum up to 15 mm of core thickness. After this thickness value, although the impulse is higher than the one registered for the TB40-15 sandwich structure, from this point forward the impulse of the pendulum stays approximately the same with increasing core thickness. An explanation for this unexpected behaviour may be the fact that for thicknesses equal to or higher than 20 mm for the NL20 MAC compound core sandwiches and equal to or higher than 15 mm for the TB40 MAC compound core sandwiches there is a strong possibility that the structure is no longer behaving as a sandwich structure but as a monolithic plate instead. Therefore, for the dimensions of the specimens considered within the scope of this work, a clear indication was found leading to the conclusion that there is a limit thickness that separates sandwich from plate behaviour. For the specific case being studied in this work, this limit value is ≈ 20 mm for the NL20 compound cores and ≈ 15 mm for the TB40 compound cores.

7.3 Structural deflection

The residual deflection of both the back and front face sheets was determined for all the tested sandwich structures using a three-dimensional coordinate measuring device. This residual deflection is most probably due to plastic strains, damage and failure possibly occurring in the MAC compound cores. The measuring device is shown in figure 7.1 where a special rigid arm was manufactured in order to measure in all extent of the sandwich (see figure 7.2).

Due to some global bending of the plates that occurred after impact, a correction plane was determined for both faces on each sandwich specimen in order to ensure that the measured deflections are the actual deflections originated from the blast. This correction plane was defined by three points (P_1, P_2 and P_3) positioned outside the effective impact area, as can be seen in figure 7.2. An example of a contour surface of both faces for one of the NL20-10 specimens is shown in figure 7.3.

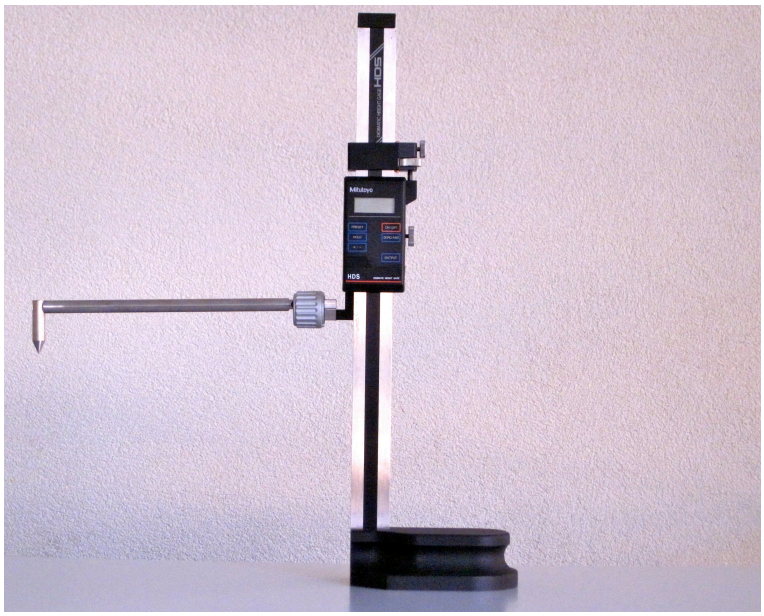

Figure 7.1: Three-dimensional coordinate measuring device for the measurement of deflections.

The representative variables obtained and analysed from these measurements were: (i) the maximum final deflection of the front and back face sheets, $D^{\mathrm{f}}_{\mathrm{max}}$ and $D^{\mathrm{b}}_{\mathrm{max}}$, respectively; (ii) the final deflection of the centre of the front face sheet, $D^{\mathrm{f}}_{\mathrm{cp}}$; (iii) and the relative thickness reduction of the whole structure after the blast event, $h^{\mathrm{p}}_{\mathrm{red}}$. The values obtained for these variables are listed in table 7.2.

Three stages were considered to analyse the deformation process and mechanisms that take place during the impact of the blast-wave, namely [Zhu *et al.* 2009a]:

- Stage I: the detonation of the explosive occurs and, once the stand-off distance is large enough, it is assumed that a uniform load (consequence of the blast impulse) is transmitted to the front face of the pendulum (and sandwich structure),

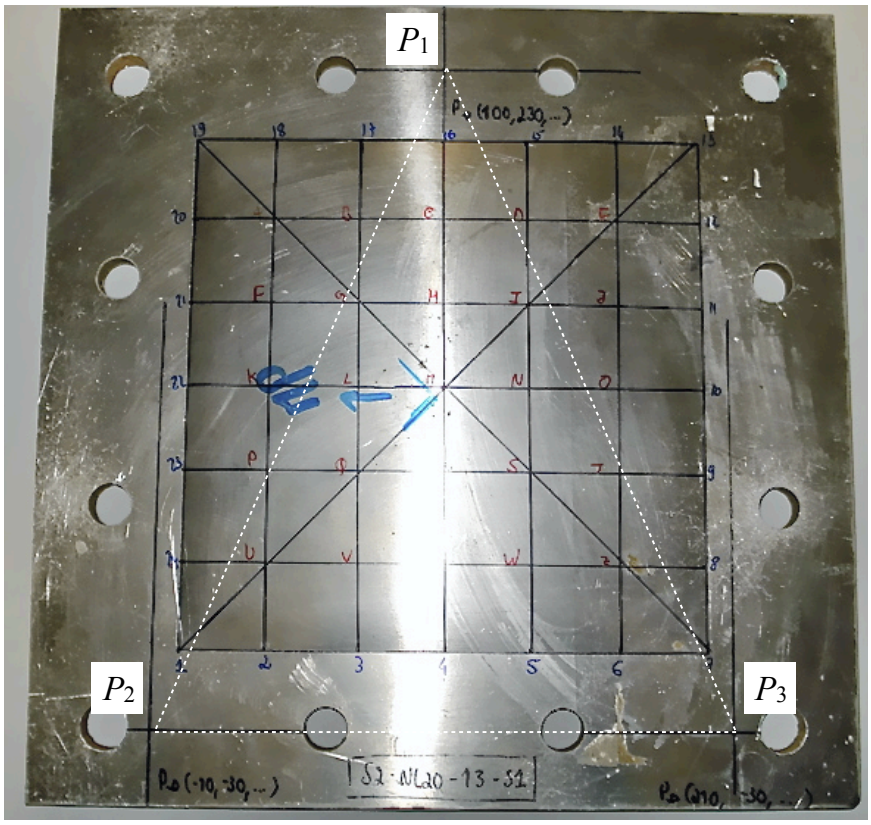

Figure 7.2: Front face markers in the NL20-10 sandwich for the correction of global bending using the three-dimensional coordinate measuring device.

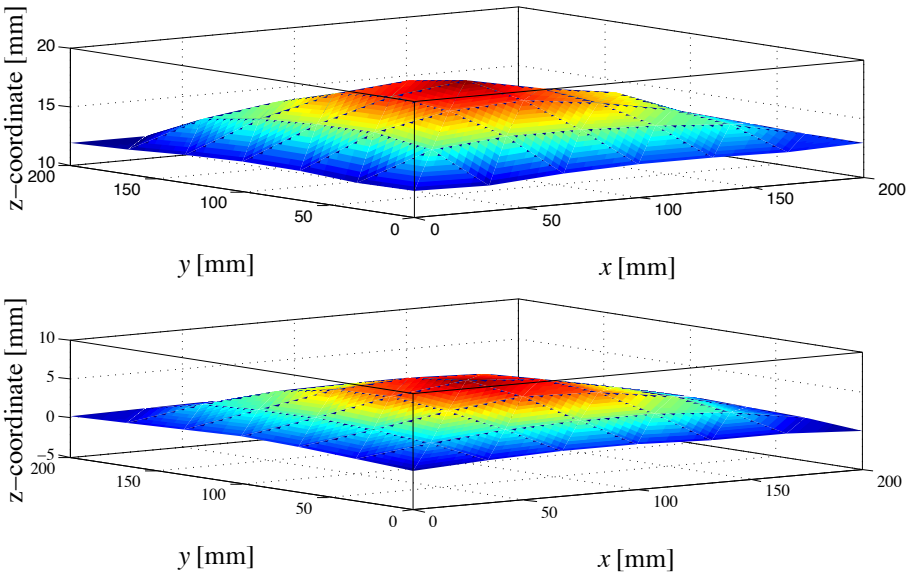

Figure 7.3: Contour surface of both faces for one of the NL20-10 specimens.

Table 7.2: Maximum deflection of the front and back face sheets, $D^{\mathrm{f}}_{\mathrm{max}}$ and $D^{\mathrm{b}}_{\mathrm{max}}$, respectively; deflection of the central point of the front face sheet, $D^{\mathrm{f}}_{\mathrm{cp}}$; and relative thickness reduction of the whole structure after the blast event, $h^{\mathrm{p}}_{\mathrm{red}}$ (*Normalised values).

Sample	$D^{\mathrm{f}*}_{\mathrm{max}}$	$D^{\mathrm{f}}_{\mathrm{max}}$ [mm]	$D^{\mathrm{b}*}_{\mathrm{max}}$	$D^{\mathrm{b}}_{\mathrm{max}}$ [mm]	$D^{\mathrm{f}*}_{\mathrm{cp}}$	$D^{\mathrm{f}}_{\mathrm{cp}}$ [mm]	$h^{\mathrm{p}}_{\mathrm{red}}$ [%]
NL20-10	1.000	5.630	0.959	5.015	1.000	5.630	10.945
NL20-15	0.912	5.136	1.000	5.227	0.912	5.136	5.308†
NL20-20	0.326	1.835	0.333	1.742	0.276	1.552	7.053
NL20-25	0.096	0.542	0.123	0.642	0.053	0.300	4.853
NL20-30	0.153	0.863	0.077	0.402	0.029	0.162	4.075
TB40-10	1.000	1.220	1.000	0.951	1.000	1.148	11.039
TB40-15	0.731	0.892	0.994	0.946	0.671	0.770	8.386
TB40-20	0.826	1.008	0.358	0.340	0.439	0.504	6.774
TB40-25	0.178	0.217	0.616	0.586	0.065	0.075	2.247†
TB40-30	0.698	0.852	0.677	0.643	0.242	0.278	5.076

† Values not considered due to excessive dispersion.

imposing an initial velocity v_{i}. At this stage the remaining components of the pendulum are considered to be stationary;

- Stage II: the compression of the sandwich structure core takes place. The back face sheet is considered to be stationary during this stage; and
- Stage III: the back face sheet deforms and all the components of the sandwich structure acquire rigid body movement with velocity v_{f}. The system will eventually return to a stationary state by stretching and bending.

The number of published studies on the deformation of rectangular sandwich structures is very limited, mostly due to the complexity of the equations governing the phase of overall bending and stretching. Some of these studies are related to the behaviour of sandwich beams and circular clamped panels [Hutchinson and Xue 2005, Deshpande and Fleck 2005, Zhu *et al.* 2009a]. As an example, Hutchinson *et al.* [Hutchinson and Xue 2005] developed extensive analyses on the behaviour of metallic sandwich beams subjected to pressure impulses. Some of these publications suggest that, if the back face deflection is higher than the initial thickness of the sandwich structure, the main global deformation mechanism in such loading conditions is stretching, and bending can be neglected. However, bending will play an important role if the back face deflection is low, and stretching can be neglected. This situation is often referred to as the small deflection case. Although the number of experimental tests done on each sample configuration may be considered to be low, the core material and sandwich configuration are distinct from the ones in literature (*e.g.* [Hutchinson and Xue 2005, Zhu *et al.* 2009a]). Results in table 7.2 might indicate that the observed impulses induce

a small deflection case, since the maximum deflection that the back face sheet suffers is lower than the initial thickness of the sandwich structure. This may indicate that bending is the main deformation mechanism and stretching can be neglected.

Front aluminium face sheet deformation

Sandwich structures with core thicknesses between 10 and 25 mm deform assuming a concave shape on the front face sheet. As expected, this effect becomes less noticeable with the increase of the thickness of the core. For a core thickness of 30 mm this effect is no longer clearly visible. In most sandwich structures, the maximum deflection is on the geometrical centre of the front face sheet.

MAC compound core deformation

In order to analyse the maximum deflection of both front and back face sheets these values were normalised, meaning that the values were divided by the highest value of its series. For comparison purposes, values of the maximum normalised front face deflection, back face deflection and deflection of the centre of the front face sheet are plotted in figures 7.4 and 7.5 against the initial core thickness for all NL20 and TB40 sandwich structures.

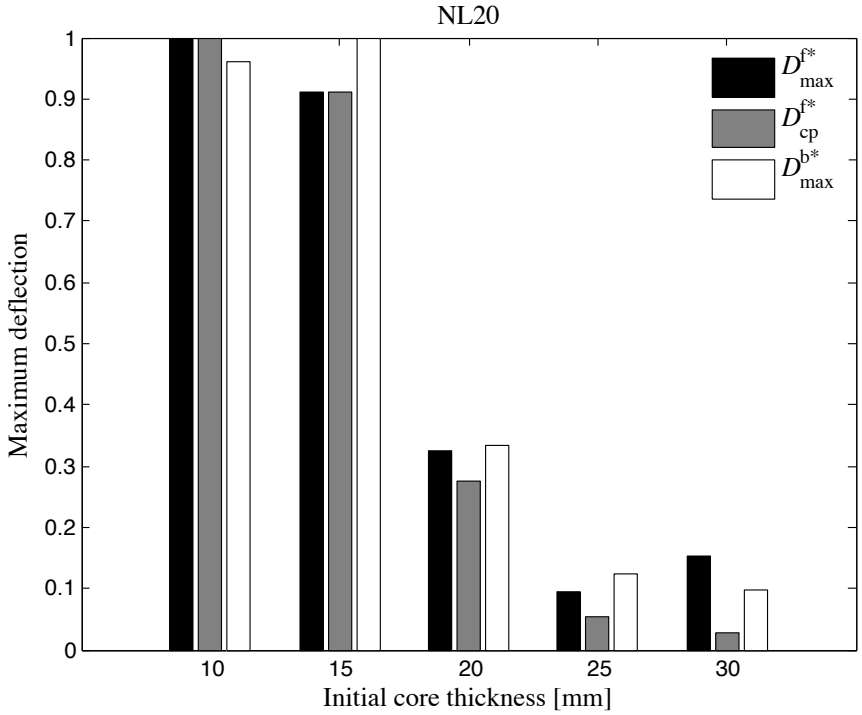

Figure 7.4: Maximum normalised values of the front face deflection, back face deflection and deflection of the centre of the front face sheet, plotted against the initial core thickness for the NL20 sandwiches.

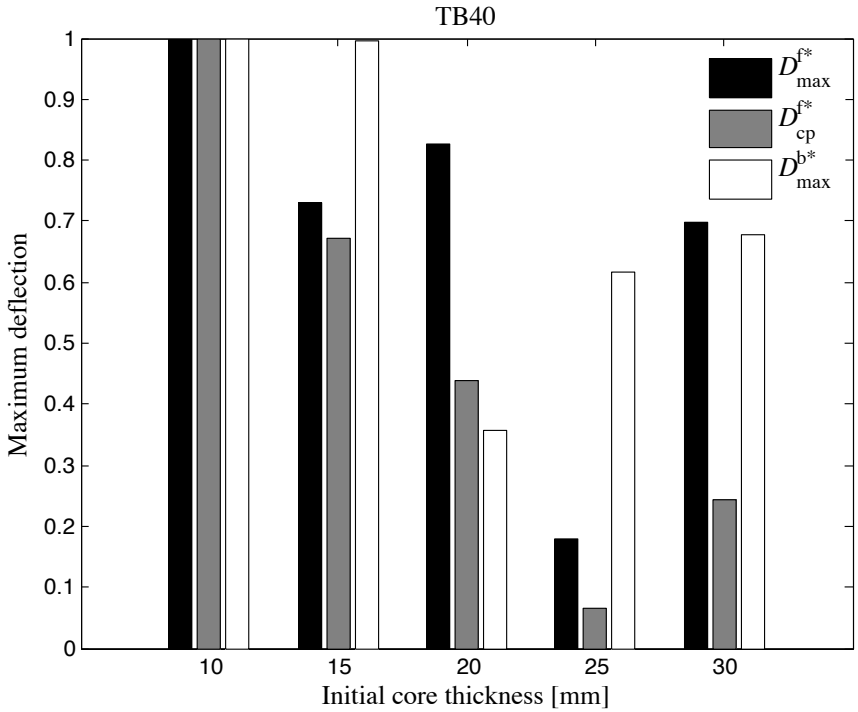

Figure 7.5: Maximum normalised values of the front face deflection, back face deflection and deflection of the centre of the front face sheet, plotted against the initial core thickness for the TB40 sandwiches.

For the NL20 MAC compound cores, as expected due to the lower density of the core, higher values of maximum deflection of the front face sheet were observed when compared to the sandwich structures with a TB40 MAC compound core (see table 7.2). The same trend is evident when analysing the maximum deflection of the back face sheet. A decrease on the deflections on the front and back face sheets as the thickness of the core increases is evident for the lower density core sandwiches (NL20) (see figure 7.4). Concerning the maximum deflection of the centre of the front face sheet, there is an agreement between this value and the value of the maximum deflection of the front face sheet, only for thicknesses lower or equal to 15 mm (see table 7.2). Nonetheless, as previously mentioned, the maximum deflection was expected on the geometrical centre of the front face sheet. This contradictory behaviour can most probably be explained due to one (or a combination of more than one) of the following facts: (i) a perfect spherical centred blast load was not achieved, leading to an off-axis first impact wave on the target; (ii) the core had minor defects in some regions that could have led to higher deflections on regions other than the centre of the front face.

TB40 MAC compound cores, that is, denser MAC compound, presented lower values of maximum deflection of the front face sheet when compared to the sandwich structures with the lower density NL20 core (see table 7.2). Additionally, the maximum deflection of the back face sheet is lower in the sandwich structures with TB40 cores then it was for the same equivalent core thickness sandwich but with NL20 core. As

with the sandwich structures with the NL20 cores, a decrease on the deflection of the front and back face sheets as the thickness of the core increases is evident (see figure 7.5). No agreement was observed between the maximum deflection of the centre of the front face sheet and the values of the maximum deflection of the front face sheet for the sandwich structures with a TB40 MAC compound core (see table 7.2). The causes previously mentioned for the sandwich structures with Nl20 MAC compound cores case, such as a non perfect spherical centred blast achieved or the minor defects in some regions of the core, can explain the higher deflections on regions other than the centre of the front face in the sandwich structures with the TB40 cores.

Back aluminium face sheet deformation

For the sandwich structures with core thicknesses between 10 and 25 mm, the back face sheet assumes a dome-like (convex) shape. As expected, this configuration becomes less evident as the thickness of the core increases and becomes unnoticeable for the core thickness of 30 mm. This deformation behaviour is more evident on the structures with lower stiffness and lower strength (NL20, lower density core). The typical dome-like deformation pattern observed in the back aluminium face sheet is shown in figure 7.6. As would be expected from the analysis of quadrangular sandwich structures, this shape is more pronounced on the centre of the structure and gradually changes to a quadrangular dome closer to the clamped edges.

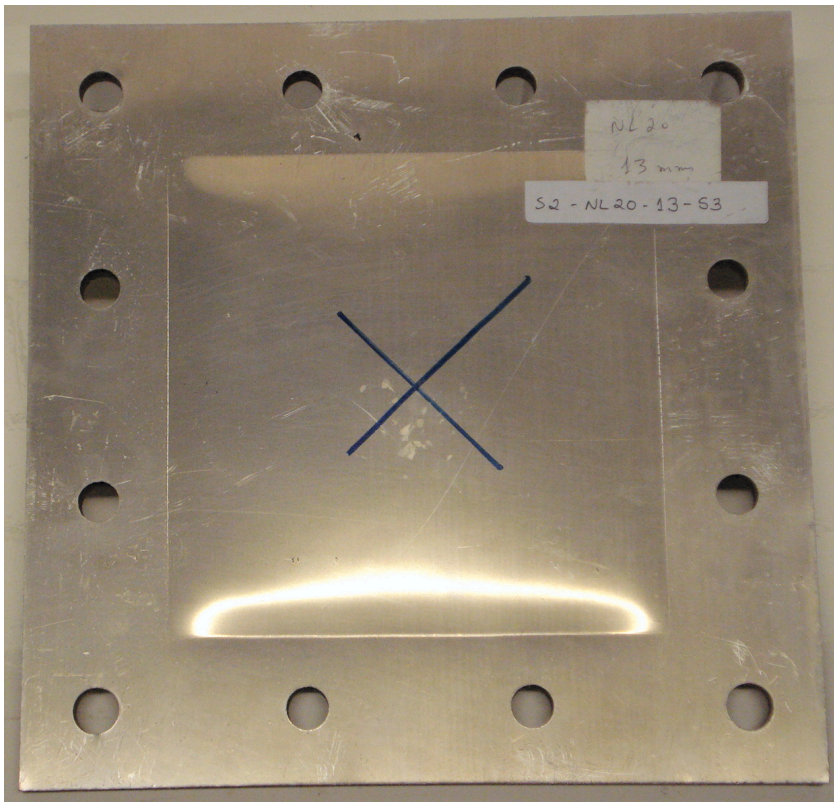

Figure 7.6: Back face deflection of the NL20-10 core sandwich specimen.

Relative thickness reduction

Based on the previous analyses it was possible to determine that, on the event of a blast-wave impact, there is a clear dependency between the density of the core and the back face sheet deflection. The values of the relative thickness reduction are shown in figure 7.7. A linear dependency between the relative thickness reduction, $h_{\text{red}}^{\text{p}}$, and the initial core thickness, h, was observed for both compounds. This dependency can be formulated as

$$h_{\text{red}}^{\text{p}} = -\alpha h + C \tag{7.1}$$

where α and C are the material dependent constants listed in table 7.3.

For sandwich structures with both NL20 and TB40 MAC compound cores, a significant thickness reduction ($\approx 11\%$) was observed for the sandwich structures with the lower thickness cores, possibly indicating that energy was dissipated in core compression during the impact of the blast-wave. As the thickness of the core increases this effect becomes less evident and for the highest core thickness (30 mm) values between 4 and 6% of thickness reduction are found for sandwich structures with NL20 and TB40 MAC compound cores, respectively.

Still related to the thickness reduction of the sandwich structures, some of the sandwich structures were cut at half width to determine the internal compaction, deformation and eventual occurrence of damage/failure within the core material. Damage was only observed close to the clamping borders of the sandwich structures and there was no debonding between the core and the face sheets. As an example, the cross section deformed profile of one of the sandwich structures is shown in figure 7.8. The specimen shown is NL20-10 since this was the one with the maximum deflection due to the relation between its density and core thickness.

Table 7.3: Material constants relating the relative thickness reduction, $h_{\text{red}}^{\text{p}}$, and the initial core thickness, h, (see equation 7.1).

Core material	α	C	R^2
NL20	0.36	14.32	0.98
TB40	0.29	13.17	0.92

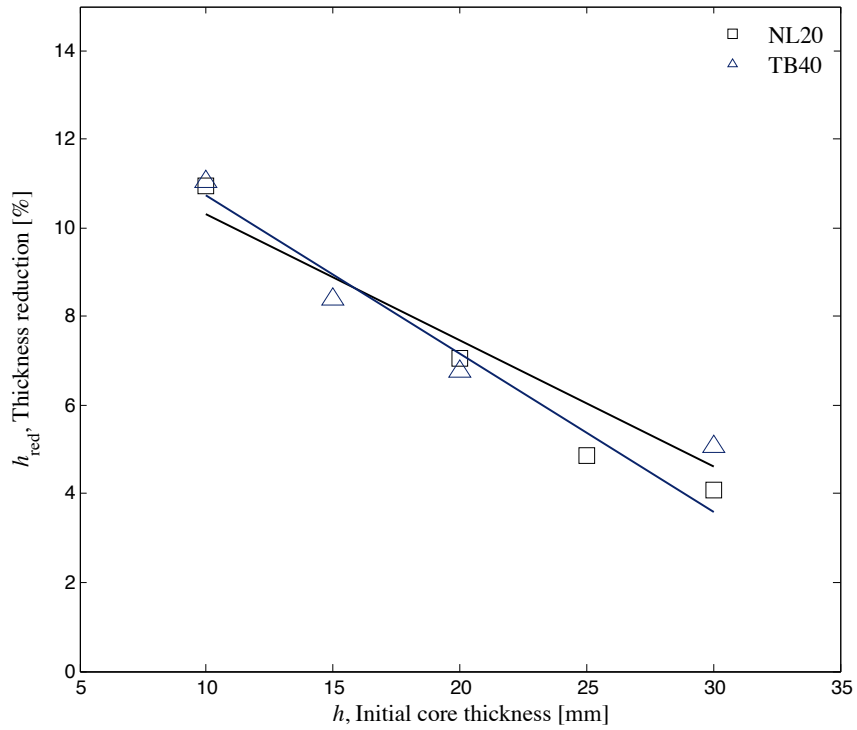

Figure 7.7: Relative thickness reduction as a function of the initial core thickness.

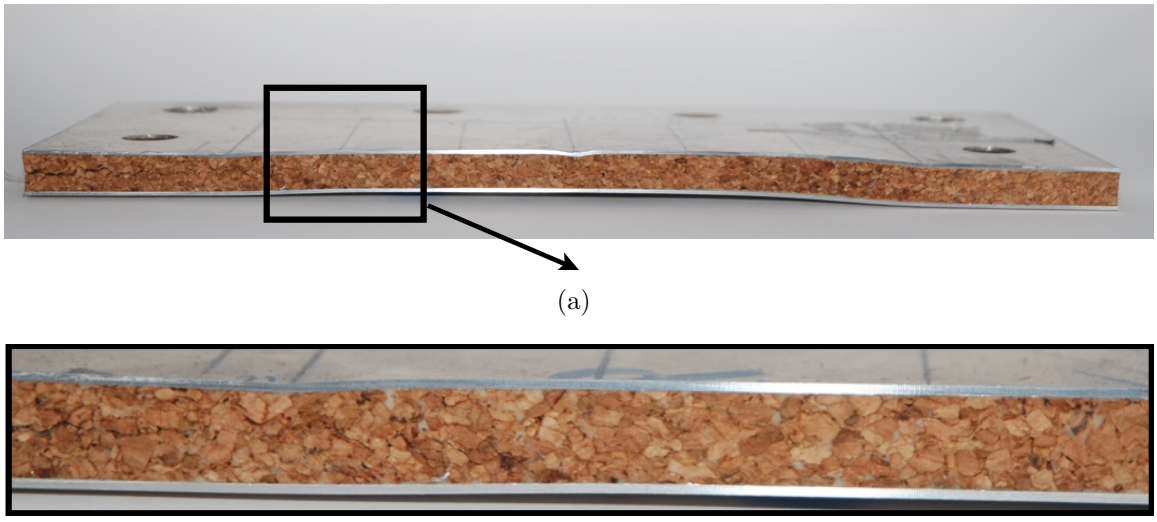

(a)

(b)

Figure 7.8: Half-width cross section of the NL20-10 MAC compound core sandwich structure. (a) Overall view and (b) insight view.

Part III

Numerical modelling

Chapter 8

FEM analysis and software

The chapter here presented is a generic overview on finite element analysis and available software that may be used to study the effects of blast-waves on structures.

8.1 Finite element analysis and software

Computational mechanics plays an important role nowadays since it is an extremely important tool in the development of new and innovative structures and applications. One of the major factors that puts computational mechanics in such a level is that it complements the experimental part of an investigation and, therefore, it becomes possible to avoid unnecessary experimental work, reducing costs. Not only the reduced costs (compared to experimental analysis) are an advantage to the numerical methods. In situations where the non-linearity of the behaviour of the material and complexity of the analytical analysis is high or even if a solution to the problem is inexistent, numerical tools are highly relevant. The finite element method (FEM) plays an important role since it allows to solve such non-linear problems by approximation. The FEM is a mathematical method in which a continuous medium is discretised in smaller domains. These domains (*i.e.* elements) are given the properties of the continuos medium in analysis. Differential equations describe these singular elements and mathematical methods are used to obtain, for example, stresses, strains, pressure, displacements, *etc.* An approach to the FEM may be divided into different steps (see, for example, [Belytschko *et al.* 1997, Zienkiewicz *et al.* 2005, Teixeira-Dias *et al.* 2010]):

1. Pre-processing;
2. Analysis;
3. Post-processing.

The main stages that constitute the FEM method are shown in figure 8.1 .

In Pre-processing the spatial domain is divided (discretised) in smaller elements. Each element has nodes associated to it in which physical properties can be determined. Between nodes the same physical properties can be obtained by means of interpolation.

All the information collected in the first stage (*i.e.* pre-processing) is computed in the Analysis stage. If no errors are detected, the numerical analysis takes place. The problem can, for example, involve obtaining the temporal solution of non-differential equations (this can be achieved through time discretisation — time integration).

Two different types of algorithms can be used in the time integration: implicit and explicit. Time integration algorithms are said to be implicit if the parameters of integration selected correspond to coupled equations. In the choice of these parameters and when the uncoupling of equations is allowed, then the algorithm is said to be explicit and is conditionally stable. Therefore, in an explicit method, the time integration of the discrete momentum equations for a finite element model does not require the solution of any equations. The advantage of implicit methods over explicit ones is that for linear transient problems, suitable implicit integrators are unconditionally stable [Belytschko *et al.* 1997].

Finally, the last stage of the finite element method corresponds to Post-Processing where the obtained output in the analysis stage is presented. The information can be presented to the user, for example, in contours, tables, profiles, animations and videos, *etc.*

Nowadays, there are several commercial software available for FEM analysis for solving non-linear structural problems. Several of theses packages are already prepared for solving problems either implicitly or explicitly. A brief presentation to methods used to predict blast loads followed by a description of the software available for such studies will be mentioned in the next section.

8.1.1 Methods for predicting blast loads

There are three main approaches to predict the effects of blast-waves on structures: (i) empirical/analytical, (ii) semi-empirical and (iii) numerical methods [Remennikov 2003, Ngo *et al.* 2007]. Since the intention is to find the best method in order to apply to the case being studied, some of the advantages and/or disadvantages of these approaches will be mentioned.

The first approach is intrinsically related to the analysis of experimental data and, therefore, the results are subjacent to the amount of experimental data available. These methods are essentially correlations with experimental data, which imply that their accuracy is highly dependent on the extent of experimental data. In addition, in blast scenarios, this first approach is said to have its accuracy reduced in situation of near field explosion [Remennikov 2003].

The second approach (semi-empirical methods) is based on simplified models of physical phenomena. Their predictive accuracy is generally better than that provided by the empirical methods [Remennikov 2003].

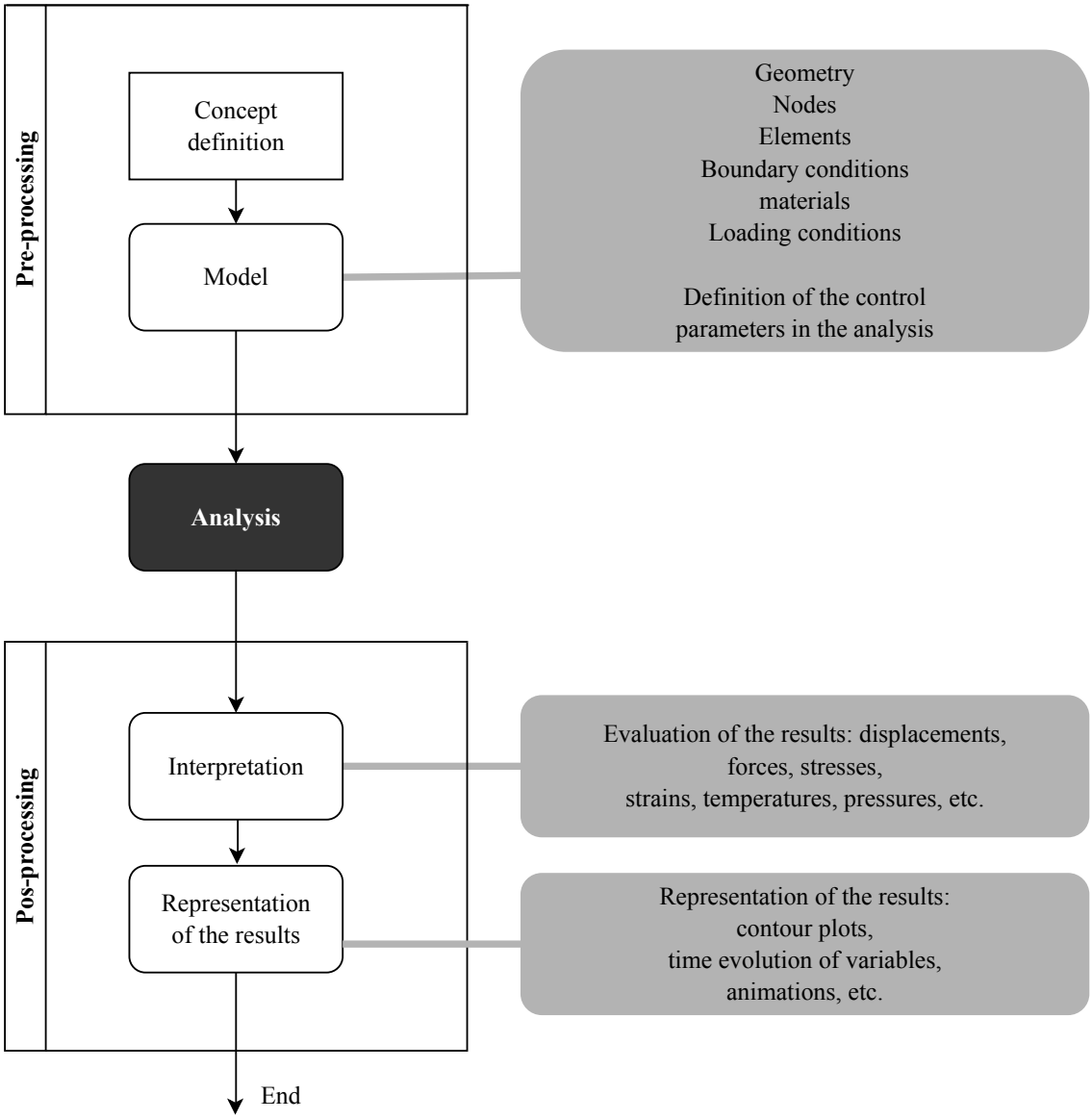

Figure 8.1: Methodology used when solving a FEM problem (adapted from [Teixeira-Dias *et al.* 2010]).

Numerical methods are characterised by mathematical equations that describe the physical phenomena and their basic principles, such as, for example, the conservation of mass, momentum and energy [Remennikov 2003].

Computational software available today for blast prediction and structural response combine both numerical and semi-empirical methods [Ngo *et al.* 2007]. When research on the mitigation of blast was at its early stages it was common practice to separate the analysis in two distinct components: the blast load and the structural response [Børvik *et al.* 2009]. Numerical methods can be divided in two categories that are intrinsically related to this separation (or non-separation) of the analysis: uncoupled and coupled numerical analysis. In the uncoupled analysis the blast load and the structural response are separated and the structures are modelled as rigid components. As a consequence of this definition, over-prediction of the blast loads might occur [Ngo *et al.* 2007]. Coupled analysis allows a coupling between the blast load component and the structural response component of the problem.

Software such as LS-Dyna™, Abaqus® and Autodyn™ use coupled analysis as the computational method on the mitigation of blast effects. Software most commonly used for blast prediction and/or their effects on structures as well as the method of analyses, are presented in table 8.1

Table 8.1: Software used for blast prediction and/or their effects on structures (adapted from Ngo *et al.* [Ngo *et al.* 2007]).

Software's name	**Purpose**	**Analysis approach**
Abaqus® [AB 2012]	Structural response + CFD	Coupled Analysis
Autodyn® [AD 2012]	Structural response + CFD	Coupled Analysis
BlastX® [BW 2012]	Blast Prediction	CFD code
Conwep [Randers-Pherson and Bannister 1997]	Blast Prediction	Empirical
CTH [CW 2012]	Blast Prediction	CFD code
LS-Dyna™ [DW 2012]	Structural response + CFD	Coupled Analysis
Shark® [SK 2012]	Blast Prediction	CFD code

LS-Dyna™ will be used in the numerical work presented in this thesis. Two different approaches in modelling the blast load will be used: (i) the first one refers to the modelling of the detonation/initial expansion of the explosive device (see chapter 9) and (ii) the second approach is with CONWEP [Randers-Pherson and Bannister 1997]. This empirical method is already implemented in LS-Dyna™ and will be referred and explained in detail in chapter 10.

8.2 Material and spatial coordinates

As previously stated in the present work, computational analysis will be performed in order to analyse the blast-wave absorption capacity of structures and, therefore, a set of alternative formulations will be addressed and analysed. When an explosive is numerically modelled, the formulation adopted does not correspond to a solid material formulation. This section will help to clarify some of the major distinctions between different types of material formulations. However, formulations used for structural deformation must be considered within this work. Eulerian coordinates define the position of a set of points in space. In a highly deformable body, the position of the material point changes in time, that is, the spatial coordinates are a function of time. Lagrangian coordinates, also known as material coordinates, define the position of a material point. A material description is related to the behaviour of a material particle, whereas a spatial description refers to the behaviour at a spatial position. As an example, fluid mechanics models are mainly based on spatial descriptions because it is not appropriate to describe the behaviour of a fluid material particle in, for example, a steady-state flow situation [Bonet and Wood 2008, de Souza Neto *et al.* 2008]. Purely eulerian methods are frequently used in fluid dynamics. In these methods, the mesh is fixed in space.

Lagrangian methods are mostly used when describing the deformation of solids (and structures). In this case, within the subject of finite element theory, the finite element mesh moves in space along with the material. The computational cost of this method is determined by the levels of distortion that may occur in the mesh [de Borst and Hughes 2004].

A third method that combines characteristics of the two previous approaches is known as Arbitrary Lagrangian Eulerian (ALE) method. In an ALE approximation, both eulerian and lagrangian features are combined, allowing for this to be the most effective element formulation to simultaneously solve fluid dynamics calculations and handle severe structural deformation. The element formulation in ALE methods is known as multi-material ALE formulation where both an eulerian mesh and lagrangian material points are used. Stress is computed on the lagrangian material points whereas the velocity of the material is calculated on the nodes of the mesh. On the one hand, stress is calculated on the lagrangian points, hence, the deformation history of the material can be easily tracked and wide varieties of constitutive relations can be easily implemented. On the other hand, since the velocity of the material is calculated on an eulerian mesh, mesh distortion issues do not exist in multi-material ALE formulation. Thus, this method has the advantages of both the eulerian and the lagrangian formulation methods but avoids their disadvantages. In terms of comparison of this method with purely eulerian or lagrangian methods, multi-material ALE method has a higher computing time since it requires the tracking of both the quantities on the material points and on the mesh nodes. Despite the computing time disadvantage, multi-material ALE method is justified in terms of accurately defining the multi-material

interactions undergoing large deformations.

Chapter 9

Cylindrical MAC compound specimens

The numerical modelling of the blast-wave absorption capacity of the cylindrical MAC compound specimens is presented in this chapter. A comparison with the experimental results is also presented. The first approach is related to the lagrangian and eulerian formulation of materials, where the explosive, as well as the air, is modelled. The second approach presented is to consider the effects of the explosive, that is, to load the specimen with a blast pressure wave.

9.1 Introduction

The experimental setup and equipment used for the characterisation of the micro-agglomerated cork (MAC) compound specimens was explained in detail in chapter 5 and the analysis of the experimental results was discussed in chapter 6. Cylindrical MAC compound specimens with two different densities NL20 (ρ = 200 kg/m^3) and TB40 (ρ = 440 kg/m^3) mounted on a 4-cable ballistic pendulum were subjected to a blast-wave originated from the detonation of 7 and 8 g of C4. Three different heights of these specimens were considered (50, 75 and 100 mm) while the radius of the specimens was kept constant throughout the experiments. The displacement of the pendulum, the loads from the force transducer and the high speed camera videos of the entire testing process were acquired. The analysed results focused the load-time profile analyses, influence of the density of the MAC compound on the response of the specimen to the load, influence of the mass of C4 and the height of the specimen. The numerical modelling using the finite element method (FEM) of the experimental tests performed with cylindrical MAC compound specimens is presented in the current chapter. The main goal is to achieve a good correlation between experimental observations and numerical results. All the numerical results were detailed compared with the equivalent

experimental observations.

LS-Dyna^{TM} was the software used for the numerical analysis. This software was first intended to be applied in highly non-linear transient dynamic finite element analysis (FEA) with explicit time integration. Besides the non-linear analysis of the response of MAC compound specimens, LS-Dyna^{TM} was also used to model the components of the ballistic pendulum. As seen in the schematic representation in figure 5.5, several different parts complete the ballistic pendulum: an I-beam, 4 cables, a cover plate, a force transducer and a special base for the cork specimen. This finite element analysis is constituted by two distinct parts (impact phase and oscillation phase) where different material models were used in the two phases for the I-beam, the cover plate, the force transducer and the base.

9.2 Axisymmetric analysis

Two different steps were considered in order to get all the input information needed for the numerical modelling of the problem. The first one was to determine the impulsive load that the specimen would be submitted to. After knowing this value, it was then possible to apply a load to the complete three-dimensional model of the pendulum. Hence, the analysis was divided in two phases: impact and oscillation.

This section is related to the numerical modelling of the explosive (explosion) with an Arbitrary Lagrangian Eulerian (ALE) formulation. The purpose of such analysis was to conclude on the exact load that the striker would feel when impacted by the blast-wave from the detonation of 7 and 8 g of C4. Although the initial velocity of the striker was already determined in the experimental analysis using linear oscillator theory (see chapter 6), this experimental velocity could have *a priori* experimental errors that could compromise the FE model. An example of a possible experimental error is the following: since the experiments resulted from an average of three tests, small discrepancies in the mass of the explosive charge of each of these tests may have lead to higher or lower values of the initial velocity of the striker than expected. Hence, to eliminate the influence of the experimental errors associated to the determination of the initial velocity of the striker, an ALE formulation model was used for the discretisation of both air and explosive, ensuring that these domains were continuous in element representation. This model is shown in figure 9.1. The complete ballistic pendulum did not need to be modelled since the only important part of the process that had relevance to the estimation of the initial velocity of the striker only involved the interaction between explosive and striker. Therefore, only an Oz-axis axisymmetric model (including striker, explosive and detonator, cover plate and air) needed to be considered. The HE charge (including detonator) was also modelled, making sure that the dimensions corresponded to exactly 7 and 8 g of C4. The used LS-Dyna^{TM} material types are listed in table 9.1, as well as the mechanical properties of the materials, air and the high explosive. The polystyrene pad was not modelled since, as previously mentioned, its influence after the detonation of the explosive is considered to be negligible [Theobald

and Nurick 2010]. The elements had sizes of 0.5 mm. Elements with axisymmetric element formulation were used for the lagrangian components (cover plate and striker) and axisymmetric multi-material ALE formulation elements for the ALE components (air and high explosive).

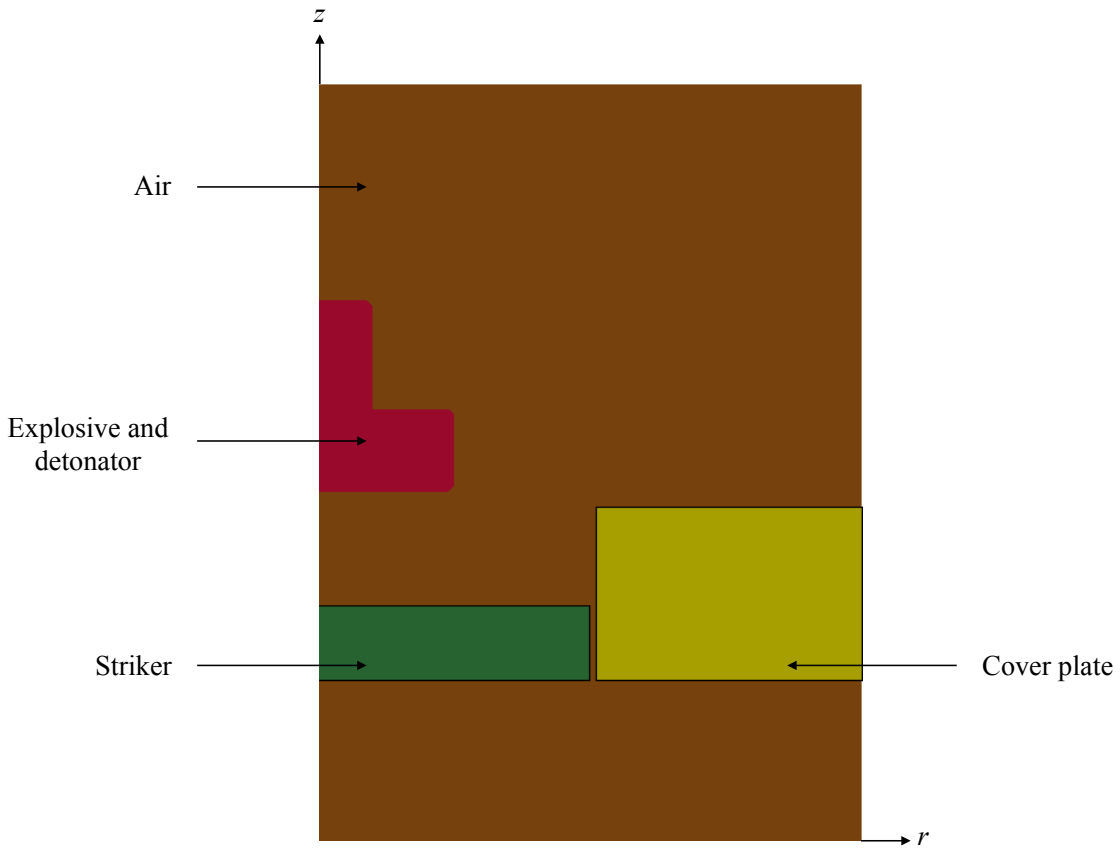

Figure 9.1: FE axisymmetric model used to analyse the detonation process and expansion of the ALE fluids.

Several time frames from the axisymmetric FEM model used to determine the velocity imparted to the striker (specifically for the 7 g of C4 case) are shown on figure 9.2. The detonation takes place immediately after $t = 0$ ms and the fluid correspondent to the expanding high-explosive reaches the striker at $t \approx 0.0045$ ms. For $t \approx 0.0219$ ms the displacement of the striker becomes more evident and it is also possible to notice that some of the ALE fluids pass through the space between the striker and the cover plate. Finally, for $t \approx 0.657$ ms the influence of the blast on the striker is almost negligible and its velocity stabilises. This final velocity is the velocity that the striker will impart on the specimen. An initial velocity of 80 and 87.5 m/s was obtained from these simulations registering the movement of the striker when loaded with 7 and 8 g of C4, respectively.

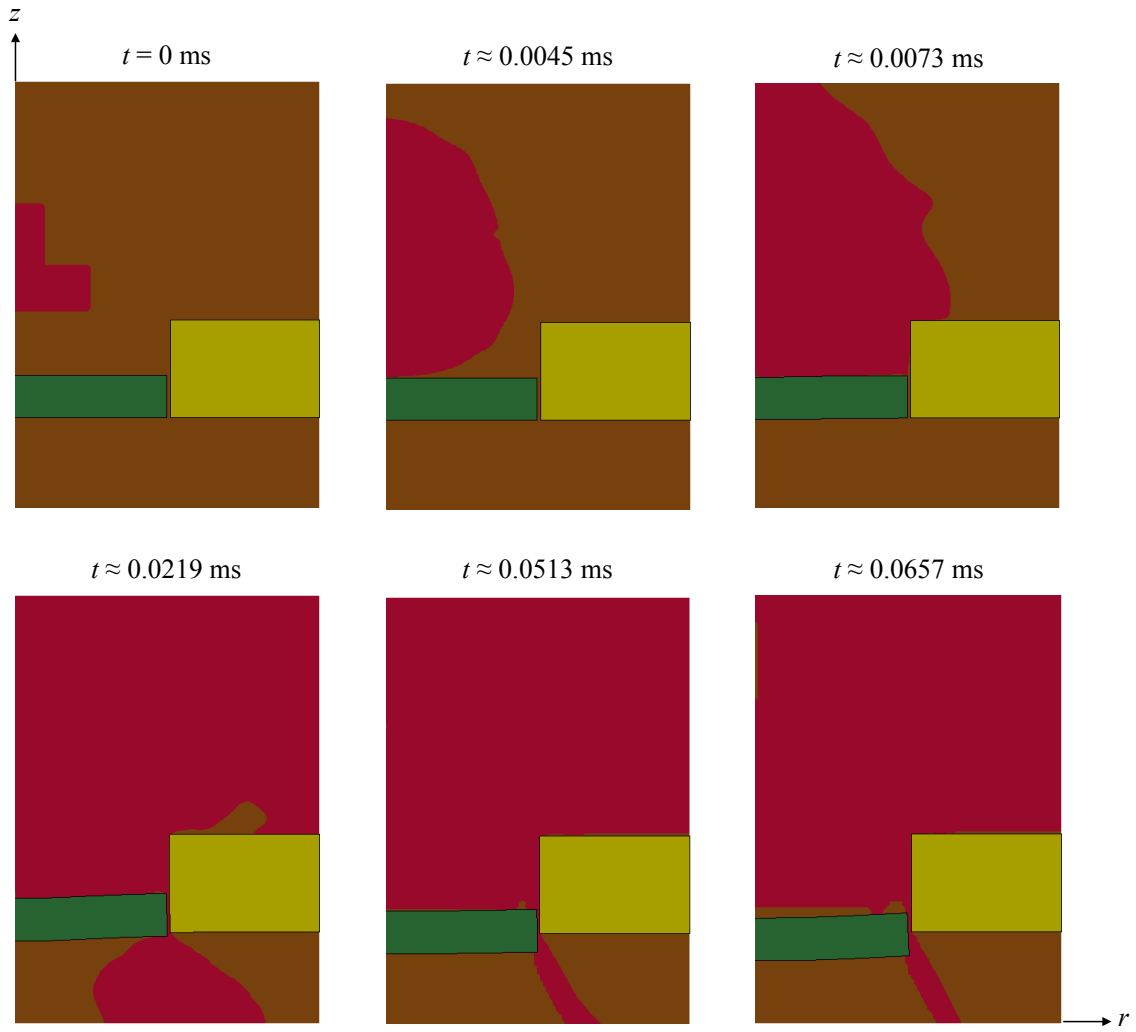

Figure 9.2: Numerical simulation sequence representing the axisymmetic detonation process and expansion of the ALE fluids.

Table 9.1: LS-Dyna^{TM} material type and material properties for the axisymmetric model (ρ is the density, E is the Young modulus, ν is the Poisson ratio, D is the detonation velocity and P_{CJ} is the Chapman-Jouguet pressure).

Formulation	**Component**	**Material type**	**Parameters**
Lagrangian (solid)	Cover plate and striker	`*Mat_Elastic`	$\rho = 7.850$ g/cm^3 $E = 210$ GPa $\nu = 0.30$
ALE	Explosive	`*Mat_High_Explosive_Burn`	$\rho = 1.601$ g/cm^3 $D = 8193$ m/s $P_{CJ} = 28$ GPa
ALE	Air	`*Mat_Null`	$\rho = 1.225 \times 10^{-3}$ g/cm^3

9.3 Impact and oscillation

The process to determine the velocity that the striker would feel due to the detonation of the explosive was explained in the previous section. This velocity can then be applied to the striker that will impact the MAC compound specimen. Knowing this velocity, a FEM model was developed where the MAC compound response to blast-waves was analysed. This FE analysis was divided in two different phases: (i) impact and (ii) oscillation. The first phase — the impact phase — corresponds to the stage where the striker is given an initial velocity (determined from the axisymmetric model) and crushes the specimen. Once the collision and consequent compression of the MAC compound specimen is achieved, the striker starts to move in the opposite direction of impact and the oscillation phase takes place, meaning that the striker no longer is in contact with the specimen and the ballistic pendulum will start to oscillate (as a rigid body).

9.3.1 Material models, boundary and contact conditions

This FE model, that takes into account these two phases, was jointly developed with the Laboratory for Analysis of Explosion Effects in the Civil and Material Engineering Department of the Royal Military Academy in Brussels [Kakogiannis 2011] and is presented in figures 9.3 (a) and (b). An insight on the force transducer is also shown. The labels in these figures correspond to (a) the I-beam, (b) the MAC compound specimen, (c) the base for the MAC compound specimen, (d) an I-shaped front plate where the base for the specimen can be attached to, (e) the striker, (f) the ballistic pendulum suspension cables and (e) the force transducer. In terms of element formulation, the cables were modelled with discrete beam elements [DK 2012], while the other components (I-beam, I-beam shaped front plate, force transducer and specimen's base) where

discretised using a constant stress solid element formulation [DK 2012]. The striker was discretised in 130 elements and the same constant stress solid element formulation was used.

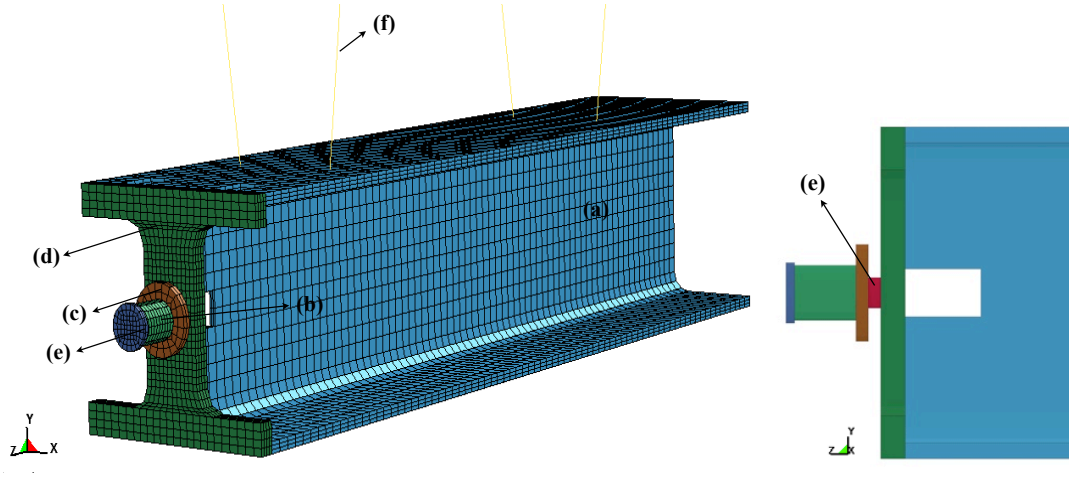

(a) (b)

Figure 9.3: (a) Finite element model and discretisation of the 4-cable ballistic pendulum and (b) insight on the force transducer.

In terms of material behaviour, the structural materials of the ballistic pendulum (*i.e.* I-beam, base for specimen, striker and I-shaped front plate) were modelled as purely elastic materials (`*Mat_Elastic`) [Hallquist 2006] and the properties used are listed in table 9.2.

Table 9.2: LS-Dyna^{TM} material type and material properties input data (ρ is the density, E is the Young modulus and ν is the Poisson ratio).

Formulation	**Component**	**Material type**	**Parameters**
Solid	I-beam, base for specimen, striker, I-shaped front plate force transducer	`*Mat_Elastic`	$\rho = 7.850$ g/cm^3 $E = 210$ GPa $\nu = 0.3$
Beam	Cables	`*Mat_Cable_Discrete_Beam`	$\rho = 7.850$ g/cm^3 $E = 210$ GPa

Once the impact phase ends and the (rigid body) oscillation phase starts, the material models are changed to rigid (`*Mat_Rigid` [Hallquist 2006]), and the striker and the cork specimen are erased. The ballistic pendulum suspension cables were modelled with the material model `*Mat_Cable_Discrete_Beam` [Hallquist 2006]. The load that

is generated by the cable, F, is non-zero only if the cable is in tension [Hallquist 2006] and is given by

$$F = k \max\{\Delta l, 0\}, \tag{9.1}$$

where Δl is the change in length of the cable due to tension, that is,

$$\Delta l = l_{\mathrm{c}} - l_{\mathrm{i}}. \tag{9.2}$$

where, l_{c} and l_{i} are the current and initial lengths of the cable. The stiffness of the cable is

$$k = \frac{EA}{l_{\mathrm{i}}}, \tag{9.3}$$

where E is the Young's modulus and A is the cross section area of the the cable. All the degrees of freedom of the top nodes of the cables, attached to the ceiling, are fixed and the bottom nodes are merged with nodes from the I-beam. The self-weight of the pendulum was naturally taken in consideration. Special contacts were defined in order to connect the different parts of the pendulum. Tied contacts were used, since in tied interfaces mesh transition is permitted, that is, these are adequate contact types to tie parts with disparate meshes [Jensen 2010]. Two different contact types from the LS-Dyna$^{\mathrm{TM}}$ data base were used: `*Contact_Tied_Nodes_To_Surface` [DK 2012] and `*Contact_Tied_Surface_To_Surface` [DK 2012]. These types of contacts are defined between master and slave parts to be tied. In general, when using tied interfaces between similar materials, the master surface should be the more coarsely meshed and this definition should only be surpassed if, for example, one material is significantly softer. In this case the master side should be the stiffest material [Bala 2001]. According to Bala [Bala 2001] in a contact tied interface, at the beginning the nearest segment of a master part is located on an orthogonal projection of the slave node to the master segment. If the slave node is considered to be close to the master segment (*i.e.* it is not mandatory that the interfaces be in contact since a tolerance distance in which the contact is active can be defined for the distance between slave node and master segment) the slave node is moved to the master surface. As the simulation progresses, the position of the slave node with respect to its master segment is held fixed using kinematic constraint equations. These contact types should preferably be used with solid elements, since rotational degrees-of-freedom of the slave node are not constrained [Bala 2001]. Contact type `*Contact_Automatic_Surface_To_Surface` was implemented between the MAC compound specimen, its base and, additionally, to the striker and MAC compound specimen. Automatic contact types are based on a penetration check, that is, the nodes of both parts are checked for potential penetration of a slave node through a master segment. When a penetration is detected a load proportional to the penetration depth is applied to resist, and ultimately eliminate, the penetration.

Several frames of the crushing process of the MAC compound specimen are shown in figure 9.4 (specifically for the NL20-50 MAC compound). Cork was modelled using

constant stress solid elements with 10 elements on its height and 16 along the circumference. For time $t = 0$ ms the striker has an initial velocity of 80 m/s. For time instants $t \approx 0.240$ ms and $t \approx 0.510$ ms the height of the specimen is reduced to approximately 32.4 mm and 20.6 mm, respectively. Finally, for time $t \approx 0.720$ ms the striker is no longer in contact with the specimen and the pendulum oscillation phase initiates. The elastic recovery stage is evident from this instant on.

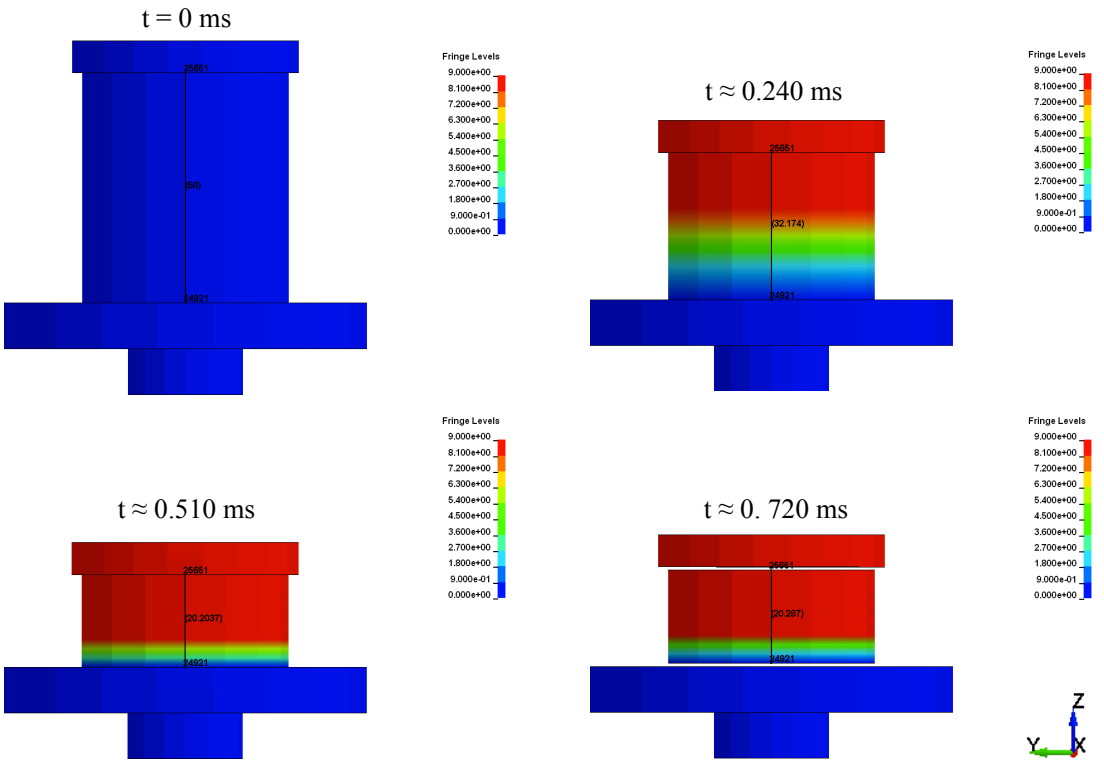

Figure 9.4: Crushing process of a MAC compound specimen.

9.3.2 Material model for MAC compounds

As stated before (see chapter 4) the material type that was used for the MAC compounds was `*Mat_Honeycomb` [DK 2012]. A detailed review on the properties and constitutive equations of this material model was presented in chapter 4 in which the materials models used within the scope of this investigation and its mechanical behaviour was presented. Nonetheless, some relevant aspects regarding the material model will be described here for the sake of clarity.

The input parameters were the density, ρ, densification Young modulus, E_d, densification Poisson ratio, ν_d, and the uniaxial compression $\sigma - \varepsilon$ curve. It should be noticed that some input parameters in this model refer to the densification state of the MAC compound. These parameters do not correspond to the MAC compound properties but to the cell wall properties (base material) of cork, since when the compound

is fully compacted it is assumed to behave as an uniform (*i.e.* non-cellular) block of suberin.

Multiplicative factor analysis

As previously mentioned, this material model allows a $\sigma - \varepsilon$ curve to be introduced. A typical stress-strain curve of a cellular material, with the ability of the material to sustain very large deformations for very low stress values, should be used as input. However, in order to accurately model the behaviour of MAC compounds, it was necessary to investigate the influence of the strain rate on the response of the material. Hence, the influence of the strain rate on MAC compounds had to be previously investigated. In the work presented by Gameiro *et al.* [Gameiro *et al.* 2007a], dynamic stress-strain curves for 4 distinct types of cork compounds are presented and analysed. These authors proved that different types of cork agglomerates have similar behaviours in the dynamic range of 200 to 600 s^{-1}, regardless of the sample tested characteristics and of the strain rate (within the range). However, the dynamic stress plateau was found to be larger than the static one, leading to the conclusion that cork agglomerates are materials whose behaviour is not fully independent of the strain rate. Gameiro *et al.* [Gameiro *et al.* 2005] also tested the application of several multiplicative factors to *quasi*-static experimental results on several types of cork and its compounds. These multiplicative factors are average values determined during the dynamic experimental tests. As an example, Gameiro *et al.* [Gameiro *et al.* 2005] determined a multiplicative factor of 2 for an agglomerate cork compound case and 3 for micro-agglomerated cork (MAC) compounds. In the study here presented, *quasi*-static stress-strain curves were obtained for the NL20 and TB40 specimens with 50 mm of height using a Shimadzu™ AG-50 kN G universal testing machine at 4 mm/min. Three tests were obtained for three different specimens with the exact same characteristics (for both NL20 and TB40 MAC specimens). An average of these three curves was used in the numerical model, in the form of true stress-true strain. An extensive study was done to determine which multiplicative factor best suited the mechanical behaviour of cork. Numerically, the simulation was performed for several multiplicative factors. The loads registered by the force transducer where compared with equivalent numerical results. The experimental and numerical loads registered by the force transducer are plotted in figures 9.5 to 9.16.

Only the specimens with 50 mm height were used to study the multiplicative factor to be applied to the *quasi*-static stress-strain curve (see figures 9.5 and 9.11 for 7 g of C4, and figures 9.8 and 9.14 for 8 g of C4) since in longer specimens slight bending occurred (see chapter 6). The experimental solid black line corresponds to an average of the multiple experimental curves.

Very good agreement between the experimental and the numerical values was obtained for the NL20 MAC compound specimens tested with 7 and 8 g of C4 in terms of the force transducer measurements, as can be seen from the results in figures 9.5 and 9.8. In terms of maximum load peak the correlation between experimental and numerical results is almost perfect for multiplicative factors of 1.80 and 3.80 for NL20

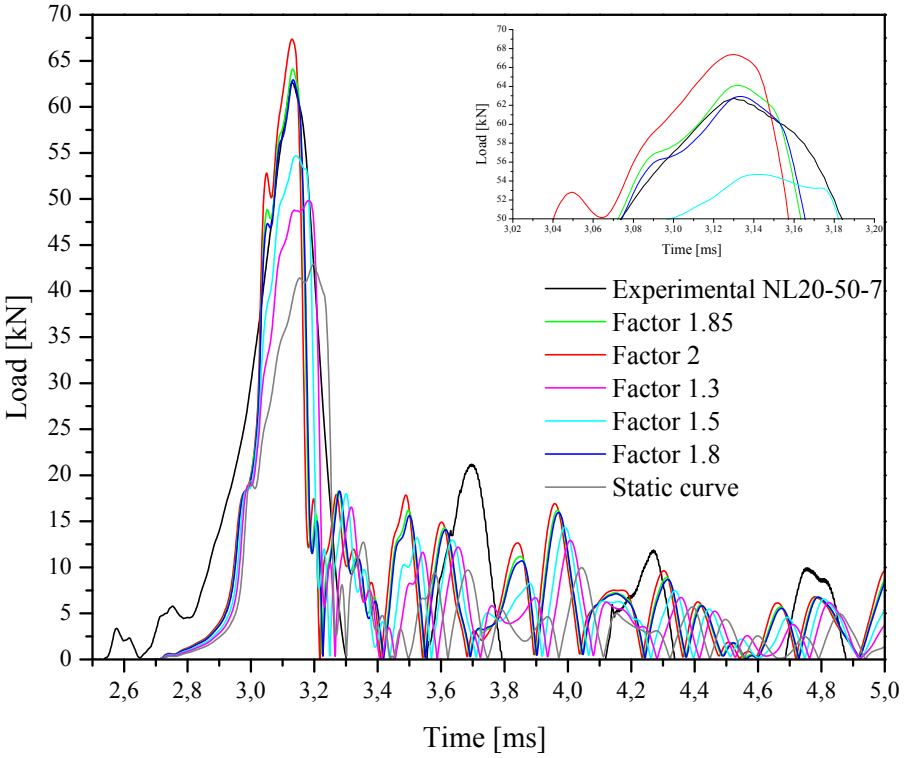

Figure 9.5: Comparison between experimental and FEM analysis of the force transducer measurements using different multiplicative factors (specimen NL20-50-7).

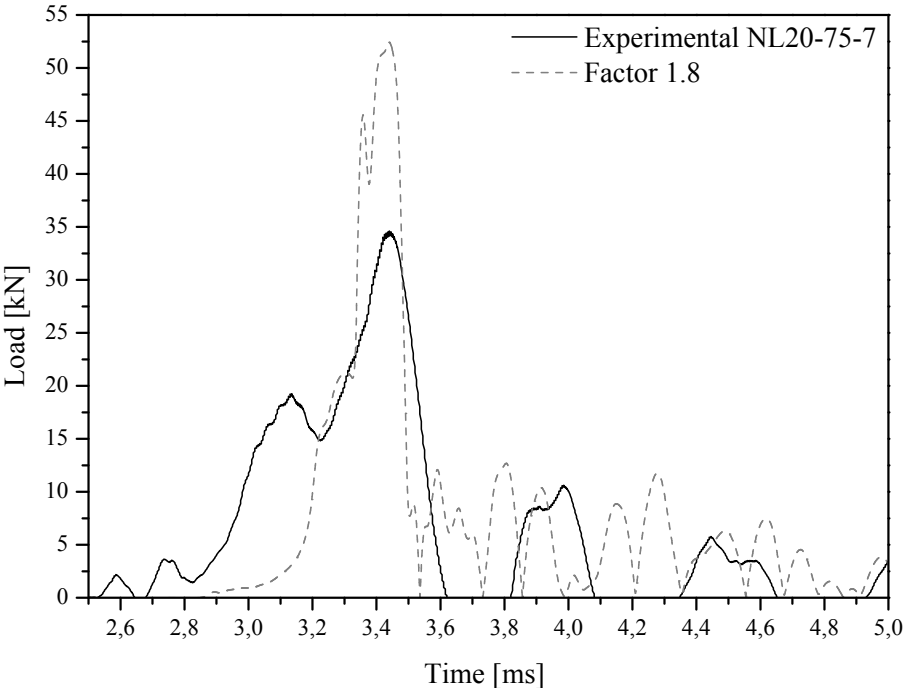

Figure 9.6: Comparison between experimental and FEM analysis of the force transducer measurements using a multiplicative factor of 1.8 (specimen NL20-75-7).

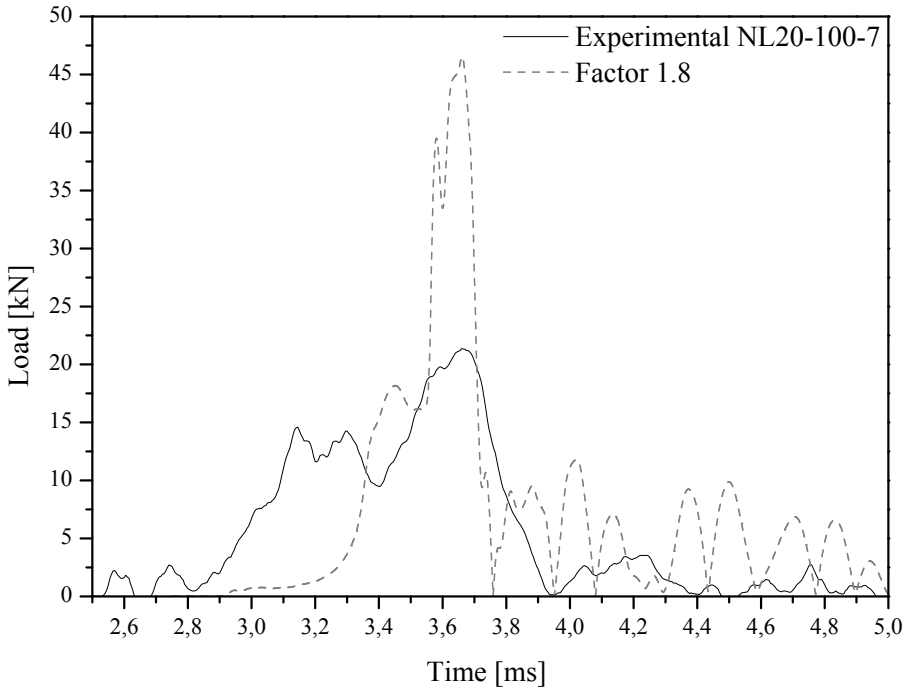

Figure 9.7: Comparison between experimental and FEM analysis of the force transducer measurements using a multiplicative factor of 1.8 (specimen NL20-100-7).

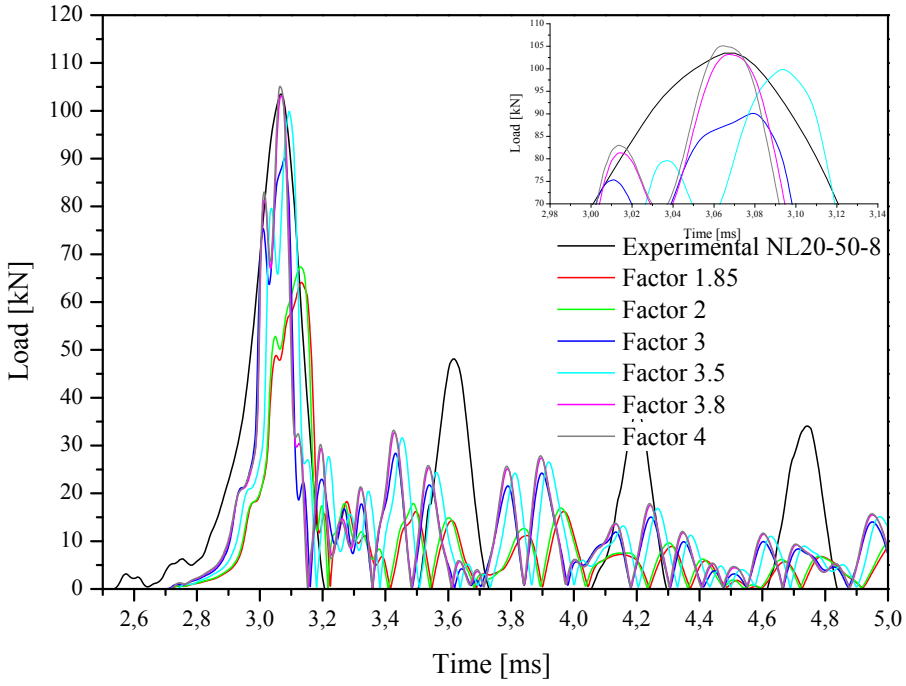

Figure 9.8: Comparison between experimental and FEM analysis of the force transducer measurements using different multiplicative factors (specimen NL20-50-8).

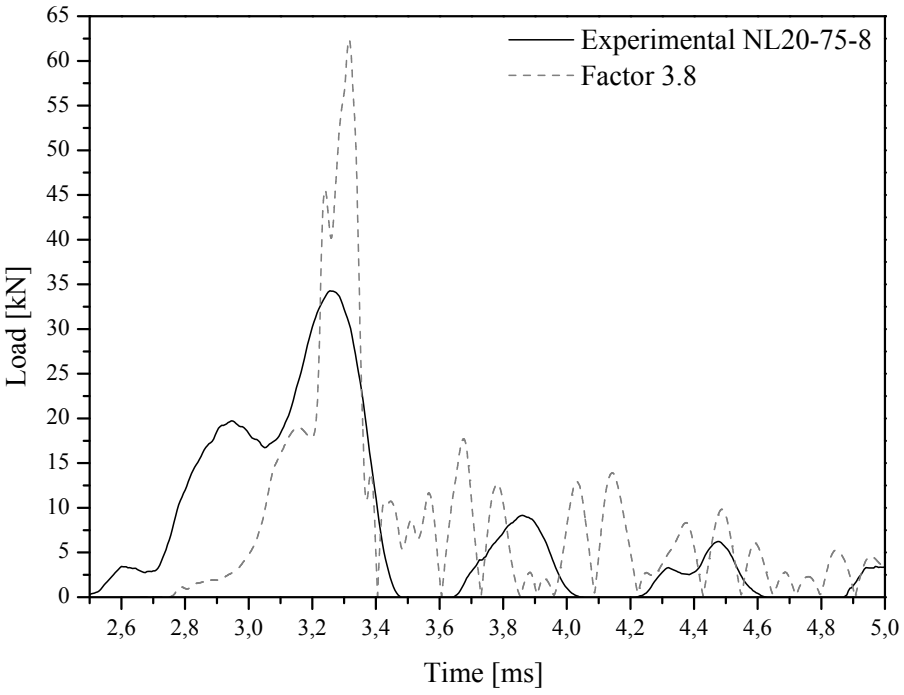

Figure 9.9: Comparison between experimental and FEM analysis of the force transducer measurements using a multiplicative factor of 3.8 (specimen NL20-75-8).

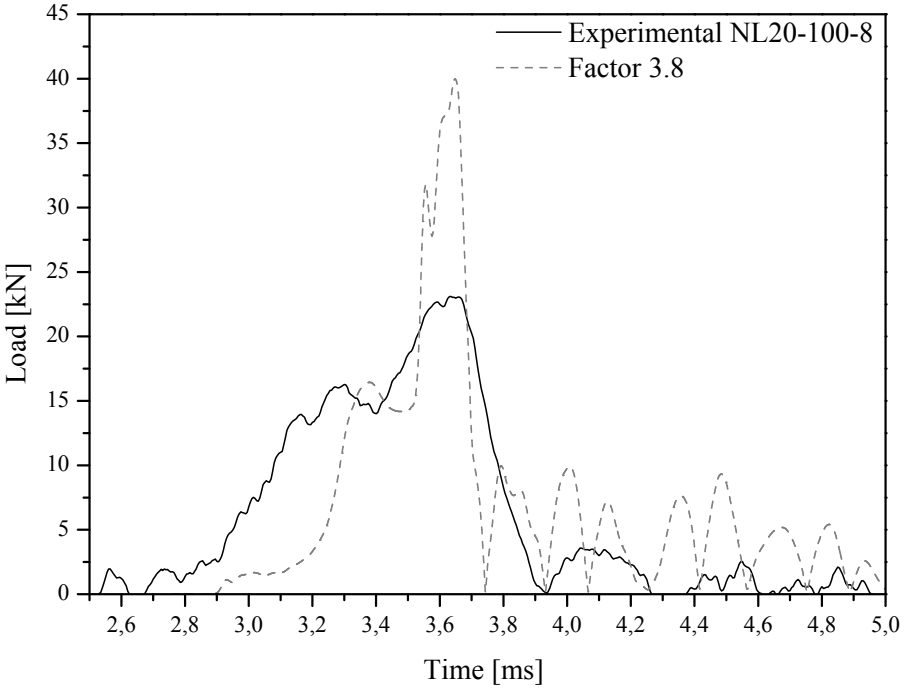

Figure 9.10: Comparison between experimental and FEM analysis of the force transducer measurements using a multiplicative factor of 3.8 (specimen NL20-100-8).

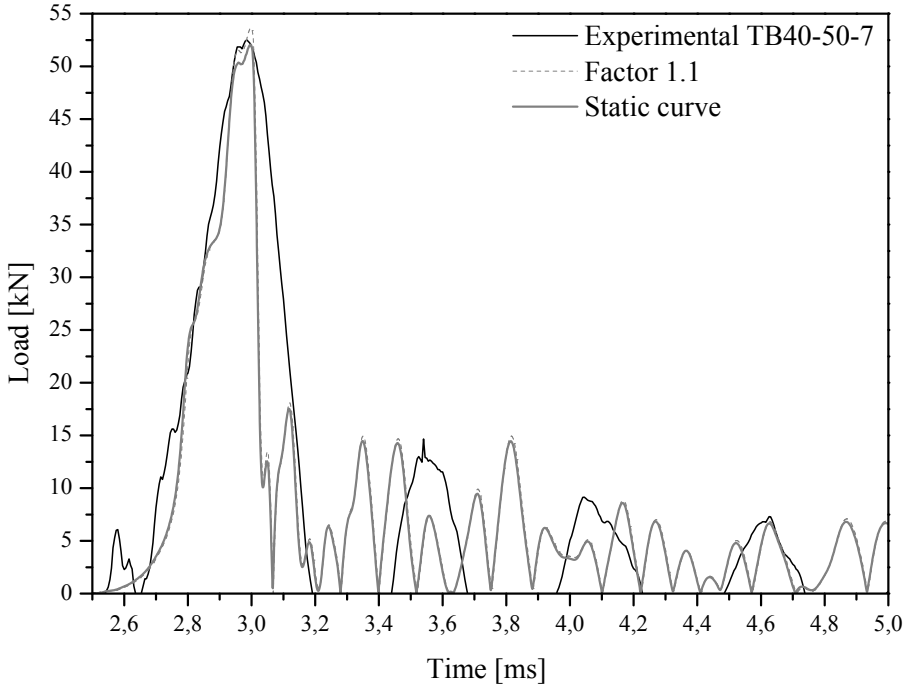

Figure 9.11: Comparison between experimental and FEM analysis of the force transducer measurements using a multiplicative factor of 1.1 and the static curve (specimen TB40-50-7).

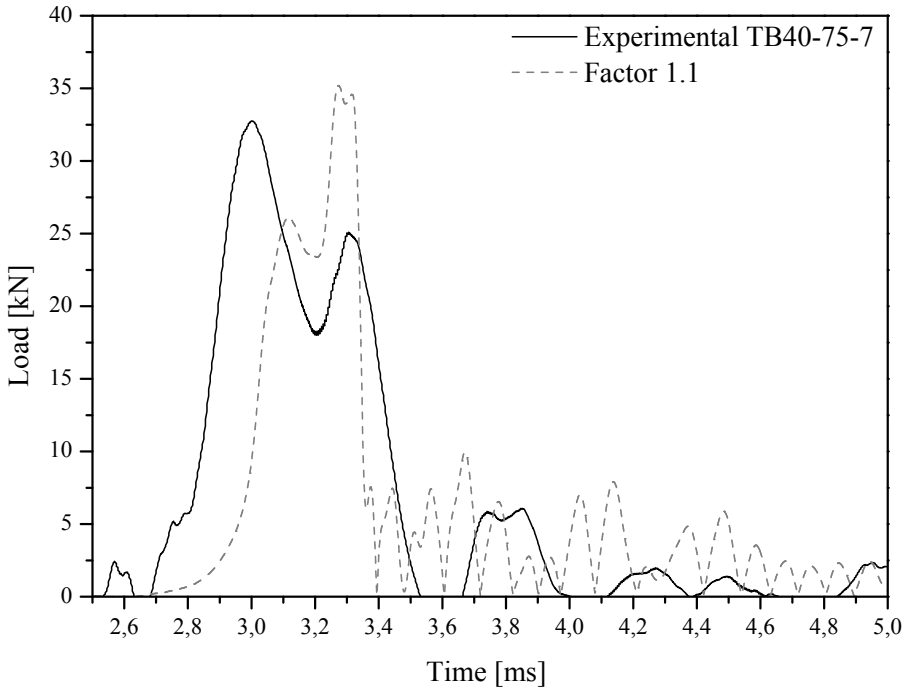

Figure 9.12: Comparison between experimental and FEM analysis of the force transducer measurements using a multiplicative factor of 1.1 (specimen TB40-75-7).

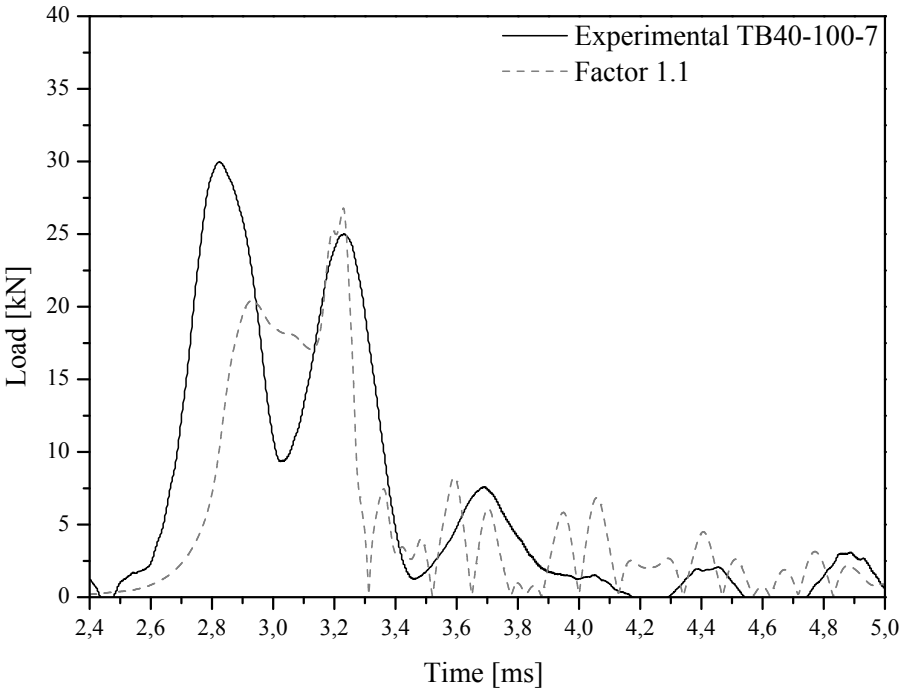

Figure 9.13: Comparison between experimental and FEM analysis of the force transducer measurements using a multiplicative factor of 1.1 (specimen TB40-100-7).

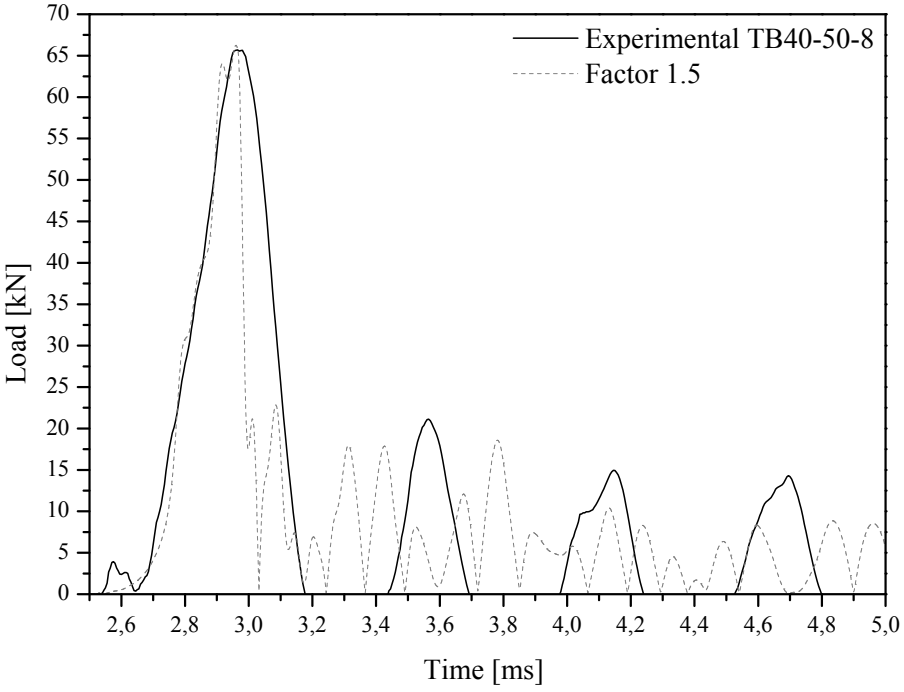

Figure 9.14: Comparison between experimental and FEM analysis of the force transducer measurements using a multiplicative factor of 1.5 (specimen TB40-50-8).

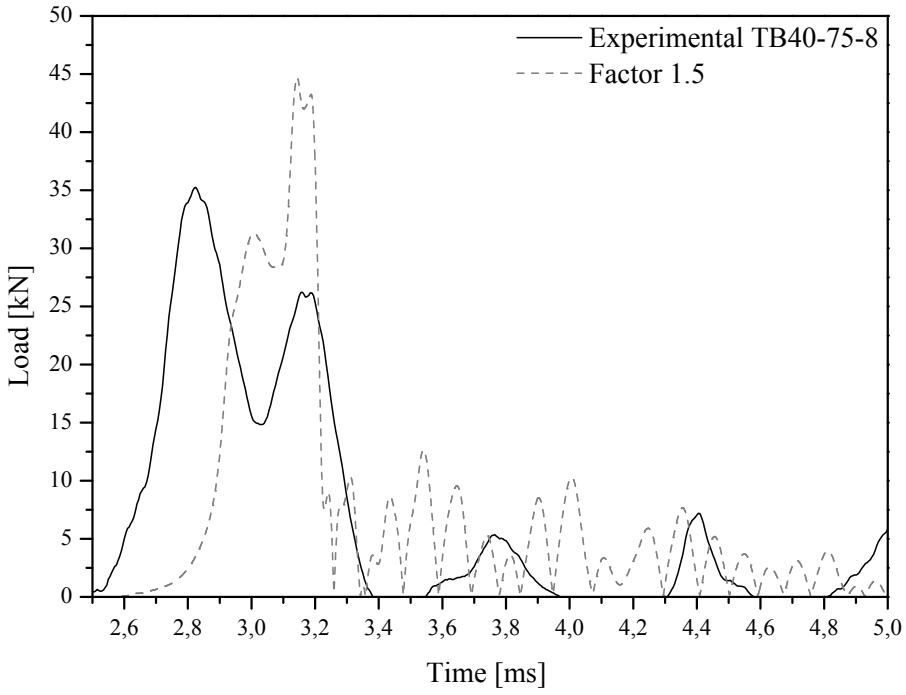

Figure 9.15: Comparison between experimental and FEM analysis of the force transducer measurements using a multiplicative factor of 1.5 (specimen TB40-75-8).

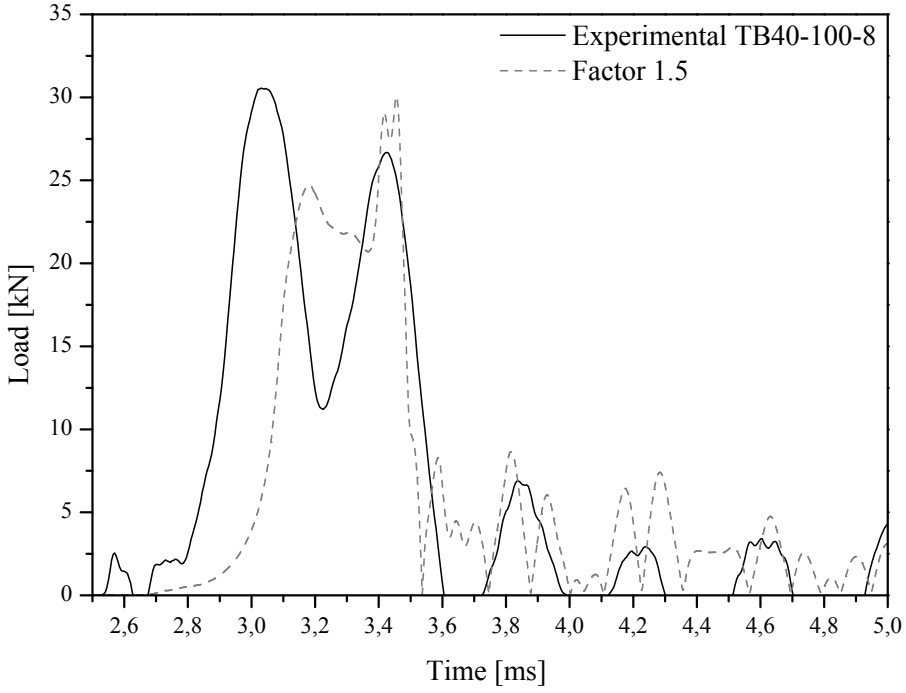

Figure 9.16: Comparison between experimental and FEM analysis of the force transducer measurements using a multiplicative factor of 1.5 (specimen TB40-100-8).

MAC specimens with 7 and 8 g of C4, respectively. In terms of time duration (width) of the first peak the numerical results slightly underestimate the experimental results.

In terms of the TB40 MAC compound specimens tested with 7 and 8 g of C4, a good agreement was also observed between the experimental and numerical results in terms of the force transducer measurements, as can be seen from the results in figures 9.11 and 9.14. Maximum load peak agreement between experimental and numerical was obtained for multiplicative factors of 1.10 and 1.50 for TB40 MAC specimens with 7 and 8 g of C4, respectively. Lower multiplicative factors were found for the denser specimens. The numerical results also slightly underestimate the experimental results in terms of time duration (width) of the first peak.

The results in figures 9.6 and 9.7 for NL20 with 7 g of C4, figures 9.12 and 9.13 for TB40 with 7 g of C4, figures 9.9 and 9.10 for NL20 with 8 g of C4 and figures 9.15 and 9.16 for TB40 with 8 g of C4 correspond to the comparison between experimental and numerical results, performed with longer specimens, using the multiplicative factor found to be the most accurate to model MAC behaviour (width the 50 mm specimens). The not so good agreement between experimental and numerical curves that can be observed in some of these results is most probably due to bending that occurred in experimental tests with longer specimens, leading to lower loads registered in the force transducer. If bending did not occur, values similar to the ones found in the numerical analysis in terms of load peak, would possibly have been registered by the force transducer.

As a conclusion, the observations from experimental results were compared with numerical results, and the multiplicative factors used for the numerical simulation that best suited the experimental results were chosen to be the ones listed in table 9.3. Consequently, the input parameters in `*Mat_Honeycomb` are presented in table 9.4. $\bar{E}$ is the compressive modulus, E^* is the Young modulus affected by the multiplicative factor, E_d is the Young modulus in densification and ν_d is the Poisson ratio.

Table 9.3: Multiplicative factors used for the numerical simulation that best suited the experimental results for both NL20 and TB40 with 7 and 8 g of C4.

MAC compound	**Mass of explosive** [g]	**Multiplicative factor**
NL20	7	1.80
	8	3.80
TB40	7	1.10
	8	1.50

Table 9.4: NL20 and TB40 mechanical properties ($\bar{E}$ is the compressive Young modulus, E^* is the elastic modulus affected by the multiplicative factor, E_d is the Young modulus in densification and ν_d is the Poisson ratio in densification [TR 2011, Gameiro and Cirne 2007]).

Material	**Density** [kg/m^3]	$\bar{E}$ [MPa]	E^* [MPa]	E_d [GPa]	ν_d [–]
NL20	200	6.0	10.8 (7 g C4) 22.8 (8 g C4)	9.0	0.30
TB40	440	8.5	9.35 (7 g C4) 12.8 (8 g C4)	9.0	0.30

9.4 Discussion

The experimental values that were obtained, such as the displacement, load and impulse, will now be compared with the ones determined from the numerical model. The experimental and numerical comparison of loads registered by the force transducer are represented in figures 9.17 to 9.20. As can be seen from these results, quite good agreement was achieved between experimental and numerical approaches in terms of magnitude of the load peak for the MAC specimens (height 50 mm). However, the time duration (width) obtained from the FEM model is slightly underestimated when compared to the experimental load-time profile. As the height of the specimen increases this correlation tends to be less acceptable since the numerical curves overestimate the experimental results. As was explained previously, the occurrence of bending in some specimens may have led to a decrease in the measured load values. Therefore, the mismatch between the FEM and the experimental results for this specific case is most probably due to the dynamic geometrical instability (buckling) of longer specimens.

In terms of impulse, the numerical results also follow quite closely the experimental behaviour as can be seen from the results in figures 9.21 and 9.22. However, slightly lower values of maximum impulse were obtained in the numerical results. This behaviour was previously observed in the simulations done in the multiplicative factor analysis. Since the numerical impulse was determined with an integration of the first (numerical) load peak, in which an underestimation was observed (in terms of peak width) compared to the experimental load peak, the numerical impulses are lower than the experimental. The experimental transmitted impulse values, I_p, determined from the laser measurements and the linear oscillator theory (see table 6.1) are lower and therefore closer to the ones determined numerically.

In general terms, comparing numerical and experimental results, it can be said that the material model implemented suits the dynamic behaviour of MAC compounds.

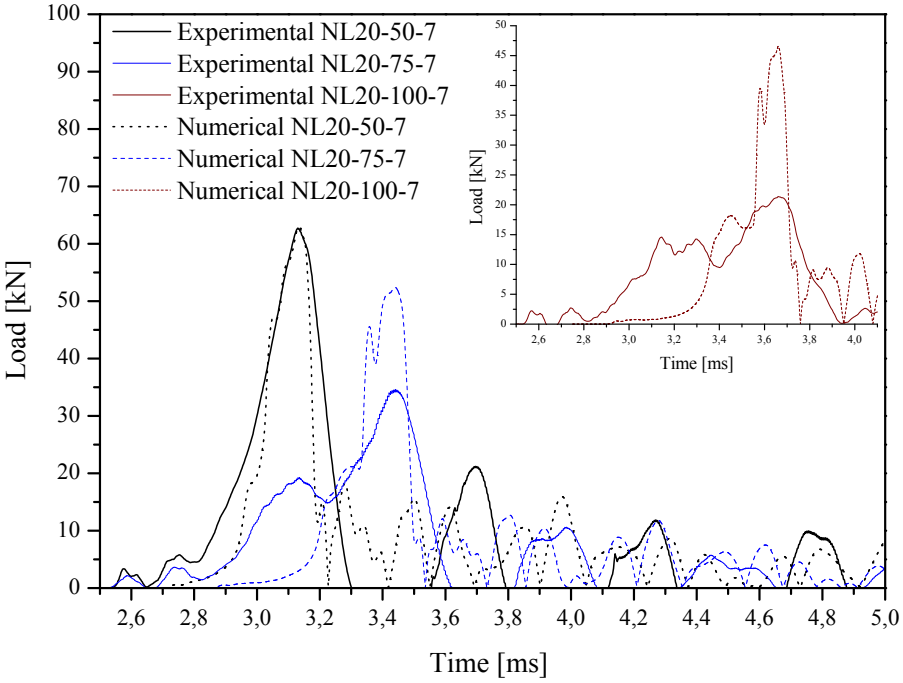

Figure 9.17: Load-time profiles for NL20 specimens (7 g of C4): comparison between experimental observations and numerical results.

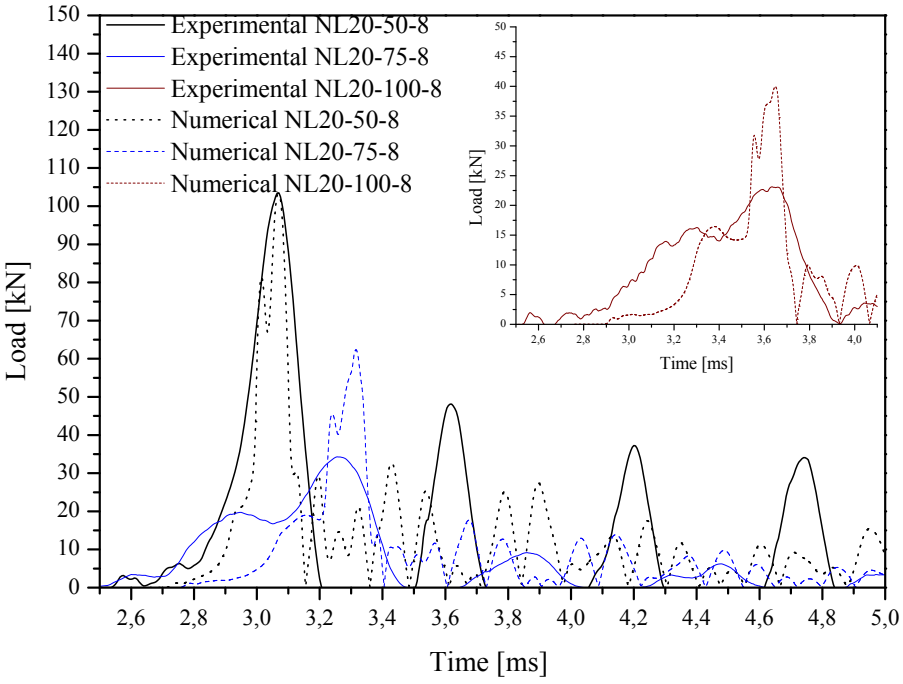

Figure 9.18: Load-time profiles for NL20 specimens (8 g of C4): comparison between experimental observations and numerical results.

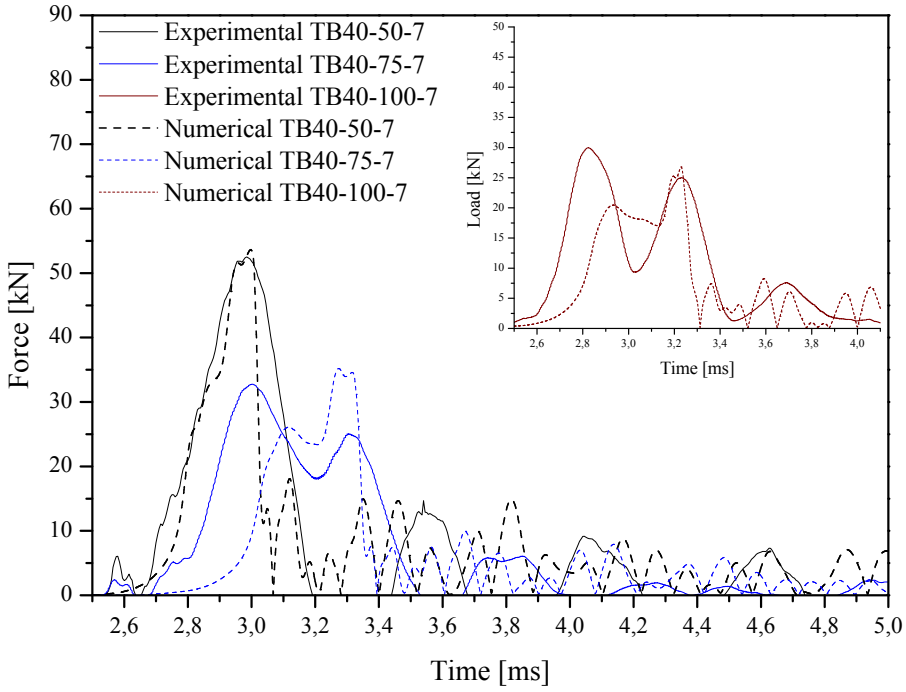

Figure 9.19: Load-time profiles for TB40 specimens (7 g of C4): comparison between experimental observations and numerical results.

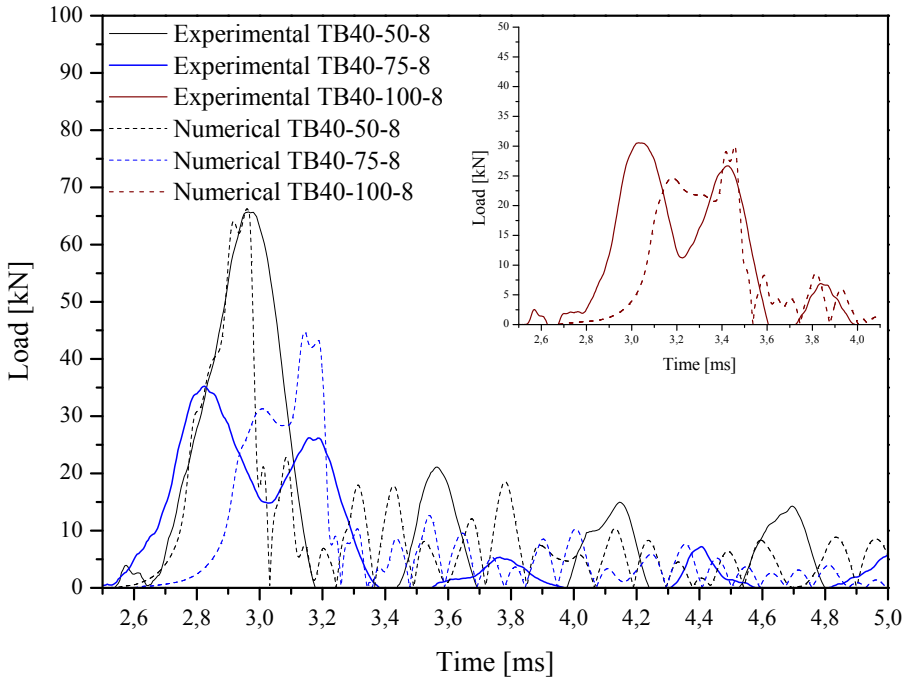

Figure 9.20: Load-time profiles for TB40 specimens (8 g of C4): comparison between experimental observations and numerical results.

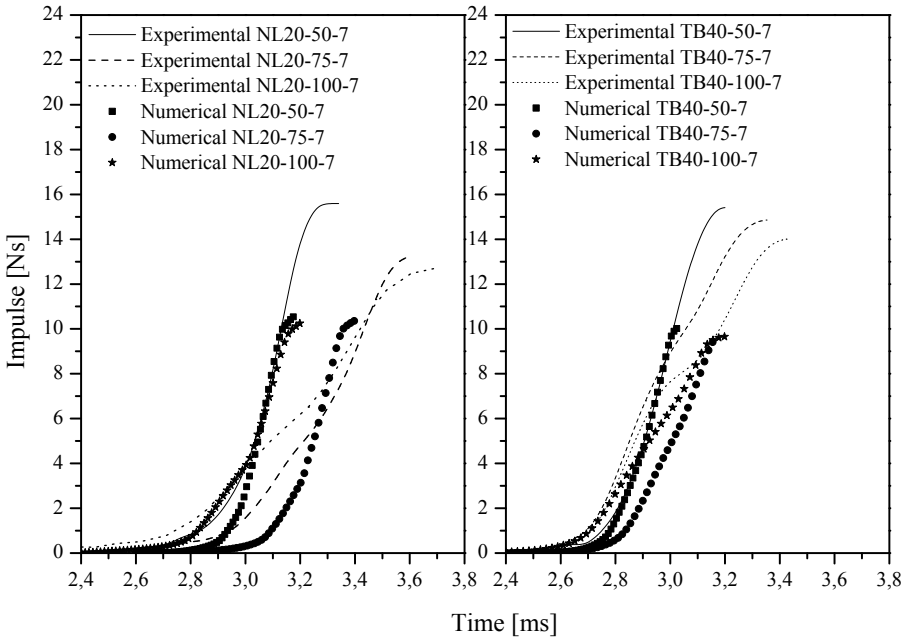

Figure 9.21: Impulse-time profiles (7 g of C4): comparison between experimental and numerical results.

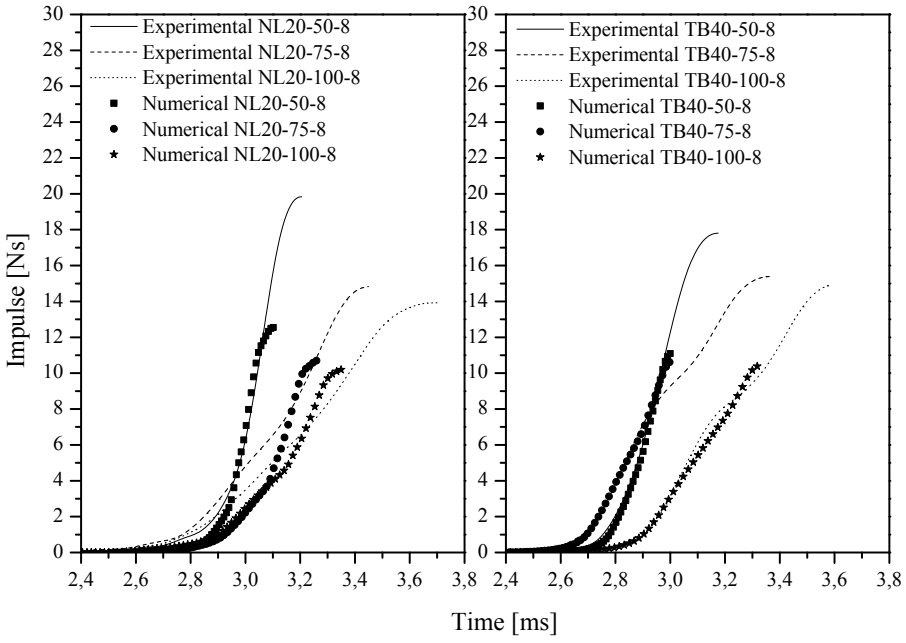

Figure 9.22: Impulse-time profiles (8 g of C4): comparison between experimental and numerical results.

Chapter 10

Sandwich structures

The numerical model developed and implemented to test the efficiency of MAC compound cores in a sandwich structure protection system is described in this chapter. Experimental results previously presented are compared with the numerical results in order to validate the FEM model.

10.1 Introduction

Experimental results on the characterisation of sandwich structures incorporating a MAC compound core were presented and discussed in chapter 7. 5754-H22 aluminium alloy face sheets were used with constant thickness. Only the core thicknesses varied. These structures were fixed on the 4-cable ballistic pendulum and subjected to blast-waves originated from the detonation of 30 g of C4 at a constant stand-off distance of 300 mm. An adaptation to the finite element model (FEM) presented in chapter 9 is described in this chapter, that consists on making the FEM model suitable to test sandwich structures. Registered results were the translational movement (displacement) of the ballistic pendulum and the deflection values of the front and back face sheets.

10.2 Model description and material models

The FEM model described in this section was developed and used to simulate the non-uniform and non-linear dynamic behaviour of the sandwich structures when impacted by blast loading, using LS-Dyna^{TM}. The behaviour of the model was divided in two phases (see chapter 9). However, in the adapted model version, the first phase corresponds to the interaction of the blast-wave with the sandwich structure and consequent deformation. The second part corresponds to the oscillation phase of the ballistic pendulum.

The geometrical model is shown in figure 10.1. In the first phase, the properties of steel (see table 9.2) are attributed to the main support parts of the ballis-

tic pendulum, that is, to (a) the I-beam, (b) the fixing nuts, (c) the I-shaped front plate, (d) the solid-plate, (e) the threaded spacers and (f) the clamping parts. The properties of the suspension cables (g) are listed in table 9.2. In addition, the position of the high explosive is represented by (h). However, as shall be seen in the following sections, the explosive was not modelled with finite elements. A different approach was used instead. The material model used for the steel components was `*Mat_Plastic_kinematic` [DS 2009]. In the specific case of the I-beam, a different value of density was used ($\rho = 1.053 \times 10^{-5}$ kg/mm^3) to compensate for the fact that the counterweights used in the experimental setup were not modelled.

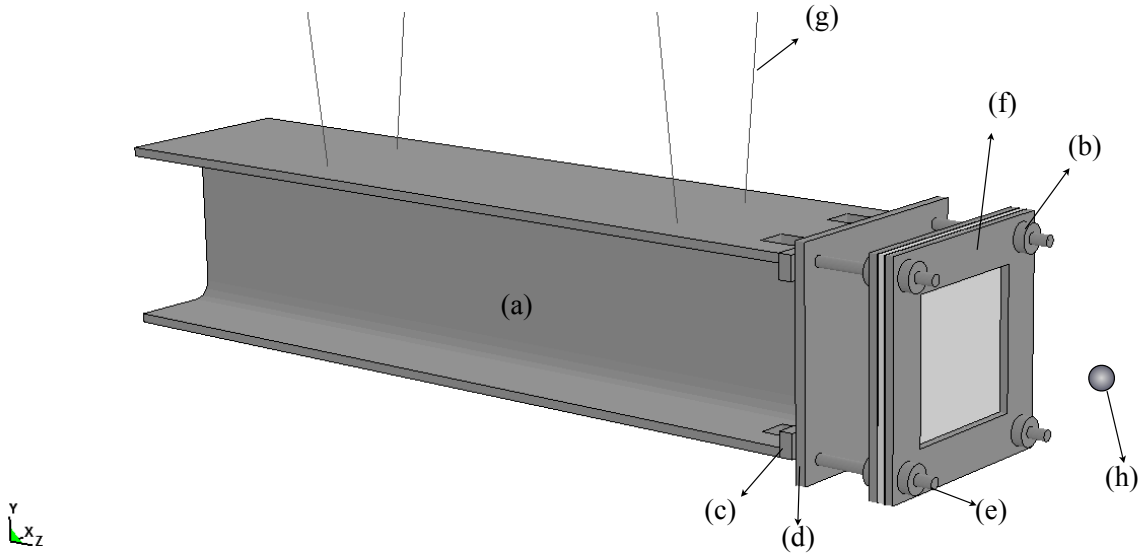

Figure 10.1: FEM model components of the ballistic pendulum adapted for the analysis of the sandwich structures.

10.2.1 Boundary conditions and contacts

Boundary conditions were defined for the cables that support the pendulum, where the top nodes of the beam elements have all their degrees-of-freedom (DOF) constrained, while the bottom nodes were merged with nodes from the solid elements. Constrained nodal sets were used to apply boundary conditions. Different types of contacts were considered. The clamping effect of the structure which locks the movement of the boundaries of the target was achieved by setting the following contacts between the components of the pendulum. Contact type `*Contact_Tied_Surface_To_Surface` was used to tie the aluminium sheets to the core. The aluminium face sheets correspond to the master, whereas the core is the slave for the contact algorithm. As stated before (see section 7.3) no significant debonding between face sheets and the core was observed in the experimental tests. Therefore, this option for contact type in the sandwich is considered to be adequate. This contact was also used to fix the I-beam to the support used for the sandwich structure. Contact type `*Contact_Tied_Nodes_To_Surface`

tied the nodes of the beam (the beam's profile) to the surface of the I-shaped part that supports the complete sandwich support system. A two-way contact was used to model the contact between parts that during impact will eventually be in contact but are not (initially) tied (`*Contact_Automatic_Surface_To_Surface`). These are:

1. The holes on the sandwich structure and the threaded spacers;
2. The holes on the clamping frames and the threaded spacers;
3. The nuts and the threaded spacers;
4. The nuts and the clamping frames;
5. The clamping system and the sandwich structure.

10.2.2 Modelling the explosive

The detonation of the explosive occurs in the first phase of the process. The resulting blast-wave expands uniformly and impacts the target. LS-Dyna^{TM} provides a blast function for the application of pressure loads due to explosive reactions from conventional weapons (function `*Load_Blast`) [DK 2012]. The implementation of this function is based on a report by Randers-Pherson and Bannister published in 1997 [Randers-Pherson and Bannister 1997]. The incorporation of the CONWEP (*Conventional Weapons* [Hyde 1993]) blast model into DYNA2D and DYNA3D is presented in this report. This model is adequate to be used, for example, in engineering studies of vehicle response due to the blast from land mines [DK 2012] and accounts for the angle of incidence of the blast-wave by combining the reflected pressure (normal incidence) and the incident pressure (side-on incidence) value. However, it does not account for shadowing by intervening objects or for confinement effects. The CONWEP blast loading equation can be defined as [Randers-Pherson and Bannister 1997]

$$P_{\text{load}} = P_{\text{r}} \cos^2\theta + P_{\text{i}}(1 + \cos^2\theta - 2\cos\theta), \tag{10.1}$$

where θ is the angle of incidence, defined by the tangent to the wave front and the target's surface, P_{i} is the incident pressure and P_{r} the reflected pressure. If the explosive is not facing the target's surface ($\cos\theta < 0$) the pressure load becomes

$$P_{\text{load}} = P_{\text{i}}. \tag{10.2}$$

This blast function can be applied in ground burst explosions and free air detonation of spherical charges. In this study the authors have restricted the analysis to the free air detonation of a spherical charge. The algorithms implemented in the CONWEP loading function provide the user parameters such as time of arrival, t_{a}, peak pressure, P_{b}, and duration and decay of the incident pressure (see figure 2.2). Values of incident pressure in the front face panel were determined by calculating the nodal forces on a

plate with rigid material properties (and the dimensions of the sandwich structure), divided by the exposed area of the rigid structure. This approach is considered to be reasonable if the loading is completed before the maximum deformation of the structure is reached. The incident pressure profile is shown in figure 10.2. The pressure-time history of a blast-wave can be characterised by its peak blast pressure which, in this case, is approximately 4 MPa, and the time of arrival of the blast-wave ($t_a \approx 0.14$ ms), after which the pressure then drops exponentially to the pre-shock pressure level.

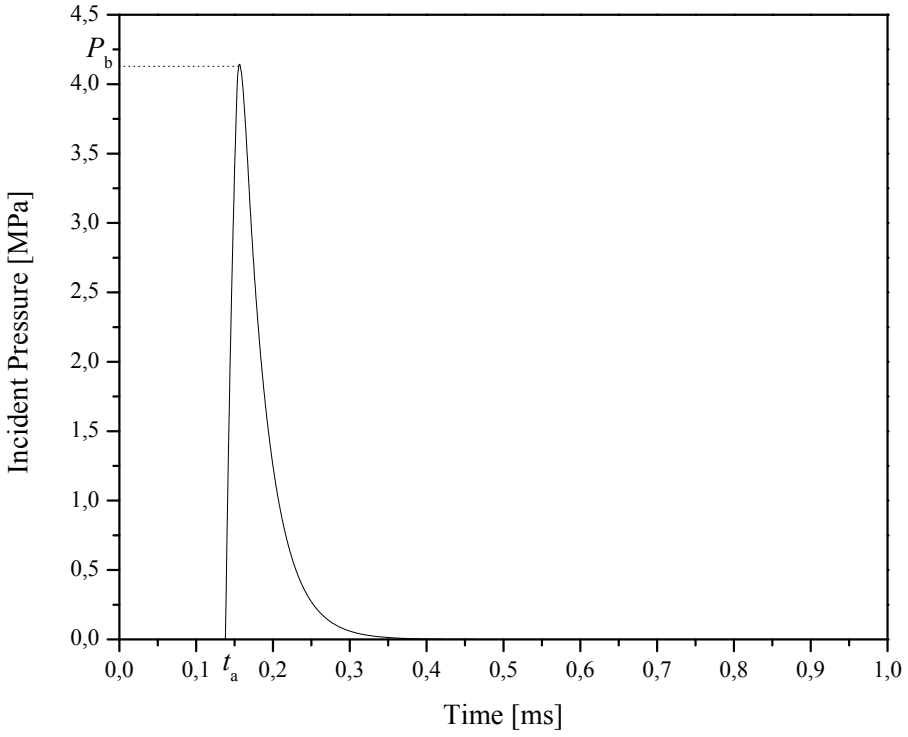

Figure 10.2: Pressure-time history of a blast-wave from the detonation of 30 g of C4 at 300 mm stand-off distance.

In the `*Load_Blast` function, the mass of the explosive is defined as an equivalent mass of TNT. 30 g of C4 were used at a stand-off distance of 300 mm, which corresponds to a TNT equivalent of 36 g [Yandzio and Gough 1999,RE 2012]. The input parameters for this function are:

- The equivalent mass of TNT, $\bar{w}_T$;
- The coordinates of the explosive, x_e, y_e and z_e;
- The time of birth of the explosion (initial time of the explosion), t_b;
- The type of burst which, in this case, is a spherical charge at least one charge length away from the impact surface, S.

These parameters have the values listed in table 10.1.

Table 10.1: `*Load_Blast` function assigned parameters.

Parameters	**Value**
$\bar{w}_{\mathrm{T}}$	0.036 kg
$(x_{\mathrm{e}},\, y_{\mathrm{e}},\, z_{\mathrm{e}})$	$(0, 0, 300)$ [mm]
t_{b}	0 s
S	2 (spherical charge)

10.2.3 Multiplicative factor

From what was described in section 9.3.2 and from the literature [Gameiro *et al.* 2005] it was experimentally proved that cork agglomerates are materials whose behaviour is not fully independent of the strain rate. Three static $\sigma - \varepsilon$ curves were obtained for three different specimens with the exact same characteristics (for both NL20 and TB40 MAC specimens). An average of these three curves was used in the numerical model, in the form of true stress-true strain. An extensive study was done to determine which multiplicative factor best suited the mechanical behaviour of cork, that is, which factor must the $\sigma - \varepsilon$ curve be multiplied by in order to accurately model the behaviour of the studied MAC compounds. The simulation was performed for several multiplicative factors and the loads registered by the force transducer were compared with the numerical results. Consequently, an optimum multiplicative factor was determined and applied. The multiplicative factors to be used in the stress-strain curves of the MAC compounds in the numerical simulation were 1.80 and 3.8 for NL20 with 7 and 8 g of C4, respectively. TB40 MAC compound led to multiplicative factors of 1.10 and 1.50 for 7 and 8 g of C4, respectively (see table 9.3). Once the multiplicative factors were determined and the numerical results were proved to be in agreement with the experimental observations, the strain rate, $\dot{\varepsilon}$, could be determined. In the analysis of the cylindrical specimens, the values of axial strain rate for the cylindrical MAC compound specimens were numerically determined. The nodes selected along the length of the cylindrical specimens are represented in figure 10.3. NL20 and TB40 MAC compounds when loaded with 8 g of C4 induced a strain rate of $\dot{\varepsilon} = 10^4$ s^{-1} as can be seen from the results in figures 10.4 (a) and (b). An estimation of the strain rate in the direction of the impact can be obtained with the relation [Jones 1989]

$$\dot{\varepsilon} = \frac{\varepsilon}{\Delta t} = \frac{\Delta L}{L}\frac{1}{\Delta t} = \frac{c}{L}, \tag{10.3}$$

where L is the thickness of the core of the sandwich and c is the sound speed in cork. The sound speed in cork is reported to be $c \approx 366$ m/s [Young 2010], which leads to a strain rate $\dot{\varepsilon}$ in the order of magnitude of 10^4 s^{-1} if an average 20 mm core of the sandwich sandwich plate is considered. Identical orders of magnitude were determined from the experiments on the cylindrical MAC compounds loaded with 8 g of C4 and

from the analytical estimation given by equation 10.3. Hence, in the numerical analysis of sandwich structures with a MAC compound core, the multiplicative factors that were used correspond to the multiplicative factor determined for 8 g of C4, that is, multiplicative factors of 3.8 and 1.5 for the NL20 and TB40 MAC, respectively.

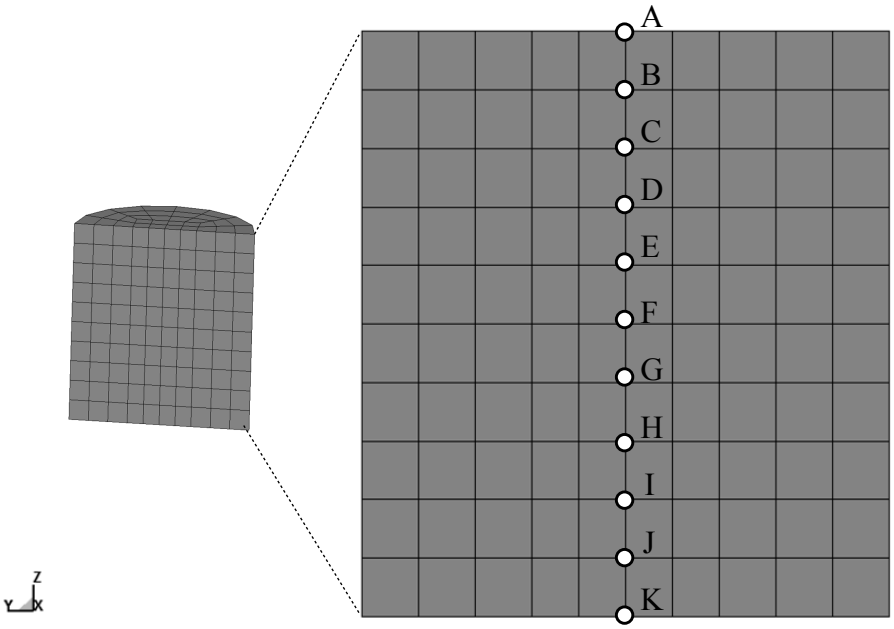

Figure 10.3: Nodes used for the FEM axial strain rate analysis in cylindrical MAC compound specimens.

10.2.4 Mesh refinement

The deformations experienced by the sandwich structure subjected to blast-waves proved to be highly dependent on the mesh refinement. Thus, a mesh convergence study was made. Mesh convergence was addressed with a series of calculations in which the sizes of the sandwich structure elements were subsequently reduced. The direct impact area is the area directly exposed to the blast load, as can be seen in figure 10.5. The area inside the white square line corresponds to the area that it is effectively impacted by the blast-wave. Elements on the boundary are covered by the clamping frames. All the finite elements used in this analysis are 8-node solid hexahedra, exception made for the cable elements. The finite element formulation used for all parts in the mesh convergence study, including the core material and the aluminium face sheets, is constant stress solid element. This first step in the analysis was to optimise the mesh division in the in-plane location (impact plane). The refinements referred are described in table 10.2 (finite element discretisation of the directly impacted area). The number of elements through thickness was kept constant and equal to 6. Only the sandwich structure with a core thickness of 20 mm was studied since this was only an in plane mesh convergence study. Three nodes were selected to analyse

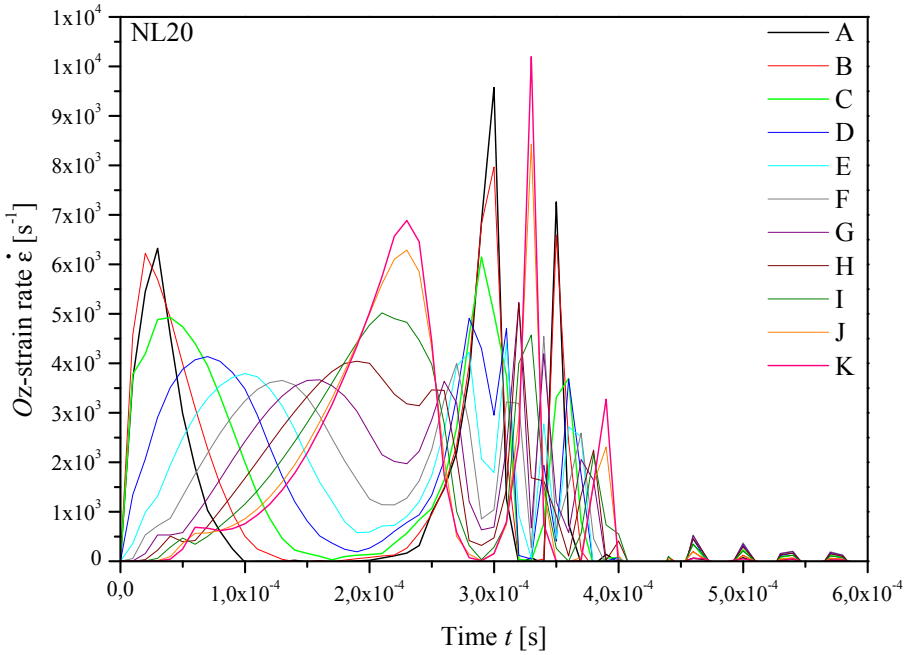

(a)

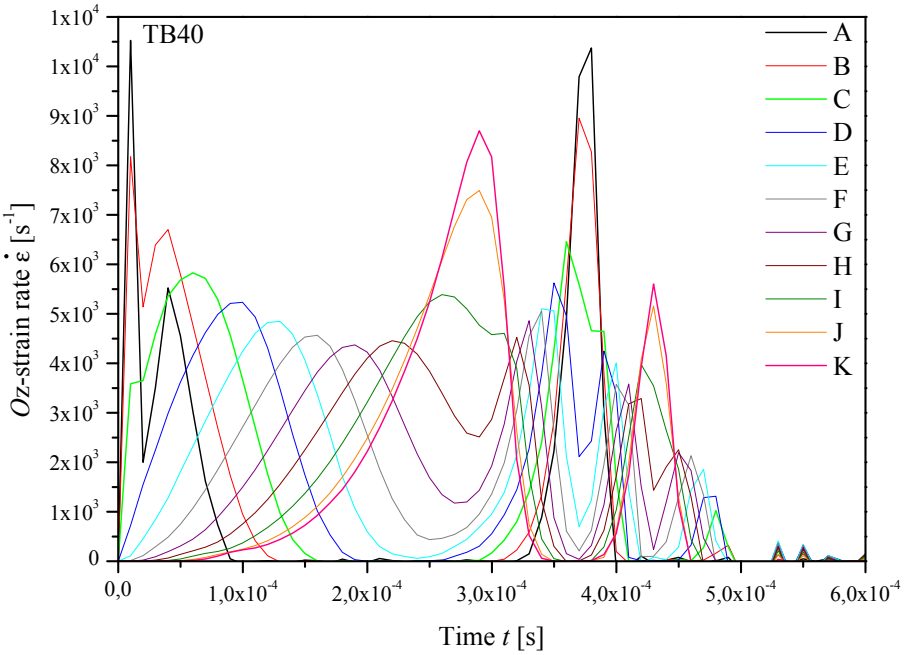

(b)

Figure 10.4: (a) Strain rate values ($\dot{\varepsilon}$) in nodes selected along the length of the cylindrical NL20 specimen and (b) strain rate values ($\dot{\varepsilon}$) in nodes selected along the length of the cylindrical TB40 specimen.

the displacement values and the influence of the mesh size: the first and second nodes placed on the centre of the impacted face for both the back and the front aluminium sheets and another one on the boundary between the impacted area and the protected area. These nodes are shown in figure 10.5 (except the central node of the back aluminium face). Von Mises stress values were also analysed and the elements used to obtain von Mises stresses are the ones highlighted in black in figure 10.5 (adjacent to nodes A, B and C). From this point forward these elements will be referred as elements A, B and C. Plots of the convergence analysis are presented in figures 10.6 and 10.7. These are normalised to the last value obtained (*i.e* divided by the value obtained in the 60×60 mesh division for Oxy plane case). The referred values of Oz-displacement and von Mises stress correspond to the maximum measured value in the simulation.

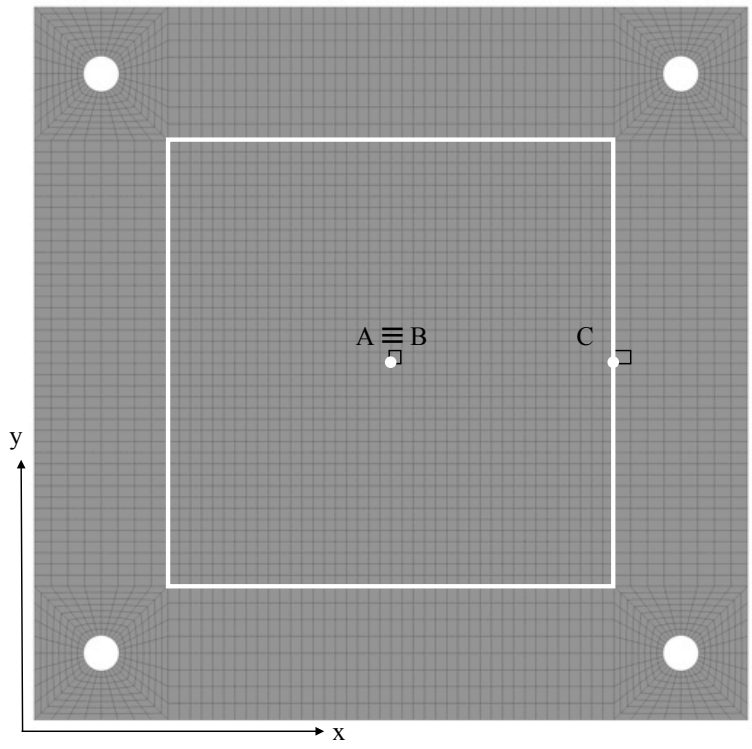

Figure 10.5: Mesh structure used in the mesh convergence study. The area inside the white square line is to the area effectively impacted by the blast-wave.

When increasing the refinement of a specific mesh it becomes noticeable that Oz-displacement has a slight tendency to increase (see figure 10.6). The error was calculated with the relation

$$e\ [\%] = \frac{v_c - v_{(60\times60)}}{v_c} \times 100, \tag{10.4}$$

where v_c is the value of the variable to be analysed (Oz-displacement or von Mises stress) to which the error is being determined and $v_{60\times60}$ is the value obtained for the most refined mesh. The criterium to choose a specific mesh was then related to the relative error associated with these values. A value lower than 8% in error was

Table 10.2: Mesh sizes on the impacted area (signatures C and FC correspond to core and face sheets, respectively).

Mesh	**DOF (C)**	**Elem. (C)**	**Nodes (C)**	**Elem. (FC)**	**Nodes (FC)**
A (20-20-6)	37152	12384	15379	4128	6591
B (30-30-6)	51912	17304	21259	5768	9111
C (40-40-6)	70272	23424	28539	7808	12231
D (50-50-6)	92232	30744	37219	10248	15951
E (60-60-6)	117792	39264	47299	13088	20271

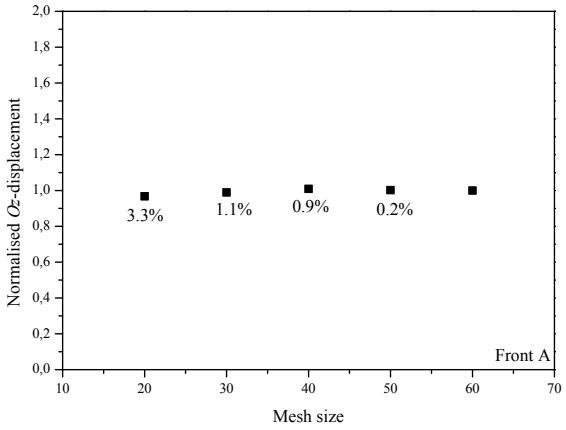

(a) Node A.

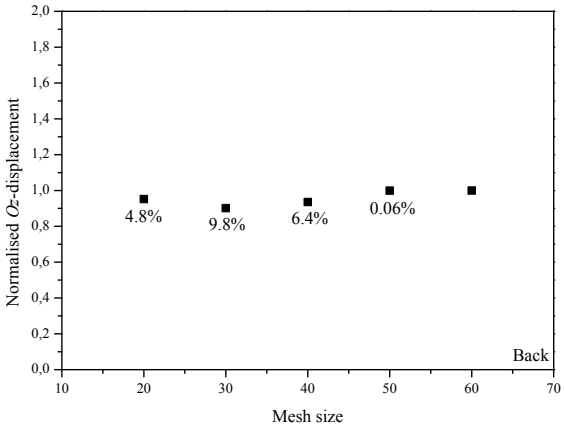

(b) Node B.

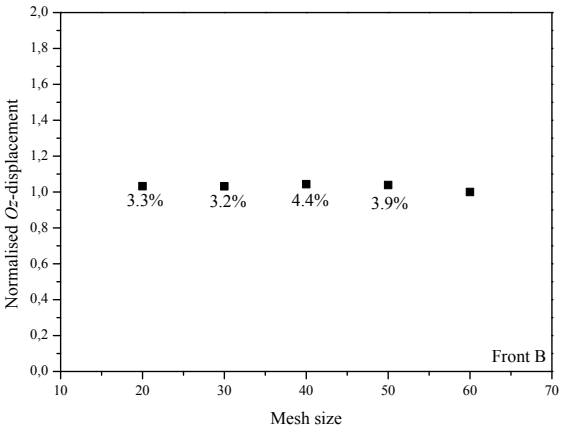

(c) Node C.

Figure 10.6: Influence of the mesh size on the FEM results: Oz-displacement of the (a) front face sheet central node (node A), (b) back face sheet central node (node B) and (c) front face sheet border node (node C) plotted against the mesh size along the plane Oxy .

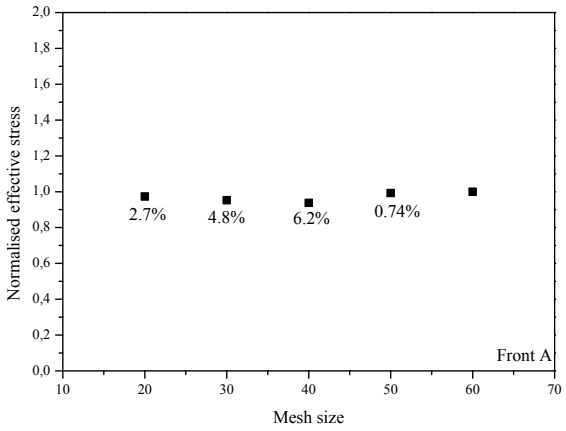

(a) Element A.

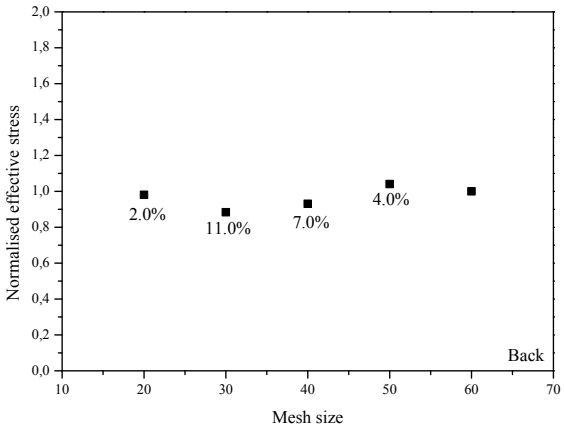

(b) Element B.

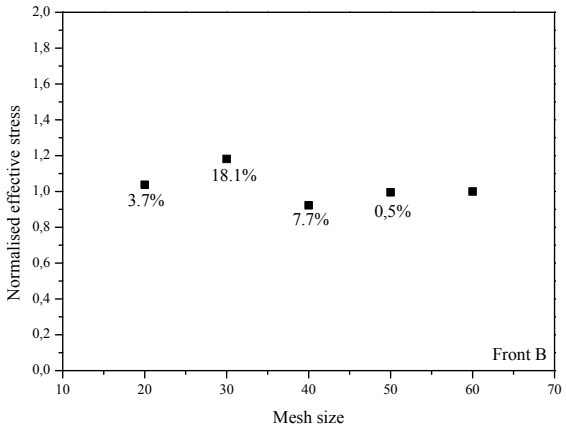

(c) Element C.

Figure 10.7: Influence of the mesh size on the FEM results: von Mises stress value of the (a) front face sheet central element (element A), (b) back face sheet central element (element B) and (c) front face sheet border element (element C) plotted against the mesh size along the plane *Oxy*.

considered acceptable. From the Oz-displacement values (see figures 10.6(a) to (c)) it was guaranteed that for all the measures the error was lower than 8%. Thus, the mesh in which all measures respect this constrain is mesh C (see table 10.2). The same conclusion can be derived from the analysis of the von Mises stresses (see figures 10.7(d) to (f)). Consequently, mesh C was adopted for all analysis.

Mesh C was then used to evaluate the effect of increasing number of elements along thickness of the MAC compound core. In table 10.3 the refinement studied is presented. Once again, only the sandwich structure with a core thickness of 20 mm was studied. All other core thicknesses had their elements along the thickness of the core found by extrapolation from the results here obtained. Two core nodes located in the direction of the centre of the impacted area were selected to analyse the displacement values. These nodes — nodes A_c and B_c — are aligned with nodes A and B from the previous analysis (see figure 10.5). Elements A_c and B_c (adjacent to nodes A_c and B_c, respectively) were chosen to analyse the evolution of the von Mises stress.

Table 10.3: Through thickness mesh sizes.

Mesh	**Elem. (core thickness)**	**DOF (C)**	**Elem. (C)**	**Nodes (C)**
F	4	46848	15616	20385
G	5	58560	19520	24462
H	6	70272	23424	28539
I	7	81984	27328	32616
J	8	93696	31232	36693

Plots of the convergence analysis for the through thickness elements are presented in figure 10.8 and 10.9. Values are normalised to mesh J. From these results it is possible to see that mesh H is the best in terms of taking into account the influence of the number of elements through core thickness. Therefore, the final mesh size used in the FEM analysis is mesh C (see table 10.2), with 40×40 elements in the Oxy plane and 6 elements in the Oz direction.

The finite element formulation used for all parts in the previous mesh convergence studies, including the core material and the aluminium face sheets, was constant stress solid elements. Thus, one last convergence analysis was also performed concerning the element formulation used. The three types of elements that were considered in the analysis were: (i) constant stress solid element; (ii) fully integrated selective reduced solid element[1] and (iii) fully integrated quadratic 8 node element with nodal rotations. Constant stress solid elements are eight node solid elements with one integration point. Although fully integrated solids tend to be less stable when large deformations occur, two types of fully integrated elements were studied. The main characteristics associ-

[1]The selective reduced integrated solid element assumes that pressure is constant throughout the element to avoid pressure locking during nearly incompressible flow [DS 2009].

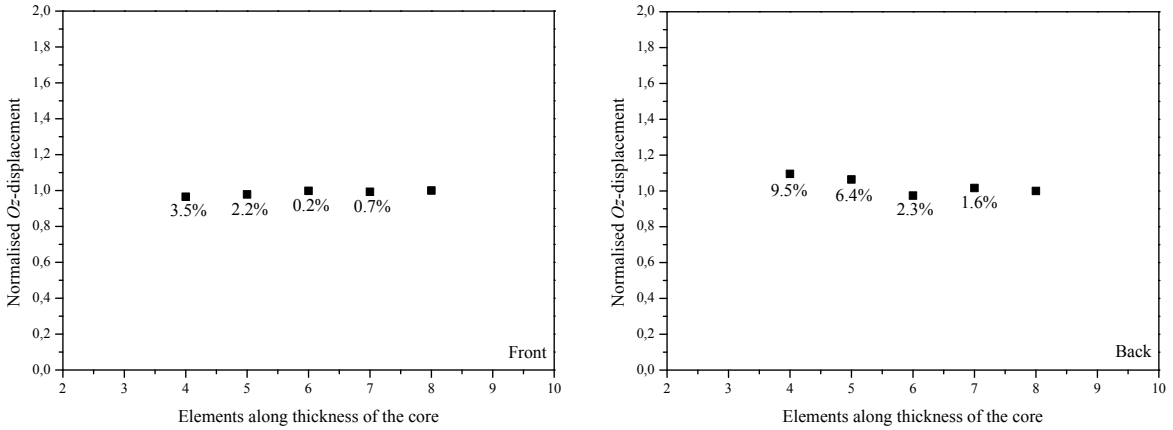

(a) Node A_c. (b) Node B_c.

Figure 10.8: Influence of the number of elements through thickness in the FEM results: Oz-displacement of the (a) front face central node (core, node A_c) and (b) back face central node (core, node B_c) plotted against mesh size through core thickness.

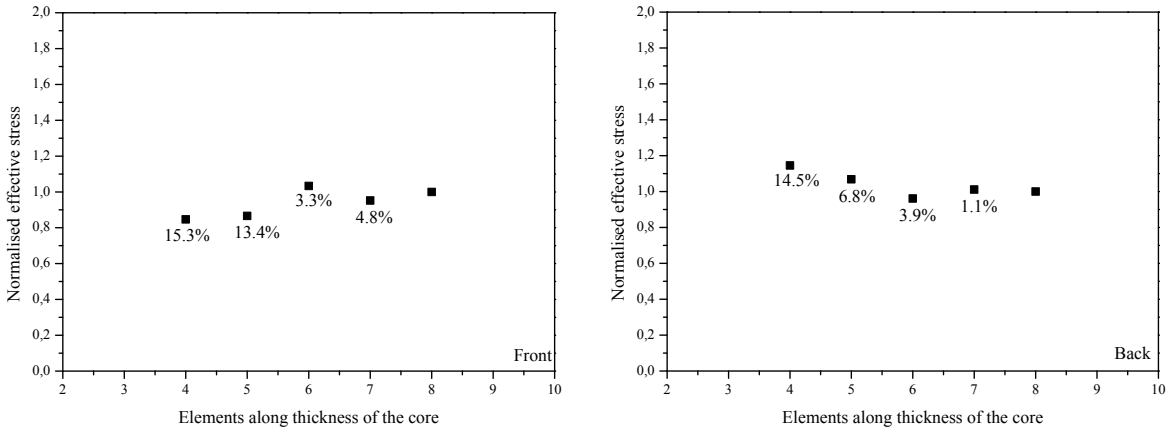

(a) Element A_c. (b) Element B_c.

Figure 10.9: Influence of the number of elements through thickness in the FEM results: von Mises stress value of the (a) front face central element (core, element A_c) and (b) back face central element (core, element B_c) plotted against mesh size through core thickness.

ated with fully integrated selective reduced solid elements are related to the fact that pressure is assumed to be constant throughout the element [DS 2009]. The last element formulation studied adds the rotations of the nodes. The results regarding the influence of the element formulation on the FEM results are shown in figures 10.10 and 10.11. It can be seen that the element formulation proved not to be very influent on the results. The 8% error criterium is no longer applicable (see figures 10.6 to 10.9). Thus, a different criteria was used to choose the best element formulation. Fully integrated quadratic 8 node element with nodal rotations was not chosen since the contribution from the rotations of the nodes in the inner part sandwich can be neglected. Additionally, even though its contribution can be neglected, rotations are considered in the calculations, which contributed to a considerable increase of the CPU time. Thus, the choice was between constants stress solid elements and fully integrated selective reduced solid elements. The difference in terms of CPU time comparing to constant stress solid elements proved to be insignificant (taking only in consideration the CPU time involved in the analysis from the impact phase) as it is shown in table 10.4. Consequently, fully integrated selective reduced solid was the element formulation chosen.

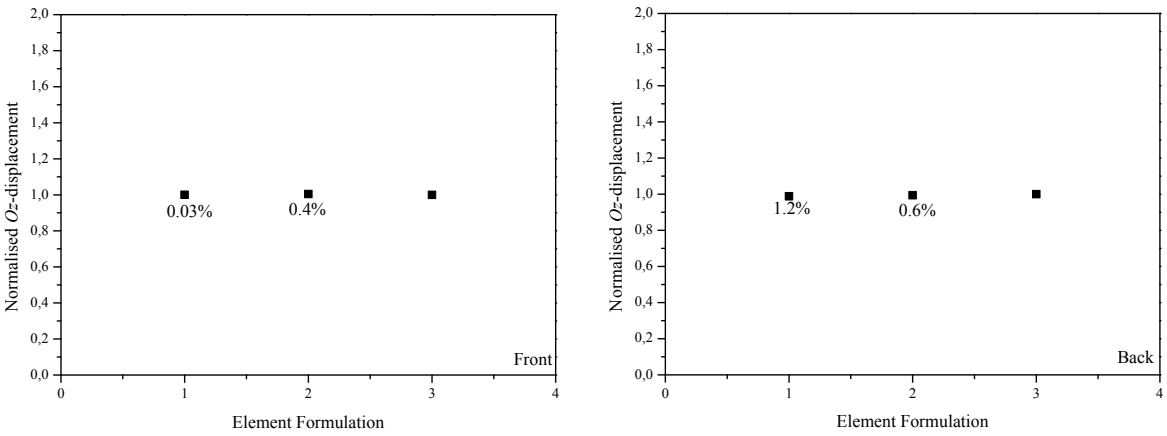

(a) Node A_c. (b) Node B_c.

Figure 10.10: Influence of the element formulation in the FEM results: Oz-displacement of the (a) front face central node (node A_c) and (b) back face central node (node B_c) plotted against element formulation.

10.3 Analysis and discussion

10.3.1 Impact phase

Simulation results on the blast loading process and consequent interaction and deformation of the MAC compound core sandwich structure are presented in this section. Several aspects will be pointed out, such as the calculated quantitative results, namely

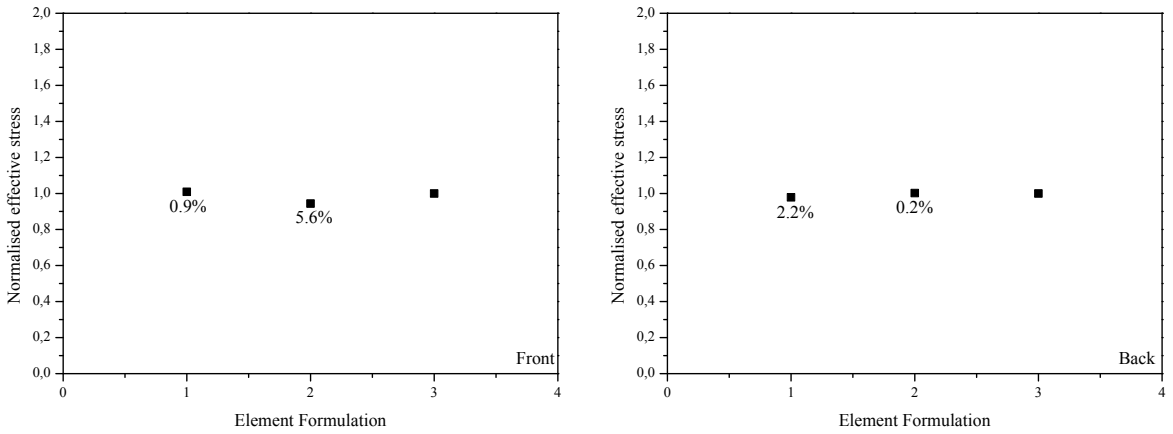

(a) Element A_c. (b) Element B_c.

Figure 10.11: Influence of the element formulation in the FEM results: von Mises stress value of the (a) front face central element (element A_c) and (b) back face central element (element B_c) plotted against element formulation.

Table 10.4: CPU time† in the simulations using constant stress solid (CSS) element formulation, fully integrated selective reduced solid (FISR) and fully integrated quadratic 8 node element with nodal rotations (FIQ).

Element formulation	**CPU time** [s]
CSS	13620
FISR	20460
FIQ	27300

† CPU: Intel® Core™ i7 @ 2.67 GHz.

the deflections experienced by the different sandwich structures (different thickness and core density), the deflection pattern exhibited by the structure and the displacement of the pendulum in the translation movement.

Selected time frames of the loading process of the NL20-10 sandwich are shown in figure 10.12. This sandwich structure was chosen as representative since, as was observed in the experiments, the larger deflections occurred in the less dense and thinnest core (fringe levels correspond to the resultant displacement)[2].

For $t = 0$ ms no loading has impacted the surface of the sandwich. Only for $t \approx 0.2$ ms it is perceptible that the blast-wave has already impacted the target. As was mentioned before (figure 10.2) the time of arrival of the blast-wave is $t_a \approx 0.14$ ms. As the time progresses it becomes more evident that the centre of the sandwich will deflect more due to the centralised uniform blast-wave (see images correspondent to $t \approx 0.3$ and 0.5 ms). The last image shown (figure 10.12 (e)), corresponds to the impact phase of the simulation model, at time $t \approx 0.8$ ms. The oscillation phase starts at $t \approx 2$ ms and the ballistic pendulum will start its oscillatory movement as can be seen from the images in figures 10.12 (f) to (h).

The time profile of the axial displacement results of the centre of the front aluminium face sheet for NL20-10 sandwich structure is shown in figure 10.13 (a). Both impact and oscillation phases are considered in this figure. An insight of the early stages of the impact (black square in figure 10.13 (a)) is represented in figure 10.13 (b). A maximum displacement value is achieved after the first impact of the blast-wave. The loading started for $t \approx 0.14$ ms and exponentially decreased to zero for $t \approx 0.35$ ms. An approach was used and presented in the beginning of the chapter (see section 10.2.2). In this approach the peak incident pressure presented in figure 10.2 could be determined by calculating the nodal forces on a plate with rigid material properties and the dimensions of the sandwich structure, divided by the area. This approach would only be reasonable if the loading was completed before the maximum deformation of the structure is reached. Hence, from the results in figure 10.13 (b) it can be seen that the maximum peak displacement was obtained for $t \approx 0.55$ ms, meaning that the condition of the approach is verified and adequate. In addition, it can be noticed that after maximum displacement is achieved, the sandwich deflection values (Oz-displacement) will decrease and stabilise. Comparing with the experimental results, only the final stabilised Oz-displacement value can be compared. Since at $t = 1$ ms the influence of the incident pressure on the structure is no longer relevant (see figure 10.2), the final deflection value of the centre of the plate, taken at $t = 1$ ms, is considered to be acceptable.

For comparison proposes the same variables that were analysed experimentally will also be studied in the finite element analysis. These are $D^{\mathrm{f}}_{\max}$ and $D^{\mathrm{b}}_{\max}$, which are

[2]Two different ranges had to be used for the fringe levels presented in this time view since the discrepancy of displacement results between impact and oscillation phases is significant. During the impact phase the fringe level range was 0 to 10 mm while in the oscillation phase the range used was 0 to 60 mm.

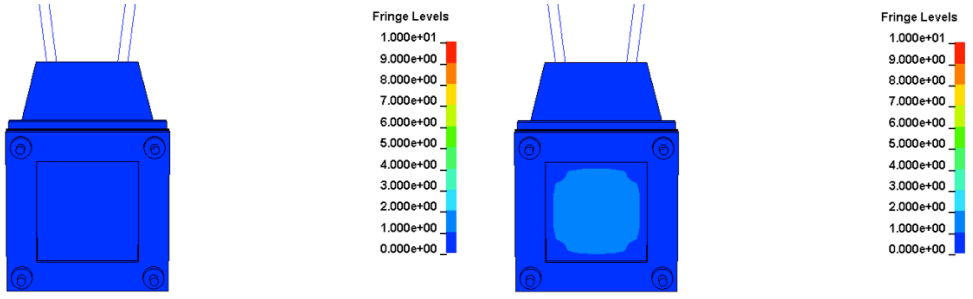

(a) $t = 0.0$ ms. (b) $t \approx 0.2$ ms.

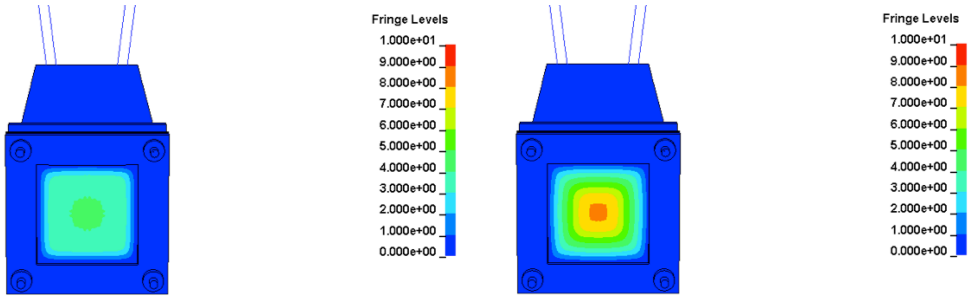

(c) $t \approx 0.3$ ms. (d) $t \approx 0.5$ ms.

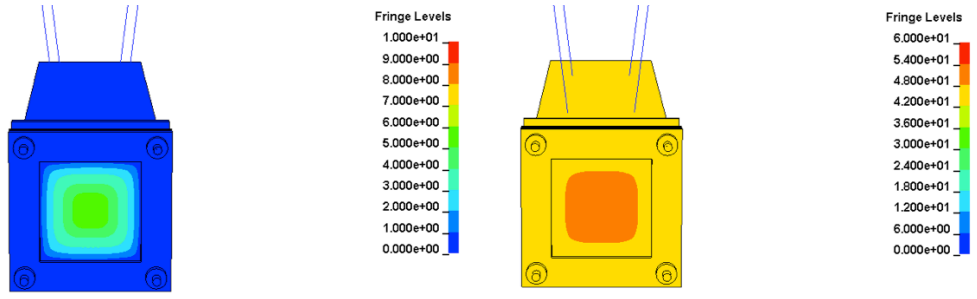

(e) $t \approx 0.8$ ms. (f) $t \approx 450$ ms.

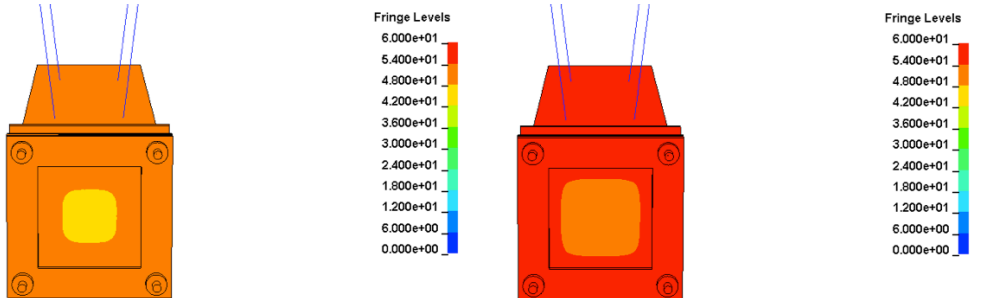

(g) $t \approx 2250$ ms. (h) $t \approx 2750$ ms.

Figure 10.12: Three-dimensional lagrangian FEM model of the ballistic pendulum showing the load blast loading in the NL20-10 sandwich. (a) to (e) impact phase and (f) to (h) oscillation phase.

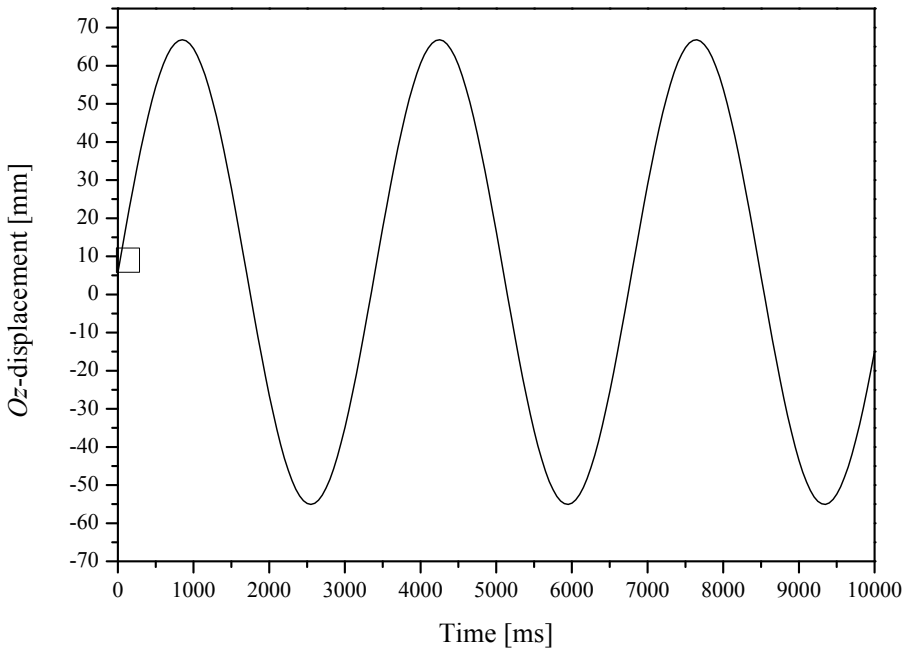

(a)

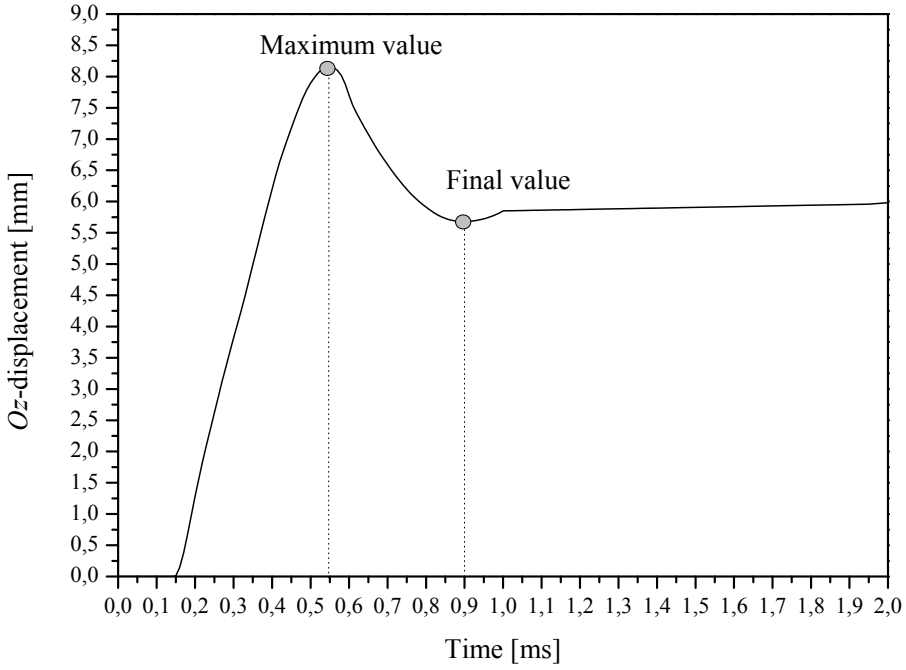

(b)

Figure 10.13: Numerical displacement of the centre of the front aluminium face sheet for the NL20-10 sandwich structure: (a) impact and oscillation time profile and (b) insight on the impact time profile.

the normalised maximum deflection of the front and back face sheets, respectively, D_{cp}^{f} which is the normalised deflection of the centre of the front panel and h_{red}^{p}, the relative thickness reduction of the whole structure after the blast event. The numerically obtained values for these variables are listed in table 10.5. d_{r}^{A} is the relative error between $D_{max}^{f^{exp}}$ and $D_{cp}^{f^{FEM}}$ while d_{r}^{B} is the relative error between h_{red}^{exp} and h_{red}^{FEM}.

Table 10.5: Deflections measured on the sandwich panels after the blast event. D_{cp}^{f} and D_{cp}^{b} are the deflection values of the centre of the front and back panel, respectively, and h_{red}^{p} is the relative thickness reduction of the sandwich structure.

Sample	$D_{max}^{f^{exp}}$ [mm]	$D_{cp}^{f^{FEM}}$ [mm]	d_{r}^{A}	h_{red}^{exp} [mm]	h_{red}^{FEM} [mm]	d_{r}^{B}
NL20-10	5.630	5.680	0.8%	1.423	1.182	16.9%
NL20-15	5.136	5.652	10.0%	0.955	1.707	78.7%
NL20-20	1.835	5.260	na	1.622	2.038	na
NL20-25	0.542	4.912	na	1.359	2.438	na
NL20-30	0.863	4.581	na	1.345	2.787	na
TB40-10	1.220	4.713	na	1.435	0.950	na
TB40-15	0.892	4.849	na	1.510	2.018	na
TB40-20	1.008	4.839	na	1.558	2.410	na
TB40-25	0.217	4.850	na	0.629	2.954	na
TB40-30	0.852	4.774	na	1.675	3.310	na

na: Not admissible.

One major fact that can be observed from the analysis of the results in table 10.5 is that the FEM model does not predict the transition between sandwich and (monolithic) plate behaviour of the structure. A limit thickness value of 20 mm was obtained experimentally for the NL20 sandwich structure for the transition from sandwich to plate behaviour. Therefore, it is impossible to define precisely where this transition occurs. This limit transition behaviour is possibly in the range of 15 to 20 mm core thicknesses. This fact explains why the FEM model accurately predicts the behaviour up to 15 mm of thickness and not beyond that. Values higher than this led to extremely large error values which can be explained by the fact that experimentally a monolithic plate behaviour was observed, whereas numerically sandwich behaviour apparently prevails. Hence, these simulations were not considered and the error values associated were considered not admissible (na). Nonetheless, when the FEM model correctly predicts the NL20 behaviour, the errors associated with the NL20-10 (0.8 %) and NL20-15 (10 %) sandwich structures can be due to several aspects such as the mass of the charge which might have not been exactly 30 g but slightly higher (or lower) which may have influenced the results, since, as previously mentioned, a slight change in the HE mass can significantly influence the results. Additionally, the stand-off distance, even with a slightly discrepancy from the 300 mm value might have produced some influence on the results, when compared to the FEM model.

For the TB40 specimens, a major discrepancy between the experimental and the numerical results was encountered as can be observed from the numerical results which clearly overestimate the experimental results. In the experimental analysis it was concluded that a limit core thickness value (15 mm) existed separating the sandwich from plate behaviour for the TB40 compound. Consequently, the discrepancy between numerical and experimental results can be derived, for example, from the fact that the transition between sandwich to plate behaviour occurred for core thicknesses lower than 10 mm for the TB40 MAC compound sandwich structures. Another possible explanation for the incapacity of the FE model to predict the TB40 behaviour might be the fact that TB40 did not behave at all like a cellular material due to its high density. Hence, the material model (`*Mat_Honeycomb`) may have been unsuitable to predict its behaviour. If the mass of the explosive charge was higher this could possibly have been avoided. Thus, due to the fact that the FEM model did not predicted the TB40 MAC compound behaviour, from this point forward the numerical results regarding the sandwich structures behaviour, will only be referred to the lower density sandwiches (NL20 MAC compounds).

Cross section cuts of the sandwich structures from the numerical analysis are shown in figures 10.14 (a) to (e). Cross section cuts of the sandwich structures from the experimental results are shown in figures 10.14 (f) to (j). The discrepancy between experimental and numerical results starting for sandwich structures with NL20 core thicknesses higher than 15 mm is also visible in these cross section representations.

10.3.2 Oscillation phase

During the oscillation phase, when the pendulum starts its oscillatory movement, the `*Load_Blast` function is not active since the influence of the incident pressure on the structure is no longer relevant. Ideally, all components of the pendulum in this part of the simulation are switched to `*Mat_Rigid` material model, except the sandwich structure which continues to be modelled with `*Mat_Honeycomb` in the core and `*Mat_Plastic_Kinematic` for the face sheets throughout the entire simulation.

From the registered displacement of the pendulum, the impulse can be analytically determined from $I_p = M\dot{x}_0$ (equation 5.6). However, a different approach was used in order to determine the impulse. Running a simulation described as before incurs on an extremely high CPU time when comparing to a simulation where in the oscillation phase the sandwich is also rigid. Therefore to determine the impulse transmitted to the pendulum, the following steps were followed:

1. Determine the values of the damping constant, β (equation 5.4), running the problem in the oscillation phase with the behaviour of all structural components switched to `*Mat_Rigid`, including the sandwich structure;

2. Run the simulations, considering that in the oscillation phase all components but the sandwich (that is, the sandwich will continue to be modelled with ma-

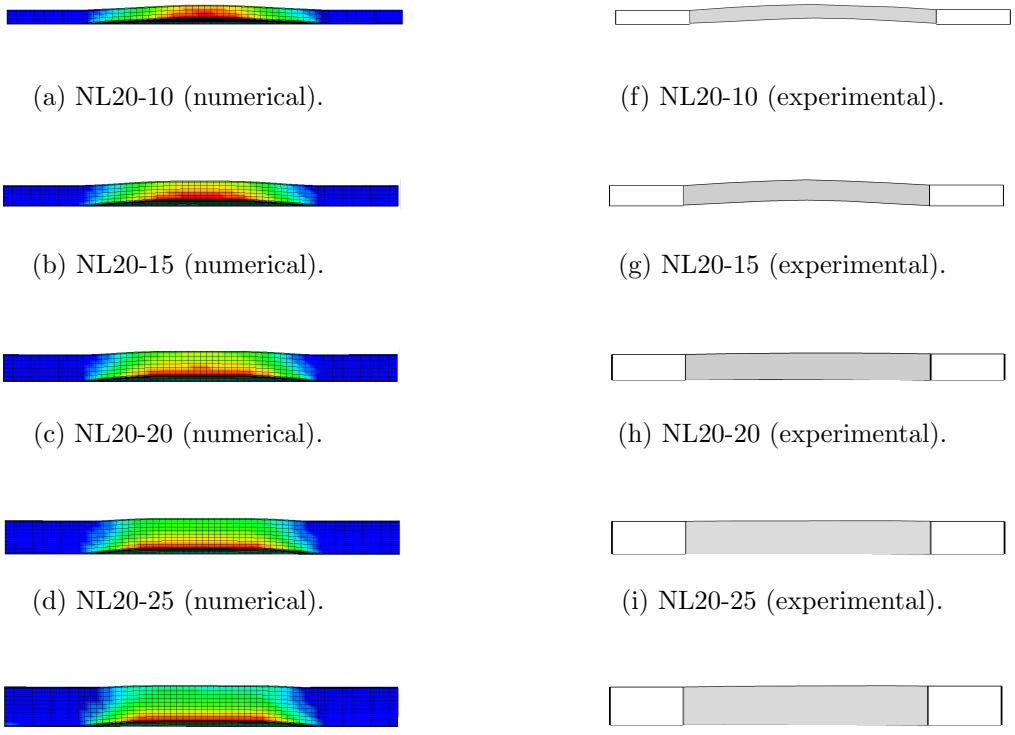

(a) NL20-10 (numerical). (f) NL20-10 (experimental).

(b) NL20-15 (numerical). (g) NL20-15 (experimental).

(c) NL20-20 (numerical). (h) NL20-20 (experimental).

(d) NL20-25 (numerical). (i) NL20-25 (experimental).

(e) NL20-30 (numerical). (j) NL20-30 (experimental).

Figure 10.14: Cross section views of the axial displacement in the NL20 sandwich structures: (a) to (e) numerical and (f) to (j) experimental results.

terial model `*Mat_Honeycomb` in the core and the aluminium face sheets with `*Mat_Plastic_Kinematic`) are switched on to `*Mat_Rigid` until maximum amplitude of the displacement of the pendulum is reached. This time of maximum amplitude corresponds to a fourth of the period T, that is, $T/4$;

3. With the values of β (obtained in step 1) and the period (obtained in step 2), and using equation 5.3, the initial velocity of the pendulum after the impact can be determined; and

4. Finally, using equation 5.6 the transmitted impulse is calculated.

Two types of transmitted impulse values (*i.e.* determined in different ways) are shown in table 10.6: the transmitted impulse determined from the simulation performed with all structural components modelled as rigid materials, $I_{\mathrm{p}}^{\mathrm{FEM_{rigid}}}$, and the transmitted impulse corrected using the previous explained steps, $I_{\mathrm{p}}^{\mathrm{FEM_{corr}}}$. Both these two impulses are related to the oscillation phase. The transmitted impulse values were numerically determined for each thickness of the core of the NL20 sandwich structures.

Low values of the relative error between $I_{\mathrm{p}}^{\mathrm{FEM_{rigid}}}$ and $I_{\mathrm{p}}^{\mathrm{FEM_{corr}}}$ ($d_{\mathrm{r}}^{\mathrm{C}}$) were obtained. Hence, it is acceptable to determine the relative error between experimental and numerical results using $I_{\mathrm{p}}^{\mathrm{exp}}$ and $I_{\mathrm{p}}^{\mathrm{FEM_{rigid}}}$ (d_{r}). Numerical impulse values slightly overestimated the experimental results. An average error of 20.5% was obtained for the comparison between experimental and numerical results. Some of the previously mentioned possible explanations for the discrepancy between experimental and numerical results also apply here, such as: discrepancies, even if small, between the actual mass of the explosive and the exact numerical mass defined to be 36 g of TNT equivalent. Similarly, discrepancies between the experimental and the numerically defined standoff distance are possible error sources. From the numerical deflection measurements a sandwich behaviour was encountered for all the tested core thicknesses. According to this, a decreasing impulse was expected as the thickness of the core increased. However, the impulse $I_{\mathrm{p}}^{\mathrm{FEM_{rigid}}}$ did not changed significantly for all the sandwiches. Impact and oscillation phases are numerically distinct. Hence, the model did predict the sandwich behaviour during the impact phase (for selected core thicknesses), but the same did not happen when the numerical model is parted to the oscillation phase.

10.4 Internal energy measurements

LS-Dyna$^{\mathrm{TM}}$ computes the internal energy based on the components of the stress and strain tensors. For each finite element, the internal energy is incrementally determined according to:

$$U^{n+1} = U^{n} + \sum_{p=1}^{n^{\mathrm{e}}} \int_{V^{\mathrm{e}}} \sigma_{ij}\varepsilon_{ij}\mathrm{d}V \tag{10.5}$$

where U^{n+1} and U^{n} are the current and previous increment internal energy values, respectively, n^{e} is the total number of elements, σ_{ij} and ε_{ij} are the element stress and

Table 10.6: Experimental and numerical values of impulse transmitted to the pendulum. $d_{\mathrm{r}}^{\mathrm{C}}$ is the relative error between $I_{\mathrm{p}}^{\mathrm{FEM_{rigid}}}$ and $I_{\mathrm{p}}^{\mathrm{FEM_{corr}}}$. d_{r} is the relative error between $I_{\mathrm{p}}^{\mathrm{exp}}$ and $I_{\mathrm{p}}^{\mathrm{FEM_{rigid}}}$.

Sample	$I_{\mathrm{p}}^{\mathrm{exp}}$ [Ns]	$I_{\mathrm{p}}^{\mathrm{FEM_{rigid}}}$ [Ns]	$I_{\mathrm{p}}^{\mathrm{FEM_{corr}}}$ [Ns]	$d_{\mathrm{r}}^{\mathrm{C}}$	d_{r}
NL20-10	15.869	17.666	17.862	1.1%	11.3%
NL20-15	15.849	18.186	18.158	0.2%	14.7%
NL20-20	13.939	18.471	18.428	0.2%	32.5%
NL20-25	14.737	18.768	18.725	0.2%	27.4%
NL20-30	16.369	19.072	19.025	0.2%	16.5%

strain components, V^{e} is the element's volume[3]. That is, the internal energy of all elements is summed to give the total internal energy [DS 2009].

As previously mentioned, the blast loading started at $t \approx 0.14$ ms. After the peak incident pressure was reached, the pressure exponentially decreased to zero for $t \approx 0.35$ ms (see figure 10.2). At $t = 1$ ms it was shown that the influence of the incident pressure on the sandwich was no longer relevant. These conclusions allowed to assume that the maximum displacement of the centre of both front and back aluminium face sheets at $t = 1$ ms are acceptable (see figure 10.13). Hence, this final deflection value is posterior to the stabilisation and, consequently, the elastic recovery of the material is no longer relevant. Combining these conclusions, if the internal energy values of the sandwich components are analysed, it only makes sense to analyse them if the structure is no longer behaving elastically and that permanent deformations already took place. If conclusions are taken at the final values at $t = 1$ ms of internal energy, a permanent deformation state is already present in the structure, thus making the internal energy analysis accurate.

For all the NL20 sandwich structures analysed, the internal energy was represented as a function of time. The values of internal energy registered in the FE model for all components and all sandwich structures are shown in figure 10.15. In order to have an estimation of the contribution of each single component in the total internal energy and consequent energy during plastic deformation, values of internal energy ratio in the FE model for all components and all the specimens studied are shown in figure 10.16.

An overall perspective on each of the sandwich components that has the higher registered internal energy value is perceptible in both figures 10.15 and 10.16. It is clear that the core has the higher internal energy values. The core itself contributes to between approximately 80 and 90% of the energy dissipation within the structure, as can be seen from the results in figure 10.16. Similar conclusions can be taken for the front face sheet, which will first move towards the core causing its compression (and eventually energy dissipation). The maximum internal energy ratio value achieved

[3]Einstein notation is assumed all over.

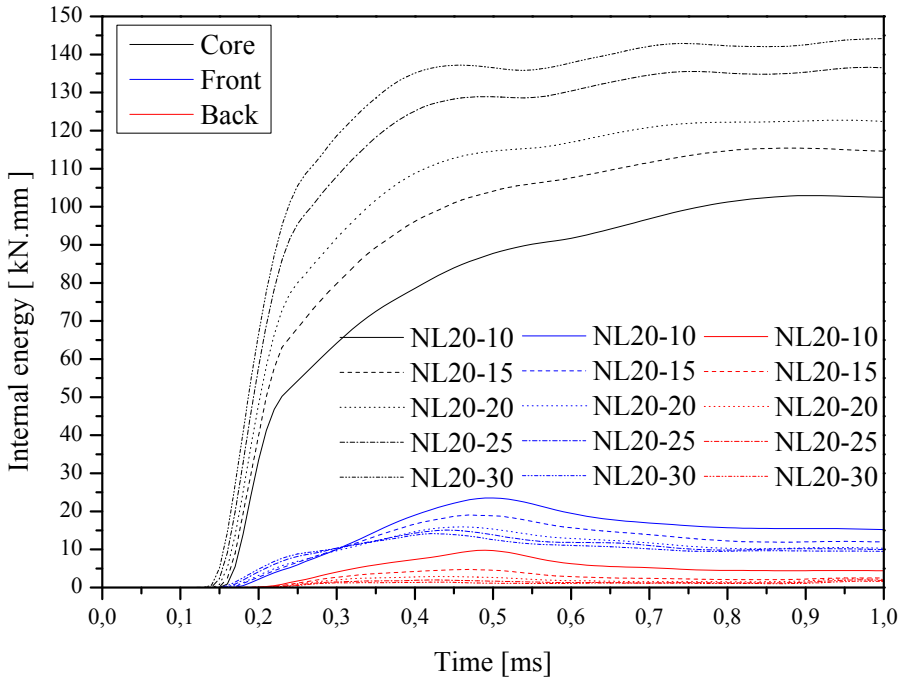

Figure 10.15: Evolution of the internal energy in the FE model for all thicknesses of the NL20 sandwich structures studied.

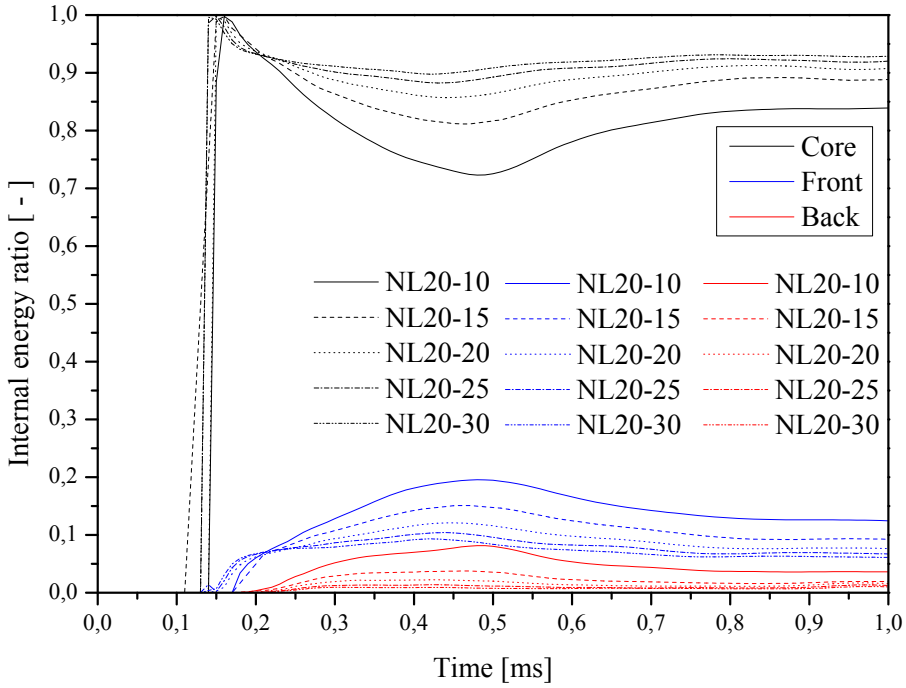

Figure 10.16: Evolution of the internal energy ratio in the FE model for all thicknesses of the NL20 sandwich structures studied.

approaches 15%. Much lower values of absorbed energy are registered for the back face sheets.

The internal energy for all the different core thicknesses, but separated by component (that is, plotted individually for the core, front and back face sheets), are shown in figures 10.17 to 10.19. The intention is to analyse the influence of the core thickness in this energy analysis.

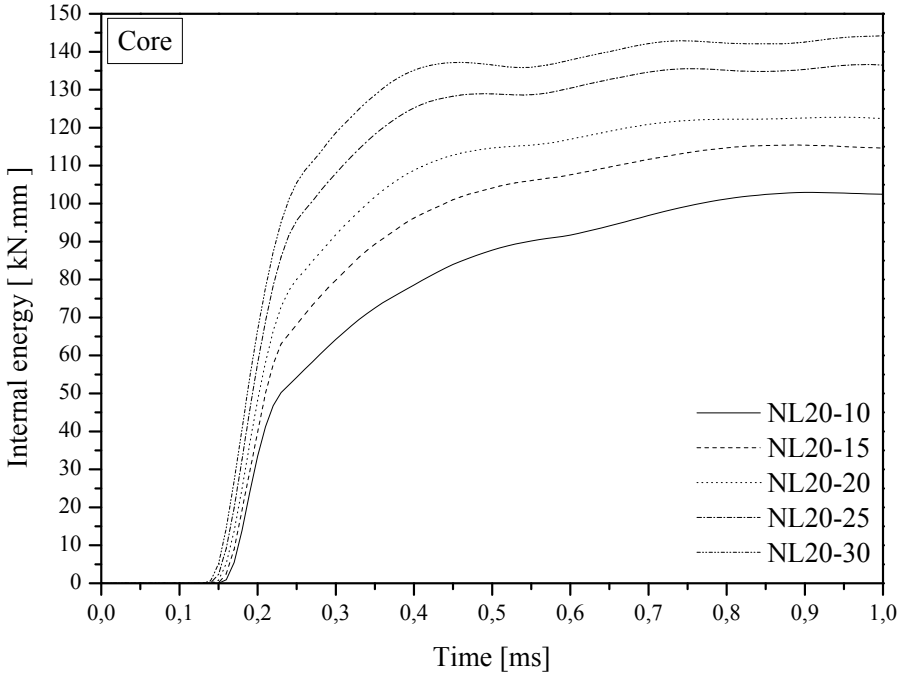

Figure 10.17: Evolution of the internal energy in the FE model for NL20 cores for the sandwich structures studied with different thicknesses.

In terms of differences between sandwiches with distinct core thicknesses, the core energy values (see figure 10.17) tend to be higher for the higher thicknesses (30 mm). This can be correlated to the fact that the numerical model assumes a sandwich like behaviour for all simulations. Hence, the higher the thickness of the core, the more it will compress and, eventually, dissipate energy.

Two distinct types of behaviour can be observed, in terms of internal energy in the front aluminium face sheet, from the results in figure 10.18. The transition between behaviours is at $t \approx 0.3$ ms. In the beginning the thinner core registers a lower energy value. For $t > 0.3$ ms the lower the thickness of the core the higher the internal energy of the front face aluminium sheet. However, only after the transition for $t > 0.3$ ms a plastic deformation state is assured, as previously mentioned. Concluding, the thinnest the core, the higher internal energy value observed of the front face sheet.

In the back aluminium face sheet, the thinner core sandwich structures are the ones which register higher internal energy values (see figure 10.19). Sandwich structures with a thicker core present lower back face deflections and, thus, less energy is dissipated by the back face sheet.

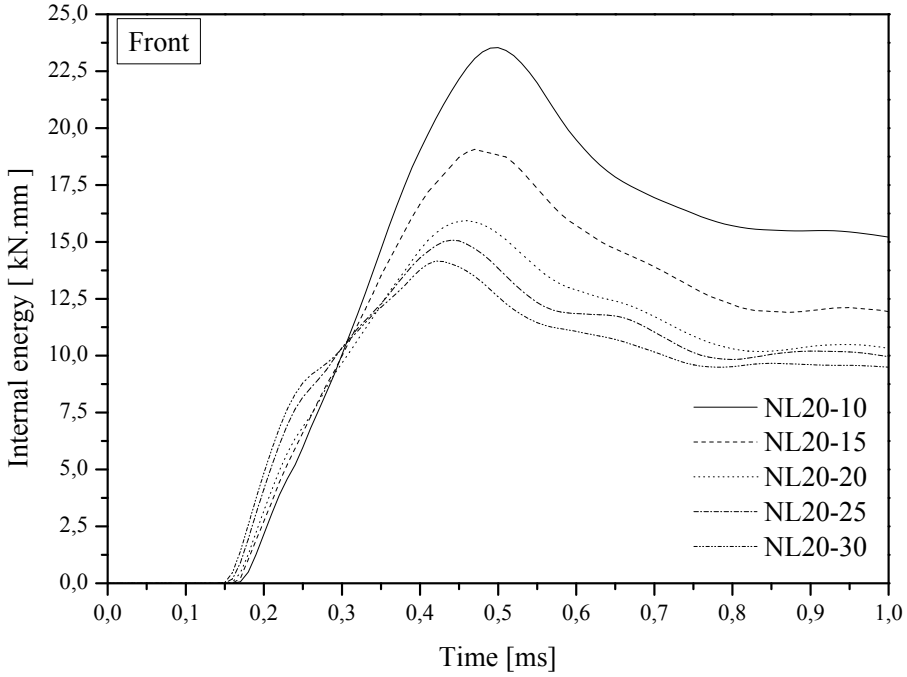

Figure 10.18: Evolution of the internal energy in the FE model for NL20 front face aluminium sheets for the sandwich structures studied with different thicknesses.

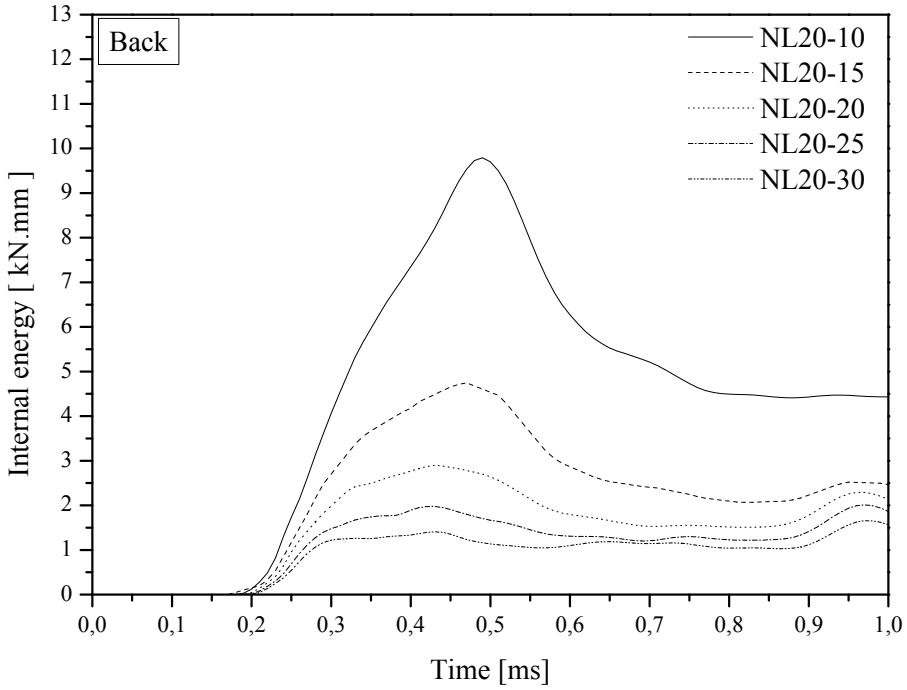

Figure 10.19: Evolution of the internal energy in the FE model for NL20 back face aluminium sheets for the sandwich structures studied with different thicknesses.

Part IV

Final remarks

Chapter 11

Conclusions and future work

The main conclusions obtained from this investigation are referred and discussed in this chapter. In the last section of the present chapter, future lines of research and work are suggested.

11.1 Conclusions

Unfortunately, nowadays terrorism is an almost daily reality. There are several types of terrorism, such as, for example, armed attacks, assassinations, skyjackings and bombings. Consequently, the concept of blast mitigation improvement, that is, the effort to reduce loss of life and property by reducing the impact of such disasters, assumes high levels of importance. Thus, strong efforts must be put on research and development concerning issues related to the impact resistance of engineering structures subjected to blast-waves. However, this is a complex subject since, for example, not only the blast can cause harm to people and structures but, in addition, there is the major threat that is the eventual subsequent failure of structures due to the effects of blast.

Protection systems (PS) are materials or structures which are expected to behave in an active way protecting buildings, people, *etc.* by many different ways. An example of a special type of protection system is sandwich structures, in which an energy absorber (EA) (*i.e* material with the ability to absorb energy) is incorporated as core. Nonetheless, in order to aim for the best PS, care must be taken on the perception of some phenomena, such as explosions, blast-waves, explosives and its classification, response of structures to blast loading, *etc.* In an explosive phenomena, great increase in heat and pressure values are experienced. This overpressure (*i.e.* the pressure above atmospheric pressure) will eventually decrease as the stand-off distance increases (*i.e.* the distance between the source of the explosion and the impact target of the blast-wave).

In terms of explosive and their characterisation, these can be categorised according to their decomposition type as high and low explosives. The explosive used in the experimental component of this investigation was a high explosive (composition C4).

Air blast loading was originated from the detonation of this high explosive. Airblast phenomena can be seen as a sum of several different phases. First, a condensed high explosive is detonated and the explosion reaction generates hot gases which achieve very high pressures and temperatures. Such conditions will provoke a violent expansion of the gases from the explosive, which will compress the air located in its front. Consequently, this compressed air forms the so called blast-wave. Thus, the blast-wave interaction with structures (*e.g.* a protection system incorporating an energy absorber) was the main objective of investigation. The capacity for energy absorption of a sandwich structure with a new innovative non-metallic and light-weight core solution (a cellular material) was experimentally and numerically investigated.

A material is considered to be cellular if it is made by empty cell elements. Cork presents remarkable properties that evidence its possible good applicability as an energy absorber in sandwich structure solutions (*e.g* its ability to sustain very large strains at very low stress values transmitted to the material, with a solid volume fraction of $\approx 15\%$). However, its potential as an energy absorber is not yet well documented and its usage for defence systems is only now emerging. Two cork compound materials were used as sandwich structure cores (NL20, with a density of 200 kg/m^3 and TB40, with a density of 440 kg/m^3). The use of natural cork was discarded due to the presence of defects and variability of the material's porosity, since these aspects might significantly affect the material's performance.

When impacted by the blast-wave the sandwich structure will be subjected to a pressure pulse transmitted to its front face sheet. The core will eventually offer resistance to the velocity of the front face sheet moving towards the back face sheet (due to core compression). The experimental measurements were performed in a 4-cable ballistic pendulum, which has been widely used to study blast-wave absorption capacity of structures.

In order to characterise the behaviour of the sandwich structures in such applications, efforts were made on the characterisation of the MAC compound behaviour itself. Hence, a first set of experimental measurements was performed to evaluate the behaviour of MAC compound specimens facing blast loads. Cylindrical MAC compound specimens with 50, 75 and 100 mm of height and a constant diameter of 45 mm, were tested for each MAC compound. A special base for these specimens was mounted on one end of the ballistic pendulum and the blast load that impacted these specimens was achieved from the detonation of 7 and 8 g of cylindrical high explosive (C4) that accelerated a striker mass. This striker mass uniformly loaded the specimens. A laser displacement sensor, a force transducer and a high speed camera were used in these experiments to gather experimental data. Two different values of impulse transmitted to the pendulum where compared: (i) rigid specimens with the same dimensional characteristics of the MAC compound specimens and (ii) the MAC compounds specimens. Similar shape of the load-time profiles were obtained for both the rigid and the MAC compounds specimens. Initial triangular impulses followed by several lower intensity peaks, that could have their origin in vibration of the base of the specimens or/and

stress wave reflections, were observed. As a consequence, in terms of energy absorption a preliminary conclusion was taken. Indeed, MAC compound specimens contributed to energy dissipation, since the load values presented were significantly lower than the ones obtained for the rigid specimens.

In addition, in this first experimental characterisation of MAC compound specimens the influence of three different parameters was analysed: influence of (i) the density of the MAC compound, (ii) the C4 mass and (iii) the specimen's height. The main conclusions obtained with this parametric study were: (i) the lower the density of the MAC compound, the higher the registered values of load peak; (ii) for both MAC compounds, increasing 1 g in the mass of explosive, resulted in an increase of the load peak; (iii) an increase in the height of the specimen produced a decrease in the magnitude of the load peak. This behaviour was observed for both densities of MAC compounds. It should be added that slight bending occurred in longer specimens (mainly due to trapping of some specimens), which can explain this decrease in the load.

A rigid body analysis was made in order to study the restitution coefficient present in the collision between striker and pendulum. This was considered to be an acceptable preliminary analysis on the applicability of MAC compounds as energy absorbers in sandwich structures. The presence of a crushable material, such as the MAC compound, between the striker and the ballistic pendulum changes the restitution coefficient of the collision. In generic terms, the closer this coefficient (c) is to one, the less energy is being dissipated on the collision. For all the specimens (different heights and densities) the values of the restitution coefficient were determined as were the subsequent percentages of energy absorption. According to the specimen's heights, the following values were obtained: MAC compound specimens contributed to approximately 82.6% (NL20–50) and 89.6% (NL20–75) of the energy dissipation, for 7 g of C4. When using 8 g of C4 the energy dissipation increased to 87.9% (NL20–50) and 93.5% (NL20-75). TB40 compound specimens presented generally lower values of energy absorption: 80.8% (TB40–50), 88.8% (TB40–100) for 7 g of explosive and 89.5% (TB40–50) and 69% (TB40–75 mm) for 8 g of C4. The decrease in the energy absorption values was attributed to the negative influence of the increase in density of the MAC compound.

In addition, the first set of experimental tests served to accurately define a constitutive model to be applied to the MAC compounds. Constitutive modelling and subsequent constitutive equations are used to relate representative variables (*e.g* the relationship between stress and strain in the material). According to what is reported in literature [Gameiro *et al.* 2005], cork and its compounds are materials that present strain rate dependent behaviour. After relating the experimental results with numerical analysis (whose main conclusions are referred in the next paragraphs) an extensive study was done to determine which multiplicative factor best suited the mechanical behaviour of cork. This multiplicative factor was applied to *quasi*-static stress-strain curves of the two MAC compounds being analysed (NL20 and TB40). An universal

testing machine Shimadzu^{TM}AG-50 kN G at a cross-beam velocity of 4 mm/min was used. In this analysis, the specimens with 50 mm height were used. The multiplicative factor used for the numerical simulation that best suited the experimental results was 1.85 for NL20 with 7 g of C4, 3.80 for NL20 with 8 g of C4, 1.10 for TB40 with 7 g of C4 and 1.50 for TB40 with 8 g of C4.

The second set of experimental testing consisted on experiments in sandwich structures subjected to blast loads. Sandwich specimens were manufactured with 5754-H22 aluminium alloy face sheets and the MAC compound cores with different densities (NL20 and TB40). A blast-wave originated from the detonation of 30 g of spherical C4 loaded the sandwich structures. The stand-off distance of 300 mm was kept constant throughout all experiments. Experimental data obtained from these experiments were values of deflection of both the front and back face sheets and overall rigid body displacement of the ballistic pendulum (measured with the laser displacement sensor). The transmitted impulse values obtained followed a decreasing tendency for increasing values of the thickness of the core. This behaviour was found for both MAC compounds. However, this behaviour was only verified until a certain core thickness. In the NL20 sandwich structures case, core thicknesses higher than 20 mm led to increasing transmitted impulses and, consequently, increasing initial velocities of the pendulum. This behaviour was also observed for the sandwich structures with TB40 MAC compound cores. Nonetheless, this transition of tendencies occurred for a lower core thickness (the tendency for increasing values of impulse for increasing core thicknesses started at 15 mm). This behaviour found in the sandwich structures was attributed to a transition between sandwich and monolithic plate behaviours.

In addition, specimens were cut half width to observe if internal compaction, deformation, eventual occurrence of damage within the core material and debonding between core and face sheets occurred. Specimens did not show any kind of damage other than the one found close to the clamping borders of the face sheets and no debonding occurred between the face sheets and the cores.

As stated before, final maximum deflections of both the front and back face sheets were measured. These values were then linked/related to the type of core compound used (*i.e* density) and the thickness of the core. Most specimens with lower density cores exhibited deflection values (for both the front and back face sheets) higher than those of the higher density. A linear dependency was determined between the relative thickness reduction and the initial core thickness of both compounds. In addition, and from comparison to what is reported in literature [Hutchinson and Xue 2005, Zhu *et al.* 2009a], the overall deformation pattern observed in the sandwich structures indicated that bending was the most probable deformation mechanism, thus indicating a small deflection case. The maximum observed relative thickness reduction was approximately 11% for the NL20–10 sandwich structures, indicating that energy dissipation may be due to the core, that is, due to crushing of its cellular structure.

Numerical modelling of the problem was also considered in the scope of the investigation here presented. The finite element (FE) method was the tool used and the

commercial software LS-Dyna^{TM} allowed to model the non-linear dynamic interaction between structures and blast-waves. Two sets of experimental measurements were numerically modelled, corresponding to: (i) the blast-wave absorption capacity of the cylindrical MAC specimens and (ii) the sandwich structures with MAC compounds cores.

The numerical modelling of the blast load on cylindrical MAC compound specimens with different heights and different densities was divided in two different stages. The velocity that the striker would feel due to the detonation of the explosive (7 and 8 g of C4) was numerically determined using an axisymmetric model combining both lagrangian and eulerian formulations. The purpose of such a simulation was to reduce eventual experimental errors that could have been accumulated in the determination of this velocity. The numerically determined initial velocity that the striker would feel due to the detonation of 7 and 8 g of C4 was 80 and 87.5 m/s, respectively.

A three-dimensional model of the ballistic pendulum adapted to test cylindrical specimens was developed and the loading on MAC compound specimens achieved by assigning the previously determined initial velocity to the striker. The problem was divided in two steps: impact and oscillation phase. In the first step, the striker impacted the specimen and compressed it, whereas in the oscillation step, both striker and specimens were no longer considered (were erased from the FEM model). Although the two steps were modelled, comparison between experimental and numerical results naturally focused on the impact phase.

A good correlation between numerical and experimental results was achieved (*e.g.* in terms of magnitude of the peak force for the smaller MAC compound specimens). This behaviour was observed for both MAC compound specimens. The width of the first numerical peak load slightly underestimated the equivalent experimental value. This underestimation manifested then in the impulse values, since these were determined by integration of the first peak of the load. Nonetheless, not so good correlation between numerical and experimental results was obtained for longer specimens with both densities. The discrepancies observed between the load values (*i.e.* numerical and experimental) were attributed to slight bending that occurred in these specimens.

A complete characterisation of the MAC compounds was obtained combining both the experimental and numerical results previously described. Hence, it was then possible to develop a finite element model of the complete 4-cable ballistic pendulum setup adapted for sandwich structures. As with the numerical model previously described, in the sandwich structure case a two step numerical analysis was performed. Regarding sandwich structures with a NL20 MAC compound cores, the FE model reasonably predicted the values of maximum front face sheet deflection up until 15 mm of core thickness. Experimentally, a limit thickness value of 20 mm was obtained for the transition from sandwich to plate behaviour. Thus, it was possible to conclude that the FE model did not predict the transition between sandwich and (monolithic) plate behaviour of the structure.

The numerical results concerning sandwich structures incorporated with TB40

MAC compounds as cores were not as satisfactory as the ones obtained for NL20 MAC. In fact, the numerical results were found to substantially overestimate the experimental results. Thus, explanations that could justify such discrepancies in results had to be found. In the experimental analysis correspondent to the sandwich structures with TB40 MAC compound cores it was observed that the transition between sandwich (monolithic) plate behaviour happened for core thickness values lower than 15 mm. Thus, the discrepancy between numerical results and experimental observations can possibly come from the fact that the transition from sandwich to plate behaviour occurred for core thicknesses lower than 10 mm for the TB40 MAC core sandwiches. Therefore, as expected, since it had already been observed that the FE model did not predict this transition, the numerical model was not capable of predicting the TB40 behaviour. It was concluded that possibly TB40 MAC compounds did not behave at all as a cellular material due to its high density.

The last numerical analysis made for the sandwich structures was relative to the internal energy. With this analysis several aspects were discussed, such as the influence of the thickness of the core (*i.e.* different densities and thicknesses) in terms of the overall energy dissipation. In addition, the contribution of the aluminium face sheets was also studied.

An estimation of the contribution of each single component to the total internal energy and consequent energy during plastic deformation was made based on the internal energy ratio in the FE model for all the components and specimens studied. Maximum values of internal energy ratio were observed for the core component of the sandwich structures and, as expected, the lower values were obtained for the back face sheets. The core itself contributed to between approximately 80 to 90% of energy dissipation in the structures. To analyse the influence of the thickness of the core, values of internal energy for all different core thicknesses, separately for the core, the front and back face sheets, were plotted as a function of time. In terms of differences between sandwich structures with distinct core thicknesses, the core energy values tend to be higher for the higher thickness value used (30 mm). This is in total agreement to the previously obtained conclusion in which it was observed that the numerical model assumes a sandwich like behaviour for all simulations. Higher values of core thickness led to higher plastic deformation energy. Hence, more energy was dissipated by the system.

On the one hand, the energy dissipation contribution of the front face aluminium sheet showed that the lower the thickness of the core the higher energy is dissipated by the front face aluminium sheet. On the other hand, for the back aluminium face sheets, the sandwich structures with a thicker core, present lower back faces deflections, and thus less energy is dissipated.

11.2 Future work

Possibilities for future work and guidelines of research are suggested. Several are the possible improvements that can be made both experimentally and numerically.

In the experimental analyses with the sandwich structures, no time history data was recorded apart from the laser displacement measurements. This happened due to the collaborative nature of the work, where the experimental setup used was adapted to pre-existing equipment. Therefore, this is a step of major importance to perform in future work.

In addition, it would be very interesting to perform not only experimental tests but also numerical simulations on sandwich structures, characterised by different properties, such as: even lower density cores, different aspect ratios of the exposed target area, different core thicknesses, different types of aluminium face sheets and respective thicknesses.

Higher explosive masses should also be experimented, since the maximum value tested within this research was restricted to the maximum permitted in the bunker laboratory where the tests were made. Changing this parameter, a wider range of impulse levels could be applied to identify possible failure patterns in the sandwich structures, damage modes (tearing, fracture and heating effects).

In terms of the performance of the innovative light-weight core solution, and having in mind the use of natural cellular cores like cork and its compounds, a possible step to follow in future work is the use other cork based cores such as compounds with a different adhesive proportion.

In a more idealistic and long-term perspective on the future guideline of research, the following ideas can be suggested:

- Research on advanced energy absorber materials, with a very high energy absorption capacity to thickness ratio;
- Consider the application of these materials in personal armour solutions; and
- Consider the incorporation of additional core materials with, for example, different deformation/damage mechanisms, in order to achieve higher levels of energy dissipation and still use a multi-layered solution.

Bibliography

[AB 2012] Abaqus®. www.3ds.com, July 2012.

[AD 2012] Ansys®. www.ansys.com, July 2012.

[Akhavan 2004] J. Akhavan. *The Chemistry of Explosives*. The Royal Society of Chemistry, 2004.

[Alcântara *et al.* 2013] I. Alcântara, F. Teixeira-Dias and M. Paulino. Cork composites for the absorption of impact energy. *Composite Structures*, **95**:16–27, 2013.

[AM 2005] *Explosive Initiation User's Manual* (Lee-Tarver Ignition & Growth) Revision 4.3, 2005.

[Ankiewicz 2010] A. Ankiewicz. *Properties of self-assembled diluted magnetic semiconductor nanostructures* (PhD Thesis). University of Aveiro, 2010.

[Ashby 1983] M.F. Ashby. The mechanical properties of cellular solids. *Metallurgical transactions A*, **14**(9):1755–1769, 1983.

[Bala 2001] S. Bala. *Contact Modeling in LS-Dyna^{TM} Part 1: Some Recommendations*. Livermore Software Technology Corporation, August 2001.

[Bambach 2008] M.R. Bambach. Behaviour and design of aluminium hollow sections subjected to transverse blast loads. *Thin-Walled Structures*, **46**(12):1370–1381, 2008.

[Bambach *et al.* 2010] M.R. Bambach, X.L. Zhao and H. Jama. Energy absorbing characteristics of aluminium beams strengthened with CFRP subjected to transverse blast load. *International Journal of Impact Engineering*, **37**(1):37–49, 2010.

[Belytschko *et al.* 1997] T. Belytschko, W.K. Liu and B. Moran. *Nonlinear Finite Elements for Continua and Structures*. John Wiley & Sons, 1997.

[Bjerketvedt *et al.* 1992] D. Bjerketvedt, J. Roar Bakke and K. van Wingerden. *Gas explosion handbook*. GexCon, 1992.

[Bodner and Symonds 1979] S.R. Bodner and P.S. Symonds. Experiments on viscoplastic response of circular plates to impulsive loading. *Journal of the Mechanics and Physics of Solids*, **27**(2):91–113, 1979.

[Bonet and Wood 2008] J. Bonet and R.D. Wood. *Nonlinear Continuum Mechanics for Finite Element Analysis*. Cambridge University Press, 2008.

[Børvik *et al.* 2009] T. Børvik, A.G. Hanssen, M. Langseth and L. Olovsson. Response of structures to planar blast loads — A finite element engineering approach. *Computers and Structures*, **87**(9-10):507–520, 2009.

[Bower 2010] A.F. Bower. *Applied Mechanics of Solids*. CRC Press, 2010.

[Bridgman 1952] P.W. Bridgman. *Studies in Large Plastic Flow and Fracture*. McGraw-Hill, 1952.

[Buchan and Chen 2007] P.A. Buchan and J.F. Chen. Blast resistance of FRP composites and polymer strengthened concrete and masonry structures – A state-of-the-art review. *Composites Part B: Engineering*, **38**(5-6):509–522, 2007.

[Bulson 1997] P. Bulson. *Explosive Loading of Engineering Structures*. Chapman & Hall, 1997.

[BW 2012] BlastX®. https://pdc.usace.army.mil/software/blastx/, July 2012.

[Castro *et al.* 2010] O. Castro, J.M. Silva, T. Devezas, A. Silva and L.Gil. Cork agglomerates as an ideal core material in lightweight structures. *Materials & Design*, **31**(1):425–432, 2010.

[Cloete *et al.* 2003] T.J. Cloete, R.Ahmed and G.N. Nurick. Pheriferally clamped centrally supported blast load circular plates: A precision test for code validation. *Journal de Physique IV France*, **110**(1):507–512, 2003.

[Cooper 1996] P.W. Cooper. *Explosives Engineering*. Wiley-VCH, Inc., 1996.

[CP 2012] Cork in Portugal. www.cork.pt, November 2012.

[CW 2012] CTH®. www.sandia.gov/CTH, July 2012.

[de Borst and Hughes 2004] R. de Borst and Thomas J.R. Hughes. *Encyclopedia of Computational Mechanics, Volume 1: Fundamentals*. John Wiley & Sons, 2004.

[de Carvalho *et al.* 2013] R. de Carvalho, F. Teixeira-Dias and H. Varum. Cyclic behaviour of a lightweight mortar with cork granulate composites. *Composite Structures*, **95**:748–755, 2013.

[de Souza Neto *et al.* 2008] E. de Souza Neto, D. Peric and D. Owens. *Computational Methods for Plasticity, Theory and Applications*. John Wiley & Sons, Ltd., 2008.

[Deshpande and Fleck 2005] V.S. Deshpande and N.A. Fleck. One-dimensional response of sandwich plates to underwater shock loading. *Journal of the Mechanics and Physics of Solids*, **53**(11):2347–2383, 2005.

[Dharmasena *et al.* 2008] K.P. Dharmasena, H.N.G. Wadley, Z. Xue and J.W. Hutchinson. Mechanical response of metallic honeycomb sandwich panel structures to high-intensity dynamic loading. *International Journal of Impact Engineering*, **35**(9):1063–1074, 2008.

[DK 2012] *LS-Dyna keyword user's manual*, Vol I of Version 971, Release 4. Livermore Software Technology Corporation, 2012.

[Dobratz and Crawford 1985] B.M. Dobratz and P.C. Crawford. *LLNL Explosives Handbook: Properties of Chemical Explosives and Explosive stimulants.* Lawrence Livernlore National Laboratory, UCRL-52997, 1985.

[DS 2009] LS-Dyna Support. www.dynasupport.com, October 2009.

[Du Bois and Schwer 2007] P. Du Bois and L. Schwer. Lecture notes of *LS-Dyna^{TM} modeling of blast & penetration: applications to protective structures, vehicles and homeland security threats (Lecture 1 — simulation of shockwaves one-dimensional examples).* Livermore Software Tecnology Corporation, 2007.

[Dunne and Petrinic 2005] F. Dunne and N. Petrinic. *Introduction to Computational Plasticity.* Oxford University Press, 2005.

[DW 2012] LS-Dyna$^{\text{TM}}$. www.lstc.com, July 2012.

[Fortes and Nogueira 1989] M.A. Fortes and M.T. Nogueira. The poisson effect in cork. *Materials Science and Engineering: A*, **122**(2):227–232, 1989.

[Fortes *et al.* 2005] M.A. Fortes, M.E. Rosa and H. Pereira. *A Cortiça.* IST Press, 2005.

[Franz *et al.* 2002] T. Franz, G.N. Nurick and M.J. Perry. Experimental investigation into the response of chopped-strand mat glassfibre laminates to blast loading. *International Journal of Impact Engineering*, **27**(6):639–667, 2002.

[Fung and Tong 2001] Y.C. Fung and P. Tong. *Classical and Computational Solid Mechancics.* World Scientific, 2001.

[Gameiro 2007] C.P. Gameiro. *Capacidade de absorção de energia de impacto de estruturas tubulares com cortiça confinada — Estudo numérico e experimental* (PhD Thesis). University of Coimbra, 2007.

[Gameiro and Cirne 2007] C.P. Gameiro and J. Cirne. Dynamic axial crushing of short to long circular aluminium tubes with agglomerate cork filler. *International Journal of Mechanical Sciences*, **49**(9):1029–1037, 2007.

[Gameiro *et al.* 2005] C.P. Gameiro, J. Cirne, G. Gary, V. Miranda, J. Pinho da Cruz and F. Teixeira-Dias. Numerical and experimental study of the dynamic behaviour of cork. In *Design and Use of Light-Weight Materials — 3rd Light-Weight Armour Group Workshop*, 65–84, 2005.

[Gameiro *et al.* 2007a] C.P. Gameiro, J. Cirne and G. Gary. Experimental study of the quasi-static and dynamic behaviour of cork under compressive loading. *Journal of Materials Science*, **42**(12):4316–4324, 2007.

[Gameiro *et al.* 2007b] C.P. Gameiro, J. Cirne, V. Miranda, J. Pinho da Cruz and F. Teixeira-Dias. Dynamic behaviour of cork and cork-filled aluminium tubes: Numerical simulation and innovative applications. *Holzforschung*, **61**:400–405, 2007.

[Gibson and Ashby 1997] L.J. Gibson and M.F. Ashby. *Cellular Solids, Structures and Properties*. Cambridge University Press, 2nd edition, 1997.

[Gil 2009] L. Gil. Cork Composites: A Review. *Composite Materials*, **2**(3):776–789, 2009.

[Giroux 1973] E.D. Giroux. *HEMP User's Manual*. Lawrence Livermore National Laboratory, 1973.

[GS 2012] Globalspec — Properties of explosives and power index. www.globalspec.com, July 2012.

[Hallquist 2006] J.O. Hallquist. *LS-Dyna™ Theory Manual*. Livermore Software Technology Corporation, 2006.

[Hanssen *et al.* 2002] A.G. Hanssen, L. Enstock and M. Langseth. Close-range blast loading of aluminium foam panels. *International Journal of Impact Engineering*, **27**(6):593–618, 2002.

[Hassan *et al.* 2012] M.Z. Hassan, Z.W. Guan, W.J. Cantwell, G.S. Langdon and G.N. Nurick. The influence of core density on the blast resistance of foam-based sandwich structures. *International Journal of Impact Engineering*, **50**:9–16, 2012.

[Hooke 1665] R. Hooke. *Micrographia: or Some Physiological Descriptions of Minute Bodies Made by Magnifying Glasses*. Royal Society of London, 1665.

[Hutchinson and Xue 2005] J.W. Hutchinson and Z. Xue. Metal sandwich plates optimized for pressure impulses. *International Journal of Mechanical Sciences*, **47**:545–569, 2005.

[Hyde 1993] D.W. Hyde. *User's guide for microcomputer programs CONWEP and FUNPRO, Applications of TM 5-855-1, Fundamentals of Protective Design for Conventional Weapons*. Technical report, SL-88-1, U.S. Army Corps of Engineers Waterways, February 1993.

[Jacob *et al.* 2004] N. Jacob, S.C.K. Yuen, G.N. Nurick, D. Bonorchis, A. Desai and D. Tait. Scaling aspects of quadrangular plates subjected to localised blast loads — Experiments and predictions. *International Journal of Impact Engineering*, **30**(8-9):1179–1208, 2004.

[Jacob *et al.* 2007] N. Jacob, G.N. Nurick and G.S. Langdon. The effect of stand-off distance on the failure of fully clamped circular mild steel plates subjected to blast loads. *Engineering Structures*, **29**(10):2723–2736, 2007.

[Jensen 2010] M.R. Jensen. *Introduction to LS-Dyna^{TM}*. Livermore Software Technology Corporation, 2010.

[Jones 1989] N. Jones. *Structural Impact*. Cambridge University Press, 1989.

[Kakogiannis 2011] D. Kakogiannis. *Evaluation and assessment of the effects of Blast Loading by means of a Ballistic Pendulum* (PhD Thesis). Vrije Universiteit Brussels, 2011.

[Kakogiannis *et al.* 2010] D. Kakogiannis, D. van Hemerlrijck, J. Wastiels, S. Palanivelu, W. Van Paepegem, J. Vantomme, A. Kotzakolios and V. Kostopoulos. Assessment of pressure waves generated by explosive loading. *Computer Modeling in Engineering & Sciences*, **65**(1):75–92, 2010.

[Karagiozova *et al.* 2005] D. Karagiozova, G.N. Nurick and S.C.K. Yuen. Energy absorption of aluminium alloy circular and square tubes under an axial explosive load. *Thin-Walled Structures*, **43**(6):956–982, 2005.

[Karagiozova *et al.* 2009] D. Karagiozova, G.N. Nurick and G.S. Langdon. Behaviour of sandwich panels subject to intense air blasts — Part 2: Numerical simulation. *Composite Structures*, **91**(4):442–450, 2009.

[Krauthammer 2008] T. Krauthammer. *Modern Protective Structures*. Taylor & Francis, 2008.

[Krehl 2009] P.O.K. Krehl. *History of Shock Waves, Explosion and Impact, a Chronological and Biographical Reference*. Springer-Verlag, 2009.

[Langdon and Nurick 2010] G.S. Langdon and G.N. Nurick. The response of honeycomb core sandwich panels, with aluminum and composite face sheets, to blast loading. *Journal of sandwich structures and materials*, **12**(6):733–754, 2010.

[Langdon *et al.* 2007] G.S. Langdon, S.L. Lemanski, G.N. Nurick, M.C. Simmons, W.J. Cantwell and G.K. Schleyer. Behaviour of fibre-metal laminates subjected to localised blast loading: Part I –Experimental observations. *International Journal of Impact Engineering*, **34**(7):1202–1222, 2007.

[Langdon *et al.* 2009] G.S. Langdon, Y. Chi, G.N. Nurick and P. Haupt. Response of GLARE® panels to blast loading. *Engineering Structures*, **31**(12):3116–3120, 2009.

[Langdon *et al.* 2012] G.S. Langdon, C.J. von Klemperer, K. Rowland and G.N. Nurick. The response of sandwich structures with composite face sheets and polymer foam cores to air-blast loading: Preliminary experiments. *Engineering Structures*, **36**:104–112, 2012.

[Lemaitre 2001] J. Lemaitre. *Handbook of Materials Behavior Models — Deformations of Materials*. Academic Press, 2001.

[Lu and Yu 2003] G. Lu and T. Yu. *Energy Absorption of Structures and Materials*. Woodhead Publishing, 2003.

[MC 2004] *FASTCAM — Ultima APX Hardware Manual*, 2004.

[Meo *et al.* 2005] M. Meo, R. Vignjevic and G. Marengo. The response of honeycomb sandwich panels under low-velocity impact loading. *International Journal of Mechanical Sciences*, **47**(9):1301–1325, 2005.

[Meyer *et al.* 2007] R. Meyer, J. Khler and A. Homburg. *Explosives*. Wiley-VCH Verlag GmbH & Co. KGaA, 6^{th} edition, 2007.

[Mines *et al.* 1998] R.A.W. Mines, C.M. Worrall and A.G. Gibson. Low velocity perforation behaviour of polymer composite sandwich panels. *International Journal of Impact Engineering*, **21**(10):855–879, 1998.

[ML 2007] *Optical Distance Sensors Series M7: Manual*, MEL Mikroelektronik GmbH, 2007.

[Moreira *et al.* 2010] R.A.S. Moreira, F.J.Q. de Melo and J.F. Dias Rodrigues. Static and dynamic characterization of composition cork for sandwich beam cores. *Journal of Materials Science*, **45**(12):3350–3366, 2010.

[Needham 2010] C.E. Needham. *Blast Waves — Shock Wave and High Pressure Phenomena*. Springer-Verlag, 2010.

[Nemat-Nasser *et al.* 2007] S. Nemat-Nasser, W.J. Kang, J.D. McGee, W.-G. Guo and J.B. Isaacs. Experimental investigation of energy-absorption characteristics of components of sandwich structures. *International Journal of Impact Engineering*, **34**(6):1119–1146, 2007.

[Ngo *et al.* 2007] T. Ngo, P. Mendis, A. Gupta and J. Ramsay. Blast loading and blast effect on structures: An overview. *Electronic Journal of Structural Engineering EJSE Special Issue: Loading on Structures*, 76–91, 2007.

[Nóvoa *et al.* 2004] P.J.R.O. Nóvoa, M.C.S. Ribeiro, A.J.M. Ferreira and A.T. Marques. Mechanical characterization of lightweight polymer mortar modified with cork granulates. *Composite Science and Technology*, **64**:2197–2205, 2004.

[Nurick and Martin 1984] G.N. Nurick and J.B. Martin. The measurements of the response of clamped circular plates to impulsive loading. In *Proc. of the 3rd Conference Mechanical Properties at High Rates of Strain*, 495–500, 1984.

[Nurick and Martin 1989] G.N. Nurick and J.B. Martin. Deformation of thin plates subjected to impulsive loading — A review (Part II: Experimental studies). *International Journal of Impact Engineering*, **8**(2):171–186, 1989.

[Nurick and Shave 1996] G.N. Nurick and G.C. Shave. The deformation and tearing of thin square plates subjected to impulsive loads — An experimental study. *International Journal of Impact Engineering*, **18**(1):99–116, 1996.

[Nurick *et al.* 1996] G.N. Nurick, M.E. Gelman and N.S. Marshall. Tearing of blast loaded plates with clamped boundary conditions. *International Journal of Impact Engineering*, **18**(7-8):803–827, 1996.

[Nurick *et al.* 2009] G.N. Nurick, G.S. Langdon, Y. Chi and N. Jacob. Behaviour of sandwich panels subjected to intense air blast — Part 1: Experiments. *Composite Structures*, **91**(4):433–441, 2009.

[Otsuka *et al.* 2004] M. Otsuka, Y. Matsui, K. Murata, Y. Kato and S. Itoh. A study on shock wave propagation processin the smooth blasting technique. In *Proc. of the 8th International LS-Dyna™ Users Conference*, 2004.

[Paulino and Teixeira-Dias 2011] M. Paulino and F. Teixeira-Dias. An energy absorption performance index for cellular materials –Development of a side-impact cork padding. *International Journal of Crashworthiness*, **16**(2):135–153, 2011.

[Paulino *et al.* 2009] M. Paulino, F. Teixeira-Dias, C.P. Gameiro and J. Cirne. Hyperelastic and dynamical behaviour of cork and its performance in energy absorption devices and crashworthiness applications. *International Journal of Materials Engineering Innovation*, **1**(2):197–234, 2009.

[PC 2012] Plascork®. http://www.plascork-automotive.com, October 2012.

[Pereira 2007] H. Pereira. *Cork: Biology, Production and Uses*. Elsevier Science B.V., 2007.

[Qiu *et al.* 2004] X. Qiu, V.S. Deshpande and N.A. Fleck. Dynamic Response of a Clamped Circular Sandwich Plate Subject to Shock Loading. *Journal of Applied Mechanics*, **71**(5):637–645, 2004.

[Qiu *et al.* 2005] X. Qiu, V.S. Deshpande and N.A. Fleck. Impulsive loading of clamped monolithic and sandwich beams over a central patch. *Journal of the Mechanics and Physics of Solids*, **53**(5):1015–1046, 2005.

[Radford *et al.* 2006] D.D. Radford, N.A. Fleck and V.S. Deshpande. The response of clamped sandwich beams subjected to shock loading. *International Journal of Impact Engineering*, **32**(6):968–987, 2006.

[Randers-Pherson and Bannister 1997] G. Randers-Pherson and K.A. Bannister. *Airblast Loading Model for DYNA2D and DYNA3D.* Technical Report 1310, US Army Research Laboratory, March 1997.

[Rathbun *et al.* 2006] H.J. Rathbun, D.D. Radford, Z. Xue, M.Y. He, J. Yang, V. Deshpande, N.A. Fleck, J.W. Hutchinson, F.W. Zok and A.G. Evans. Performance of metallic honeycomb-core sandwich beams under shock loading. *International Journal of Solids and Structures*, **43**:1746–1763, 2006.

[RC 2012] RTM composites. www.rtmcomposites.com, October 2012.

[RE 2012] Ribbands Explosives. www.ribbands.co.uk/prod-c4.html, July 2012.

[Remennikov 2003] A.M. Remennikov. A review of methods for predicting bomb blast effects on buildings. *Journal of Battlefield Technology*, **6**(3):5–10, 2003.

[Rizov *et al.* 2005] V. Rizov, A. Shipsha and D. Zenkert. Indentation study of foam core sandwich composite panels. *Composite Structures*, **69**(1):95–102, 2005.

[Roach *et al.* 1998] A.M. Roach, N. Jones and K.E. Evans. The penetration energy of sandwich panel elements under static and dynamic loading. Part II. *Composite Structures*, **42**(2):135–152, 1998.

[Rodrigues 2003] J.D. Rodrigues. Lecture Notes of *Vibrações de Sistemas Mecânicos* (Faculdade de Engenharia da Universidade do Porto – FEUP), October 2003.

[Rodrigues and Martins 2005] J. Rodrigues and P. Martins. *Tecnologia Mecânica — Tecnologia da Deformação Plástica.* Escolar Editora, 2005.

[Rosa and Fortes 1988a] M.E. Rosa and M.A. Fortes. Rate effects on the compression and recovery of dimensions of cork. *Journal of Materials Science*, **23**(3):879–885, 1988.

[Rosa and Fortes 1988b] M.E. Rosa and M.A. Fortes. Stress relaxation and creep of cork. *Journal of Materials Science*, **23**(1):35–42, 1988.

[Rosa and Fortes 1991] M.E. Rosa and M.A. Fortes. Deformation and fracture of cork in tension. *Journal of Materials Science*, **26**(2):341–348, 1991.

[Serway and Jewett 2003] R.A. Serway and J.W. Jewett. *Physics for Scientists and Engineers*. Brooks Cole, 6^{th} edition, 2003.

[SH 2012] Operation "Sailor Hat" Explosive Tests (February–June 1965). www.history.navy.mil, August 2012.

[Shukla *et al.* 2010] A. Shukla, G. Ravichandran and Y.D.S. Rajapakse. *Dynamic Failure of Materials and Structures*. Springer, 2010.

[Sierakowski and Hughes 2006] R.L. Sierakowski and M.L. Hughes. Force protection using composite sandwich structures. *Composites Science and Technology*, **66**(14):2500–2505, 2006.

[Silva *et al.* 2011] J.M. Silva, C.Z. Nunes, N. Franco and P.V. Gamboa. Damage tolerant cork based composites for aerospace applications. *The Aeronautical Journal*, **115**(1171):567–575, 2011.

[SK 2012] Shark®. www.shark-software.com, July 2012.

[Smith and Hetherington 1994] P.D. Smith and J.G. Hetherington. *Blast and Ballistc Loading of Structures*. Elsevier Sciense Ltd., 1994.

[Sousa-Martins *et al.* 2012] J. Sousa-Martins, D. Kakogiannis, F. Coghe, B. Reymen and F. Teixeira-Dias. Response of cork compounds subjected to impulsive blast loads. *The European Physical Journal, Special Topics*, **206**(1):61–70, 2012.

[Sousa-Martins *et al.* 2013] J. Sousa-Martins, D. Kakogiannis, F. Coghe, B. Reymen and F. Teixeira-Dias. Behaviour of sandwich structures with cork compound cores subjected to blast waves. *Engineering Structures*, **46**:140–146, 2013.

[Tagarielli *et al.* 2007] V.L. Tagarielli, V.S. Deshpande and N.A. Fleck. The dynamic response of composite sandwich beams to transverse impact. *International Journal of Solids and Structures*, **44**(7-8):2442–2457, 2007.

[Tagarielli *et al.* 2010] V.L. Tagarielli, V.S. Deshpande and N.A. Fleck. Prediction of the dynamic response of composite sandwich beams under shock loading. *International Journal of Impact Engineering*, **37**(7):854–864, 2010.

[Teixeira-Dias *et al.* 2010] F. Teixeira-Dias, J. Pinho da Cruz, R.F. Valente and R.A. de Sousa. *Método dos Elementos Finitos, Técnicas de Simulação Numérica em Engenharia*. ETEP — Edições Técnicas e Profissionais, 2010.

[Theobald and Nurick 2007] M.D. Theobald and G.N. Nurick. Numerical investigation of the response of sandwich-type panels using thin-walled tubes subject to blast loads. *International Journal of Impact Engineering*, **34**(1):134–156, 2007.

[Theobald and Nurick 2010] M.D. Theobald and G.N. Nurick. Experimental and numerical analysis of tube-core claddings under blast loads. *International Journal of Impact Engineering*, **37**(3):333–348, 2010.

[TR 2011] Amorim Cork Composites S.A. — CORECORK® Technical Data. Technical report, NL10, NL20 and NL25 series and TB40 and 50 series, 2011.

[Urtiew and Hayes 1991] P.A. Urtiew and B. Hayes. Parametric study of the dynamic JWL-EOS for detonation products. *Combustion, Explosion, and Shock Waves*, **27**(4):505–514, 1991.

[Vaz and Fortes 1998] M.F. Vaz and M.A. Fortes. Friction properties of cork. *Journal of Materials Science*, **33**(8):2087–2093, 1998.

[Vaziri and Hutchinson 2007] A. Vaziri and J.W. Hutchinson. Metal sandwich plates subject to intense air shocks. *International Journal of Solids and Structures*, **44**(6):2021–2035, 2007.

[Vlot 2001] A. Vlot. *Glare — History of the Development of a New Aircraft Material*. Kluwer Academic Publishers, 2001.

[Wadley *et al.* 2007] H.N.G. Wadley, K.P. Dharmasena, D.T. Queheillalt, Y. Chen, P. Dudt, D. Knight, K. Kidd, Z. Xue and A. Vaziri. Dynamic compression of square honeycomb structures during underwater impulsive loading. *Journal of Mechanics of Materials and Structures*, **2**(10):2025–2048, 2007.

[Wang *et al.* 2009] E. Wang, N. Gardner and A. Shukla. The blast resistance of sandwich composites with stepwise graded cores. *International Journal of Solids and Structures*, **46**(18-19):3492–3502, 2009.

[Whittaker 1988] E.T. Whittaker. *A Treatise on the Analytical Dynamics of Particles and Rigid Bodies*. Cambridge University Press, 1988.

[Wilkins 1964] M.L. Wilkins. Calculations of Elastic Plastic Flow. *Methods in Computational Physics*, **3**:211–263, 1964.

[Winterbone 1996] D.E. Winterbone. *Advanced Thermodynamics for Engineers*. Butterworth Heinemann, 1996.

[Xue and Hutchinson 2003] Z. Xue and J.W. Hutchinson. Preliminary assessment of sandwich plates subject to blast loads. *International Journal of Mechanical Sciences*, **45**(4):687–705, 2003.

[Xue and Hutchinson 2004] Z. Xue and J.W. Hutchinson. A comparative study of impulse-resistant metal sandwich plates. *International Journal of Impact Engineering*, **30**(10):1283–1305, 2004.

[Yandzio and Gough 1999] E. Yandzio and M. Gough. *Protection of Buildings Against Explosion*. The Steel Construction Institute, 1999.

[Young 2010] C. Young. *Metrics and Methods for Security Risk Management*. Syngress, 2010.

[Yu *et al.* 2006] M.-H. Yu, G.-W. Ma, H.-F. Qiang and Y.-Q. Zhang. *Generalized Plasticity*. Springer-Verlag Berlin Heidelberg, 2006.

[Zhang *et al.* 2012] L. Zhang, J.M.F. Ferreira, S. Olhero, L. Courtois, T. Zhang, E. Maire and J. C. Rauhe. Modeling the mechanical properties of optimally processed cordierite-mullite-alumina ceramic foams by X-ray computed tomography and finite element analysis. *Acta Materialia*, **60**(10):4235–4246, 2012.

[Zhu and Lu 2007] F. Zhu and G. Lu. A review of blast and impact of metallic and sandwich structures. *Electronic Journal of Structural Engineering, Special Issue: Loading on Structures*, 92–101, 2007.

[Zhu *et al.* 2008a] F. Zhu, G. Lu and R. Zou. On the development of a knowledge-based design support system for energy absorbers. *Materials & Design*, **29**(2):484–491, 2008.

[Zhu *et al.* 2008b] F. Zhu, L. Zhao, G. Lu and Z. Wang. Deformation and failure of blast-loaded metallic sandwich panels — Experimental investigations. *International Journal of Impact Engineering*, **35**(8):937–951, 2008.

[Zhu *et al.* 2009a] F. Zhu, Z. Wang, G. Lu and L. Zhao. Analytical investigation and optimal design of sandwich panels subjected to shock loading. *Materials & Design*, **30**(1):91–100, 2009.

[Zhu *et al.* 2009b] F. Zhu, L. Zhao, G. Lu and E. Gad. A numerical simulation of the blast impact of square metallic sandwich panels. *International Journal of Impact Engineering*, **36**(5):687–699, 2009.

[Zienkiewicz *et al.* 2005] O.C. Zienkiewicz, R.L. Taylor and J.Z. Zhu. *The Finite Element Method: Its Basis and Fundamentals*. Butterworth-Heinemann, 5^{th} edition, 2005.